

*Imaging Microphysiometry
of 2D and 3D Tissue Models:
Method Development and Application*

DISSERTATION

zur Erlangung des

DOKTORGRADES DER NATURWISSENSCHAFTEN

(Dr. rer. nat.)

der Fakultät für Chemie und Pharmazie der Universität Regensburg



vorgelegt von

Lisa Pütz (geb. Sauer) aus Dachau

im Jahr 2021

*Imaging Microphysiometry
of 2D and 3D Tissue Models:
Method Development and Application*

DISSERTATION

zur Erlangung des

DOKTORGRADES DER NATURWISSENSCHAFTEN

(Dr. rer. nat.)

der Fakultät für Chemie und Pharmazie der Universität Regensburg



vorgelegt von

Lisa Pütz (geb. Sauer) aus Dachau

im Jahr 2021

Diese Arbeit entstand in der Zeit von April 2017 bis Juli 2021 am Institut für **Analytische Chemie, Chemo- und Biosensorik der Fakultät für Chemie und Pharmazie** der Universität Regensburg.

Die Arbeit wurde unter der Leitung von Prof. Dr. Joachim Wegener angefertigt.

Promotionsgesuch eingereicht am: _____

Kolloquiumstermin: _____

Prüfungsausschuss:

Vorsitzender: Prof. Dr. Oliver Tepner

Erstgutachter: Prof. Dr. Joachim Wegener

Zweitgutachter: Prof. Dr. med. Stephan Schreml

Drittprüfer: Prof. Dr. Hans-Heiner Gorris

Für meine Familie

“If you can dream it, you can do it!”

WALT DISNEY

CONTENTS

1	INTRODUCTION	1
1.1	pO ₂ and pH as Two Fundamental Parameters in Living Organisms	1
1.2	Multicellular Spheroids as <i>In Vitro</i> Tissue Models	7
1.3	Strategies of Pharmacological Intervention with Energy Metabolism	9
1.4	Technical State-of-the-Art in Oxygen and pH Measurements for <i>In Vitro</i> Models	12
2	OBJECTIVES	21
3	MATERIALS AND METHODS	24
3.1	Cell Culture Techniques	24
3.1.1	Cultivation of Adherent Mammalian Cell Lines	24
3.1.2	Subcultivation	26
3.1.3	Cultivation of Spheroids	28
3.1.4	Cryopreservation	29
3.1.5	Buffer and Solution Compositions	29
3.2	Microscopic Techniques	32
3.2.1	Phase Contrast Microscopy	32
3.2.2	24-Channel Optical Microscopy	32
3.2.3	Confocal Laser Scanning Microscopy (CLSM)	34
3.2.4	Cytochemical Staining	34
3.2.4.1	Live/Dead Staining	34
3.2.4.2	Cytoskeleton and Cell Nucleus Staining	36
3.3	Impedance Spectroscopy	38
3.3.1	Electric Cell-Substrate Impedance Sensing (ECIS™)	38
3.3.2	Array Types & Experimental Setup	39
3.3.3	Preparation for Cell Experiments	41
3.3.4	Impedance-based Sensing of Cellular Phenotypes	42
3.3.4.1	Monitoring the Kinetics of Cell Spreading	43
3.3.4.2	Monitoring the Kinetics of Cell Proliferation	44
3.3.4.3	Monitoring the Wound Healing Behavior	45

3.3.4.4	Monitoring the Cellular Motility by Micromotion Measurements	45
3.4	Ratiometric Optical Oxygen Sensing	47
3.4.1	Principle of Ratiometric Optical Sensing	47
3.4.2	Measurement Setup to Monitor Oxygen Concentrations	50
3.4.2.1	Ratiometric Oxygen Sensing	50
3.4.2.2	Oxygen Sensing on the Basis of Fluorescence Decay Time Detection	51
3.4.3	Cell Preparation for Optical Sensing	52
3.4.4	Calibration of the Oxygen-sensitive Sensor Foil	53
3.4.5	Calculation of the <i>Apparent Oxygen Consumption Rate</i>	54
3.5	Monitoring the Intracellular pH _i Value	56
3.5.1	Working Principle of Intracellular pH _i Sensing	56
3.5.2	Staining Protocol for the pH-sensitive Dye	57
3.6	Cytotoxicity Study of Bisphenol A	58
3.7	Monitoring the Biological Impact of Glyphosate on Animal Cells	60
3.7.1	Cell Viability Assay	60
3.7.2	Impedance-based Phenotypic Assays	62
3.7.3	Monitoring of the Respiratory Activity	62
3.7.4	Post-Exposure Cell Staining	63
4	IMAGE-BASED SENSING OF OXYGEN CONCENTRATIONS AND DIFFUSION PROCESSES	65
4.1	Respiratory Activity of Different Cell Lines	65
4.1.1	Experiments with Cell Monolayers (2D)	65
4.1.2	Experiments with 3D-Tissue Models	67
4.2	Influence of the Sensor Foil Thickness	75
4.3	Detection of Horizontal Oxygen Gradients	77
4.4	Visualization of Vertical Oxygen Gradients above Adherent Cells	81
4.5	Discussion	85
4.6	Outlook	95
5	MONITORING OF THE PH-DEPENDENCY OF CELLULAR PHENOTYPES	97

5.1	pH-Dependency of Adhesion Processes	97
5.2	pH-Dependency of Proliferation Rates	104
5.3	pH-Dependency of Wound Healing Behavior	109
5.4	pH-Dependency of Cellular Micromotion	116
5.5	pH-Dependency of the Respiratory Activity	118
5.5.1	Experiments with 2D Cell Monolayers	118
5.5.2	Experiments with 3D Tissue Models	120
5.6	Adaption of the Intracellular pH_i to Changes in the Extracellular pH_e	125
5.7	Discussion	128
5.8	Outlook	141
6	CYTOTOXICITY STUDY WITH BISPHENOL A	143
6.1	Influence on the Respiratory Activity	143
6.1.1	Image-based Sensing of Oxygen Consumption of Cells on Top of the Sensor Foil	143
6.1.2	Sensing of Oxygen Consumption of Cells in Proximity to the Sensor Spot	145
6.2	Discussion	148
6.3	Outlook	150
7	PROFILING THE BIOLOGICAL IMPACT OF GLYPHOSATE ON ANIMAL CELLS	152
7.1	Acute Toxicity of Glyphosate	152
7.1.1	Cell Viability Assay for Acute Toxicity Examinations	152
7.1.2	Impedance-based Sensing of the Acute Toxicity	154
7.2	Comparison of Cellular Phenotypes under the Influence of Glyphosate	156
7.2.1	Influence on Proliferation Rates	156
7.2.2	Influence on Migration Behavior	158
7.2.3	Influence on Cellular Micromotion	160
7.3	Respiratory Activity under Glyphosate Exposure	162
7.4	Post-Exposure Cell Staining	164

7.5	Discussion	166
7.6	Outlook	173
8	SUMMARY	175
9	ZUSAMMENFASSUNG	178
10	REFERENCES	182
11	APPENDIX	198
11.1	Supplementary Information	198
11.2	List of Abbreviations	207
11.3	Materials and Instrumentations	210
11.4	Curriculum Vitae	213
11.5	Danksagung	216
11.6	Eidesstattliche Erklärung	219

1 INTRODUCTION

1.1 PO₂ AND PH AS TWO FUNDAMENTAL PARAMETERS IN LIVING ORGANISMS

Living organisms are highly dependent on sensitively adjusted oxygen tensions as well as on pH milieus and gradients within their bodies. The metabolism of every single cells is set in a special environment with an adapted intracellular equilibrium with respect to oxygen and pH conditions. Oxygen is a chemical element being the most frequent element in the earth crust with a mass portion of around 50 % and after iron, it is the second most common element on earth. It is a colorless and odorless gas making up 21 % of the ambient air. Oxygen is produced by the photosynthesis of plants and other organisms e.g. algae and cyanobacteria, during the conversion of carbon dioxide and water into sugar and oxygen which is driven by light energy (Dogutan, D. *et al.* 2019). Inversely, oxygen is consumed by respirating organisms in order to produce energy in form of adenosine triphosphate (ATP). The respiration under aerobic conditions normally encompasses glycolysis, the oxidative decarboxylation of pyruvate, the generation of reduction equivalents NADH/H⁺ in the tricarboxylic acid cycle (citric acid cycle) and eventually the reduction of O₂ in the oxidative phosphorylation (OXPHOS). This series of reactions including the final reduction of oxygen to water in the respiratory chain, produces 32 ATP molecules from one initial glucose molecule. The respiratory chain is basically an electron transport chain consisting of multiple redox reactions in series. This reaction chain is driven by the enzyme complexes I to IV as well as the coenzyme Q and cytochrome c while all are located in the inner mitochondrial membrane. The mitochondrion is a cell organelle which is enclosed by a phospholipid double layer and additionally contains an inner membrane while both membranes have different properties. The outer membrane of the mitochondrion is highly permeable for ions and small molecules due to integral membrane proteins, the so-called porins. The inner membrane is heavily folded in order to enhance the surface area for protein localization being important for the respiratory chain. The maintenance of the complex O₂ homeostasis is crucial for the survival of all living organisms. The oxygen concentrations within a body and certain tissues strongly differ due to temporal variations in oxygen availability e.g. as muscles work or embryonic development. Furthermore, the occurrence of a vascular occlusion for instance can interrupt the local blood supply meaning oxygen levels can change in small parts or the entire body. Distinct tissues within the human body have developed different metabolisms which are adapted to their respective demands and consequently show individual *oxygen consumption rates*. Oxygen is mainly transported by the blood circulation when being reversibly bound to the protein hemoglobin in red blood cells with about 0.2 mL of oxygen per milliliter of arterial blood. While the oxygen release to the tissue is enhanced by decreasing oxygen partial pressure as well as increasing CO₂ levels, it is additionally influenced by temperature and pH (Popel, A. *et al.* 1989). Since variations in the oxygen supply can occur, it is highly necessary for cells to be able to sense oxygen levels in their extra- and intracellular compartments and hence to adapt their

respiratory activity accordingly. William G. Kaelin, Peter J. Ratcliffe and Gregg L. Semenza found the molecular switch that regulates the cellular adaptation to low oxygen levels (hypoxia) and were able to explain the phenomenon which is schematically illustrated in Fig. 1.1.

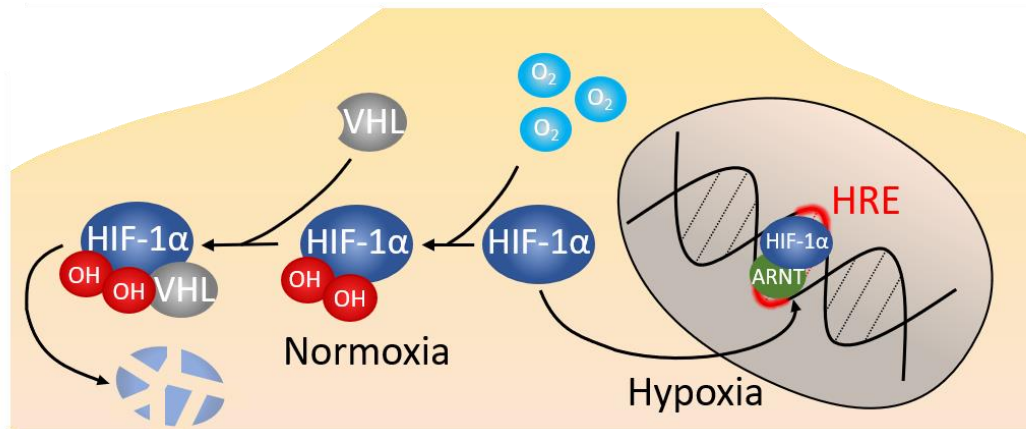


Fig. 1.1 Schematic illustration of the principle of how cells sense different oxygen levels. If oxygen levels are high, the *hypoxia-inducible transcription factor* (HIF-1 α) is hydroxylated twice, leading to the recognition of the *von Hippel-Lindau* (VHL) tumor suppressor protein resulting in proteasomal degradation of the complex at normoxic conditions. In contrast, low oxygen levels (hypoxia) lead to the accumulation of HIF-1 α and consequently the formation of a complex binding to the DNA which causes the activation of the *hypoxia response element* (HRE) resulting in the expression of the respective genes and proteins. Adapted from the Prize announcement (NobelPrize.org).

In 2019 they were awarded the Nobel prize in physiology and medicine for their discoveries. The first noted physiological change due to low oxygen caused by high altitudes or anemia (insufficient number of red blood cells) was the detection of enhanced expression rates of the hormone erythropoietin (EPO) in the kidney. The enhanced expression of EPO is triggered by the activation of a specific region on the EPO gene, the so-called *hypoxia response element* (HRE). The release of EPO leads to an increased production of red blood cells and hence increased O₂-carrying capacity in the blood. The increased expression of EPO allowed for the identification and isolation of a protein complex called transcription factor protein complex HIF (*hypoxia-inducible transcription factor*) which binds to a specific DNA segment in an O₂-dependent manner. HIF is present in all cell types and regulates the activation and expression of more than 70 genes. It consists of a heterodimeric protein which is composed of two subunits. The HIF-1 β (or ARNT - *aryl hydrocarbon receptor nuclear translocator*) being constitutively expressed binds to the DNA within the HRE after the binding of the second subunit HIF-1 α . HIF-1 α accumulates under hypoxia and is degraded under normoxic conditions (Semenza, G. *et al.* 2004). The first step of the degradation is the two-fold hydroxylation of HIF-1 α by a set of enzymes. The hydroxylation allows for the recognition by the *von Hippel-Lindau* (VHL) tumor suppressor protein revealing ubiquitin ligase activity resulting in the proteasomal degradation (Brunelle, J. *et al.* 2005). The ability to accurately sense oxygen concentrations is crucial for cells in order to adapt their respiratory and metabolic activity appropriately to certain conditions.

Another key factor controlling metabolic activity is the pH value in the extracellular environment as well as in the intracellular compartments of living cells. Already in 1906, the pH was defined as the negative decimal

logarithm of the activity - or approximately the concentration - of hydrogen ions by Sørensen (Buck, R. *et al.* 2002). The higher the hydrogen concentration is, the lower is the corresponding pH value and hence the more acidic is the respective solution.

The maintenance of specific pH values and gradients as well as sensing of pH changes is essential for mammalian cells. The pH value varies between different cells and even within one cell considering that cells are highly compartmentalized and exhibit different organelles. The individual organelles reveal individual pH values to provide an optimized chemical environment for the organelle-specific proteins. All proteins are highly dependent on pH since protonation or deprotonation events ensure or trigger physiologically important conformations and hence their function (Whitten, S. *et al.* 2005). Furthermore, pH also determines the charge of biological surfaces as well as metabolic reactions via the proton motive force for instance being the key for the generation of cellular energy. Slight variations in pH levels can be counterbalanced by the cells due to inherent buffer capacities of various weak acids and bases like phosphate groups and certain side chains of amino acids being localized in the intracellular cytosolic compartment (Roos, A. *et al.* 1981). Another effective proton buffer is provided by HCO_3^- ions which can be generated by the hydration and subsequent deprotonation of CO_2 in a pH-dependent manner, while the uncharged carbon dioxide can freely diffuse over biological membranes (Missner, A. *et al.* 2008) (see Fig. 1.2). Over the last 20 years researchers were able to identify 14 genes which encode proteins related to bicarbonate transport activity which can be divided into two groups: (i) electroneutral acid loading transporters or exchanger and (ii) electrogenic plasma transmembrane co-transporter (Cordat, E. *et al.* 2009). The driving forces of both transporters are ion gradients across the membrane. Anion exchangers (AEs) or acid-loadings transporters exchange the intracellular basic HCO_3^- ions by the import of pH-neutral Cl^- ions causing a cytosolic acidification while Na^+ -coupled HCO_3^- transporter (NBCs) incorporate extracellular Na^+ and HCO_3^- ions due to the inward-directed sodium gradient of mammalian cells leading to an internal alkalinization due to the accumulation of the base HCO_3^- (Cordat, E. *et al.* 2009). Another important and well-characterized group of transmembrane transporting proteins are the Na^+ - H^+ exchanger (NHE1 – NHE7). NHE1 is present in almost every cell and reveals twelve membrane-spanning segments (Bookstein, C. *et al.* 1994, Slepko, E. R. *et al.* 2007) exporting H^+ out of the cytosol of the cells in exchange for monovalent sodium ions due to the sodium gradient. Notable is the fact that the NHE1 transporter is quiescent at a set point pH value of 7.0 (Cardone, R. *et al.* 2005). All these systems working to stabilize the pH inside the cells are crucial to enable the homeostasis of the finely controlled cytosolic pH. However, intracellular acidification can be caused by the continuous uptake of protons and the simultaneous efflux of negatively charged ions with alkaline properties driven by the electrical potential across the membrane which is negatively charged on the inside and positively charged on the outside. Another factor contributing to the intracellular acidification is the generation of net acid equivalents during ATP-production (Casey, J. *et al.* 2010). The slightly acidic intracellular pH values of $\text{pH}_i \sim 6.9 - 7.2$ are normally accompanied by a slightly alkaline extracellular milieu ($\text{pH}_e \sim 7.2 - 7.5$) at

physiological conditions. This pH gradient is shown by normal or healthy cells and is known to be reversed in cancer cells. Cancer cells tend to acidify their extracellular milieu to $\text{pH}_e \sim 6.7 - 7.1$ with a corresponding slightly more alkaline intracellular pH value ($\text{pH}_i \sim 7.2 - 7.5$) (Webb, B. *et al.* 2011).

Otto Warburg was the first to observe this specific metabolic pattern in living tissue slices of tumors in 1924. The lactate production was reported to occur in tumor tissue even under aerobic conditions (Warburg, O. *et al.* 1924). In general, mammalian cells can generate energy by two major metabolic processes: the lactic acid production (anaerobic respiration) or by aerobic respiration via oxidative phosphorylation taking place in the mitochondria of cells. In contrast to the respiratory chain, lactic acid production only occurs in the cytosolic compartment. Metabolic glycolysis under anaerobic conditions leads to the conversion of glucose ($\text{C}_6\text{H}_{12}\text{O}_6$) to pyruvate ($\text{C}_3\text{H}_5\text{O}_3$) followed by a reduction to lactate ($\text{C}_3\text{H}_7\text{O}_3$) yielding two ATP per glucose molecule. In contrast to the respiratory chain, this process is independent of the presence of oxygen and was found to be related to an increased glucose uptake in cancer cells with the consequence of decreasing extracellular pH values (Warburg, O. *et al.* 1927). This phenomenon is called the *Warburg effect* and ensures a functioning cellular metabolism even under hypoxic conditions caused by the lack of blood vessels. The reversed pH gradient promotes cancer progression-inducing migration and tumor invasion, leads to increased proliferation rates and enhances cell survival since apoptosis is associated with acidic intracellular pH values. These inverted pH values require an adapted regulation and sensing of pH and thus changes in expression and activity of transmembrane transporters. The reversed pH gradient homeostasis is mainly maintained and generated by NHE1, V-ATPases, monocarboxylate transporters (MCTs), (bi)carbonate co(transporters), and carbo-anhydrases (CA, CAIX, CAXII) which are schematically shown in Fig. 1.2.

Boedtkjer, E. *et al.* 2013 reported about 20 – 30 % higher density of NBC1 and NHE1 in primary breast carcinomas and metastases compared to normal breast tissue. The upregulated expression of these cotransporters seems to be a major cause for extracellular acidification and intracellular alkalinization. There are also studies indicating that the increased proton transport activity of NHE1 seems to accelerate the degradation of the extracellular matrix in invadopodia of human breast cancer (Busco, G. *et al.* 2010) facilitating cellular migration.

Monocarboxylate cotransporters (MCTs) catalyze the transport of metabolic products like lactate, pyruvate and ketone bodies across the plasma and the mitochondrial membranes. The MCT family consists of 14 members while only MCT1 – MCT4 have been characterized as proton-dependent membrane-mediating transporters. The efflux of lactic acid and protons being the byproducts of glycolysis under anaerobic conditions is fundamental for pH regulation and maintenance (Halestrap, A. *et al.* 2004). Since cancer cells are known to exhibit enhanced anaerobic metabolism in the form of glycolysis, the efflux of lactic acid is drastically increased contributing to the extracellular acidification.

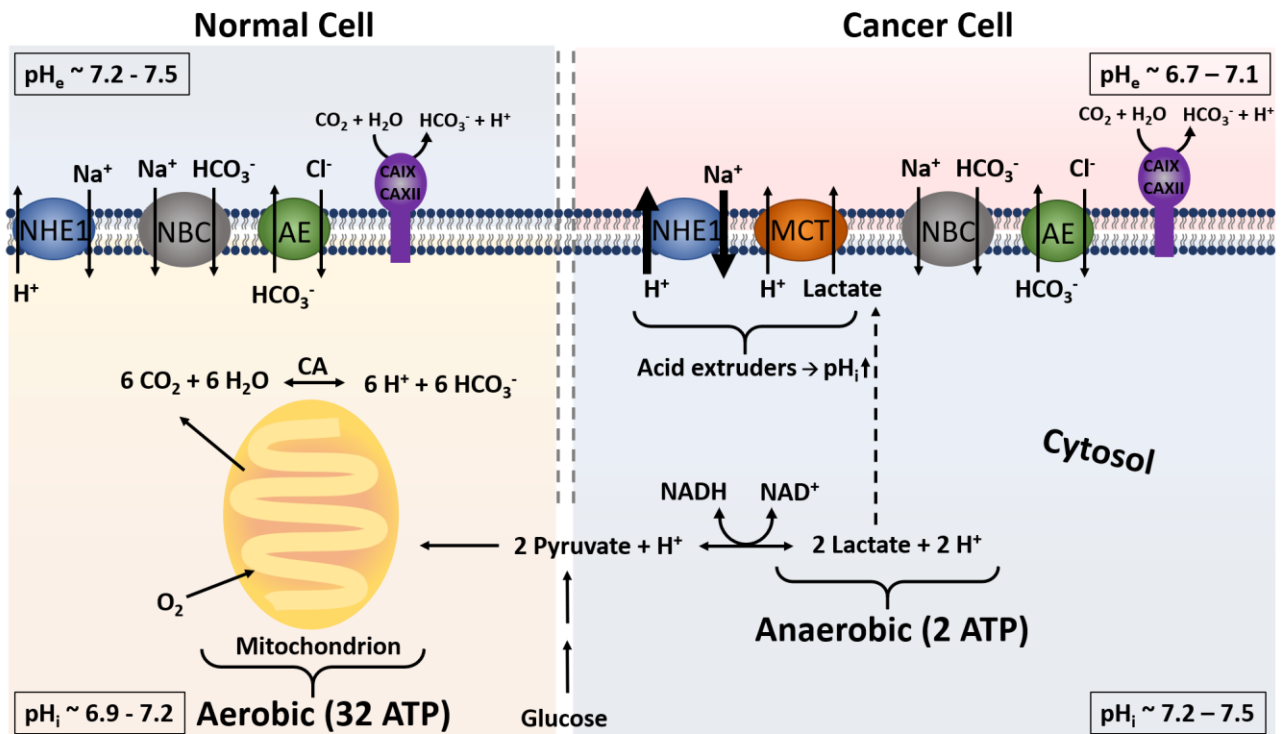


Fig. 1.2 Schematic illustration of the pH gradient of normal cells and the reversed pH gradient in cancer cells which is called the *Warburg effect*. The reversed pH gradients are caused by aerobic or anaerobic respiration and maintained due to altered ion transporter activities of the Na^+ - H^+ exporter (NHE1) and the monocarboxylate transporter (MCT) equally pumping protons out of the cytosol causing extracellular acidification of cancer cells. Adapted from Casey, J. *et al.* 2010.

In addition to transmembrane transport systems working along the chemical gradient, cells have surface receptors sensing minute pH changes to be able to respond appropriately. These surface receptors can be divided into two groups: pH-sensitive receptors like G protein-coupled receptors (GPCRs) and ion channels like acid-sensing ion channels (ASICs) or transient receptor potential channels (TRPs). pH-sensitive GPCRs are thought to respond to extracellular acidification due to the protonation of the imidazole side chain of histidine residues resulting in conformational changes of the seven transmembrane receptors (Wiley, S. *et al.* 2019). The conformational changes cause the receptor activation and mediate signals inside the cells triggering downstream pathways. Up to now, GPR4, GPR65 (TDAG8), GPR68 (ovarian cancer GPCR 1 or OGR1) and GPR132 (G2A) were demonstrated to be pH-sensitive and were found to be overexpressed in various human cancers e.g. tumors of the breast, ovary, prostate, skin, pancreas, colon, liver and kidney (Sun, X. *et al.* 2010; Wiley, S. *et al.* 2019). The four GPCRs likely regulate cancer cell metastasis, proliferation, functions of the immune system, inflammatory reactions as well as angiogenesis (Justus, C. *et al.* 2013). The low pH-driven activation of GPR4 is discussed to increase adhesiveness of endothelial cells and potentially serves as pH sensor for vascular cells and blood cells. pH sensing within the bloodstream is crucial for the detection of inflammatory sites as they exhibit an acidic microenvironment with subsequent activation of certain signaling pathways (Chen, A. *et al.* 2011). In contrast to GPR4 expression in normal cells, cancer cells seem to use overexpressed GPR4 for tumor growth and angiogenesis since tumor growth is observed to be strongly

reduced in mice lacking GPR4 (Wyder, L. *et al.* 2011). GPR65 was reported to show functions as a contextual tumor suppressor (Justus, C. *et al.* 2017) and to support the survival of photoreceptors in the degenerating retina (Ail, D. *et al.* 2015) and was also discussed to be associated with multiple sclerosis since higher GPR65 signals have been demonstrated to suppress autoimmune diseases (Wirasinha, R. *et al.* 2018). Nevertheless, other studies indicate that overexpressed GPR65 in glioblastoma seem to predict significantly shorter survival rates of patients (Wang, H.-X. *et al.* 2018). Some studies addressing GPR68 imply tumor suppression effects due to significantly inhibited cell proliferation and migration of ovarian cancer cells (Ren, J. *et al.* 2011) and of prostate cancer (Singh, L. *et al.* 2007) while on the other hand some studies suggest GPR68 deficiency seems to reduce the tumorigenesis of melanoma cells significantly (Li, H. *et al.* 2009) which stands in stark contrast to the aforementioned findings. The same seems to be the case for the GPR132 as it seems to play a crucial role in autoimmune reactions (Kabarowski, J. *et al.* 2009), is also discussed to be related to inflammatory autoimmune disease as well as atherosclerosis (Kabarowski, J. *et al.* 2001) and GPR132 also activates a specific G protein combination inducing apoptosis (Lin, P. *et al.* 2003). In contrast to these disease-suppressing properties it was also reported to promote breast cancer metastasis by tumor-macrophage interplay stimulation (Chen, P. *et al.* 2017).

All in all, the known functions of pH-sensing GPCRs are strongly cell type-dependent and differ between tumor-suppressing effects and tumor-inducing transformations. Moreover, signaling triggered by the activation of pH-sensitive proteins is very complex and leads to various changes in the cellular response and metabolic activity. There are a number of proteins and receptors being overexpressed in certain cancer tissues and numerous molecular interactions with specific recognition elements are known. The aforementioned pH regulations and sensing mechanisms only account for a small part and are far from complete. Nevertheless, the process of pH homeostasis is highly cell type-specific and many processes are still being investigated indicating the importance of further insight into specific relations between pH values and cell fate.

1.2 MULTICELLULAR SPHEROIDS AS *IN VITRO* TISSUE MODELS

In vitro studies with two-dimensional cell layers allow for initial investigations in the context of drug development and testing, toxicity studies or the examination of changes in proteomic expression levels with the advantage of relatively easy assay protocols and well-defined readout techniques. Since multicellular organisms are highly complex systems showing diverse tissue architectures and cellular compositions, it is crucial to develop tissue-like *in vitro* models as well as appropriate sensing and readout methods.

Several non-scaffold-based methods are known for the cultivation of three-dimensional tissue constructs. A prominent example are so-called spheroids which are spherical cell aggregates consisting of some thousand cells. The most widely used techniques for the formation of spheroids are: (i) the liquid overlay technique (LOT), (ii) the hanging drop technique (HDT) and (iii) the carboxymethyl cellulose technique (CCT) (Fig. 1.3).

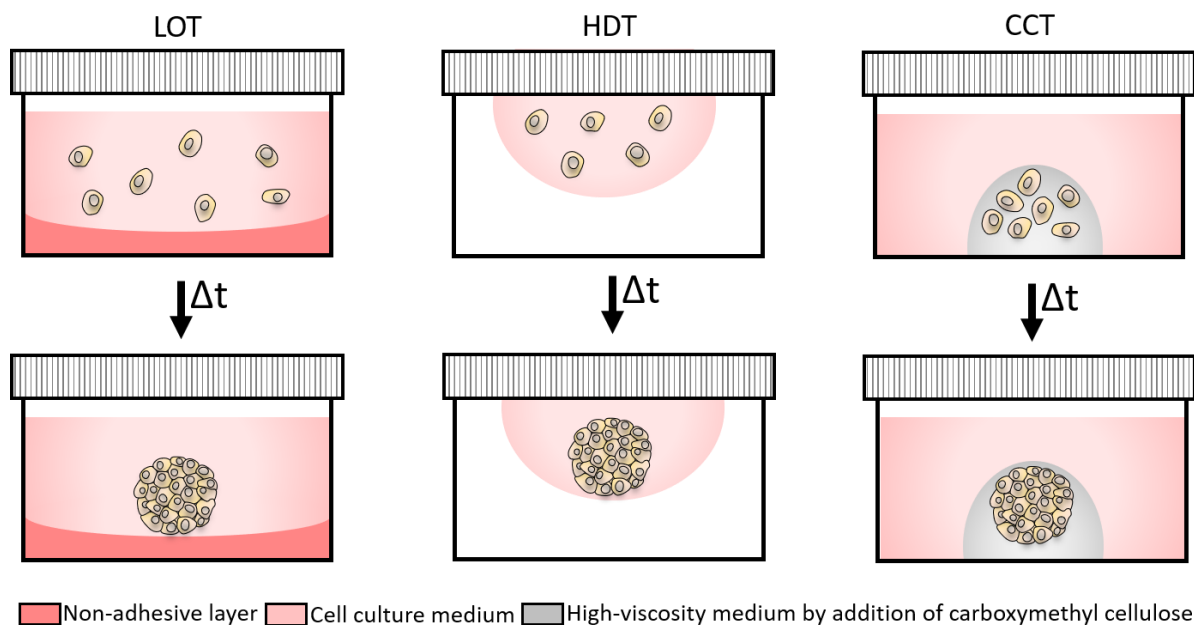


Fig. 1.3 Methods for the formation of 3D tissue/spheroids: liquid overlay technique (LOT), hanging drop technique (HDT) and the carboxymethyl cellulose technique (CCT) using the advantage of non-adhesive coated substrates, the cell sedimentation inside a liquid droplet and the decreased sedimentation due to increased viscosity in the cell culture medium, respectively, leading to the formation of cell aggregates. Adapted from Gaebler, M. *et al.* 2017.

LOT relies on non-adhesive surfaces forcing the cells to adhere to each other, resulting in cell aggregation and spheroid formation. The HDT is based on the sedimentation of cells in a cell culture medium droplet which is placed on the underside of the lid of an appropriate cell culture vessel. Sedimentation within the droplet also leads to spheroid formation due to the lack of adhesive surfaces. The CCT relies on the addition of carboxymethyl cellulose to the cell culture medium in order to increase the viscosity which prevents cell sedimentation and in turn accelerates spheroid formation (Metzger, W. *et al.* 2011).

Spheroids reflect the *in vivo* situation more precisely than cell monolayers and can mimic the characteristics of solid tumors like physiological responses, stimulus conduction due to the spherical architecture as well as gene expression patterns and even drug resistances (Costa, E. *et al.* 2016).

Therefore, three-dimensional tissue models like spheroids are celebrated to bridge the gap between two-dimensional *in vitro* testings and *in vivo* animal experiments although these tissue models are not interlaced with blood vessels and therefore only represent non-vascularized tissue. Blood vessels are normally responsible for oxygen and nutrient supply as well as for the elimination of metabolic waste. Due to the cell-cell contacts to neighboring cells in all directions within the cultured spheres as well as the lack of blood vessels, metabolic zones in a core-shell-like structure are formed. Oxygen and nutrient accessibility decreases towards the spheroid's core and inversely the metabolic waste concentration, lactate accumulation and H^+ concentration increases towards the center where cell density is highest. The emerging metabolic zones differ with respect to the metabolic and respiratory activity of the cells located within (compare Fig. 1.4).

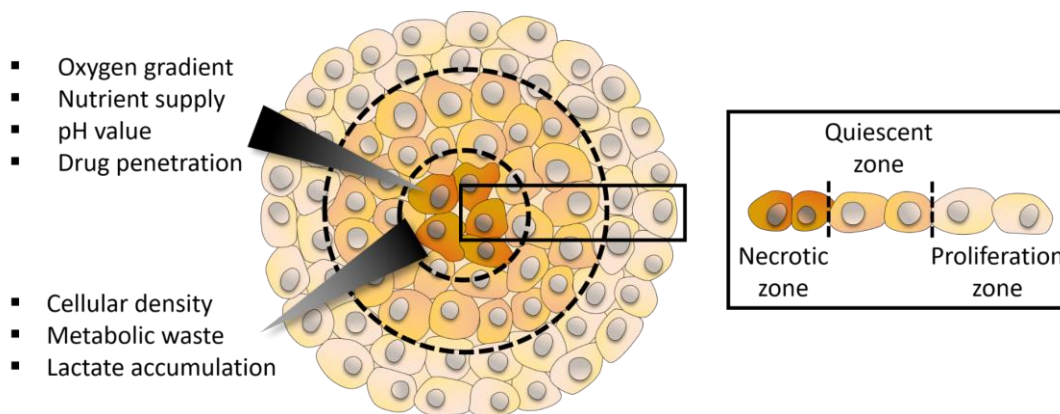


Fig. 1.4 Schematic illustration of emerging metabolic zones within a three-dimensional spheroid. Starting with proliferating cells in the periphery, a zone of quiescent cells is found underneath, and hypoxic or even necrotic tissue is located in the spheroid's core. The consumption of oxygen by the cells in the proliferating zone leads to oxygen depletion in the center and the lack of blood vessels also causes an inhibited nutrient supply towards the center as well as increasing lactate and metabolic waste accumulation. Adapted from Costa, E. *et al.* 2016.

Three different zones can be observed within a spheroid: going from the outside to the inside, the zone closest to the surface consists of vital cells forming a proliferating layer which is followed by a zone of quiescent or senescent cells reaching the innermost zone of hypoxic or even necrotic tissue in the core of the spheroid (Hirschhaeuser, F. *et al.* 2010; Costa, E. *et al.* 2016).

The spheroid formation can also be performed using different cell lines to create co-cultured core-shell-like tissues. Co-cultured spheroids can possibly mimic natural situations even more precisely. Spheroids additionally allow for the examination of the penetration depth of certain drugs, the development of specific tissue-targeting diagnostics or therapeutic agents, proof-of-concept measurements for designed recognition elements on a molecular level and are furthermore highly important to develop appropriate measurement techniques. These desirable measurement devices and techniques could further improve *body-on-a-chip* approaches and enable accurately adjusted treatment strategies for the individual patient.

1.3 STRATEGIES OF PHARMACOLOGICAL INTERVENTION WITH ENERGY METABOLISM

A deeper understanding of the metabolism of cancer cells is important for a continuing improvement of therapeutic strategies. A few selected approaches will be discussed to demonstrate the potential of possible cancer treatments. One of the key differences between normal and cancer cells is the *Warburg effect* and its influence on the cellular metabolism as is shown in Fig. 1.2. Increased glucose uptake in metabolically active cancer cells on the one hand leads to accelerated glycolysis and on the other hand to slowed down mitochondrial activity as glycolysis with subsequent lactic acid production is the preferred form of energy generation in cancer cells. This in turn leads to an extracellular acidification and intracellular alkalinization as protons accumulate on the extracellular side of the membrane. These pH gradients are possible targets for drug design since their inversion could cause an inhibition of migration and angiogenesis or even cell death for cancer cells. The challenge for drug development is the highly specific targeting of cancer cells while avoiding side effects.

Drugs targeting the reversed pH gradient are often used in combination with anticancer drugs. Schwartz, L. *et al.* 2017 reported about decreased cancer growth in murine xenografts after treatments with a combination of α -lipoic acid and hydroxycitrate. α -lipoic seems to inhibit the pyruvate dehydrogenase kinase (PDK). PDK is known to be upregulated in cancers cells in order to inactivate the enzyme pyruvate dehydrogenase. This enzyme pyruvate dehydrogenase (PDH) catalyzes the first step of the pyruvate conversion via aerobic respiration. The inhibition of PDK in cancer cells consequently leads to increased PDH activity which favors the oxidative phosphorylation pathway and consequently less lactic acid is produced which is important for the homeostasis of the inverse pH gradient in cancer cells. The combination of the metabolic treatment with α -lipoic acid / hydroxycitrate and a cancer therapy drug (Naltrexone) is already reported to show promising effects with respect to the survival rate of patients (Schwartz, L. *et al.* 2017).

An alternative approach to downregulating glycolysis and the lactic acid production in cancer cells via targeted inhibition of e.g. PDK is, on the contrary, to significantly increase glycolysis and at the same time to impair the pH-stabilizing systems of the cancer cell. The combination of both factors should cause uncontrollable intracellular acidification resulting in cancer cell death (Lee, Z.-W. *et al.* 2017). It was shown that GYY4137 (sodium salt) is a slow H_2S -releasing donor, leading to increased glycolysis and impaired activity of anion exchangers as well as NHE1, resulting in cancer-specific intracellular hyper acidification. The combination of GYY4137 with the anti-cancer drugs simvastatin (inhibiting MCT4) or metformin were demonstrated to even cause cancer cell death in more aggressive cancers.

Another idea is the selective inhibition of carbonic anhydrase (CAII, CAIX, CAXII) being overexpressed in glioblastoma multiforme brain tumors (Marathe, K. *et al.* 2016). The inhibition of CA with the drug topiramate seems to induce acute intracellular acidification while contralateral tissue was not affected.

The acidic extracellular environment of tumors can also be used as an “activating environment” for targeted drug release or enhanced specific interactions of e.g. proteins, antibodies or receptors with the cancer cells. A promising tumor-targeting approach is the formation of pH-responsive polymeric micelles out of amphiphilic MPEG-poly(β -amino ester) block copolymers (MPEG - hydrophilic methyl ether poly(ethylene glycol)) which may serve as drug delivery systems (Ko, J. *et al.* 2007; Min, K. *et al.* 2010). These self-assembled micelles are a few nanometers in size and can be loaded with doxorubicin or camptothecin - two well-characterized anti-cancer drugs - and the targeted rapid release in weakly acidic environments is reported to entail suppressed tumor growth and increased therapeutic efficacy with simultaneously fewer side effects compared to free anti-cancer drugs. The acidic extracellular pH of cancer cells has been proven to be a powerful point of application for pharmacological interventions. There are several nano-delivery systems showing highly promising pH sensitivity; however, the biocompatibility and biodegradability still need to be improved. Nevertheless, the tissue-targeted accumulation of multifunctional diagnostic and therapeutic delivery systems could offer the possibility of continuous cancer tracking with simultaneous treatment (Liu, J. *et al.* 2014).

Regarding the respiratory activity and the oxygen sensing of cells, there are also treatment strategies being explored. The hypoxia sensing element HIF-1 α is known to be overexpressed in many human cancers due to the intertumoral hypoxia as well as genetic alterations causing accelerated angiogenesis (blood vessel formation) and glucose transport, increased amounts of glycolytic enzymes and invasion factors, the inhibition of apoptosis and the promotion of metastatic behavior (Semenza, G. *et al.* 2003). All these factors are important for tumor growth and metastasis and explain why HIF-1 α is often overexpressed. Furthermore, HIF-1 α is possibly associated with enhanced anti-cancer drug resistance. There are studies indicating that a number of anti-cancer agents show a decreasing HIF production even though they have not been directly designed to inhibit the transcription factor (Welsh, S. *et al.* 2003). Accordingly, Yeo, E.-J. *et al.* 2003 reported about targeted inhibition of HIF-1 α by a small molecule (YC-1) causing decreased angiogenesis and inhibition of tumor growth. Recent studies of Zhang, X. *et al.* 2020 demonstrated positive effects regarding the inhibition of tumor growth and metastatic behavior using a combination of common anti-cancer drugs and a HIF-1 α -inhibitor encapsulated in specially designed nanoparticles. The applied anti-cancer drug cisplatin alone has the grave disadvantage of nonselective tissue distribution and hence serious side effects. The loading of microporous organosilica shell-coated nanoparticles with the drug however enables a more tissue-targeted drug release. The co-delivery of acriflavine which inhibits HIF-1 from being overexpressed causes an accelerated expression of glutathione (GSH) resulting in a 100 – 1000-fold higher concentration of GSH in the intracellular compartment compared to the extracellular space. A tetrasulfide-bridged silicon framework on the nanoparticle surface facilitates a GSH-triggered degradation of the nano particles and leads to the targeted drug release. The combinatory delivery system seems to enhance the efficacy of cisplatin on the one hand and to inhibit cancer metastasis on the other hand.

The metabolic differences between normal and cancer cells enable specific points of application for a variety of cancer treatment agents. Especially the combination of targeted and common anti-cancer drugs turned out to have higher efficiencies. Nevertheless, further fundamental investigations are required for a complete understanding of cancer cell behavior to ultimately design cancer type-specific drugs showing less or no harmful side effects.

1.4 TECHNICAL STATE-OF-THE-ART IN OXYGEN AND PH MEASUREMENTS FOR *IN VITRO* MODELS

The oxygen and pH sensing within cellular monolayers and especially within three-dimensional tissue models is still challenging. The advantage of more physiological conditions in spherically-shaped three-dimensional cellular aggregates is on the other side inevitably accompanied by more challenging detection techniques. There are several experimental approaches described which differ in the detection method - either in an on-line mode or as an endpoint assay - as well as with respect to the degree of invasiveness. Since the techniques applied in this thesis are exclusively non-invasive detection methods and it is still unclear how cellular metabolism and hence the response to certain external stimuli is altered by invasive methods, the following overview of methods will focus only on non-invasive techniques capable of simulating the native *in vivo* situation as best as possible. Generally, non-invasive techniques can be divided into two main groups: label-free methods on the one hand and label-based ones on the other hand. One of the main advantages of label-free methods is the undisturbed cellular metabolism allowing for the detection of native oxygen tensions or pH-levels.

Label-free, electrochemical approaches

The easiest label-free and non-invasive technique is the use of electrodes or microelectrodes which are placed inside the measurement chambers or are externally attached to a measurement setup without establishing physical contact to the cells or spheroids. Typically, Clark-type electrodes are used for oxygen determination. The Clark-type electrode normally consists of a platinum (Pt) cathode and a silver (Ag) anode being electrically connected via an electrolyte solution. An oxygen-permeable membrane (e.g. Teflon) separates the electrodes and an inner electrolyte solution from the sample solution. The working principle relies on the measurement of the current due to the reduction of oxygen which changes according to the partial pressure-dependent diffusion of dissolved oxygen across the membrane into the measurement chamber. An applied negative potential on the working electrode (cathode) relative to the counter electrode (anode) causes the reduction of oxygen to hydroxide ions ($O_2 + 2 e^- + 2 H_2O \rightarrow H_2O_2 + 2 OH^-$, $H_2O_2 + 2 e^- \rightarrow 2 OH^-$) while silver molecules are oxidized to form AgCl in the presence of chloride ions. Consequently, the detected electrical current is directly proportional to the oxygen partial pressure in the analyte solution (Clark, L. *et al.* 1953; Park, J. *et al.* 2007). This electrochemical reduction of oxygen was used to create a broad variety of electrodes over the last 50 years which can be divided into two major groups: (i) metal electrodes (Pt and Au) and (ii) carbon-based electrodes (glassy carbon, carbon fibers and carbon paste) (Bolger, F. *et al.* 2011). In addition, there are multiple reports about modified, target-specific electrodes e.g. the investigation of lactate production after external stimulation. These examinations were reported to be performed using a

microelectrode being coated with the enzyme lactate oxidase immobilized in a hydrogel and placed in proximity to an adherent spheroid (Weltin, A. *et al.* 2017). The detection of the metabolic activity in form of lactate production and the use of the microsensors system seemed to be possible for almost three days. A similar non-invasive approach for monitoring the metabolic state and vitality was described using embryonic bodies as these *in vitro* systems are supposed to be potentially transferred to *in vivo* systems in the field of regenerative medicine. The *oxygen consumption rate* can be considered an indicator for metabolic activity, reflecting the activity of mitochondrial oxidative phosphorylation and hence the production of adenosine triphosphate (ATP). This fundamental relation highlights the importance of the investigation of *oxygen consumption rates*.

The combination of a measurement chamber with eight embedded microelectrodes for a new clinically applicable device (chip-sensing embryo respiration monitoring system, CERMs) was introduced by Kurosawa, H. *et al.* 2016 and is depicted in Fig. 1.5.

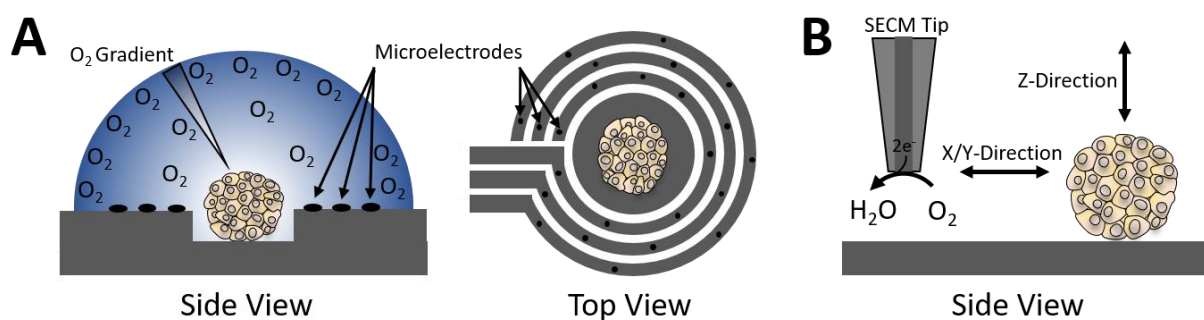


Fig. 1.5 Schematic depictions of (A) the CERM (chip-sensing embryo respiration monitoring system) measurement chamber for the analysis of the respiratory activity of three-dimensional tissue models as described by Kurosawa, H. *et al.* 2016 and (B) the SECM (scanning electrochemical microscopy) scanning modes for the detection of oxygen gradients around spheroids which was adapted from Shiku, H. *et al.* 2001.

The measurement device consists of five individual wells, each offering a cavity for spheroid positioning in the middle as well as multiple circular microelectrodes in eight different positions (see Fig. 1.5 A). This enables the possibility to observe an evolving gradient of the dissolved oxygen concentration due to the respiration of the cells. The electrodes measure the oxygen reduction current under an applied potential. To validate the use of the microelectrode chamber, the *oxygen consumption rate* was investigated via scanning electrochemical microscopy (SECM). SECM constitutes an electrochemical multiparameter analysis to examine tissue models for instance according to their intracellular redox activity or the transport of ions across the membrane. A high sensitivity was observed in both cases, with the advantages of easy handling and the possibility of parallelization in the case of CERM in contrast to the SECM measurement where the tip needs to be adjusted manually for the individual scanning modes. Shiku, H. *et al.* 2001 used the tip of an SECM microelectrode (tip radius of 1.8 μm) to measure oxygen concentration profiles around a single bovine embryo by scanning in the x/y- and z-directions up to a distance of 500 μm at 14.7 $\mu\text{m/s}$ and 160 μm at

4.9 $\mu\text{m/s}$, respectively (compare Fig. 1.5 B). SECM was also used to compare different cell culture techniques according to the respiratory activity of the formed tissue. Zhou, Y. *et al.* 2013 examined differences in the cellular respiration between spheroids created either via the hanging drop method or with a liquid overlay method in specially designed PDMS chambers. In addition to the formation method, different cell numbers were investigated. The respiratory activity increased with higher cell numbers equally for the hanging drop method as for the PDMS array technique.

Apart from the detection of oxygen there are many more electro-active species detectable with the help of SECM. Arai, T. *et al.* 2013 monitored p-aminophenol (PAP), the substrate of the enzymatic hydrolysis of p-aminophenylphosphate (PAPP), to evaluate the activity of the enzyme alkaline phosphatase (ALP). ALP is a biomarker for undifferentiated embryonic stem cells (Shamblott, M. *et al.* 1998), for bone and liver diseases as well as for many electrochemical immunoassays (Warsinke, A. *et al.* 2000). As a control experiment for the SECM investigations, cell staining with alkaline phosphatase was conducted (Arai, T. *et al.* 2013) by the addition of p-nitrophenyl phosphate as the substrate and the increase in absorbance was measured due to the enzymatically catalyzed formation of the product p-nitrophenol. A decreased ALP activity during the cultivation time was observed and it was suggested that this noninvasive measurement technique is able to discriminate between embryoid bodies with high and embryoid bodies with low potential to differentiate into cardiomyocytes.

The second key parameter this thesis focuses on, is the pH value in and around living organisms and the detection of changes in the normally sensitively maintained equilibria of pH tensions. Conventionally, pH values are detected by set of two separate electrodes (one glass electrode and a reference electrode) being incorporated into one body and arranged like a galvanic cell. The glass electrode (Ag/AgCl) is surrounded by an inner buffer solution (KCl adjusted to pH 7) and separated by a glass membrane from the test solution. A ceramic junction separates the test solution from the reference electrode (Ag/AgCl in aqueous KCl solution). The glass membrane as well as the ceramic junction act as diffusive barriers. The resulting measurable potential between the two electrodes is dependent on interactions of the glass membrane with the surrounding test solution. The glass structure of the membrane allows Na^+ and Li^+ ions to freely pass, whereas it is impermeable for H^+ ions although they can occupy free lattice sites in the glass structure. Consequently, a high concentration of H^+ ions (low pH value) causes a higher degree of proton occupation and hence an electrical repulsion of Na^+ and Li^+ ions from the inner membrane side. Vice versa, low H^+ concentrations (high pH values) lead to a repulsion of Na^+ and Li^+ ions from the test solution because the protons from the inner buffer solution occupy the free spaces in the membrane. This H^+ -dependent displacement causes detectable potential shifts allowing for the measurement of pH in the test solution. The process at the membrane surface had been unclear for a long time (Shangguan, J. *et al.* 2016; Pungor, E. *et al.* 1998), but the principle could nevertheless be used for designing other ion-selective sensor electrodes. This technique offers the possibility of pH detection in solution, for instance in the supernatant of adherent cells. A miniaturization of

glass pH electrodes with nonaqueous internal reference was introduced by Savinell, R. *et al.* 1981. Nevertheless, the use of these fragile glass electrodes in *in vivo* or *in vitro* studies was challenging. Liu, C. *et al.* 1980 reported about Pd/PdO wire-form electrodes with an Ag/AgCl reference electrode to overcome the drawback of pH-sensing electrodes made from glass. The development of planar electrodes would make the investigation of pH values in the microenvironment of attached cells feasible. Mingels, R. *et al.* 2019 introduced miniaturized, planar pH sensors consisting of a Pt electrode layout being coated with iridium and ruthenium oxide layers for potentiometric pH measurements. The combination of an iridium oxide pH sensor with a miniaturized solid-state reference electrode and additional sensor chips for temperature and conductivity detection are already used for water quality monitoring (Zhou, B. *et al.* 2017) and would also be an interesting approach for *in vitro* studies.

Optical imaging and non-imaging approaches

Apart from the robust and well-established electrochemical approaches, optical methods allow for cost-effective, non-invasive and highly versatile multiparametric investigation of living organisms. This assay format is easy to miniaturize being a crucial point when it comes to examinations using *in vitro* tissue models or biopsy material. Optical methods in general can either be label-free or label-based by using luminophores. However, the use of luminophores poses risks of photobleaching, interference with background emissions (autofluorescence) or the generation of singlet oxygen ($^1\text{O}_2$) which is potentially dangerous for living organisms. Despite these drawbacks, the luminophore method comes with the advantage of a high lateral resolution and, in contrast to electrochemical methods, no oxygen is consumed.

The easiest optical methods to gain information about the size and viability of cells or spheroids are microscopical studies. They are routinely used to monitor time-dependent changes in size or growth as well as to investigate morphological changes induced by different cancer drugs (Gaio, E. *et al.* 2016; Raghavan, S. *et al.* 2015). Ekstrand, A. *et al.* 1991 and Pedersen, P.-H. *et al.* 1994 investigated the influence of growth factors on spheroid growth, migration and invasion and could show by using phase contrast microscopy that the growth factor EGF is overexpressed in 50 % of malignant human gliomas and seems to be the most stimulating growth factor. A two-dimensional observation of three-dimensional tissue models however offers some disadvantages: (i) it is only possible to image the projected area of the tissue, (ii) no information can be gained on the actual 3D shape and (iii) it is difficult to judge uniformity of the surface of the grown tissue. For the examination of the cytoskeleton, the metabolic activity, proliferation rates or viability of the cells within a spheroid, there are several staining techniques available. As the nutrient supply is predicted to decrease towards the center of most tissue models due to the lack of blood vessels, the diffusion, exchange or active transport of dyes should also be restricted depending on the respective tissue or cell type. In addition to the complicated cell staining procedure in the center, a confocal laser visualization of the possible

dyes in the inner compartment of the spheroids poses additional difficulties because the penetration depth of visible light into the tissue as well as the fluorescence emission out the tissue is limited to approximately 100 μm (Costa, E. *et al.* 2019). Nevertheless, the stainings help to reveal important information on several cell phenotypes even though only the cells from the outer layer of the spheroid are considered. Changes in oxygen levels, lactate concentrations and pH are important parameters playing decisive roles in mirroring the vitality state of cells. The process of cell staining with subsequent imaging at different focal planes in z-direction is an established method for functional investigations.

As oxygen generally is a very important metabolite and involved among others in reductive processes at the cytochrome c oxidase in the oxidative phosphorylation, the production of reactive oxygen species in the mitochondria and many enzymatic reactions, it would be most desirable to develop processes to be able to detect oxygen levels within the tissue. Optical oxygen sensing using luminophores offers spatially resolved data either by quenching processes, intensity- or lifetime-based techniques or by ratiometric methods. Prominent oxygen probes for biological samples are the oxygen-sensitive reagents image-iTTM Red (Sarkar, S. *et al.* 2018), platinum (II) tetra (carboxyphenyl) porphyrin (PtTCPP) (Kurokawa, H. *et al.* 2015) and Pt(II)-tetrakis-(pentafluorophenyl)-porphyrin (PtPFPP) (Fercher, A. *et al.* 2011). The protocols mostly differ regarding the time point of application of the oxygen-sensitive dyes. Some probes are already added to the cell suspension during spheroid formation whereas other staining procedures are performed on mature spheroids. However, the detection method and therefore the penetration depth is similar as all methods require confocal z-directional scanning. Kurokawa, H. *et al.* 2015 investigated the intracellular oxygen concentration (OC) depending on changes of the extracellular environment and could observe increasing intracellular OC with increasing extracellular OC. In single cell experiments, he was able to distinguish between distinct organelle-specific OC within one cell. The distribution of the dye inside one cell does not matter as the measured lifetime is independent from the concentration of the phosphorescent dye. The research of alternative probes is still a focus of interest. The metal complex compounds are widely used and described and offer the possibility of chemical modification according to distinct purposes. Thus, the complexes were used to design nanoparticle-based probes which should exhibit good cell-penetration, require low working concentrations, exhibit small particle sizes and excellent biocompatibility (Kondrashina, A. *et al.* 2012).

In addition to metabolic investigations, the use of nanoparticles presents an opportunity of drug loading, different surface modifications for specific receptor recognition or surface loading for enzymatic release of diagnostic or therapeutic drugs.

Next to the uptake of probes into the intracellular compartments, it is of great interest to be able to collect information from the nearest extracellular environment of monolayers or the small spaces between the cells within one spheroid. A direct addition of microbeads or paramagnetic probes to the respective cell

suspension prior to tissue formation leads to the inclusion of the probes into the paracellular clefts. Leshere-Pérez, S. *et al.* 2017 reported about PDMS microbeads being infused with tris(4,7-diphenyl-1,10-phenanthroline) ruthenium(II) dichloride, an oxygen-sensitive metal complex, which was either deposited around the spheroids or alternatively the cells were seeded around the sensor beads. The microbeads allowed for the detection of oxygen levels in a time- and cell mass-dependent manner by phase fluorimetry. Additionally, different oxygen levels depending on the spheroid formation technique were observed. Spheroids having been formed via the hanging drop method exhibited oxygen levels similar to the atmospheric oxygen level while spheroids cultivated in microwells showed lower oxygen levels.

Another widely used technique for the 3D visualization of different tissues e.g. areas of hypoxic tissue after previous addition of [^{18}F]-labeled tracers (Dubois, L. *et al.* 2011; Lee, S. *et al.* 2007), is the positron emission tomography (PET). PET is an imaging technique for the three-dimensional detection of targeted, positron-emitting radioisotope-labeled tracers which are intravenously injected and distributed across the body. The radioactive decay leads to the formation of positron-electron pairs producing two photons being emitted in opposite directions. The detection of the two photons is achieved by opposing pairs of detectors yielding three-dimensional images of the tracer distribution in the corresponding tissue (Del Guerra, A. *et al.* 2016). The drawback of PET is a limited spatial resolution of around 4 – 6 mm with a relatively low temporal resolution of 1 s – 10 min (Nestle, U. *et al.* 2009). The PET technology was also reported to be suitable for pH investigations of the acidic environment of prostate cancer. Vāvere, A. *et al.* 2009 described the application of *pH low insertion peptides*, that predominantly insert into the lipid bilayer of tumor cells as an α -helix and are labeled with [^{64}Cu], allowing for the investigation of acidic environments with the drawback that physiological pH could cause inaccurate results.

Luminophore-based sensing is not only a reliable method with respect to the detection of oxygen tensions but can also be deployed in pH sensing to measure extra- and intracellular pH values. The intracellular pH value is a highly important parameter closely associated with cell behavior and vitality as well as for the understanding of physiological and pathological processes. A multitude of luminophores was reported offering a broad variety of sensitivities regarding pH ranges, photophysical properties, cell permeability, photobleaching and quantum yield. The most applied and highly promising fluorophores are reported to be BCECF-AM (2',7'-bis(2-carboxyethyl)-5-(and-6)-carboxyfluorescein, acetoxymethyl ester) and SNARF-1 (Seminaphtharhodaflorescein 5-(and-6)-carboxylic acid acetoxymethyl ester). The two dyes can be used for the detection of near-neutral intracellular pH conditions (Han, J. *et al.* 2010). Fluorescein and its derivatives are reported to rapidly leak from the cellular cytosol compared to HPTS (8-Hydroxypyrene-1,3,6-trisulfonic acid) which is trapped inside the cells after injection. This entrapment after injecting HPTS into the cell simultaneously is the major drawback due to the highly invasive character (Han, J. *et al.* 2010). So far, other organic fluorophores exhibit poor photostability and low quantum yield. Nevertheless, TPE-Cy (tetraphenylethene-cyanine) is reported to be highly biocompatible and show good cell-permeability (Chen,

S. *et al.* 2013). Also, studies have been carried out with multiple probes carrying pH-sensitive dyes like: (i) phospholipid-coated particles with covalently attached fluorescein (pH-sensitive) and tetramethylrhodamine (pH-insensitive) dyes (McNamara, K. P. *et al.* 2001), (ii) carbon dots made from citric acid and basic fuchsin showing a linear pH-dependent ratiometric signal after incorporation into HeLa cells (Shangguan, J. *et al.* 2016), (iii) nanoscale metal-organic frameworks with covalently conjugated FITC (fluorescein isothiocyanate) for real-time intracellular pH sensing (He, C. *et al.* 2014) and (iv) water-soluble cationic but cell-permeable porphyrin derivatives allowing for intracellular pH investigations (Liu, Y. *et al.* 2015).

Fluorescence detection is also used in combination with optical micro fibers for measuring extracellular pH levels close to biological samples. Yang, Q. *et al.* 2015 introduced a fiber-optic micro pH-sensor with a tip diameter of around 70 μm being coated with a thin film of an organically modified silicate-based *aerogel* including the covalently bound pH-sensitive dye BCECF already discussed before. The microfibers show a high spatial resolution and a linear response to pH values ranging from six to eight. Similar studies were performed with optical fibers with a tip diameter of 1 mm where the tip is modified with bromocresol purple being immobilized by sol-gel dip-coating making sensitive pH sensing possible in a range of 5.3 to 8.7 (Deng, S. *et al.* 2017).

A simultaneous, fluorescence-based detection of changes in oxygen concentrations and pH levels in the microenvironment of cells is offered by Agilent Technologies, Inc., with their Seahorse XF analyzer as depicted in Fig. 1.6. A disposable sensor cartridge is equipped with two fluorophores embedded in a polymer-based sensor unit, one being sensitive for oxygen and the other one for pH. The sensor unit is placed 200 μm above adherent cells and the detected fluorescence is automatically translated into corresponding oxygen consumption rates (OCR) and extracellular acidification rates (EACR) by the respective software in real-time.

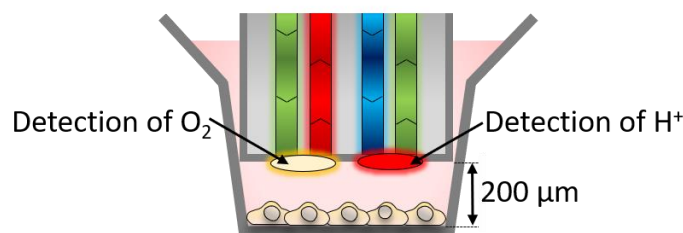


Fig. 1.6 Schematic of the Seahorse XF analyzer by Agilent Technologies, Inc., for the simultaneous detection of oxygen concentrations and pH via the detection of analyte-specific fluorescence emission in the cellular microenvironment. Adapted from www.agilent.com.

Magnetic resonance-based measurement techniques

The physical phenomenon of magnetic resonance is the fundamental process of the powerful spectroscopic tools electron paramagnetic resonance (EPR) as well as nuclear magnetic resonance spectroscopy (NMR) and the medical application thereof which is called magnetic resonance imaging (MRI). EPR is based on the interaction of paramagnetic probe molecules with paramagnetic oxygen resulting in changes of the linewidth of the recorded EPR spectrum (Lurie, D. *et al.* 2005). Langan, L. *et al.* 2016 used the EPR oximetry for direct measurements of oxygen gradients in spheroids. Cell aggregates encasing small lithium phthalocyanine (LiPc) paramagnetic probe particles (average size of $(11.20 \pm 1.02) \mu\text{m}$) were drawn into a glass capillary and sealed air bubble-free. The changes in the oxygen level were investigated based on the EPR measurement yielding the *oxygen consumption rate* of the spheroids. It was reported that the oxygen consumption of spheroids is not showing a linear dependence on the oxygen amount below a concentration of $100 \mu\text{M}$ possibly due to the formation of oxygen diffusion gradients within the tissue. In addition to LiPc probes, nitroxides can also be used as paramagnetic probes. Ongoing refinements and further development of the nitroxide-based probes have shown a significantly improved resolution, reconstruction and spectral response to oxygen tensions within *in vitro* and *in vivo* tissue (Weaver, J. *et al.* 2016).

Magnetic resonance imaging (MRI) or magnetic resonance spectroscopy (MRS) are based on the detection of the tissue-dependent relaxation of hydrogen atoms [^1H] after the application of a strong external magnetic field which induces different transitions of nuclear spin states of ^1H causing detectable radiofrequency radiations. The recorded relative pixel intensities depend on proton densities as well as on tissue-specific relaxation times (Khoora, V. *et al.* 1997). The *in vivo*-targeted investigation of oxygen tensions or pH conditions is mostly done by using exogenous perfluorinated carbon compounds [^{19}F], while the detection of endogenous signals from ^1H , ^{31}P and ^{23}Na is also used (Gillies, R. *et al.* 2005). Crayton, S. *et al.* 2011 developed pH-responsive superparamagnetic iron oxide nanoparticles with a conjugated glycol chitosan polymer on its surface being metabolically directed since they show increased accumulation tendencies in acidic tumor environments. The MRI technique can also be used for oxygen sensing, mapping of hypoxia-revealing tissue, lactate concentration determination and many other metabolic parameters. Nevertheless PET, EPR and MRI are cost-intensive techniques being mostly used in clinical research for *in vivo* investigations of large tissue areas.

The fundamental microphysiometric investigations with the dynamic activity of the energy metabolism and its respective key parameters are crucial for a better understanding of how life works. The broad variety of approaches for oxygen and pH sensing are – in parts – well-established but also contain some drawbacks. Oxygen-sensing electrodes and electrochemical methods generally come with the disadvantage of being oxygen-consuming and thereby causing inaccurate detection of oxygen levels. Additionally, Clark-type electrodes exhibit a weak oxygen sensitivity at low concentrations with a limited spatial resolution. Optical

or image-based methods are often performed using certain labels, luminophores or designed nanoparticles which are claimed to be non-invasive. However, a cellular recognition and interaction of these labels with the cell's metabolism cannot totally be ruled out and could consequently lead to a misinterpretation of any measured cellular response. Therefore, the development of novel oxygen- and pH-sensing setups which are biocompatible, non-invasive, cost-effective, durable and at the same time offer a high lateral and temporal resolution, is still part of an ongoing research topic and this thesis aims to contribute to that research.

2 OBJECTIVES

The cell microphysiometry not only provides information about the state of vitality and metabolic activity of the cells but is also an important factor to distinguish normal from cancerous cells. Reversed pH gradients, altered respiratory chains as well as different proliferation and migration behavior between normal and cancerous cells shall be compared as a function of extracellular pH.

Experimental techniques to conduct these studies are supposed to be non-invasive with the possibility of real-time monitoring in a label-free manner giving access to cellular responses with a good temporal and spatial resolution. A major objective of this thesis is to characterize different cell lines with respect to potentially specific pH-dependent phenotypes using, among others, oxygen consumption as well as toxicity as indicator.

To study cellular respiration, oxygen-sensitive sensor foils should be used. The sensor foils present the advantage of being reusable and biocompatible with easy cellular attachment while a ratiometric readout approach overcomes drawbacks like photobleaching or background fluorescence.

To validate the experimental studies, the oxygen-sensitive sensor foil shall be characterized regarding its sensitivity range as well as temporal and spatial resolution abilities. With regard to the sensor foil sensitivity, it should be examined whether varying respiratory activities can be detected using different cell lines since the individual organs in a body are also exposed to specific oxygen tensions. As this measurement setup enables a high spatial resolution, it should be tested whether different cell lines can be monitored simultaneously while being attached to one piece of sensor foil. Also, the different metabolic zones known to exist within cultured tissues should be mimicked by the inhibition of oxygen diffusion from the supernatant medium similar to multiple cell layers acting as barrier. Furthermore, different metabolic activities of the three-dimensional tissue models using spheroids as a well-behaved model system should be analyzed and visualized with the help of oxygen-sensitive sensor foil. These investigations could reveal interesting insights into oxygen diffusion processes within the tissue and could allow for the detection of different respiratory activities in the individual zones within a 3D tissue due to possibly emerging horizontal oxygen gradients. Consequently, the development of a detection device to assess oxygen gradients could help to provide an estimation of oxygen diffusion rates above adherent cells. The last aspect to be considered when looking at oxygen diffusions close to adherent cells is hidden in the sensor foil matrix itself. It should be examined to what extent the sensor foil thickness influences the changes in oxygen concentrations detected by the sensor readout. The multitude of investigations is supposed to provide a comprehensive picture of the oxygen-related diffusion processes around cultivated cells.

The focus of the second chapter should be placed on the reversed pH gradient of cancer cells in contrast to normal cells. In this chapter, various cell phenotypes of normal cells as well as the ones of cancer cells shall be characterized with respect to their pH dependencies. Three different non-invasive techniques should be implemented to yield and compare information about adhesion processes, proliferation rates, migration rates and micromotion as well as respiratory activities under the influence of altered extracellular pH conditions. The primary objective in this chapter is to investigate if normal cells can be discriminated from cancerous on the basis of their pH-dependent phenotypic behavior.

In this thesis, experimental protocols should also be established to perform cytotoxicity investigations of two substances – bisphenol A and glyphosate - which have recently been fervently discussed in literature and media. Bisphenol A and glyphosate are both said to have cancerogenic and tumor-promoting effects by affecting cell cycle regulations (Marc, J. *et al.* 2004). The goal is to be able to determine toxic concentrations of the two toxins and to observe possibly distinct effects for different cell lines. There are many, however also controversial, publications addressing this issue and the results of this thesis could complement this field of research and shed additional light on the toxic influences on living organisms.

3 MATERIALS AND METHODS

3.1 CELL CULTURE TECHNIQUES

All cell culture-related work was performed under a laminar airflow cabinet (Thermo Fisher Scientific Inc.) to minimize the risk of contaminations. All consumables were either autoclaved (Systec GmbH) or purchased in disposable sterile packages. The cells were exposed only to sterile media and solutions. All buffers and reagents were sterilized either by autoclaving or by passing through a sterile filter (TPP Techno Plastic Products AG). Before cell contact, all media, buffer or analyte solutions were prewarmed to 37 °C in a water bath (Julabo GmbH). The cells were grown on the bottom of polystyrene (PS) culture flasks (Sarstedt AG & Co. KG) with a growth area of 25 cm² and a supernatant volume of 4 mL or a growth area of 75 cm² and 10 mL supernatant culture medium (Sigma-Aldrich). To provide an optimal growth environment, the cells were cultivated in an incubator (Thermo Fisher Scientific Inc.) at 37 °C in an atmosphere of 5 % CO₂ and 95 % relative humidity. The supernatant cell culture medium was routinely exchanged every three to four days and also one day before the experiment.

3.1.1 CULTIVATION OF ADHERENT MAMMALIAN CELL LINES

In this work a total of nine different cell lines has been used which will be described in detail in the following. All of the cell lines are adherent mammalian cell lines growing in spread monolayers and require slightly different compositions of their culture medium (see Tab. 3.1).

A549 cells are human lung adenocarcinoma type II alveolar epithelial cells. The cell line was initiated in 1972 by Giard, D. J. *et al.* 1973 by the explantation of a lung adenocarcinoma. A549 cells grow in well-spread monolayers with a uniform distribution and a regular epithelial morphology. The monolayers are made from cuboidal and polygonal-structured cells which are closely packed (Croce, M. V. *et al.* 1999). The A549 cell line was kindly provided by Prof. Dr. Heilmann, chair of the Department of Pharmaceutical Biology at the University of Regensburg.

Human dermal microvascular endothelial cell (HDMEC) were isolated from human foreskin and kindly provided by the University Hospital Regensburg. They grow in monolayers with a cylindrical classic cobblestone morphology (Blair R. J. *et al.* 1997). As the cells are derived from a finite cell line, they could only be subcultured between four to seven times.

Madin-Darby canine kidney (MDCK) cells are epithelial kidney cells isolated from the distal tubule of the nephron of an adult cocker spaniel 1958 by Madin and Darby (Valentich, J. D. *et al.* 1981). Two sublines of

the parent strain have been used in this thesis: MDCK I and II cells and were derived from early and later passages, respectively. They can be distinguished by morphological characteristics and due to their transepithelial resistance (Zimmer, G. *et al.* 1997). MDCK I cells form very strong tight junctions with a transepithelial resistance of around $4 \text{ k}\Omega\text{-cm}^2$ in contrast to $70 \text{ }\Omega\text{-cm}^2$ exhibited by the more moderately tight monolayers formed by MDCK II cells (Richardson, J. *et al.* 1981). MDCK cells display a cuboidal cobblestone-like morphology, but MDCK I and MDCK II cells differ strongly with respect to their size and apical microvilli distribution (Richardson, J. *et al.* 1981). Confluent MDCK II monolayers show domes or blisters due to fluid being pumped from apical to the basolateral side of the cells leading to locally detached cells with intact cell-cell contacts (Cereijido, M. *et al.* 1981).

Normal rat kidney (NRK-52E) cells were first described in 1978 as an epithelial-like cell type with a flat polygonal shape (DeLarco, J. E. *et al.* 1978). They have been derived from *rattus norvegicus*. NRK cells grow in a perfect cobblestone morphology and were purchased from the *Deutsche Sammlung von Mikroorganismen und Zellkulturen* (DSMZ).

The human skin melanoma cell line SK-MEL-28 was isolated from a 51-year-old man suffering from a malignant melanoma in 1976 (Carey, T. E. *et al.* 1976). The cells form adherent, epithelial-like monolayers with polygonal-shaped cell bodies. A cell line derived from an oral squamous cell carcinoma (UPCI-SCC-111, SpiCa) was established using a biopsy sample of a 69-year-old Caucasian woman collected between 1992 and 1997 at the University of Pittsburgh (Martin, C. L. *et al.* 2008, White, J. S. *et al.* 2007). SpiCa cells form well-spread adherent monolayers. Both of the described cancer cell lines were purchased from the DSMZ.

U373 MG cells are human astrocytoma cells derived from a malignant brain tumor displaying glial morphology and forming a polygonal morphology with moderately dense cytoplasm (Lee, C.-M. *et al.* 1989; Bigner, D. D. *et al.* 1981). The cell line was kindly provided by Prof. Buschauer from the Department of Pharmaceutical & Medicinal Chemistry at the University of Regensburg.

The MCF-7 (Michigan Cancer Foundation-7) cell line was derived from a human breast carcinoma and shows adherent cells with polygonal epithelioid morphology (Abe, M. *et al.* 1984) which were kindly provided by Prof. Göpferich from the Department of Pharmaceutical Technology at the University of Regensburg. U373 MG and MCF-7 cells were only used to grow three-dimensional tissue models.

Tab. 3.1 Compositions of cell culture medium for all cell lines used in this thesis.

Cell line	Culture medium	FCS / % (v/v)	Penicillin/streptomycin / $\mu\text{g}\cdot\text{mL}^{-1}$	L-Glutamine / mM	Additional supplements
A549	Dulbecco's Modified Eagle's Medium (DMEM) (50 %) 3.7 $\text{g}\cdot\text{L}^{-1}$ NaHCO_3 4.5 $\text{g}\cdot\text{L}^{-1}$ D-Glucose Nutrient Mixture F-12 Ham Medium (50 %)	5	100	1	
HDMEC	Endothelial Cell Growth Medium MV	5	100		
MCF-7	Minimum Essential Medium Eagle (MEM-Eagle) 2.2 $\text{g}\cdot\text{L}^{-1}$ NaHCO_3 1 $\text{g}\cdot\text{L}^{-1}$ D-Glucose	10	100	2	1 mM Pyruvate
MDCK I / II	Minimum Essential Medium Eagle (MEM-Eagle) 2.2 $\text{g}\cdot\text{L}^{-1}$ NaHCO_3 1 $\text{g}\cdot\text{L}^{-1}$ D-Glucose	5	100	4	
NRK- 52E	Dulbecco's Modified Eagle's Medium (DMEM) 3.7 $\text{g}\cdot\text{L}^{-1}$ NaHCO_3 4.5 $\text{g}\cdot\text{L}^{-1}$ D-Glucose	5	100	2	
SK- MEL-28	Dulbecco's Modified Eagle's Medium (DMEM) 3.7 $\text{g}\cdot\text{L}^{-1}$ NaHCO_3 4.5 $\text{g}\cdot\text{L}^{-1}$ D-Glucose	10	100	2	
SpiCa	Dulbecco's Modified Eagle's Medium (DMEM) 3.7 $\text{g}\cdot\text{L}^{-1}$ NaHCO_3 4.5 $\text{g}\cdot\text{L}^{-1}$ D-Glucose	20	100	2	1x non- essential amino acids
U373 MG	Minimum Essential Medium Eagle (MEM-Eagle) 2.2 $\text{g}\cdot\text{L}^{-1}$ NaHCO_3 1 $\text{g}\cdot\text{L}^{-1}$ D-Glucose	5	100	2	

3.1.2 SUBCULTIVATION

Once a week the cells were subcultured to provide them with enough proliferation space on the cultivation substrate. The different cell lines require slight adaptations in their subcultivation protocols. Tab. 3.2 describes the individual steps for the respective cell line.

Tab. 3.2 Overview of the subcultivation protocols for the individual cell lines.

Cell line	Washing with PBS ⁻	Addition of EDTA/ PBS ⁻	Incubation with EDTA/ PBS ⁻ (37 °C)	Addition of trypsin/ PBS ⁻	Incubation with trypsin/ PBS ⁻ (37 °C)	Medium for enzyme inactivation	Centrifugation (RT)
A549	2x	-	-	1 mL 0.05 % (w/v)	10 min	10 mL	10 min, 110 x g
HDMEC	2x	-	-	1 mL 0.05 % (w/v)	2 min	10 mL	5 min, 200 x g
MCF-7	2x	-	-	1 mL 0.25 % (w/v)	3 min	10 mL	5 min, 110 x g
MDCK I	2x	2x $\left(\begin{array}{l} 4 \text{ mL} \\ 1 \text{ mM} \end{array} \right)$	10 min	1 mL 0.25 % (w/v)	10 min	10 mL	10 min, 110 x g
MDCK II	2x	4 mL 1 mM	10 min	1 mL 0.05 % (w/v)	10 min	10 mL	10 min, 110 x g
NRK 52E	2x	4 mL 1 mM	10 min	1 mL 0.05 % (w/v)	10 min	10 mL	10 min, 110 x g
SK-MEL-28	2x	-	-	1 mL 0.05 % (w/v)	3-5 min	5 mL	5 min, 200 x g
SpiCa	2x	-	-	1 mL 0.05 % (w/v)	3-5 min	5 mL	5 min, 200 x g
U373 MG	1x	-	-	1 mL 0.05 % (w/v)	3 min	-	10 min, 110 x g

The initial aspiration of the culture medium was followed by washing with PBS⁻ (phosphate-buffered saline, without Ca²⁺- und Mg²⁺ ions, 4 mL, Tab. 3.4, Sigma-Aldrich) to remove dead cells and medium residues. A subsequent detachment of the cells from each other was achieved by a cell line-dependent incubation step with EDTA (ethylenediaminetetraacetate, 1 mM in PBS⁻, 4 mL, 10 min, 37 °C, 5 % CO₂, Sigma-Aldrich) due to the complexation of bivalent cations in solution which are essential for the formation of cell junctions. The exchange against a trypsin solution (1 mL, 0.05 – 0.25 % (w/v) in PBS⁻, 5 – 10 min, 37 °C, 5 % CO₂, Sigma-Aldrich) led to a complete detachment of the cells from the surface. Trypsin is a protease, digesting proteins involved in cell-cell and cell-matrix adhesion. To prevent further enzymatic cell digestion, culture medium (5 – 10 mL) was added to the cell suspension followed by a centrifugation step (5 – 10 min, 110 – 200 x g, RT, Thermo Fisher Scientific Inc.). After centrifugation, the cells were resuspended in fresh culture medium (4 mL) and seeded into new culture flasks in a dilution of 1:20 with respect to the growth area.

For reproducible cell inoculation on different substrates, the cell number was determined with the help of a *Bürker* counting chamber (Paul Marienfeld GmbH & Co. KG). Cells were either seeded to yield a confluent

monolayer or subconfluently with a lower cell density. As the cellular appearance differs in size and shape, every cell line was seeded in an appropriate cell density which is listed in Tab. 3.3.

Tab. 3.3 Cell line-specific seeding densities.

Cell line	Confluent monolayer -adhesion/migration/RTC measurements-	Subconfluent layer -proliferation measurements-
A549	$32 \cdot 10^4$ cells \cdot cm ⁻²	$2 \cdot 10^4$ cells \cdot cm ⁻²
HDMEC	$5 \cdot 10^4$ cells \cdot cm ⁻²	
MDCK I & II	$25 \cdot 10^4$ cells \cdot cm ⁻²	
NRK	$25 \cdot 10^4$ cells \cdot cm ⁻²	
SK-MEL-28	$10 \cdot 10^4$ cells \cdot cm ⁻²	$2 \cdot 10^4$ cells \cdot cm ⁻²
SpiCa	$20 \cdot 10^4$ cells \cdot cm ⁻²	

After cell seeding in culture medium, a *standard pre-experiment protocol* was carried out to ensure reproducible conditions. Therefore, 24 h after seeding, the cell culture medium was exchanged to provide sufficient nutrient supply for the cells and to remove dead cells. After another 24 h, the cells were prepared for the individual experiments. During the *standard pre-experiment protocol*, culture substrates were incubated in a standard cell culture incubator (37 °C, 5 % CO₂ and 95 % humidified atmosphere).

3.1.3 CULTIVATION OF SPHEROIDS

For the formation of three-dimensional spheroids, the liquid overlay technique was used (Metzger, W. *et al.* 2011). This technique is based on the cell inoculation on non-adhesive substrates. The cells start to build cell-cell contacts resulting in a spherically shaped structure, the so-called spheroids. To create non-adhesive substrates for the generation of spheroids, a 96-well plate (Sarstedt AG & Co. KG) was coated with a solution of 1.5 % (w/v) agarose (Sigma-Aldrich) in serum-free culture medium (50 μ L / well), wherefore the agarose solution was previously heated in a microwave. After the plates had cooled down to 37 °C leading to a solidification of the agarose solution, the cells could be seeded. After the detachment of the cells from the culture flasks and subsequent counting, the cell suspension was diluted to $1 \cdot 10^5$ cells \cdot mL⁻¹ with culture medium additionally supplemented with HEPES ((4-(2-hydroxyethyl)-1-piperazineethane-sulfonic acid, 20 mM, Carl Roth GmbH). HEPES is required to maintain a physiological pH value during the shaking process (Edmund Bühler GmbH) in the absence of CO₂ atmosphere. The cells were then seeded in different cell numbers per well into the respective wells (200 μ L / well) of the pre-coated well plate in order to generate

different spheroid sizes. The plate was shaken on an orbital shaker inside an incubator (37 °C, 0 % CO₂) for 4 h at 120 rpm and 50 rpm overnight to additionally prevent the adhesion to the non-adhesive agarose surface and to promote the formation of cell-cell contacts instead.

3.1.4 CRYOPRESERVATION

The long-term storage of mammalian cells is possible by cryopreservation in a liquid nitrogen tank (Jutta Ohst german-cryo GmbH). When the cells reached confluency in the culture flasks, they were detached from the substrate according to the subcultivation protocol (see chapter 3.1.2). After the centrifugation step, the cells were resuspended in 1.5 – 1.8 mL cryopreservation medium per T-25 cell culture flask and subsequently transferred into 2-mL cryovials (Sigma-Aldrich). The cryo medium composition was chosen as recommended by the DSMZ. All media were supplemented with 10 % (v/v) DMSO (dimethyl sulfoxide) to prevent crystallization because the formation of crystals could harm the cell membranes. The cryovials were evenly cooled down to -80 °C via an isopropanol-filled CryoBox™ (Nalgene®) overnight and placed into the liquid nitrogen tank the day after.

In order to thaw and reactivate the cells, the cryovials were moved from the liquid nitrogen tank to a normal freezer set to -20 °C for 1 – 2 h. After a quick thawing step of the still frozen cell suspension, the cells were transferred to a 50-mL centrifugation tube and after the dropwise addition of pre-warmed cell culture medium (15 mL), the cells were centrifugated, resuspended and seeded to standard cell culture flasks according the subcultivation protocol for the respective cell line (see Tab. 3.2). 24 h after thawing, the cell culture medium was exchanged (4 mL) to remove dead cells as well as DMSO residues. Approximately two weeks after thawing, with regular splitting once a week, the cells were ready for first experiments.

3.1.5 BUFFER AND SOLUTION COMPOSITIONS

All media, buffers and prepared solutions were stored at 4 °C and pre-warmed to 37 °C before cell contact. The final dilutions of different toxins as well as pH-adjusted solutions were sterilized by sterile filtration.

The toxicity of Bisphenol A (BPA, Sigma-Aldrich) was investigated using NRK cells as an *in vitro* model. A stock solution (20 mM) was prepared by diluting the respective amount of BPA (228.28 g·mol⁻¹) in ethanol (Merck). For the measurements, concentrations of 200 µM, 100 µM, 80 µM, 60 µM and 30 µM BPA in Leibovitz (L-15, Sigma-Aldrich) medium were prepared and L-15 medium supplemented with 0.5 % (v/v) ethanol served as control.

In a comparative toxicity study between the commercially available herbicide Roundup® (Monsanto Agrar GmbH) and the active ingredient glyphosate (Sigma-Aldrich) in its pure form, every experiment was performed using glyphosate and Roundup® in the same concentrations with respect to molecular concentration of glyphosate. Stock solutions (40 mM) were created for glyphosate ($169.07 \text{ g}\cdot\text{mol}^{-1}$) and Roundup® ($360 \text{ g}\cdot\text{L}^{-1}$ glyphosate concentration) by dissolving and diluting the required mass and volume in L-15 medium, respectively. The glyphosate solution yielded a pH value of approximately 2.4 and a pH value of 5.8 was measured for the Roundup® stock solution. For some experiments, the solutions were adjusted to a physiological pH value of 7.4. The pH adjustment was done to be able to discriminate between the contribution of the acidic environment on the one hand and the effect of the herbicide itself on the other hand to the overall cell response. Since glyphosate is known to adhere to plastic surfaces, the stock solutions were stored in glass containers and dilutions were only prepared directly before application.

Tab. 3.4 Compositions of all media, buffers and solutions applied in cell experiments.

Buffer & Solution name	Composition
Cysteine/NaCl	10 mM cysteine supplemented with 150 mM NaCl in ddH ₂ O
Leibovitz medium (L-15)	w/o phenol red supplemented with 1 % (v/v) P/S ($100 \mu\text{g}\cdot\text{mL}^{-1}$) 1 % (v/v) FCS for experiments with SK-MEL-28 & SpiCa cells
L-15 with pH 5.5, 6.0, 6.4, 6.5	L-15, pH-adjusted with 1 M/0.1 M NaH ₂ PO ₄
L-15 with pH 7.0, 7.2	L-15, pH-adjusted with 0.1 M NaH ₂ PO ₄
L-15 with pH 7.4, 7.5	L-15, pH-adjusted with 0.1 M NaH ₂ PO ₄ / 0.1 M K ₃ PO ₄
L-15 with pH 7.8, 8.0	L-15, pH-adjusted with 1 M/0.1 M K ₃ PO ₄
PBS ⁻	140 mM NaCl 2.7 mM KCl 8.1 mM Na ₂ HPO ₄ 1.5 mM KH ₂ PO ₄
EDTA/PBS ⁻	PBS ⁻ with 1 mM EDTA
PBS ⁺⁺	PBS ⁻ with 0.9 mM Ca ²⁺ and 0.5 mM Mg ²⁺
PBS ⁺⁺ /Glucose	PBS ⁺⁺ with $1 \text{ g}\cdot\text{L}^{-1}$ D-glucose
Trypsin/PBS ⁻	PBS ⁻ with 0.05 / 0.25 % (w/v) trypsin and 1 mM EDTA

Phenotypic analysis of cells being exposed to different pH were performed using L-15 medium adjusted to distinct pH values (Tab. 3.4). Leibovitz medium is pH-buffered by basic amino acids and phosphate buffers like tribasic potassium phosphate (K_3PO_4 , $60 \text{ mg}\cdot\text{L}^{-1}$, Sigma-Aldrich) and monobasic sodium phosphate (NaH_2PO_4 , $190 \text{ mg}\cdot\text{L}^{-1}$, Sigma-Aldrich). Due to the absence of the bicarbonate buffer system, L-15 is a designated culture medium in a CO_2 -free environment. In the experiments using SK-MEL-28 and SpiCa cells, L-15 was additionally supplemented with 1 % (v/v) FCS to enhance metabolic activity and to ensure sufficient nutrient supply.

3.2 MICROSCOPIC TECHNIQUES

3.2.1 PHASE CONTRAST MICROSCOPY

Phase contrast microscopy provides the visualization of living and unstained microscopic structures. Microscopically small structures like any other medium other than vacuum interact with light waves and cause changes in the amplitude and phase of the electromagnetic radiation. Variations in the amplitude are perceived as brightness differences by photographic equipment and the human eye, whereas the corresponding phase shift is unnoticeable without additional arrangements. The technique of making the information from the phase shift available was originally described by Frits Zernike in 1932 and he was awarded the Nobel Prize in 1953 (Zernike, F. *et al.* 1942). The basic idea is the conversion of the phase shift, resulting from slightly different refractive indices of the specimen, into differences in the light intensity. In order to achieve the difference in light intensity, the illuminating light is first guided through a ring-shaped condenser annulus before a condenser focuses the light on the sample. A part of this illuminating light is scattered and consequently phase-shifted by the specimen while the background light is made up by the unscattered part of the light. The objective collects the scattered light as well as the background light and directs the light waves to a phase plate. The phase plate selectively shifts the phase of the background light by -90° (negative phase contrast) or $+90^\circ$ (positive phase contrast) to interfere either constructively or destructively with the background light. Biological samples normally shift the phase of the light by -90° due to the thickness of the sample and differences in the refractive indices between the sample and the medium. Thus, the sample appears bright before a dark background when the background light is also shifted by -90° because the scattered and the background light constructively interfere with each other. However, if the background light is phase-shifted by $+90^\circ$, the phases are separated by 180° and the sample appears dark before a brighter background due to destructive interference.

Phase contrast images were taken with the *Nikon Diaphot microscope* equipped with three different magnification objectives (4x (PLAN, 4x / 0.13), 10x (E 10x / 0.25) and 20x (DL 20x, 0.4) as well as an attached digital camera (Nikon D5000).

3.2.2 24-CHANNEL OPTICAL MICROSCOPY

Microscopy-based investigations of the different cellular phenotypes following extracellular pH changes were performed using the zenCell owl (innoME GmbH). It is a 24-channel microscope (see Fig. 3.1) designed for cell experiments inside a cell culture incubator (37°C , 0% CO_2). Each individual field of view (1.2 mm x 0.9 mm) offers a resolution of 2592 x 1944 pixels per well. The instrument is connected to a computer for

experimental control and data acquisition with the corresponding software provided by innoME GmbH. The software determines the number of attached and dead cells in real-time as well as the overall cell coverage within the field of view on the substrate surface. This technique allows for an undisturbed observation of proliferation and migration events, as the cell culture plate does not need to be moved from the incubator to the stage of a standard phase contrast microscope.



Fig. 3.1 Picture of the zenCell owl with an inserted 24-well plate taken from www.zencellowl.com. Illumination units are located in the upper part of the device and the objectives are incorporated directly beneath each well of a 24-well-plate.

Cell proliferation and migration were documented using the zenCell owl. The cells were seeded either in a low seeding density or seeded to yield a confluent monolayer (see Tab. 3.3) for the investigation of proliferation rates and migration behaviour, respectively. The culture medium was exchanged 24 h after seeding and another 24 h later, the cells were washed twice with the respective pH-adjusted L-15 medium (+ 1 % P/S, + 1 % FCS for experiments with SK-MEL-28 and SpiCa cells, pH values 6.4, 7.2, 7.4 and 7.8). After the addition of the pH-adjusted L-15 medium (2 mL / well), the measurement was started with a monitoring period of 24 h and images were recorded every 30 min. In migration assays, the cells were wounded using a physical scratch prior to the washing steps meaning that the cells were mechanically removed with a pipette tip (pipette tip for a maximum pipetting volume of 200 μ L) to create a cell-free area in the field of view of the zenCell owl. The corresponding software determined the degree of cell coverage for every recorded image. The changes in cell coverage determined by the software were plotted as function of time and the slope was determined for the approximately linear part until 100 % cell coverage was reached. The individual slopes were averaged and expressed with the respective standard error of mean taking the Gaussian propagation of uncertainty into account.

3.2.3 CONFOCAL LASER SCANNING MICROSCOPY (CLSM)

A confocal laser scanning microscope (CLSM) was used to image fluorescently labelled biological specimen. This technique provides a resolution of around 300 nm to make cellular structures visible. In contrast to conventional fluorescence microscopes, the CLSM technique is able to scan the sample with a very focused illumination. In addition, there are two optically conjugated pinholes integrated in the optical path. The first one is located in the illumination path between the light source and the dichroic mirror and the other pinhole is located in the observation path between the dichroic mirror and the detector. Monochromatic laser light passes the first pinhole, gets reflected by a dichroic mirror and is subsequently focused on the sample by the objective. The emitted red-shifted fluorescence is collected by the objective, passes the dichroic mirror (which filters scattered incident light) as well as the second pinhole and is finally collected by a photomultiplier tube. The second pinhole excludes fluorescence originating from axial positions other than the focal plane. This allows for an optical sectioning of the sample with very detailed visualization of biological structures due to little background fluorescence. Apart from the two-dimensional optical recordings, it is possible to create 3D images by collecting several optical sections at different vertical positions of the sample.

In this work the confocal microscope *Eclipse 90i* was used with a C1 scanning unit. The microscope is equipped with three different excitation light sources (lasers) and three different detector units to record the emitted fluorescence. To adjust the magnification and resolution to the individual sample, there are three objectives with the different numerical apertures (NA) to choose from (see Tab. 3.5).

Tab. 3.5 Technical data of the confocal laser scanning microscope.

Laser / power	Detector unit	Objective / magnification / NA	Pinhole size / diameter
408 nm / < 500 mW	450/35 nm BP (blue)	PLAN / 10x / 0.25	Pinhole S / 30 µm
488 nm / < 50 mW	515/30 nm BP (green)	PLAN / 20x / 0.40	Pinhole M / 60 µm
543 nm / < 5 mW	650 nm LP (red)	NIR Apo / 60x / 1.0 / water	Pinhole L / 100 µm

3.2.4 CYTOCHEMICAL STAINING

3.2.4.1 LIVE/DEAD STAINING

A widely used staining method to distinguish between living and dead cells is a simultaneous labeling with calcein acetoxymethyl ester (CaAM, Invitrogen) and ethidium homodimer (EtHD-1, Biotrend Chemikalien GmbH). CaAM is a membrane-permeable non-fluorescent molecule, which after cleavage of the ester bonds by intracellular esterases, is turned into the fluorescing calcein (Liminga, G. *et al.* 1995). Since CaAM is cell

membrane-permeable, it can freely diffuse into living and dead cells alike but due to the necessary active enzymes, it can only be hydrolyzed to calcein in living cells exhibiting bright green fluorescence. Simultaneously, the non-membrane-permeable EtHD-1 is only able to enter dead cells due to the loss of their membrane integrity. The intercalation of the dye between the base pairs of the DNA increases the red fluorescence of EtHD-1 significantly due to the changed environment and the inhibition of quenching processes of the emitted fluorescence by solvent molecules like water. The complex is very stable, highly fluorescent and exhibits a ratio of one homodimer molecule to four or five base pairs (Glazer, A. N. *et al.* 1990). The staining principles are depicted in Fig. 3.2.

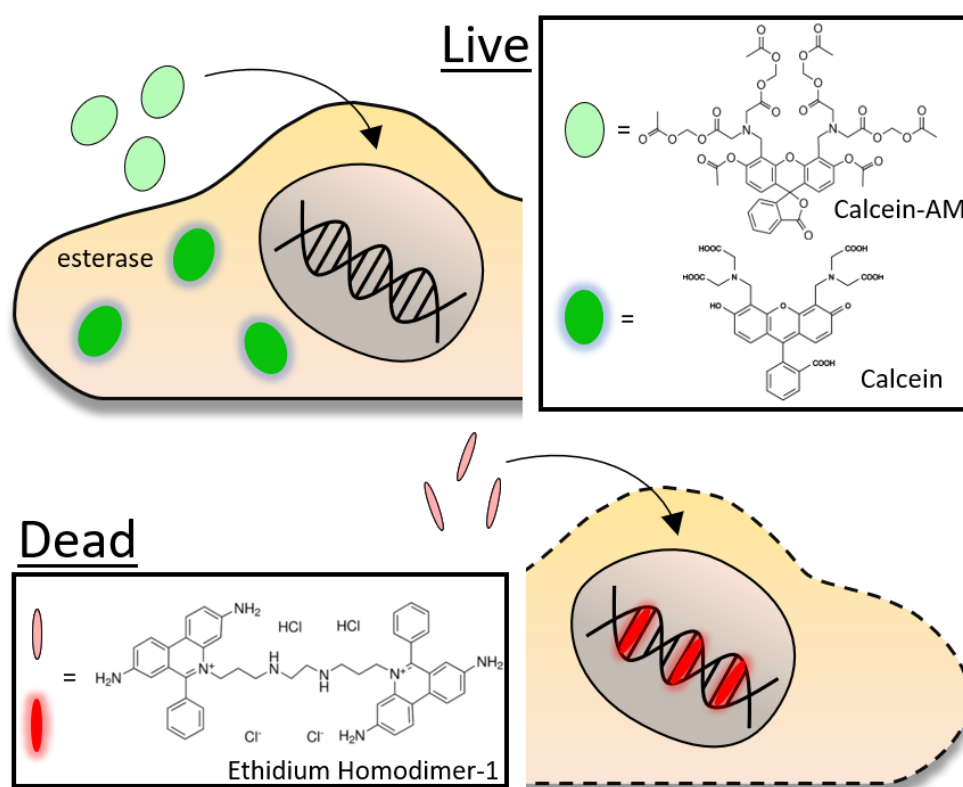


Fig. 3.2 Schematic illustration of the live/dead staining with CaAM and EtHD-1. CaAM can freely diffuse across the cell membranes and emit bright green fluorescence after the cleavage of the ester bonds by esterase enzymes in living cells. EtHD-1 is only able to diffuse into dead cells and emit bright red fluorescence after the intercalation between base pairs of the DNA located in the nucleus of the cells.

The live/dead staining was performed after the treatment with glyphosate and Roundup® as well as for the visualization of spheroids growing on oxygen-sensitive sensor foils. The dyes were stored in DMSO stock solutions at -20 °C in concentrations of 1 mM and 2 mM for CaAM and EtHD-1 and were diluted to final concentrations of 2 μM and 4 μM in PBS⁺⁺, respectively. The cells were washed twice with PBS⁺⁺ before the staining solutions were added and incubated for 45 min (37 °C, 5 % CO₂, darkness). After the staining process, the cells were kept in PBS⁺⁺ buffer and the fluorescence was examined using a confocal laser scanning microscope (Nikon Eclipse 90i). CaAM was excited at 488 nm and the fluorescence recorded with a 515/30 nm bandpass filter and EtHD-1 was excited at 543 nm and the emitted fluorescence signal recorded with a 650 nm longpass detector.

3.2.4.2 CYTOSKELETON AND CELL NUCLEUS STAINING

To visualize the cytoskeleton as well as the nucleus of the cells, tetramethylrhodamine isothiocyanate-labeled phalloidin (TRITC phalloidin, Sigma-Aldrich) and 4',6-Diamidino-2-phenylindole (DAPI) were used. Phalloidin is a bicyclic heptapeptide from the poisonous mushroom *Amanita phalloides* (Lynen, F. *et al.* 1938) which binds to the filamentous actin of the cytoskeleton. The binding to the actin filaments prevents filament depolymerization and shifts the equilibrium from actin monomers to actin filaments (Dancker, P. *et al.* 1975) making it possible to visualize the actin filaments in fixated cells. Since phalloidin itself is not fluorescing, it is labeled with the fluorophore rhodamine which is exhibiting bright red fluorescence.

DAPI can freely enter the cell through the lysed cell membranes in fixated cells. The DNA-specific probe forms fluorescent complexes by intercalation into AT-rich sequences of the DNA located in the cell nucleus emitting bright blue fluorescence (Kapuscinski, J. *et al.* 1995) as depicted in Fig. 3.3.

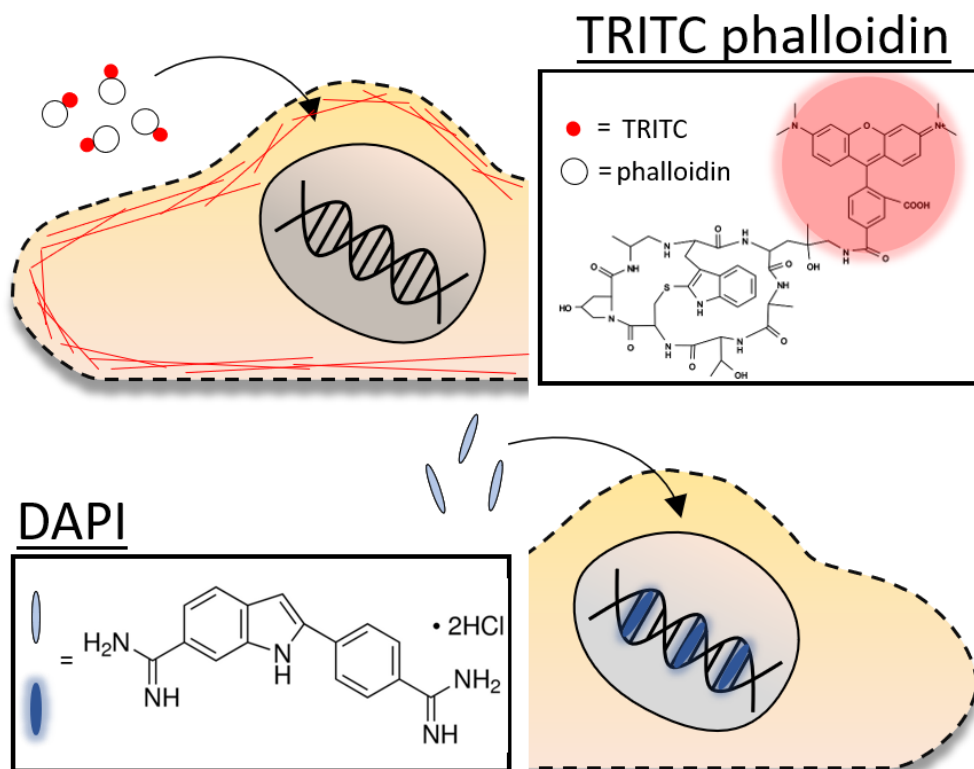


Fig. 3.3 Schematic illustration of the staining process of the cytoskeleton with TRITC phalloidin and of the cell nucleus with the help of the DNA-specific dye DAPI. Phalloidin binds to the filamentous actin of the cytoskeleton and the attached TRITC dye emits red fluorescence after excitation. To visualize the nucleus of the cells, DAPI is added after fixation. The DNA-specific probe enters the permeabilized membrane and intercalates into the DNA, leading to the emission of blue fluorescence after excitation.

The cytoskeleton/nucleus staining was performed after the treatment of confluent cell monolayers with glyphosate and Roundup®. Stainings have also been performed on spheroids growing on sensor foils. The respective cell sample was washed twice with PBS⁺⁺ and subsequently fixated using PFA (paraformaldehyde, 4 % (w/v), 10 min, RT). The cells were washed twice before Triton X-100 dissolved in PBS⁺⁺ was added to the

cells (0.5 % (v/v), 10 min) to permeabilize the cell membranes for the subsequent addition of TRITC phalloidin ($3 \mu\text{g}\cdot\text{mL}^{-1}$ in PBS⁺⁺, 40 min, 37 °C, 5 % CO₂). The cell nuclei were then stained by adding the DAPI solution ($10 \text{ ng}\cdot\text{mL}^{-1}$ in PBS⁺⁺, 2 min, RT). After two minutes, the staining solution was removed. CLSM images of the stained cells were taken with a 60x immersion objective and PBS⁺⁺ as immersion medium. TRITC-phalloidin was excited at 543 nm and the emission fluorescence was recorded with a 650 nm long pass detector. The nucleus-staining dye DAPI was excited at 408 nm and the emitted fluorescence detected with a 450/35 nm bandpass detector.

3.3 IMPEDANCE SPECTROSCOPY

3.3.1 ELECTRIC CELL-SUBSTRATE IMPEDANCE SENSING (ECIS™)

Electric cell-substrate impedance sensing is a non-invasive, label-free and real-time technique with high throughput and time resolution for *in vitro* investigations of changes in the cell morphology and cell dynamic.

This method was first described in 1984 by Ivar Giaever and Charles R. Keese and is based on the frequency-dependent measurement of the alternating current resistance (impedance) which can then, at a selected frequency, be plotted against time. The measurement setup consists of a small working electrode and a significantly larger counter electrode, both being thin planar goldfilm electrodes which are electrically connected by the bulk medium (see Fig. 3.4) and showing a smooth surface cells can be cultivated on. Due to the inverse proportionality of the impedance to the electrode area, the small working electrode contributes the most to the overall impedance, outweighing the resistance of the counter electrode and the bulk medium. The cultivated cells adhering to the gold surface behave like dielectric particles due to the insulating properties of their plasma membrane resulting in significantly increasing impedance with increasing cell-coverage of the working electrode. The total impedance of the cell-covered electrode can be condensed to a simplified three-parameter equivalent circuit where all three elements are connected in series representing the integrated impedance from the bulk resistance (R_{bulk}), the resistive and capacitive properties of the cell layer (Z_{cl}) and the influence of the electrode-electrolyte interface (CPE – constant phase element). As the measured impedance is strongly dependent on the three-dimensional structure of the cells, the impedance (Z_{cl}) can be broken down to three major pathways of the current contributing to the overall cell signal. Thus, changes in the cellular morphology lead to altered current pathways: beneath the cells, through the cell-cell contacts or directly through the cytoplasm of the cells which together are mirrored by increasing or decreasing impedance values. Since these pathways are strongly frequency-dependent, the current in the low to medium frequency range ($f < 10$ kHz) will predominantly flow through the narrow cleft underneath the cells (represented by the parameter α in the ECIS™ model) and pass the cell layer via paracellular pathways (the resistance of the cell-cell contacts is taken into account in the parameter R_b of the ECIS™ model). At higher frequencies ($f > 10$ kHz) the AC current primarily takes the transcellular route leading directly through the cellular membranes and the cytosol (the capacitive properties of the cell membranes are represented in the parameter C_m). The three major pathways of the current with the corresponding ECIS™ parameters are illustrated in Fig. 3.4.

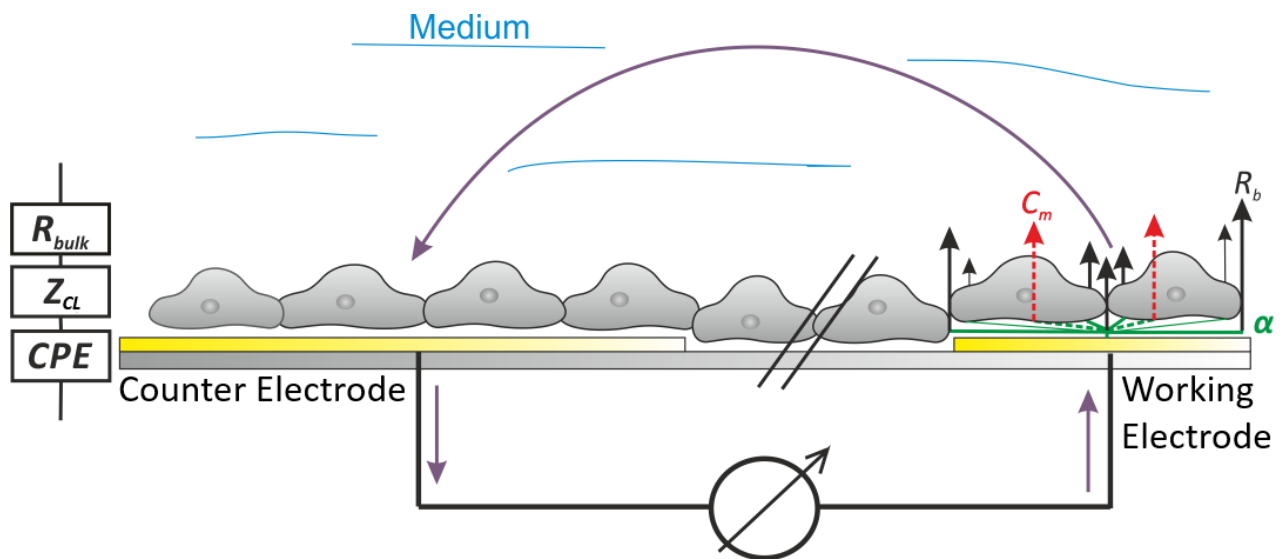


Fig. 3.4 Schematic of the working principle of ECISTM. It illustrates the general layout revealing the working and the counter electrode being electrically connected by the supernatant medium. On the left-hand side, the equivalent circuit is shown with the overall impedance consisting of three individual elements connected in series: the contribution of the electrode-electrolyte interface (CPE constant phase element), the impedance of the cell monolayer (Z_{cl}) and the resistance of the electrolyte solution (R_{bulk}). On the right-hand side, an illustration of the three pathways of the current contributing to Z_{cl} is shown: the transcellular pathway at $f > 10$ kHz directly through the cell body (C_m) as well as the paracellular pathways of the current at $f < 10$ kHz through the cell-cell contacts (R_b) and through the cell-substrate contacts beneath the cells (α).

3.3.2 ARRAY TYPES & EXPERIMENTAL SETUP

In this work all ECISTM-based experiments were performed using commercially available ECISTM electrode arrays purchased from Applied BioPhysics. Three different electrode layouts were selected for the investigations of the different phenotypes of the cells. All arrays contain eight measurement chambers (8-well) with a growth area of 0.75 cm^2 . The arrays are generally equipped with one counter electrode (CE) in the center of the array which reaches in every well. A photopolymer defines different numbers of $250\text{-}\mu\text{m}$ working electrodes (WE) in each well. In the case of only one WE (8W1E, Fig. 3.5 A) and ten WE (8W10E, Fig. 3.5 B), the CE is significantly larger than the cumulative area of the working electrode(s). The 8W10E+ array forms an exception because the sizes and numbers of the working and counter electrodes are equal (Fig. 3.5 C). The working electrodes (WE) from each well can then be measured sequentially against the counter electrode (CE). An 8-well ECISTM array is schematically illustrated in Fig. 3.5.

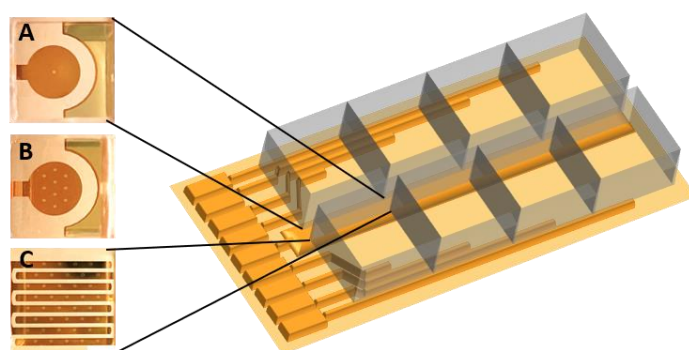


Fig. 3.5 Illustration of the electrode layouts applied in this thesis. **(A)** 8W1E arrays exhibiting one small working electrode used for migration and micromotion monitoring. **(B)** 8W10E equipped with 10 small working electrodes per well, designed for the measurement of adhesion processes and cytotoxic effects on cells. **(C)** 8W10E+ arrays with interdigitating electrode fingers where each electrode finger contains five working electrodes. The 8W10E+ electrodes were applied to perform proliferation studies. The schematically illustrated array is equipped with the central counter electrode reaching in every well and the different electrode layouts are depicted in detail in A – C (working electrode on the left-hand side and part of the counter electrode on the right-hand side). Pictures from the electrode layouts were adapted from www.biophysics.com/cultureware.php.

The area of 0.049 mm^2 for one circular working electrode (see Tab. 3.6) is significantly smaller compared to the area of the counter electrode which amounts to 0.15 cm^2 on 8W1E arrays. The ECIS™ technique reveals a remarkable sensitivity since the size ratio between WE and CE in the case of 8W1E arrays as well as the WE diameter of only $250 \text{ }\mu\text{m}$ allows for the observation of only 50 – 100 cells. Increasing numbers of working electrodes and therefore a larger active electrode area for 8W10E and 8W10E+ arrays, respectively, enable the detection of an increasing number of cells but is simultaneously accompanied by a decreasing sensitivity. 8W1E arrays were used for migration and micromotion measurements in order to be able to create a small, defined wound in the cell layer for migration experiments and to gain highly time-resolved and sensitive conditions for micromotion measurements by only recording the impedance of one working electrode. To monitor cell attachment and spreading as well as cytotoxicity studies, 8W10E arrays with ten working electrodes per well were used to obtain an average signal of a higher number of cells. Using arrays with multiple working electrodes, the impedance values are integrated over all working electrodes in one well (see Tab. 3.6). An even further increased electrode area is exhibited by 8W10E+ arrays which are especially designed for proliferation measurements showing two sets of 20 circular working electrodes with $250 \text{ }\mu\text{m}$ in diameter located on interdigitated fingers.

Tab. 3.6 Technical data for the individual ECIS™ arrays showing different electrode layouts.

Electrode layout	Working electrodes per well	Electrode area	Detectable number of cells
8W1E	1	0.049 mm^2	50 – 100
8W10E	10	0.49 mm^2	500 – 1000
8W10E+	40	1.96 mm^2	2000 – 4000

The electrode arrays were contacted in an array holder from Applied BioPhysics via small gold pins in a cell culture incubator (37 °C, 0 % CO₂, humidified atmosphere). Fig. 3.6 shows the relay between the array holder and the impedance analyzer which enables the switching between the individual electrode combinations. The relay and the impedance analyzer are controlled by the microcontroller which is connected to a computer.

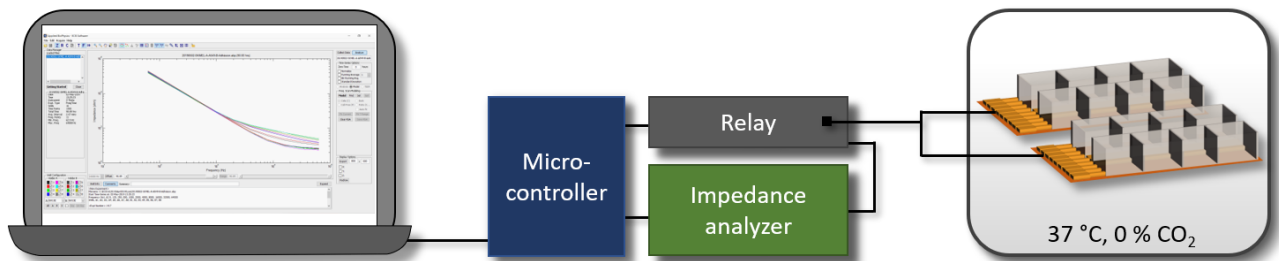


Fig. 3.6 ECIS™ measurement setup. A computer is connected to the microcontroller which controls relay and impedance analyzer. The relay is furthermore connected to the array holder where ECIS™ arrays are contacted. The relay switches between the individual electrode combinations.

All ECIS™-based measurements were recorded in an MFT mode (time-dependent impedance measured at multiple frequencies) with a simultaneous recording of eleven frequencies in a range between 62.5 Hz and 64 kHz. The ECIS™ software was used to control the data acquisition during the measurement and data evaluation was done afterwards with *OriginPro*. All time courses of the ECIS™ measurements were plotted at the respective sensitive frequency. Therefore, the impedance (IZI) or the capacitance (C) spectrum (IZI, C plotted against the frequency) of the cell-covered electrode was divided by that of the same cell-free electrode. The resulting normalized IZI was again plotted against the frequency yielding a gaussian-like peak which revealed the sensitive frequency as the maximum. In the case of the normalized capacitance, a sigmoidal curve with higher values at low frequencies and lower values at high frequencies was obtained. The sensitive frequency for the normalized capacitance thus could be determined by choosing the minimum value. These cell line-dependent sensitive frequencies were used for data evaluation.

3.3.3 PREPARATION FOR CELL EXPERIMENTS

The commercially available ECIS™ electrode arrays were first exposed to an argon plasma for 30 s to hydrophilize and sterilize the electrode surfaces. Following the addition of a cysteine/NaCl solution (200 µL / well, see Tab. 3.4) the arrays were placed into the array holder and connected to the ECIS™ instrument. The cysteine solution supplemented with NaCl as electrolyte was used as conductive buffer during the application of electrical pulses to remove residues of the fabrication process. The applied pulse parameters strongly depend on the different electrode layouts (see Tab. 3.7). The cysteine forms a self-assembled amino acid layer due to the adsorption of the thiol groups to the gold surface (Lee, J. M. *et al.* 2007). The amino acid

layer hydrophilizes the surface which promotes cellular adhesion since the ECM proteins are able to adhere to the surface without denaturation. Without pulsing the electrodes prior to initial use, the residues lead to higher cell-free impedance values and thus lower measurement sensitivities. After washing with double-distilled H₂O and drying overnight, a substrate coating with fibronectin (FN) was done if necessary. Therefore, a droplet (30 μ L) of a fibronectin solution (20 μ g·mL⁻¹ in ddH₂O) was placed directly on the working electrode. After incubation (1 h, RT) and two washing steps with culture medium, the cells could be inoculated. The coating procedure was performed before all adhesion experiments and for all experiments using SpiCa and SK-MEL-28 cells due to more reproducible and more sensitive impedance signals after coating.

Tab. 3.7 List of the pulse parameters and coating protocols for the different array types.

Array type	Pulse parameters	Coating	Assay type
8W1E	2400 μ A, 32 kHz, 30 s	FN (20 μ g·mL ⁻¹), 1 h, RT*	Migration & Micromotion
8W10E	1000 μ A, 1500 Hz, 30 s	FN (20 μ g·mL ⁻¹), 1 h, RT	Adhesion
8W10E+	1000 μ A, 800 Hz, 30 s	FN (20 μ g·mL ⁻¹), 1 h, RT*	Proliferation

(*) coating protocol only used for experiments carried out with SK-MEL-28 and SpiCa cells.

Cell seeding was done immediately after subcultivation (see chapter 3.1.2) using the respective cell density in culture medium (400 μ L / well) according to Tab. 3.3. 24 h after seeding, the cell culture medium was exchanged (400 μ L / well) to ensure sufficient nutrient supply for the cells. 48 h after cell inoculation, the wells were rinsed twice with L-15 medium and after the addition of the pH-adjusted or toxin-supplemented L-15 medium, the experiment was started. The recording of a baseline signal in L-15 medium was substituted by the parallel measurement of an L-15 control over the entire course of the measurement. L-15 medium was supplemented with 1 % P/S for all experiments and additionally with 1 % FCS for the experiments performed with SpiCa and SK-MEL-28 cells. The experimental procedure only differed for the adhesion assays as can be seen in chapter 3.3.4.1. All ECISTM measurements were conducted in a standard cell culture incubator at 37 °C, 0 % CO₂ and humidified atmosphere.

3.3.4 IMPEDANCE-BASED SENSING OF CELLULAR PHENOTYPES

The ECISTM technique offers the possibility of investigating different cell phenotypes. Each assay addresses a cellular developmental stage during the *in vitro* lifetime of cells, each stage entailing different metabolic requirements for the cells.

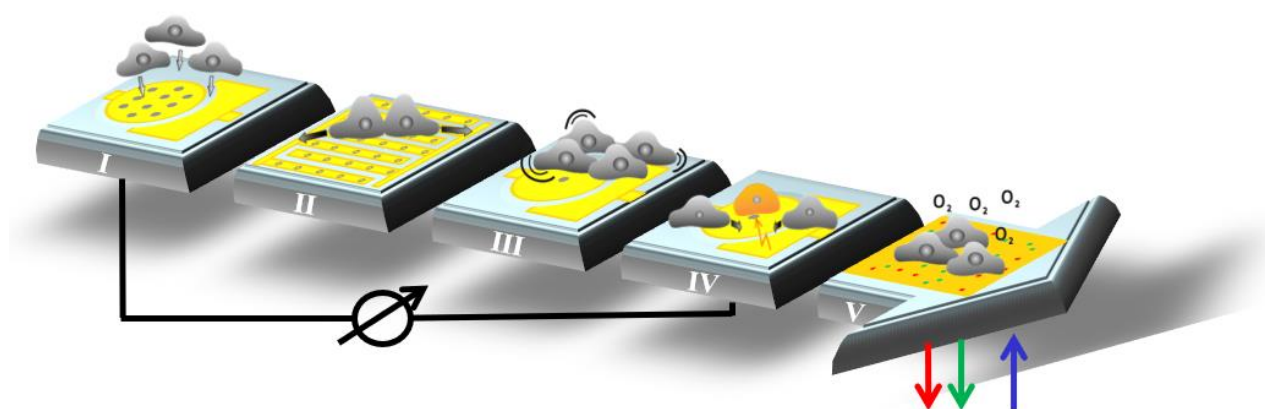


Fig. 3.7 Schematic lifetime of cells after the subcultivation with the different developmental phenotypes, starting with adhesion and spreading (I), followed by cell division and proliferation (II). Upon reaching a confluent monolayer, the cellular micromotion (III) and the migration behavior (IV) can be detected via ECISTM and the respiratory activity (V) can be monitored using an image-based oxygen-sensing readout technique.

Fig. 3.7 schematically shows the lifetime of cells *in vitro*, starting directly after the subcultivation. The first step after detachment, subcultivation and reseeding is the sedimentation to the bottom of a substrate with subsequent attachment or adhesion followed by spreading of the cells. This phenotype can be observed best with 8W10E arrays (Fig. 3.7 I) using ECISTM. After the attachment, the cells start to proliferate which can be monitored using 8W10E+ arrays (Fig. 3.7 II). Confluent cell monolayers are studied with respect to: (i) cellular micromotions (Fig. 3.7 III), (ii) the migration behavior after generating a cell-free area by the application of electrical pulses to the cells on the electrode (Fig. 3.7 IV) or (iii) the respiratory activity via oxygen-specific sensor foils and an imaging-based readout technique (Fig. 3.7 V).

3.3.4.1 MONITORING THE KINETICS OF CELL SPREADING

The monitoring of the attachment and spreading of mammalian cells on suitable substrates provides information about complex processes like spreading kinetics with high relevance to various physiological and pathological processes (Hynes, R. O. *et al.* 1992). The resuspended cells were inoculated in the desired cell density on the arrays and the initial sedimentation towards the goldfilm electrodes as well as the subsequent adhesion and spreading can be observed with a decrease of the capacitance or an increase in the impedance (Lukic, S. and Wegener, J. *et al.* 2015). ECISTM offers an experimental method to investigate cell-substrate interaction in a quantitative, real-time manner with a very high temporal resolution (Wegener, J. *et al.* 2000). To achieve complete attachment of the cells, the working electrodes were pre-coated with the protein fibronectin (FN). This extracellular matrix protein is recognized by integrin receptors and thereby accelerates cell attachment to the electrode surface. The recognition of integrins was first described in 1984 (Hynes, R. O. *et al.* 1992; Pierschbacher, M. D. *et al.* 1984).

After the initial pre-coating of the gold electrodes with fibronectin, the arrays were washed several times and finally the wells were filled with pH-adjusted L-15 medium (200 μL / well) and the arrays placed into the array holder which was connected to the ECISTM instrument. The cells were subcultivated as described in chapter 3.1.2 but instead of normal cell seeding, the cells were again transferred into centrifugation tubes using a defined volume of cell suspension to achieve the necessary cell number. After the second centrifugation step and the aspiration of the culture medium, the cells were resuspended in L-15 medium with the respective pH_e (extracellular pH) and afterwards inoculated directly into the wells (200 μL cell suspension per well yielding a total volume of 400 μL / well). Subsequent cell sedimentation, attachment and spreading were observed via changes in the capacitance signal. The capacitance is directly proportional to the area of the working electrode ($C = \epsilon_0 \cdot \epsilon_r \cdot A \cdot d^{-1}$ with ϵ_0 being the vacuum permittivity, ϵ_r the relative permittivity, A the area of the working electrode and d the thickness of the dielectric layer on the electrode including coating and cells). As the relative permittivity changes due to the presence of the cells, the capacitance reflects the degree of cell coverage on top of the electrode. The total capacitance of the cell-covered electrode can be calculated by the reciprocal addition of the individual capacitive elements (the bare electrode and the cell layer on top) connected in series ($1/C_{\text{cell-covered electrode}} = 1/C_{\text{bare electrode}} + 1/C_{\text{cell layer}}$). The reciprocal addition leads to a decrease in capacitance with cell coverage. The monitoring of the capacitance signal at high frequencies reflects the cell coverage even more precisely as the current pathway at frequencies ≥ 10 kHz predominantly leads across the cellular membranes and directly through the cytoplasm of the cells. Consequently, low capacitance signals at these frequencies are an indication for adherent cell monolayers.

3.3.4.2 MONITORING THE KINETICS OF CELL PROLIFERATION

The proliferation rate of the cells is a characteristic phenotype to draw conclusions about the doubling time. In contrast to migration assays (see chapter 3.3.4.3) where the focus lies on cell motility and the spreading ability of the cells, the monitoring of proliferation is well-suited to get an estimate of the velocity of cell growth and division. In contrast to all other assay types, the cells were seeded in a subconfluent density in the proliferation studies. The continuing cell proliferation and growth is indicated by a continuous decrease of the capacitance signal.

The subcultivation (see chapter 3.1.2) and seeding procedure for ECISTM arrays was described previously. 48 h after cell inoculation and several washing steps of the adherent cells on top of 8W10E+ electrodes to remove cell culture medium residues, the measurement medium (L-15) adjusted to the respective pH_e (400 μL /well, pH_e 6.4, 7.2, 7.4 and 7.8) was added and the proliferation was recorded.

3.3.4.3 MONITORING THE WOUND HEALING BEHAVIOR

The migration behavior of different cell lines under various extracellular conditions was investigated using an automated, ECISTM-based wound healing assay provided by Applied BioPhysics. The cells were grown to confluence onto 8W1E arrays, yielding a complete cell coverage of working and counter electrode in each well. The application of lethal electrical pulses for several seconds in a microampere-range led to cell death and subsequent detachment of the cells growing directly on the working electrodes. The cells in the periphery of the working electrode were not affected by the pulse and started to repopulate the cell-free area of the artificially created wound in the dimensions of the circular working electrode ($5 \cdot 10^{-4} \text{ cm}^2$) (Keese, C. R. *et al.* 2004). The electrical wounding provoked a sharp decrease in the impedance to values of the cell-free electrode. Due to the migration of the still vital cells surrounding the working electrode, the impedance values increased again and reached values obtained before the pulse application as soon as a confluent monolayer was re-established. From the time courses, information about the ability of the cells to migrate and the rate of the wound healing behaviour can be deduced (Lukic, S. and Wegener, J. *et al.* 2015).

In this thesis, the wound healing technique was used to investigate the migration phenotype for several cell lines under various extracellular pH_e as well as under the influence of toxins. In the pH studies, three different cancerous cell lines (A549, SK-MEL-28 and SpiCa) were examined in contrast to “normal” cells represented by the NRK cell line. Four different extracellular pH_e (6.4, 7.2, 7.4 and 7.8, see Tab. 3.4) were applied during the migration experiments. The cells were cultivated in 8W1E arrays according to the protocol mentioned in chapter 3.3.3 and were wounded 24 h after the start of the measurement with an electrical pulse (30 s, 2400 μA , 32 kHz for 8W1E arrays). The 24 h recording time prior to the pulse application was taken to create a constant baseline signal and to provide enough time for the cells to adapt their metabolism to the pH-adjusted medium or to toxic substances added to their environment. After the wounding, the impedance signal was recorded for at least 80 h. The migration protocol for the SK-MEL-28 cells deviated from that of the other cell lines regarding the time point of wounding. The cells were wounded as soon as 3 h after the start of the measurement corresponding to approximately 5.5 h after cell inoculation. The premature wounding is due to their insusceptibility to the applied current pulse which becomes more pronounced with increasing adhesion and spreading time resulting in less complete wounding efficiency.

3.3.4.4 MONITORING THE CELLULAR MOTILITY BY MICROMOTION MEASUREMENTS

Living cell monolayers are highly dynamic systems. The cells do not only migrate into open spaces after cell wounding (compare chapter 3.3.4.3) but they constantly show fluctuations and motility even in a confluent monolayer. These motions reflect the metabolic activity of the cells and are provoked by changes of the

cytoskeleton. Cell motility is crucial for tissue formation in *in vivo* systems, wound healing in organisms, immune responses and the development of the early embryo (Giaever, I. *et al.* 1991). Other studies reported a correlation between metastatic behaviour of cancer cells and their motility (Partin, A. W. *et al.* 1988). The actin cytoskeleton is important for the regulation of the dynamic behavior due to assembling and disassembling of actin filaments as a response to different signals (Lambrechts, A. *et al.* 2004). As ECIS™ provides a time resolution in the range of milliseconds and is sensitive to changes of the cell morphology, it is perfectly suited to monitor cellular *micromotions* which was first described in 1984 (Giaever, I. *et al.* 1984).

For the monitoring of the cellular micromotion, the cells were seeded to confluence according to the protocol in chapter 3.3.3. 24 h after the addition of L-15 medium with the respective pH_e , the impedance was recorded in the *rapid-time-collection* (RTC) mode with a resolution of five data points per second, at a frequency of 4 kHz over a period of time of 10 minutes. The time-resolved impedance signal can be converted into the variance, which offers the possibility to compare the cell's movement under different extracellular pH_e (pH 6.4, 7.2, 7.4 and 7.8). Therefore, the impedance signal was divided into constant time segments, each 32 seconds in length. The impedance values of each segment were fitted by linear regression. The individually determined trendlines from each segment were used to subtract the fitted value at each data point from the corresponding measured one which led to a fluctuation curve around the zero line. Squaring the standard deviation of these fluctuations yielded the variance for every segment. The individual variance values were averaged to a mean variance which could be used to compare the cellular micromotion.

Every experiment was performed using the four pH_e in duplicates. Initially, the variance values for the cells being exposed to a physiological pH_e of 7.4 were averaged. The variances of all the other wells were normalized with respect to the calculated mean variance value of the physiological pH_e . Thereafter, all normalized variances of the same pH_e from all performed experiments were averaged and the respective standard error of mean was calculated.

3.4 RATIOMETRIC OPTICAL OXYGEN SENSING

3.4.1 PRINCIPLE OF RATIOMETRIC OPTICAL SENSING

Reliable measurements of oxygen concentrations are of high interest as this parameter is crucial for all living organisms. The detection of changes in the oxygen concentration in the microenvironment of cells was performed using a sensor foil with a ratiometric signal readout. This technique is based on two dyes which are embedded in a matrix material with one dye being oxygen-sensitive and one reference dye being independent of the presence of oxygen concentrations (see Fig. 3.8). The sensitivity or dependency on oxygen levels relies on changing luminescence intensities with differing analyte concentration.

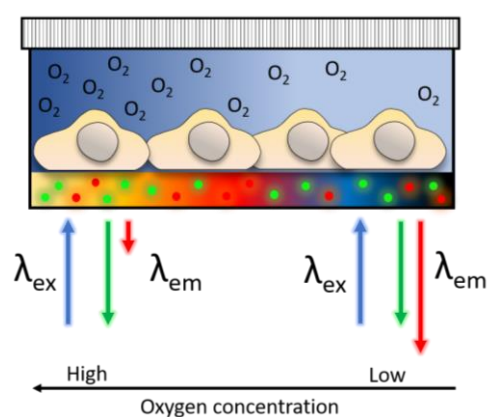


Fig. 3.8 Schematic illustration of the ratiometric optical oxygen-sensing principle. In the experiments conducted in this thesis, mammalian cells were grown directly on top of the sensor foil. The supernatant medium is oxygen-saturated on the left-hand side and the oxygen concentration is decreasing towards the right-hand side being measured by the ratiometric luminescence signal of the oxygen-sensitive dye (red) and the reference dye (green) located in an oxygen-permeable matrix. A yellow sensor foil color-codes the calculated ratio at 100 % dissolved O_2 after conversion into false color images (see chapter 3.4.4). When cells respire the available oxygen, this is observable by changes of the luminophore intensity ratio and color-coded by a dark blue sensor foil color (0 % O_2).

The intensity ratio of both dyes generally can be determined either by recording two images with different excitation wavelengths but the same emission wavelength (Hulth, S. *et al.* 2002) or with two different emission wavelengths after excitation with the same wavelength (Song, A. *et al.* 1997). This technique offers advantages as for example not being as susceptible to variations in the background signal, reflections or inhomogeneous distribution of the luminophores in contrast to pure intensity measurements (Larsen, M. *et al.* 2011). Prerequisites of this technique are (i) that the maxima of the two luminophore emission spectra are sufficiently separated, (ii) high photostability of the dyes, (iii) minimal cytotoxicity and (iv) linear or sigmoidal relationships between the analyte concentration and the luminescence intensity, allowing for a precise and quantitative determination of the oxygen concentration (Wang, X.-D. *et al.* 2008, Wang, X.-H. *et al.* 2012, Chu, C.-S. *et al.* 2015).

The dependency of the luminescence intensity on the oxygen concentration is based on collision quenching. These quenching processes occur between dissolved oxygen molecules and the excited luminophores with the luminescence intensity decreasing with increasing quencher concentration (Xiong, X. *et al.* 2006). The quenching process can be described by the Stern-Volmer equation:

$$\frac{I_0}{I} = 1 + K_{SV}[Q] \quad [3.1]$$

I_0 and I are the detected luminescence intensity at 0 % oxygen and at the present partial oxygen pressure, respectively; $[Q]$ is the oxygen concentration and K_{SV} the Stern-Volmer quenching constant (Fujiwara, Y. *et al.* 2003). The luminescence quenching can be detected via a decrease in luminescence intensity or with regard to the lifetime when measuring the decay time of the luminescence (Demas, J. N. *et al.* 1999). In this thesis both measurements techniques were applied (see chapter 3.4.2).

Luminescence can occur in the form of fluorescence as well as phosphorescence after excitation. The Jablonski diagram (see Fig. 3.9) illustrates the electronic states involved in the excitation and emission processes. Fluorescence and phosphorescence are photon emission events due to molecular relaxations from electronically excited states. Each electronic state is divided into several sublevels representing different vibrational modes. Light with a certain wavelength excites a molecule in the electronic ground state (S_0) and the lowest vibrational level to a certain vibrational level in an electronically excited state (S_1) due to the absorption of photons (Geddes, C. D. *et al.* 2002). After the excitation, the molecule gets relaxed to the lowest vibrational level in the respective excited state due to vibrational relaxation called *internal conversion* on the time scale of femtoseconds to picoseconds, leading to the Stokes shift. This Stokes shift is responsible for the red-shifted emission wavelength of fluorescent photons compared to the excitation wavelength. Fluorescence is observed as the molecule eventually falls back to the electronic ground state with a fluorescence lifetime of nanoseconds. Fluorophores in excited states can also be relaxed by collisional quenching where the energy is transferred to the quencher molecule (due to *external conversion*) leading to a nonfluorescent relaxation to the electronic ground state of the fluorophore (So, P. *et al.* 2002).

Instead of directly emitted fluorescence, *intersystem crossing* processes can occur. Intersystem crossing is the molecular relaxation from a singlet excited state (S_1) to an energetically lower triplet excited state (T_1). The spin-orbit coupling, responsible for intersystem crossing, describes the reversion of the spin of the electron and thus the change of the multiplicity. Since the relaxation from T_1 to S_0 requires another spin conversion, phosphorescence lifetime lasts for microseconds to seconds and displays a significantly larger Stokes shift (So, P. *et al.* 2002). The increased phosphorescence lifetime leads to an increased possibility of collision quenching processes. Generally, quenching occurs by the transfer of energy from the excited luminophore to the quencher (Callis, P. R. *et al.* 2014).

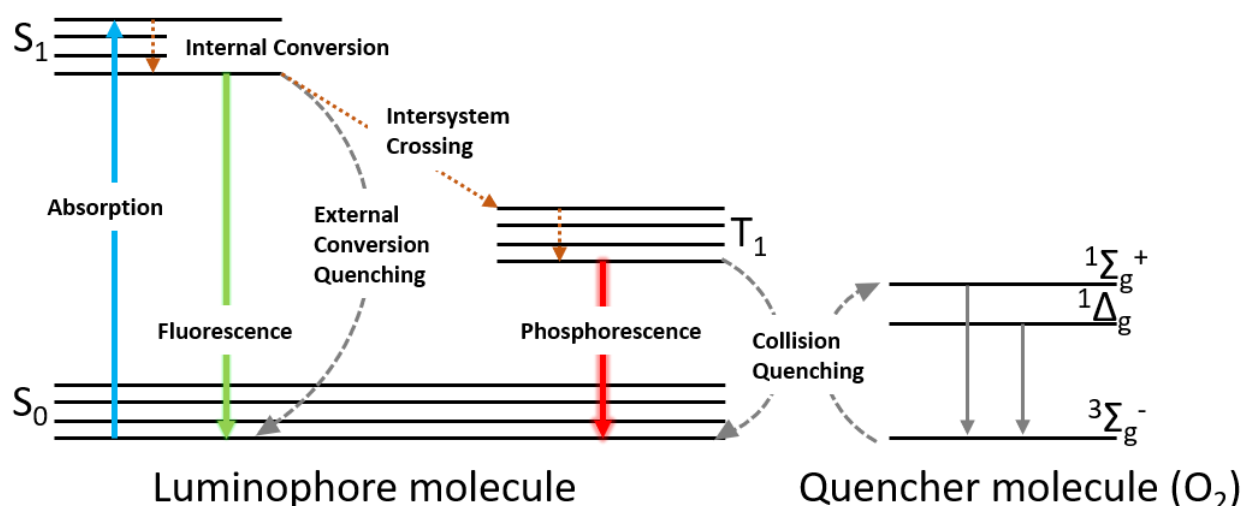


Fig. 3.9 The Jablonski diagram depicts the different electronic states involved in fluorescence and phosphorescence emission. After the initial photon absorption, the luminophore is raised to the excited electronic state (S_1). Internal conversion leads to electronic relaxation to the vibrational ground state in S_1 . The conversion back to S_0 can occur via fluorescence emission or due to external conversion, meaning the energy is transferred to quencher molecules. Intersystem crossing explains the electronic relaxation from a singlet excited state to a triplet excited state (T_1). After an internal conversion within T_1 , the decay to S_0 can happen by emission of phosphorescence or by luminescence-free quenching events initiated by oxygen molecules which will be excited from the triplet ground state to its first or second excited singlet-state. The Jablonski diagram was adapted from So, P. *et al.* 2002.

In this case, the collisional quencher molecule is dissolved oxygen. During the energy transfer, the oxygen molecule itself undergoes an electronic conversion. The paramagnetic oxygen molecule in its triplet ground state ($^3\Sigma_g^-$) can take over the energy from an electronically excited luminophore in the excited triplet state, resulting in a ground state donor luminophore and an electronically excited singlet state oxygen molecule (Kawaoka, K. *et al.* 1967). There are two singlet states of the oxygen molecule: the first excited state ($^1\Delta_g$) and the second excited state ($^1\Sigma_g^+$). A luminescence-free relaxation of the oxygen molecule from the excited singlet states to the triplet ground state then occurs due to collision events with solvent molecules like H₂O (Schweitzer, C. *et al.* 2003). The oxygen collision quenching leads to an oxygen concentration-dependent decrease of the phosphorescence intensity and lifetime and can thus be used to determine unknown O₂ concentrations.

One prominent candidate for oxygen sensing is the probe platinum(II)-5,10,15,20-tetrakis-(2,3,4,5,6-pentafluorophenyl)porphyrin (Pt-TPFPP). The emitted red luminescence of Pt-TPFPP decreases with rising oxygen partial pressure due to its ability as dynamic luminescence quencher (Dissertation Dr. Lorenz Fischer). The combination of the oxygen-sensitive probe with a reference fluorophore diphenylanthracene (DPA, $\lambda_{em} = 440$ nm) allowed for a ratiometric luminescence readout of the two dyes with an RGB technique using one 405-nm excitation wavelength (Meier, R. J. *et al.* 2011).

3.4.2 MEASUREMENT SETUP TO MONITOR OXYGEN CONCENTRATIONS

The measurement of the oxygen concentration in the environment of adherent cells was performed using two different systems. On the one hand, the VisiSens TD and on the other hand, the SensorDish Reader® (SDR®) were used to investigate cellular respiration following different extracellular changes and to compare the results. The VisiSens TD is based on the ratiometric method (see chapter 3.4.1) whereas the SDR® system relies on the measurement of the decay time of the fluorescence lifetime. Both systems were developed by and purchased from PreSens GmbH. The VisiSens TD can be used in two different modifications with different spatial resolutions (see chapter 3.4.2.1) allowing for the examination of adherent cell monolayers as well as 3D tissues like spheroids with respect to oxygen changes due to the metabolic activity of the cells. For these investigations, commercially available sensor foils were provided by PreSens GmbH.

The oxygen-sensitive sensor foil consists of three different layers: the support layer, the sensor layer and the isolation layer. The support layer, composed of polyester, is transparent and oxygen-impermeable. The oxygen-sensitive sensor layer contains the oxygen-sensitive dye as well as the reference dye and exhibits a thickness of 6 μm – 8 μm . The silicon-based isolation layer in a thickness of 20 μm – 50 μm is permeable for dissolved oxygen and suitable for the protection from ambient light. The isolation layer was removed for all measurements in order to achieve a better attachment of the cells to the sensor layer. The oxygen sensor foil reveals an overall thickness of 150 μm – 190 μm for all three layers. The sensor foil was glued into normal cell culture dishes either by a self-adhesive layer or using silicon glue and were afterwards stored in the dark.

3.4.2.1 RATIOMETRIC OXYGEN SENSING

The VisiSens TD system was used for all image-based oxygen measurements with different cell lines and models. It was manufactured and provided by PreSens GmbH. Fig. 3.10 depicts the VisiSens TD consisting of a camera containing a charge-coupled device (CCD) progressive camera chip with a 12-bit ADC (analog to digital converter). The tube is equipped with a sample holder, an excitation light source (LED) and several filters to block interfering light. This tube offers a 2x magnification lens, a field of view of 2064 x 1540 μm^2 (1292 x 946 pixels) and a focus adjustment ring. The microscopic ratiometric imaging kit was used for the investigation of three-dimensional tissue samples due to the very high lateral resolution (Fig. 3.10 A).

Since the tube is removable, it can be substituted by a second height-adjustable aluminum tube equipped with 16 circularly arranged LEDs (Fig. 3.10 B). Half of the LEDs are necessary for the excitation of the oxygen-sensitive dyes and the other eight LEDs are needed for the pH sensing. This measurement setup exhibits a variable field of view between 4 x 3 cm^2 and 8 x 6 cm^2 with an image resolution of 1292 x 964 pixels allowing

for a parallel detection of multiple petri dishes. Both systems were set up in an incubator at 37 °C and 0 % CO₂ and connected to a computer with the *VisiSensTM AnalytiCal 1* software for data acquisition and evaluation. Images were taken every 10 min with an exposure time of 750 – 1000 ms during the time course of 24 h.

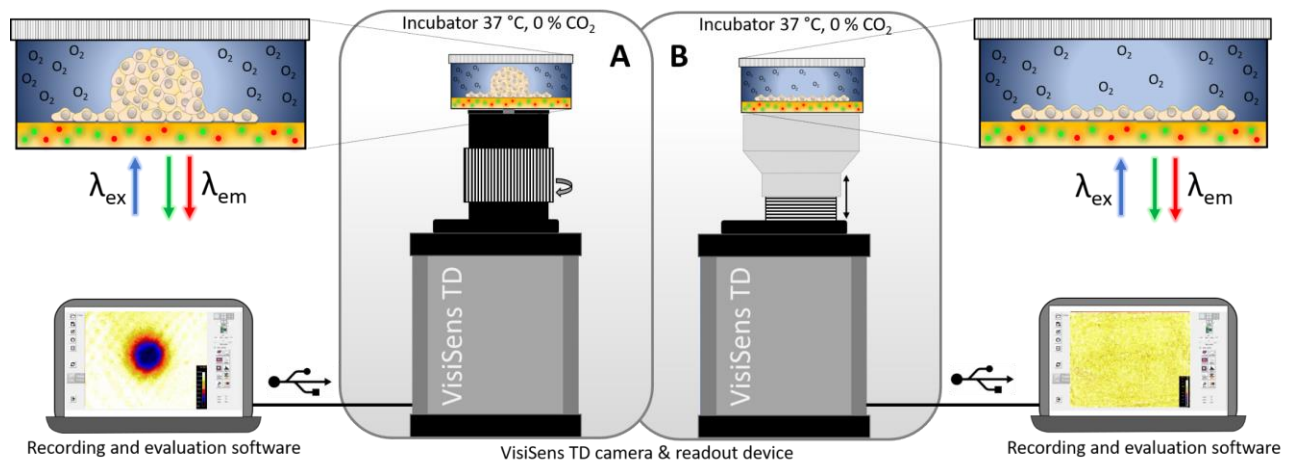


Fig. 3.10 Schematic illustration of the VisiSens TD system used for oxygen sensing. (A) VisiSens TD with a microscopic tube for the investigation of 3D tissue connected to a computer with the corresponding software. (B) VisiSens TD with a height-adjustable tube providing a larger field of view used for measurements with different types of monolayers, connected to a computer for data acquisition and evaluation. The picture was adapted from the dissertation of Dr. Carina Schmittlein (University of Regensburg, 2018).

3.4.2.2 OXYGEN SENSING ON THE BASIS OF FLUORESCENCE DECAY TIME DETECTION

The SensorDish Reader® (SDR®) is a 24-channel reader for the non-invasive and real-time monitoring of the oxygen consumption of adherent cells and was also purchased from PreSens GmbH. Each well contains one oxygen-sensitive sensor spot and the measurement was done with the corresponding SensorDish Reader® (see Fig. 3.11). The SDR® is necessary for fluorophore excitation as well as emission detection and the whole setup was installed in an incubator at 37 °C and 0 % CO₂ and connected to a computer with the corresponding software. In contrast to the ratiometric readout technique of the VisiSens TD, the SDR® measures the air saturation, where 100 % air saturation is equal to 20 % oxygen saturation in solution and an oxygen partial pressure of 149.3 torr which is the unit commonly displayed by the VisiSens TD.

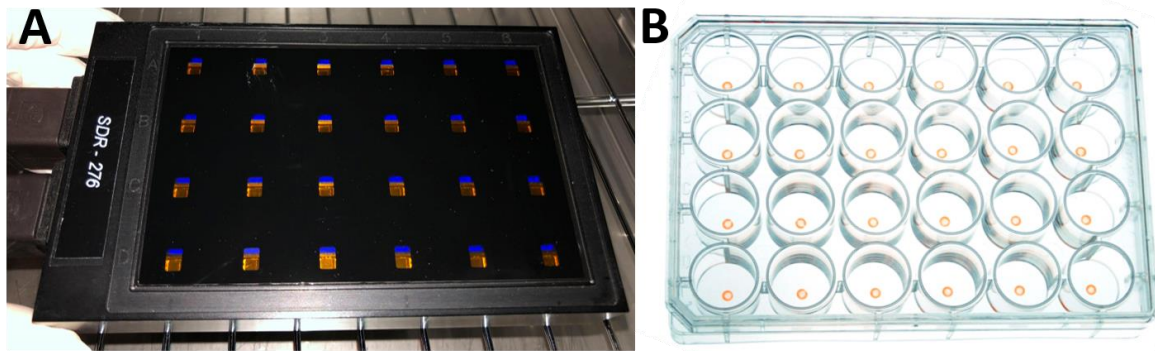


Fig. 3.11 (A) Picture of the SensorDish Reader[®] with 24 LEDs for the excitation of either oxygen-sensitive dyes or pH-sensitive dyes incorporated in the sensor spot in each well. (B) During the measurement, the 24-well plate with the sensor spots in each well needs to be placed on top of the reader purchased from PreSens GmbH.

The measurement principle of the SDR[®] relies on the detection of fluorescence lifetime and, in contrast to the VisiSens TD, it is not based on ratiometric intensity readout techniques. Nevertheless, the oxygen sensitivity results from quenching processes due to oxygen molecules leading to an increasing fluorescence lifetime with decreasing oxygen concentration. Like the ratiometric methods, the determination of the decay time is independent of fluctuations in the light intensity.

Cells being inoculated into the wells containing the oxygen-sensitive spot grow around the sensor spot which is different from imaging where the cells are growing directly on top of the sensor foil. This different setup leads to deviating values of the oxygen concentration due to different geometrical constraints of diffusion. For the SDR[®] measurement setup to yield meaningful results, the cells growing in proximity to the oxygen-sensitive spot in the SDR[®] system need to consume the available oxygen in their environment faster than additional dissolved oxygen can diffuse from the surrounding medium to the sensor spot. If the oxygen consumption is not fast enough, only a steady-state system is established in which the oxygen consumption is merely compensated by the diffusion of fresh oxygen from the supernatant medium.

3.4.3 CELL PREPARATION FOR OPTICAL SENSING

The oxygen sensor foil was provided by PreSens Precision Sensing GmbH. The foil (oxygen sensor foil SF-RPSu4) was either self-adhesive or fixed with silicon glue onto the bottom of standard cell culture petri dishes ($d = 3.5$ cm, growth area 9.6 cm²) with subsequent drying for at least 24 h. This attachment step was performed very carefully with the help of tweezers to avoid scratching the sensor surface. The prepared petri dishes with the immobilized sensor foils were stored at room temperature and protected from light. The oxygen-sensitive sensor foil was additionally equipped with an optical isolation layer which was removed directly before the experiment. Prior to cell inoculation, the sensor foils were cleaned in an argon plasma for

1 min to hydrophilize and sterilize them. After washing twice with cell culture medium, the cells were seeded to confluence (see Tab. 3.3) in standard cell culture medium (2 mL). 24 h after cell inoculation, the medium was exchanged (2 mL). 48 h after seeding, the cells were washed twice with the respective measurement medium (L-15 either adjusted to different pH values or supplemented with toxins) to remove residues of phenol red from the cell culture medium. In order to avoid the diffusion of ambient oxygen into the measurement chamber, the petri dishes were filled air bubble-free with the respective medium (9.6 mL) and were sealed airtight. For that purpose, the inner perimeter of the lid of the petri dish was lined with *Blu-Tack*[®] allowing for tight attachment to the bottom part. A small hole made in the lid offers the possibility to completely fill the petri dish using a syringe. The hole was also sealed with a small piece of *Blu-Tack*[®].

For the detection of changes in the oxygen concentration surrounding spheroids, a small glass ring was glued around the sensor foil. The glass ring ensured the attachment of the spheroid on top of the sensor foil.

During the measurement, the petri dishes were placed on top of the VisiSens TD (see Fig. 3.10) for a total measurement time of 24 h, with 10 min pauses in between the individual recordings.

3.4.4 CALIBRATION OF THE OXYGEN-SENSITIVE SENSOR FOIL

Since different batches of the sensor foil may contain a slightly varying amount of dyes, it was necessary to calibrate every sensor foil individually.

The calibration of the oxygen-sensitive sensor foil was done via a two-point calibration at 37 °C and 0 % CO₂. Differently treated L-15 medium yielded normoxic and hypoxic calibration solutions. To meet normoxic conditions (149.3 torr), L-15 medium was warmed to 37 °C and after the addition to the oxygen-sensitive foil, a snapshot was taken to record the luminescence signal. The second calibration point was done by using the hypoxic solution (0 torr), generated by the addition of 10 g·L⁻¹ sodium sulfite (Na₂SO₃) to L-15 medium. Sodium sulfite reacts with oxygen in a redox reaction to form sodium sulfate (Na₂SO₄) (Fujie, K. *et al.* 1994). Oxygen reduction leads to a strong decrease of dissolved oxygen in solution enabling the calibration. After incubation with the hypoxic solution, the signal was recorded by taking a second snapshot. The two recorded snapshots were used to create a linear calibration curve by determining the respective ratios within the region of interest (ROI). With the linear regression, the red/green ratios of the measurement images can be converted into false color images. Accordingly, the false color images depict the spatial distribution of the available oxygen partial pressure (pO₂). To be able to plot changes of the partial oxygen pressure as a function of time, the false color images were used to determine pO₂ by the Z-profile function (see Fig. 3.12) of the VisiSensVS software (Version 1.0.1.49 from PreSens Precision Sensing GmbH 2018). This software function calculates the averaged pO₂ with the corresponding standard error for the respective ROI for every image

taken during one measurement. Data evaluation was done with OriginPro software and image processing for the examination of oxygen gradients beneath spheroids was done using the software ImageJ.

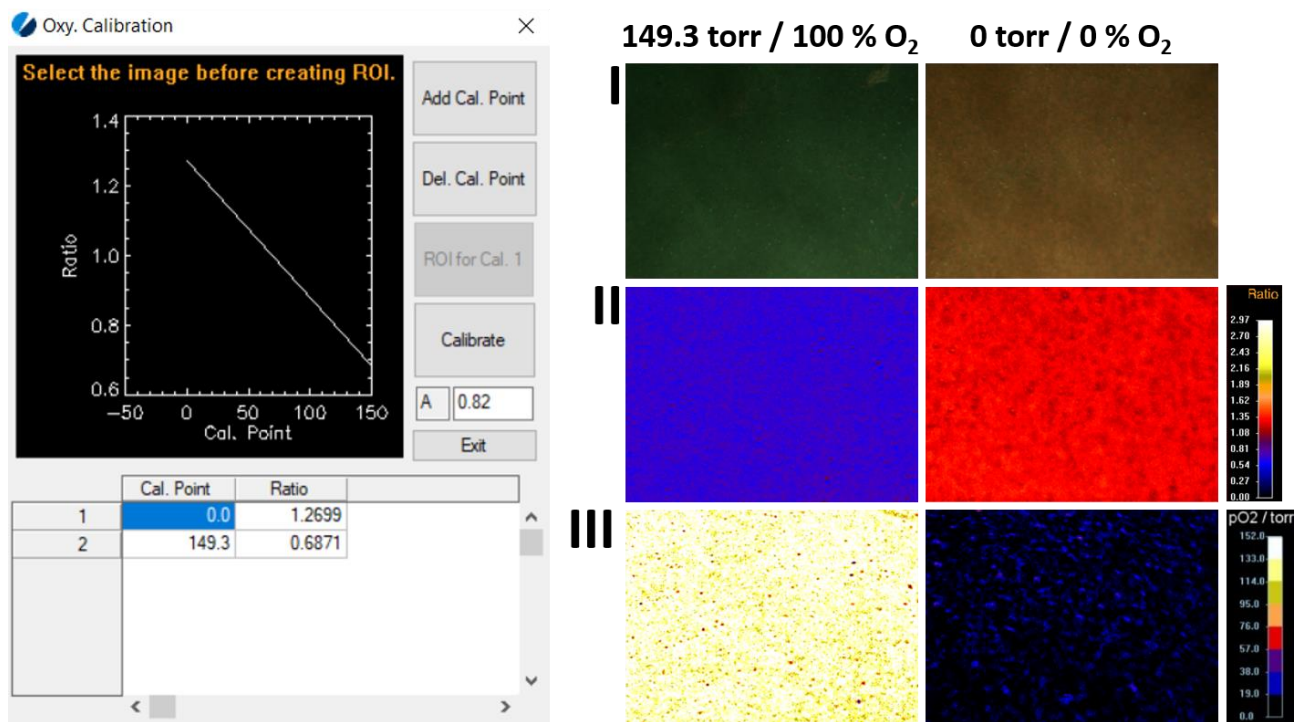


Fig. 3.12 Proprietary software for the oxygen sensor foil calibration. (Left) Software tool for the calibration of the oxygen-sensitive sensor foil prior to experiments. (I) Live preview of the sensor foil at 100 % and 0 % present oxygen. (II) False color images, indicating the measured fluorescence ratio. (III) False color images after the calibration with 100 % oxygen yielding a yellowish color while dark blue represents the condition with 0 % present oxygen.

3.4.5 CALCULATION OF THE APPARENT OXYGEN CONSUMPTION RATE

The measured changes of the partial oxygen pressure due to the respiration of the cells and the resulting conversion of oxygen to CO₂ was plotted as a function of time. Commonly, there was an initial increase in the oxygen partial pressure to be observed due to temperature effects. After the first hour of the measurement, the oxygen concentration decreased at specific rates. A linear regression of the time interval from 1 h – 4 h yielded the *apparent oxygen consumption rate* (AOCR) representing the change of oxygen as function of time.

$$pO_2(t) = AOCR \cdot t + B \quad [3.2]$$

In equation 3.2, B is the y-intercept of the linear regression and AOCR represents the slope in [torr·h⁻¹]. For further evaluation, AOCR values were used to calculate the *oxygen consumption rates* (OCR) on a single cell

level. Therefore, the oxygen partial pressure unit *torr* was translated into a molar oxygen concentration since 149.3 torr are equal to 210.43 $\mu\text{mol}\cdot\text{L}^{-1}$ at atmospheric pressure (1013 hPa) and 37 °C. Division by the respective cell number (cell seeding density multiplied with the growth area) and by the volume of the supernatant medium (9.6 mL in the case of petri dishes) as well as the expression of the time unit in seconds yielded the OCR values [$\text{amol}\cdot\text{s}^{-1}\cdot\text{cell}^{-1}$]. This conversion of the AOOCR into OCR values was only valid for experiments in which complete oxygen depletion could be detected within the course of the measurement.

As the measurements using the SDR® instrument were performed in an open system, it was necessary to convert the AOOCR into the *oxygen consumption rate*, to be able to compare the results with measurements performed in closed systems. For this calculation, the following equation was used as described by Mamchaoui, K. *et al.* 2000:

$$OCR = \frac{-D \cdot S \cdot \alpha [pO_2(h) - pO_2(0)]}{h} \quad [3.3]$$

D is the diffusion coefficient of dissolved oxygen at 37 °C in water ($3.3 \cdot 10^{-5} \text{ cm}^2 \cdot \text{s}^{-1}$), S represents the cell-covered area of the substrate (1.9 cm^2 in each well of a 24-well plate), α is the solubility coefficient of oxygen ($0.94 \mu\text{mol}\cdot\text{cm}^{-3}\cdot\text{atm}^{-1}$ at 37 °C), $pO_2(h)$ constitutes the partial oxygen pressure at the cell layer, $pO_2(0)$ the oxygen partial pressure at the medium surface and h is the height of the supernatant medium.

3.5 MONITORING THE INTRACELLULAR pH_i VALUE

3.5.1 WORKING PRINCIPLE OF INTRACELLULAR pH_i SENSING

One of the main objectives of this work was the detection of the commonly reported inverse pH gradient over the cell membrane of cancer cells in contrast to normal ones. Furthermore, the measurement of the intracellular pH_i in response to changes in the extracellular pH_e would complement the investigations of phenotypic behavior of different cell lines at different extracellular pH_e.

2',7'-bis-(2-carboxyethyl)-5(6)-carboxyfluorescein acetoxymethyl (BCECF-AM) was used to examine the intracellular pH_i. The uncharged and nonfluorescent BCECF-AM ester can rapidly diffuse through the cell membrane into the cytosol, and once the ester bonds are cleaved by esterases inside the cytosol, it is trapped inside the cell in the form of a charged and green-fluorescing dye (Ozkan, P. *et al.* 2002).

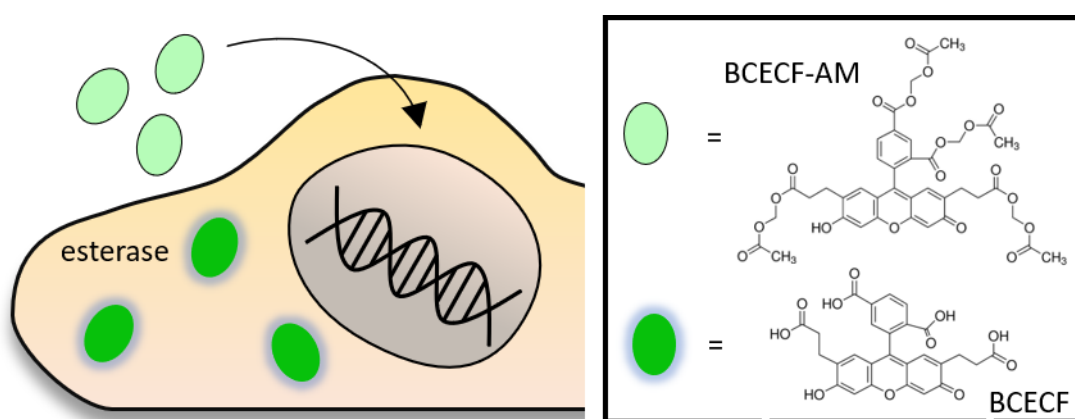


Fig. 3.13 Schematic illustration of the working principle of the pH-sensitive probe BCECF-AM. The probe can freely diffuse across the cell membrane in the form of the uncharged ester molecule. The esterases inside the cell then hydrolyze the ester bonds. The enzymatic cleavage of the acetoxymethyl ester groups leads to the entrapment of the green-fluorescing dye BCECF inside the cytosol. The fluorescence intensity of BCECF is highly pH-dependent.

After the staining with the BCECF dye, the pH-dependent fluorescence can be detected using excitation at $\lambda_{\text{ex}} = 485 \text{ nm}$ and simultaneous emission detection at two wavelengths ($\lambda_{\text{em}} = 535 \text{ nm}$ and 612 nm). The pH_i can be estimated according to the fluorescence emission ratio at $535 \text{ nm}/612 \text{ nm}$ (Perez-Sala, D. *et al.* 1995), which gradually increases as a function of pH_i (Franck, P. *et al.* 1996). Since the pH_i values are calculated with the help of the measured fluorescence intensities, it was necessary to create a calibration curve beforehand. The use of the K⁺/Na⁺ ion carrier (ionophore) nigericin ensures a pH adaption of the pH_i to the externally adjusted extracellular pH_e environment. Nigericin is a monocarboxylic acid antibiotic which is isolated from *Streptomyces* and transports monovalent cations across membranes (Sutko, J. L. *et al.* 1977). The exchange of protons, in turn, enables the equilibration of the pH_i to various pH_e (5.5, 6, 6.4, 7.2, 7.4, 7.8 and 8).

The fluorescence ratios plotted against the respective pH_e, revealed a linear correlation (eq. 3.4) used as a calibration curve.

$$\frac{\lambda_{em, 535 nm}}{\lambda_{em, 612 nm}} = A \cdot pH_e + B \quad [3.4]$$

In equation 3.4, ($\lambda_{em, 535 nm} / \lambda_{em, 612 nm}$) indicates the ratio of the fluorescence intensities, A the slope of the linear regression and B the y-axis intercept. Using this equation, the measured fluorescence emission ratio following cell stimulation with differing extracellular pH_e but without the addition of nigericin, could be used to determine the respective pH_i (eq. 3.5):

$$pH_i = \frac{\frac{\lambda_{em, 535 nm}}{\lambda_{em, 612 nm}} - B}{A} \quad [3.5]$$

3.5.2 STAINING PROTOCOL FOR THE pH-SENSITIVE DYE

A stock solution of BCECF-AM (10 mM) in dimethyl sulfoxide (DMSO) was prepared and diluted 1:1000 in PBS⁺⁺ (10 μ M) for the measurement. The cells were seeded to confluence (see Tab. 3.3) into 96-well plates 48 h before the measurement, with a medium exchange after 24 h. After rinsing the cells twice with PBS⁺⁺, they were stained with BCECF-AM via incubation with the dye (50 μ L / well, 10 μ M in PBS⁺⁺, 10 min, 37 °C, 5 % CO₂, darkness). After the incubation, the cells were rinsed again and subsequently incubated with L-15 medium adjusted to various pH_e (5.5, 6, 6.4, 7, 7.4, 7.8 and 8, supplemented with 1 % P/S and 1 % FCS, 15 min, RT, darkness) with and without additionally added nigericin (10 μ M). Every condition was measured in quadruplicate in three individual experiments for each cell line. The fluorescence intensity was measured upon excitation at the wavelength of 485 nm and the emitted fluorescence was monitored simultaneously at 535 nm and 612 nm (dual band pass filter) with the help of a Tecan reader.

3.6 CYTOTOXICITY STUDY OF BISPHENOL A

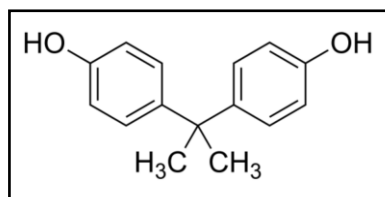


Fig. 3.14 Molecular structure of BPA.

Bisphenol A (4,4'-(propane-2,2-diyl)diphenol, BPA) is obtained by the reaction of two phenol molecules with one acetone molecule and was developed in the 1890s. The global demand is expected to reach approximately 9.6 million tons in 2020 (GrandViewResearch). It is used as

a precursor for polycarbonate and epoxy resin production. It can also be found in adhesives, powder paints, protective window glazing, building materials, lenses, thermal paper and several synthetic materials, e.g. baby bottles (Staples, C. A. *et al.* 1998). The unwanted release of BPA from plastics occurs during handling and heating processes and should especially be taken into account during food production and storage. In the 1930s, BPA was reported to be an estrogen-mimic leading to disorders of the female reproductive system in rats (Dodds, E.C *et al.* 1936). Since then, reports of BPA affecting human health increased significantly. BPA is known to be an endocrine disruptor, it binds to estrogen receptors producing estrogenic effects (Viñas, R. *et al.* 2012) but can also act as an antiestrogen by blocking the estrogenic response (Richter, C. A. *et al.* 2007). BPA affects several organs and can interrupt the developing central nervous system and the immune system (Wetherill, Y. B. *et al.* 2007). BPA is furthermore discussed to cause fertility problems, reduced sperm quality, breast cancer, miscarriages and promotes metabolic diseases like diabetes, oxidative stress, inflammations and many more (Rochester, J. R. *et al.* 2013). BPA has become so ubiquitous, it was found in the urine of almost all tested adults and children (Braun, J. M. *et al.* 2011), as well as in fetal plasma and placental tissue (Schönfelder, G. *et al.* 2002).

The public discussion about BPA so far has not shown signs of abatement and the substance can still be detected in many products. The cytotoxic concentration of BPA, as reported throughout the literature, is broad and rather inconsistent which led to a cytotoxicity study with respect to cellular respiration within the scope of this thesis. The effects on several cellular phenotypes were investigated by Maria Zinkl and Saphia Assam (2019 at the University of Regensburg under the supervision of Prof. Dr. Joachim Wegener). Complementary studies were performed by monitoring the respiratory activity during BPA exposure within this thesis. Two different measurement techniques were applied to validate the results: on the one hand, the respiratory activity was measured using the SensorDish Reader[®], and on the other hand, investigations were performed with the help of the VisiSens TD (see chapter 3.4.2).

The experimental procedure was similar in both cases. NRK cells were seeded to confluence (see Tab. 3.3) into petri dishes with integrated oxygen-sensitive sensor foil or into 24-well plates containing an oxygen-

sensitive sensor spot. After the *standard pre-experiment protocol*, the cells were rinsed twice and after addition of the respective BPA solution (see chapter 3.1.5) in L-15 medium, the measurement was started. Prior to the measurement, the petri dishes were filled air bubble-free and sealed airtight. Data was collected for a time period of 24 h with a time resolution of 10 min. All experiments were done in triplicate.

3.7 MONITORING THE BIOLOGICAL IMPACT OF GLYPHOSATE ON ANIMAL CELLS

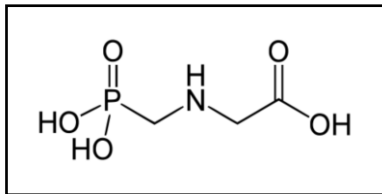


Fig. 3.15 Molecular structure of the herbicide glyphosate.

Glyphosate (N-(phosphonomethyl)glycine) is the active ingredient in the herbicide Roundup®, which is commercially available since 1974. There are several publications which reported about toxic effects on mammalian cells (Gasnier, C. *et al.* 2009). Due to the increasing number of lawsuits being filed against the Roundup® producer Monsanto, which is a subsidiary of Bayer since 2018, the toxicity and potentially cancerogenic properties of Roundup® are highly discussed issues.

Glyphosate is applied in herbicides because it inhibits the 5-enolpyruvyl-shikimate-3-phosphate synthase (EPSPS) which is part of the shikimate pathway in plants and most microorganisms (Zabalza, A. *et al.* 2017). The structural similarity of glyphosate to phosphoenolpyruvate, the natural substrate of EPSPS, leads to inhibition of the synthase. This inhibition in turn prevents the biosynthesis of the aromatic amino acids phenylalanine, tyrosine and tryptophan, resulting in the death of the plant. Cultivated plants can be genetically engineered to be glyphosate-resistant, while the growth of unwanted plants or weeds is irreversibly inhibited (Arregui, M. C. *et al.* 2004). For the commercially available formulation Roundup®, glyphosate is transferred to its ionic form with isopropylamine as counter ion to improve the water solubility.

Glyphosate is reported to act as endocrine disruptor leading to changes in protein synthesis, altering the metabolism, provoking morphological and neurological changes as well as disfunctions of the immune system and many more (Darulich, J. *et al.* 2001; Walsh, L. P. *et al.* 2000). It is also discussed to accelerate hormone-dependent cancers like breast and prostate cancer (Thongprakaisang, S. *et al.* 2013).

The aim was to perform a comprehensive toxicity study comparing the herbicide formulation Roundup® and its active ingredient glyphosate in the pure form. Analyzing the effect of those two toxins on eukaryotic cells was supposed to yield information on whether glyphosate itself or the total composition of the chemicals used in Roundup® reveals higher toxicity.

3.7.1 CELL VIABILITY ASSAY

PrestoBlue™ is a resazurin-based, membrane-permeable reagent for the quantification of the cell viability after exposure to toxic substances. Resazurin is a non-fluorescent blue dye which can be irreversibly reduced to the pink-fluorescent resorufin by NADH/H⁺-dependent dehydrogenases in the cytosol of the cells. NADH is formed in many metabolic reactions in the cells and thus it can be used to reduce resazurin to resorufin

(Lall, N. *et al.* 2013). Therefore, a high intensity of the measured fluorescence signal can be quantitatively interpreted as a normal metabolic activity of the cells and thus no influence of toxic substances on the cells.

For the PrestoBlue™ assay, NRK, A549 and MDCK II cells were seeded to confluence on 96-well plates with a growth area of 0.31 cm² (200 µL / well) and medium was exchanged 24 h after seeding. 48 h after seeding, the culture medium was replaced with L-15 medium (200 µL / well) as negative control and Roundup® or glyphosate equivalent to following concentrations of the active ingredient glyphosate: 40 mM, 20 mM, 10 mM, 8 mM, 5 mM, 2 mM, 1 mM, 0.5 mM, 0.2 mM and 0.1 mM. Since the commercially available mixture Roundup® as well as the dissolved pure glyphosate revealed strongly acidic pH values of around 5.8 and 2.4, respectively, experiments were not only performed using the acidic solutions but for reasons of comparison, solution with a neutrally adjusted pH were also prepared. Therefore, the stock solutions were adjusted to a pH value of 7.4 using K₃PO₄ and NaH₂PO₄.

After an incubation period of 24 h (37 °C, 0 % CO₂), the glyphosate solutions were replaced with the PrestoBlue™ solution (100 µL / well, 1:10 dilution in PBS⁺⁺ supplemented with 1 g·L⁻¹ glucose). A positive control was created by using the PrestoBlue™ solution mixed with Triton-X-100 (0.05 % v/v). The colorimetric change due to the reduction of resazurin to the fluorescing resorufin was spectrometrically detected with a *Tecan Reader* (λ_{ex.} = 532 nm, λ_{em.} = 600 nm) after a previous incubation period of 1 h (37 °C, 0 % CO₂).

The measured fluorescence intensities were corrected by the background fluorescence (I_{blank}) and then used to calculate the cytotoxicity index (CI) for each concentration of glyphosate and Roundup® using the following formula:

$$CI = \left(1 - \frac{\text{corr. fluorescence intensity } I_{\text{sample}}}{\text{corr. fluorescence intensity } I_{\text{negative control}}} \right) \cdot 100 \quad [3.6]$$

The fluorescence intensity I_{sample} refers to the averaged intensity for a given concentration of the cytotoxins and the fluorescence intensity I_{negative control} represents the averaged intensity of the negative control. To determine the standard deviation of CI for each concentration, equation 3.7 was used:

$$SD = \left(\frac{SD_{\text{blank}}}{I_{\text{blank}}} + \frac{SD_{\text{sample}} + SD_{\text{blank}}}{I_{\text{sample}} - I_{\text{blank}}} \right) \cdot CI \quad [3.7]$$

I_{blank} describes the averaged fluorescence intensity of the blank sample and I_{sample} refers to the average fluorescence intensity for each concentration of glyphosate or Roundup®. SD_{blank} and SD_{sample} represent the standard deviations of the averaged blank samples and the individual concentrations of the toxins, respectively.

3.7.2 IMPEDANCE-BASED PHENOTYPIC ASSAYS

The ECIS™ technique was used to investigate the toxic effect of glyphosate and Roundup® on NRK cells. The phenotypes proliferation, migration and micromotion under the influence of different concentrations of glyphosate within the commercial Roundup® formulation or as pure substance were examined. The experiments were prepared as described in chapter 3.3.3. NRK cells were seeded either in a low cell density ($2 \cdot 10^4$ cells·cm⁻²) for proliferation monitoring or seeded to confluence ($25 \cdot 10^4$ cells·cm⁻²) for migration assays, cellular micromotions and for the acute toxicity experiments. The cells were provided with fresh culture medium 24 h after seeding and after 48 h, the cell culture medium was replaced with L-15 medium and data was collected for 3 h. Following the baseline recording, L-15 medium was replaced with the respective concentration of Roundup® or glyphosate. For the examination of the three phenotypes proliferation, migration and micromotions of the cells, three different concentrations (5 mM, 1 mM, 0.2 mM) were used in duplicates as well as two controls without the addition of any toxin. In the migration experiments, the cells were wounded after having been exposed 24 h to the respective herbicide concentration by the application of an electrical pulse. The repopulation of the cell-free electrode, which could be followed by an increasing impedance value, could be observed in a concentration-dependent manner (see chapter 3.3.4.3). Since cell layers are dynamic systems, highly time-resolved impedance data (micromotion measurements) were used to unveil information about the motility of the cells covering the working electrode. This investigation was performed 24 h after the addition of the respective toxin concentration at the frequency of 4 kHz with five readings per second for a total of 10 min. In addition to the three phenotypic experiments and to complement the viability investigation via PrestoBlue™, ECIS™-based acute toxicity experiments were performed. The protocol differed only in the concentration with respect to the described proliferation, migration and micromotion experiments. After baseline recording for 3 h, glyphosate and Roundup® were applied to the wells of the ECIS™ arrays in concentrations of 40 mM, 20 mM, 10 mM, 5 mM, 2 mM, 1 mM, 0.2 mM and a toxin-free control. The cellular response to the respective glyphosate or Roundup® solutions were recorded for at least 68 h.

3.7.3 MONITORING OF THE RESPIRATORY ACTIVITY

The consumption of oxygen provides quantitative information about the cellular respiration and consequently the metabolic activity of the cells. In these experiments, the cells were grown to confluence in petri dishes (9.6 cm²) containing a piece of self-adhesive oxygen-sensitive sensor foil. With the help of the VisiSens TD changes in the partial oxygen pressure in the microenvironment of the cell layer could be measured. 24 h after cell inoculation, the cell culture medium (2 mL) was exchanged and after another 24 h,

the cell culture medium was replaced with different dilutions (9.6 mL) of glyphosate and Roundup® in L-15 (10 mM, 2 mM, 0.2 mM and 0 mM). To prevent the diffusion of atmospheric oxygen into the solutions which would distort the results, the petri dishes were hermetically sealed and filled air bubble-free using Blu-Tack®. Each measurement was conducted in a cell incubator (37 °C, 0 % CO₂) over a period of 24 h with the camera taking pictures every 10 min. Every condition was examined in triplicate.

3.7.4 POST-EXPOSURE CELL STAINING

After the treatment described in chapter 3.7.3, some kind of cellular fixation on the substrates could be observed. To further investigate these observations, CaAM/EtHD-1 and TRITC phalloidin/DAPI stainings were performed to distinguish between living and dead cells as well as to highlight the cytoskeleton and the nuclei, respectively. Detailed staining protocols can be found in chapter 3.2.4.

The cells were inoculated in Lab-Tek® 8-well chamber arrays which were glued onto glass slides using silicon grease. 24 h after seeding, the cell culture medium was exchanged and after another 24 h, it was replaced by glyphosate and Roundup® dissolved in L-15 medium yielding the same final concentration of glyphosate in the mixture and as pure substance (40 mM, 20 mM, 1 mM and 0 mM). The cells were incubated for 24 h (37 °C, 0 % CO₂) with the different glyphosate and Roundup® concentrations before the staining was performed. In a control experiment, cells were equally incubated in L-15 medium but without glyphosate being added. The cell staining was performed according to chapter 3.2.4.

4 IMAGE-BASED SENSING OF OXYGEN CONCENTRATIONS AND DIFFUSION PROCESSES

Oxygen is essential for almost all living organisms. From an evolutionary standpoint, oxygen marks the beginning of life and simultaneously it is the final electron acceptor during the oxidative phosphorylation on the molecular level. Energy is being converted in the mitochondrial respiration from reduced carbon to energy-rich phosphates in adenosine triphosphate (ATP) which serves as the universal energy currency in all forms of life (Semenza, G. *et al.* 2012). The fundamental role of oxygen explains the importance of being able to sense oxygen concentrations in proximity to cellular systems. The sensor foil-based system provided by PreSens GmbH allows for the detection of changes in oxygen levels due to the respiratory activity of cells.

4.1 RESPIRATORY ACTIVITY OF DIFFERENT CELL LINES

4.1.1 EXPERIMENTS WITH CELL MONOLAYERS (2D)

The monitoring of cellular respiration was performed 48 h after seeding, with the cells being covered by L-15 medium. For the experiments, standard cell culture petri dishes ($A = 9.6 \text{ cm}^2$) were used, filled air bubble-free and sealed airtight. The petri dish growth area was divided into four equally large parts with the help of PDMS spacers to be able to observe the respiration of four different cell lines (MDCK I & II, NRK and SK-MEL-28) simultaneously within one measurement.

Fig. 4.1 A shows phase contrast images of the cell monolayers (MDCK I & II, NRK, SK-MEL-28), taken right after the 24-h measurement. Fig. 4.1 B illustrates the calibrated false color images of the sensor foil after 0 h, 3 h, 6 h and 12 h with bright yellow meaning 100 % dissolved oxygen and black representing the state of 0 % dissolved oxygen. A cross can be observed due to the PDMS spacer glued on top of the oxygen sensor foil in order to separate the growth area of the respective cells. 3 h into the measurement, it could be seen that MDCK II and SK-MEL-28 cells consumed the available oxygen slightly faster than MDCK I and NRK cells as indicated by the blue areas in the upper left and lower right quadrant of the image. With more time passing by, the cells converted more of the available oxygen, eventually resulting in 0 torr oxygen partial pressure as indicated by the false color image after 12 h showing nearly completely black quadrants. Only beneath the PDMS spacer some oxygen was left as can be seen by the blue-colored cross in the false color image after 12 h.

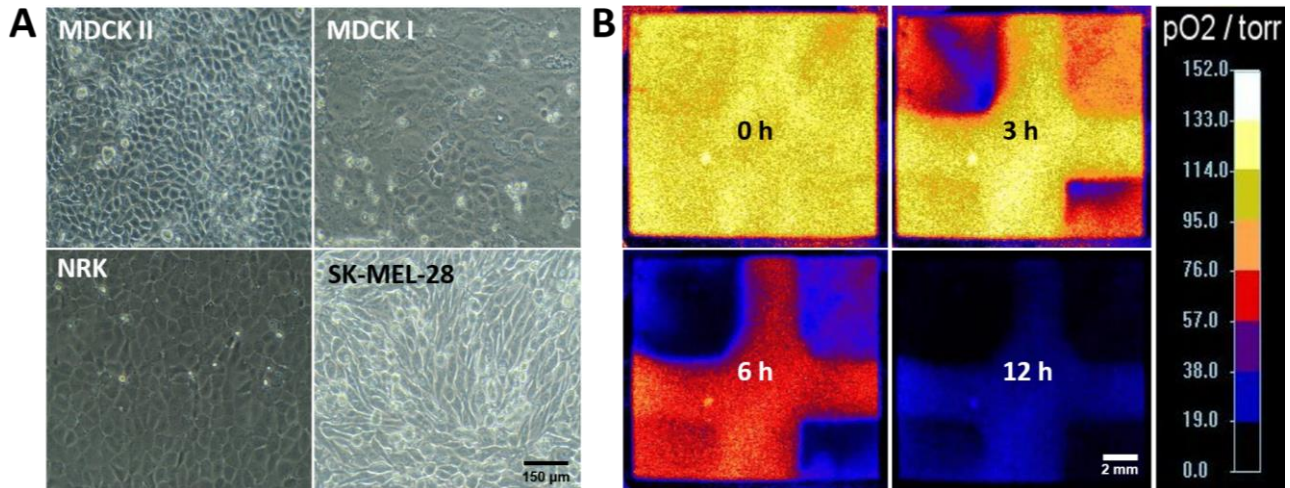


Fig. 4.1 Parallel image-based detection of the time-dependent oxygen depletion due to cellular respiration of MDCK I & II, NRK and SK-MEL-28 cells. **(A)** Phase contrast images taken after 24 h of measurement time. **(B)** Calibrated false color images of the sensor foil from the beginning of the experiment, after 3 h, 6 h and 12 h of recording with bright yellow indicating 149.3 torr pO_2 and black showing a 0 torr pO_2 level. The experiments were performed in a standard cell culture incubator at 37 °C and 0 % CO_2 . Scale bar depicts 150 μm **(A)** and 2 mm **(B)**.

Calibrated false color images were taken every 10 min and the oxygen partial pressure (pO_2) was calculated from each picture. The pO_2 values were plotted as a function of time and fitted linearly between 1 h and 4 h. The linear regression revealed the *apparent oxygen consumption rate* (AOCR) for each individual cell line. This technique was also used in further investigations with additional cell lines and the AOCR values for all tested cell lines are summarized in Fig. 4.2 A.

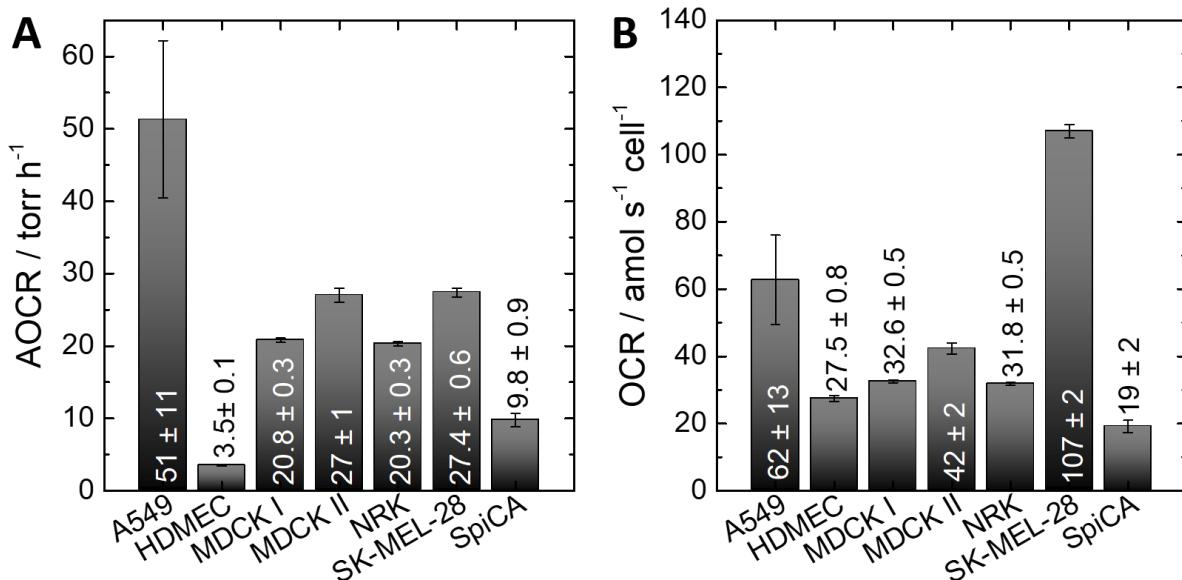


Fig. 4.2 (A) Apparent oxygen consumption rates (AOCRs) for all monitored cell lines. The AOCRs were determined by linear regression from 1 h to 4 h of the time-dependent pO_2 values. **(B)** Oxygen consumption rates (OCRs) for the direct comparison of the respiratory activity on a single cell level (compare chapter 3.4.5) Experiments were performed at 37 °C and 0 % CO_2 .

The four cell lines revealed AOCR values of around $(20.3 \pm 0.3) \text{ torr}\cdot\text{h}^{-1}$, $(20.8 \pm 0.3) \text{ torr}\cdot\text{h}^{-1}$, $(27 \pm 1) \text{ torr}\cdot\text{h}^{-1}$ and $(27.4 \pm 0.6) \text{ torr}\cdot\text{h}^{-1}$ for NRK, MDCK I & II, and SK-MEL-28 cells, respectively. MDCK II and SK-MEL-28 cells displayed the highest respiration rates, which was also optically observable due to the color changes of the calibrated false color images. Compared to that, the A549 cell line, which was monitored separately, yielded AOCR values of $(51 \pm 11) \text{ torr}\cdot\text{h}^{-1}$ which was the highest AOCR value observed in this thesis. However, since the cell lines were all seeded in different cell densities due to their individual cell sizes, AOCRs were converted into *oxygen consumption rates* (OCR) expressing the amount of oxygen being consumed by only one cell per second (see Chap. 3.4.5). This conversion led to OCR values of $(107 \pm 2) \text{ amol}\cdot\text{s}^{-1}\cdot\text{cell}^{-1}$ for SK-MEL-28 cells trailed by $(62 \pm 13) \text{ amol}\cdot\text{s}^{-1}\cdot\text{cell}^{-1}$ for A549 cells. The two epithelial skin cancer types SK-MEL-28 and SpiCa cells ($(19 \pm 2) \text{ amol}\cdot\text{s}^{-1}\cdot\text{cell}^{-1}$) revealed the highest and the lowest consumption rates comparing all cell lines under test. NRK, HDMEC and MDCK I & II exhibited OCRs of approximately $20 \text{ amol}\cdot\text{s}^{-1}\cdot\text{cell}^{-1}$, $28 \text{ amol}\cdot\text{s}^{-1}\cdot\text{cell}^{-1}$ and 33 & $42 \text{ amol}\cdot\text{s}^{-1}\cdot\text{cell}^{-1}$, respectively.

4.1.2 EXPERIMENTS WITH 3D-TISSUE MODELS

Cell culture is a useful tool for *in vitro* investigations and hence for initial drug screenings, toxicity studies and fundamental cell research. Since cells cultured in monolayers behave differently from cells growing in *in vivo* tissue, the formation of three-dimensional tissue models can bridge the gap between 2D cell culture and lab animals as 3D equivalent. Cells growing in cultured networks constitute models that are more complex and react differently than cells growing on planar substrates due to altered nutrient and oxygen supply, changed waste disposal and higher amounts of cell-cell contacts leading to adapted cell-cell communication. Since spheroids are not vascularized, different zones within one spheroid have been found. The cells growing in the outer spheres have easy access to nutrients and dissolved oxygen but this supply is decreasing towards the spheroid's core. The aim was to be able to investigate the respiratory activity of cells growing in three dimensions.

The spheroids were placed on top of the oxygen-sensitive sensor foil and were allowed to attach to the surface for 24 h. The attachment of the spheroid led to the formation of a cell monolayer around the spheroid on the sensor foil which grew with time. This attachment allowed for the investigation of the respiratory activity in a cross section of the spheroid. Fig. 4.3 illustrates spheroids growing on top of the sensor foil. The spheroids were either live/dead- or DAPI-stained (Fig. 4.3 A & C, compare chapter 3.2.4) and Fig. 4.3 shows photographs in different magnifications of the spheroid sitting on the sensor foil surface within a petri dish.

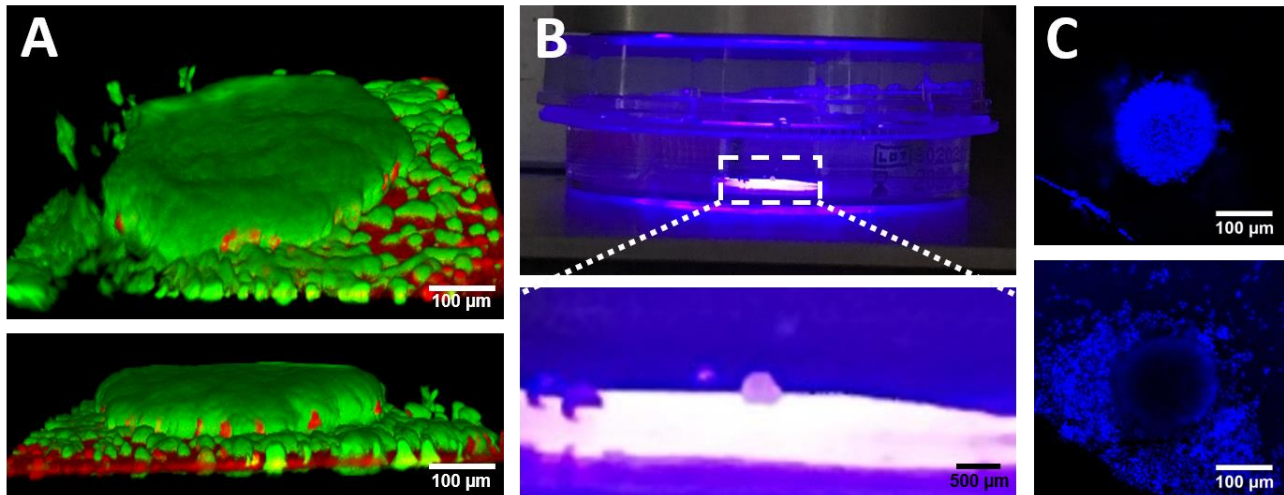


Fig. 4.3 Images of spheroids growing on top of oxygen-sensitive sensor foils. (A) 3D CLSM image of an SK-MEL-28 spheroid after live/dead staining and (B) a picture showing the spheroid on top of the oxygen-sensitive sensor foil in a standard petri dish with an enlargement below. (C) Upper row: CLSM image of an MCF-7 spheroid after DAPI staining with the focal plane at the top of the spheroid and in the lower row, the focal plane was located directly above the sensor foil.

The sensor foil-based sensing of the respiration of spheroids revealed oxygen gradients beneath the tissue. The images were evaluated either from line profiles across the entire spheroid or by plotting changes of the pO_2 within three different regions of interest (ROI) as a function of time. One ROI was located in the center beneath the spheroid, the second in the periphery of the spheroid and the last one next to the spheroid. The profile evaluation was done using ImageJ with profile dimensions of 850×12 pixels. Fig. 4.4 displays the two different evaluation methods.

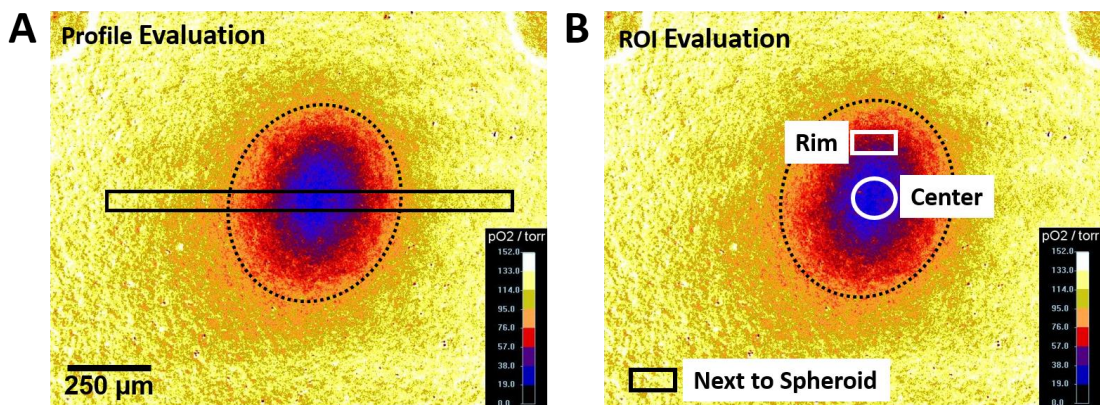


Fig. 4.4 Schematic illustration of data evaluation following image-based oxygen sensing beneath spheroids (indicated by the dotted line). (A) Profile evaluation in an area of 850×12 pixels in size with a pixel resolution of $1.6 \mu\text{m}$. (B) Region of interest (ROI) evaluation with three different ROIs in the field of view: one ROI was located centrally beneath the spheroid growing on top of the sensor foil, one ROI in the spheroid's periphery (rim) and one next to the spheroid.

Within this thesis, three different cell lines were used to form spheroids to be investigated. The spheroids were placed on top of the sensor foil 7 days after formation (see chapter 3.1.3) and were allowed to attach for 24 h before the cell culture medium was exchanged for L-15 medium and the recording was started. The

images were calibrated and used to evaluate profile plots 1 h, 6 h, 12 h and 24 h after measurement start (see Fig. 4.5). The profile data was afterwards smoothed according to the Savitzky Golay method by fitting successive sub-sets of 20 data points by the method of linear least squares. The profiles seemed to be strongly dependent on the cell line and the tissue structure of the spheroid. The dotted lines mark the area directly beneath the spheroid growing on the sensor foil.

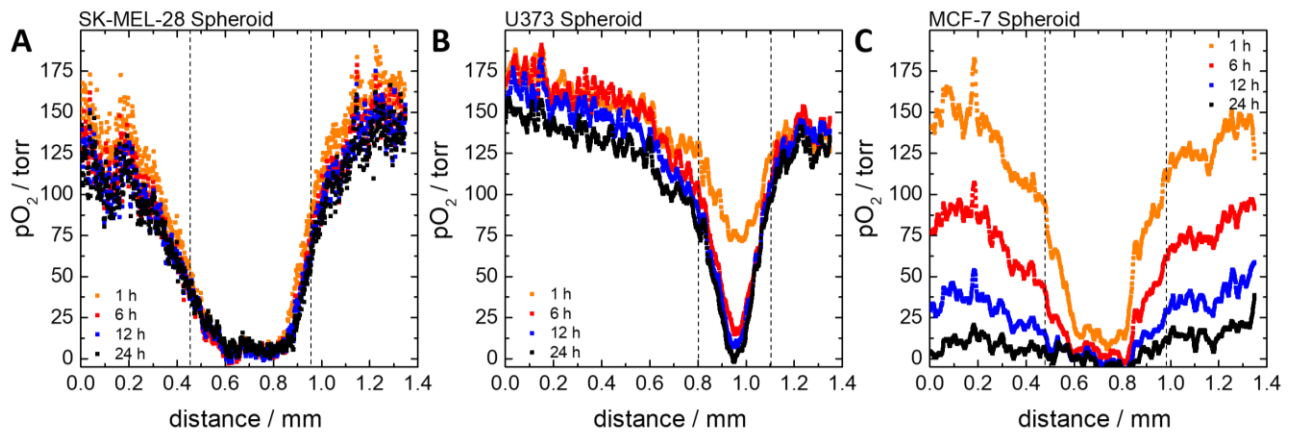


Fig. 4.5 Image-based detections of spatial oxygen-profiles due to the respiratory activity of spheroids growing on oxygen-sensitive sensor foils. The images were calibrated, and profile plots were evaluated with data smoothing according to the Savitzky Golay method over 20 data points. Experiments were performed using L-15 medium. **(A)** Time-dependent profile plots obtained from the measurement of an SK-MEL-28 spheroid. **(B)** Examination of the respiration of a 7-day-old U373 spheroid and **(C)** of a 7-day-old MCF-7 spheroid. Experiments were performed in a cell culture incubator at 37 °C and 0 % CO₂.

The SK-MEL-28 spheroid was 500 μm in size and the corresponding profile plot hinted at a W-shaped form showing no significant changes with time as can be seen in Fig. 4.5 A. Next to the spheroid, a slight decrease in pO_2 from around 130 torr to 100 torr and 160 torr to 125 torr could be observed on the left-hand and the right-hand side, respectively. The oxygen concentration centrally beneath the spheroid was constantly found to be between 0 torr and 10 torr and oxygen values steadily increased with increasing distance from the spheroid center. Fig. 4.5 B shows the U373 spheroid, only 300 μm in size, which led to steeper profiles with time. 1 h after the start of the measurement, the oxygen partial pressure right below the spheroid was determined to be 73 torr, followed by a continuing decrease from 15 torr after 6 h over 7 torr after 12 h to a final value of 0 torr pO_2 after 24 h. The oxygen concentration which was very low directly below the core of the spheroid increased with a steep oxygen concentration gradient towards the spheroid's edge. Directly adjacent to the spheroid, a decrease in pO_2 from 175 torr to 150 torr was detected. The third spheroid consisting of MCF-7 cells (see Fig. 4.5 C), 500 μm in size, showed a significant decrease in the oxygen concentration with time. Beneath the spheroids core, O₂ was completely consumed within 12 h of recording, and a strong oxygen depletion next to the spheroid from initially 150 torr to 80 torr, 30 torr and then 10 torr after 24 h was observed. The oxygen profiles also reflected the microscopically observed characteristics of the individual spheroids: SK-MEL-28 cells tended to grow into bigger spheroids which seemed to be rather soft since the structure was mostly elliptical when growing on a surface (compare Fig. 4.3). U373 spheroids

formed very tight and nearly perfectly round-shaped spheres which possibly led to the V-shaped profiles. MCF-7 spheroids tended to form a monolayer around the sphere which could also have been responsible for the fast oxygen depletion next to the spheroid.

The second method for data evaluation using different ROIs is shown in Fig. 4.6. The quantification of the respiration of SK-MEL-28 spheroids showed initial pO_2 values of (162 ± 28) torr next to the spheroid, (54 ± 13) torr in the periphery of the spheroid and (9 ± 5) torr at the center beneath the 3D tissue model. Directly at the center beneath the spheroid, the oxygen partial pressure was constantly showing low values of (9 ± 5) torr during the measurement. Next to the spheroid, only 23 torr of dissolved oxygen were respired within the time span of 24 h, with pO_2 only slightly decreasing to (133 ± 30) torr. A linear regression between 1 h and 4 h of the time-resolved pO_2 values yielded AOCRs for the different regions of interest. If the cells next to the spheroid were taken as the reference, the cells in the periphery of the spheroid exhibited AOCRs which were 12 % lower and the AOCRs for the cells located in the core of the spheroid even decreased by 95 %. However, it must be taken into account that oxygen was already almost depleted right in the beginning.

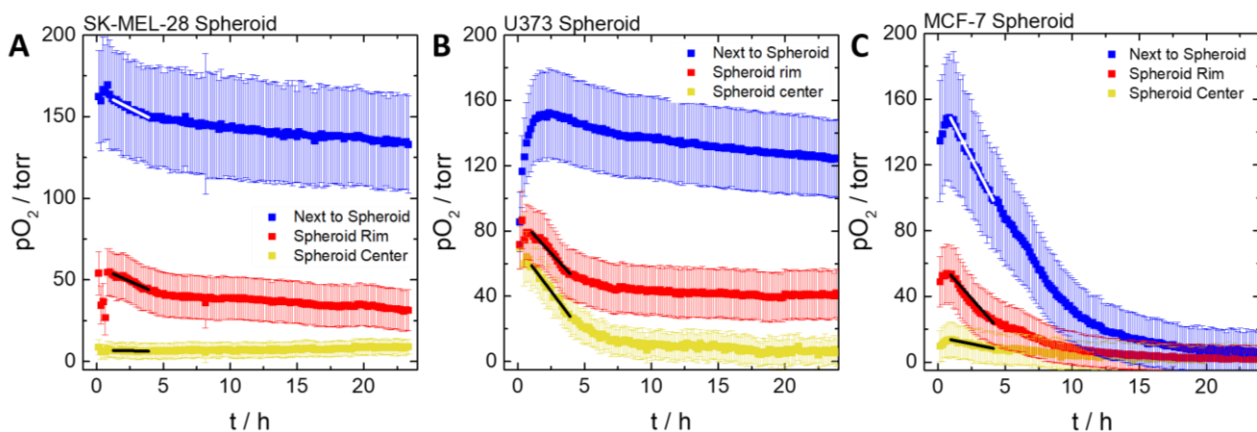


Fig. 4.6 Sensor foil-based and time-dependent sensing of the respiratory activity of spheroids evaluating three different regions of interest (ROIs): one situated next to the spheroid, one located under the outer layers of the tissue and one ROI placed centrally beneath the spheroid. Experiments were performed using L-15 medium. (A) 7-day-old SK-MEL-28 spheroid, (B) 7-day-old U373 spheroid and (C) 7-day-old MCF-7 spheroid. Black and white lines show the linear regression which was used for the AOCR determination. Experiments were performed in a cell culture incubator at 37 °C and 0 % CO_2 .

Changes in the oxygen partial pressure revealed by U373 spheroids were quite similar (see Fig. 4.6 B). Next to the spheroid, the initial pO_2 value of (86 ± 18) torr increased up to (152 ± 27) torr after 2.3 h, followed by a decrease to (124 ± 23) torr after 24 h. In the outer layer of the spheroid, the pO_2 decreased from (79 ± 15) torr (0.6 h) to (41 ± 15) torr after 24 h. The cells consumed (8.0 ± 0.6) torr·h⁻¹ of dissolved oxygen in the time interval between 1 h and 4 h of the measurement. Centrally beneath the spheroid, the initial oxygen level of (70 ± 13) torr decreased to a final oxygen partial pressure of (6 ± 8) torr with a corresponding consumption rate of (14.6 ± 0.3) torr·h⁻¹ between 1 h and 4 h of recording. Fig. 4.6 C illustrates the ROI evaluation of the experiment with an MCF-7 spheroid. After 24 h of measurement time, the available oxygen

was completely consumed; the consumption took place even in areas next to the spheroid due to cell monolayer formation around the attached spheroid. The initial pO_2 levels of (14 ± 11) torr, (54 ± 18) torr and (145 ± 38) torr after 1 h were followed by a steady decrease to values of (3 ± 8) torr, (2 ± 8) torr and (6 ± 12) torr for the ROI at the spheroid center, located in the periphery and next to the spheroid, respectively. The calculation of the respective AOCR values resulted in a 42 % and 90 % decrease of the respiration rates going from the vicinity of the spheroid to the periphery and the core. Tab. 4.1 summarizes the individual AOCR values.

Tab. 4.1 Summary of the *apparent oxygen consumption rates* (AOCR) determined by linear regression of time-resolved changes in the partial oxygen pressure beneath spheroids generated from different cell lines (compare Fig. 4.6).

	SK-MEL-28 spheroid	U373 spheroid	MCF-7 spheroid
	AOCR / torr·h ⁻¹		
Next to the spheroid	4.1 ± 0.2	-	15.8 ± 0.1
Spheroid periphery (rim)	3.6 ± 0.2	8.0 ± 0.6	9.1 ± 0.4
Spheroid center	0.2 ± 0.1	14.6 ± 0.3	1.6 ± 0.1

During the experiments, it became apparent that the results were strongly depending on the size and shape of the spheroid. The shape of the spheroids varied between spherically shaped ones, spheroids assuming ellipsoidal as well as club-shaped forms. The attachment speed also depended on the surface of the spheroids: while convex parts attached very fast, the attachment of concave areas was significantly slower due to sterical reasons leading to differing profile plots. MCF-7 and SK-MEL-28 cells were used to create spheroids in different sizes, and these differently sized spheroids were used to monitor the impact of the size on the profiles. Fig. 4.7 shows images of four MCF-7 spheroids (S1-S4) in increasing size with the corresponding false color images of the sensor foil at the beginning of the measurement as well as after 24 h and 48 h. The initial diameter of the spheroids increased from 410 μm (S1), over 465 μm (S2) and 500 μm (S3) to 540 μm for the last spheroid (S4). The spheroid size was determined from the area of the spheroid seen on the images. The sensor foil beneath S1 exhibited a small scratch, which was used by the spheroid to attach. In the image of S3, the edge of the outgrowing cell monolayer can be seen, indicated by the small white arrowhead. The false color images mirror the available oxygen concentration in a color-coded manner. Light yellow corresponds to an oxygen partial pressure of 149.3 torr (100 % dissolved oxygen) and the darker the color (going from yellow over orange and red to blue and black), the lower is the oxygen concentration, eventually reaching 0 torr of the oxygen partial pressure (black color).

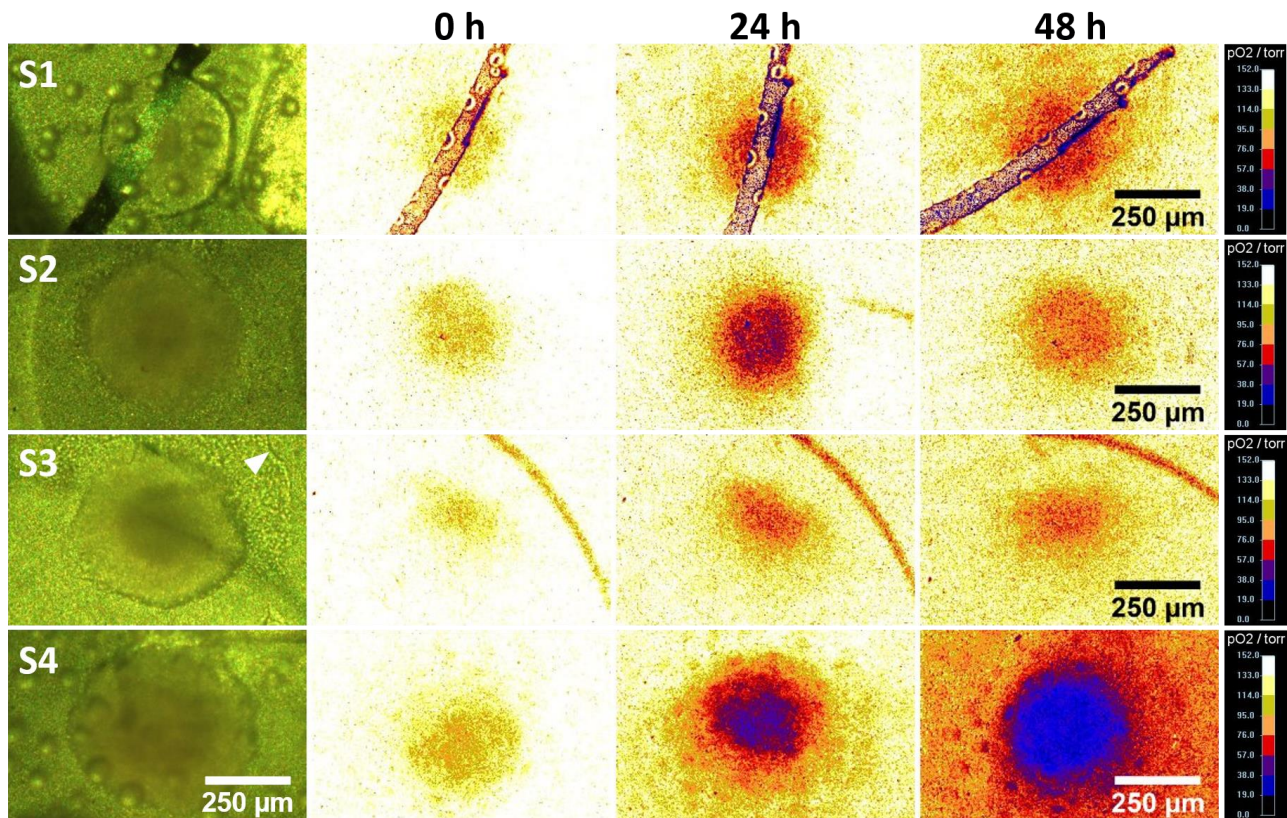


Fig. 4.7 Images of four MCF-7 spheroids (S1-S4) in increasing sizes from 410 μm (S1), 465 μm (S2), 500 μm (S3) and 540 μm (S4) each with the corresponding false color images of the sensor foil at the beginning of the measurement as well as after 24 h and 48 h. The light-yellow color mirrors 149.3 torr of pO_2 while black areas correspond to 0 torr pO_2 . Experiments were performed at 37 $^\circ\text{C}$, 0% CO_2 in L-15 medium. Scale bar depicts 250 μm .

Profile plots were evaluated using the calibrated images at three different time points (see Fig. 4.8). The oxygen partial pressure beneath every spheroid decreased with time. The time needed for the decrease is strongly dependent on the size and attachment of the spheroid. The largest spheroid S4 achieved an oxygen depletion of an initial 130 torr to 60 torr next to the spheroid and 75 torr in the beginning centrally beneath the spheroid to 3 torr in the end. The smallest spheroid S1 with 410 nm in size exhibited an irregular dip in pO_2 values at a distance of around 0.4 mm in the ROI of the profile. The dip emerged due to the scratch on top of the sensor foil, as shown in Fig. 4.7. The oxygen consumption beneath S1 was expected to be smallest but within the last 24 h of measurement time, the pO_2 values of S2 and S3 increased by 24 torr and 2 torr, while pO_2 values beneath S1 stayed constant. The images of S3 in Fig. 4.7 suggested that the spheroid was not entirely attached to the sensor foil and only an elliptical part had adhered, possibly leading to the increased oxygen concentration beneath the tissue. The oxygen consumption of S4, showing a diameter of 540 μm in the beginning which grew to 610 μm within 48 h, revealed a possibly characteristic pO_2 profile underneath the spheroid. The oxygen concentration was found to be 6 torr in a distance of 0.35 mm followed by a slight increase to 8 torr at 0.4 mm and a subsequent decrease in the oxygen partial pressure to 3 torr in a distance of 0.45 mm. It was also noticeable that the pO_2 values decreased the most next to S4 in comparison to S1-S3. The depicted spheroid diameters in Fig. 4.8 were determined from the area of the spheroids seen

on the images. The outgrowing cell monolayers were not taken into account. The slightly increased diameters could be due to cell proliferation in the three dimensional tissue or due to a slow flattening of the initially spherical structure of the spheroid.

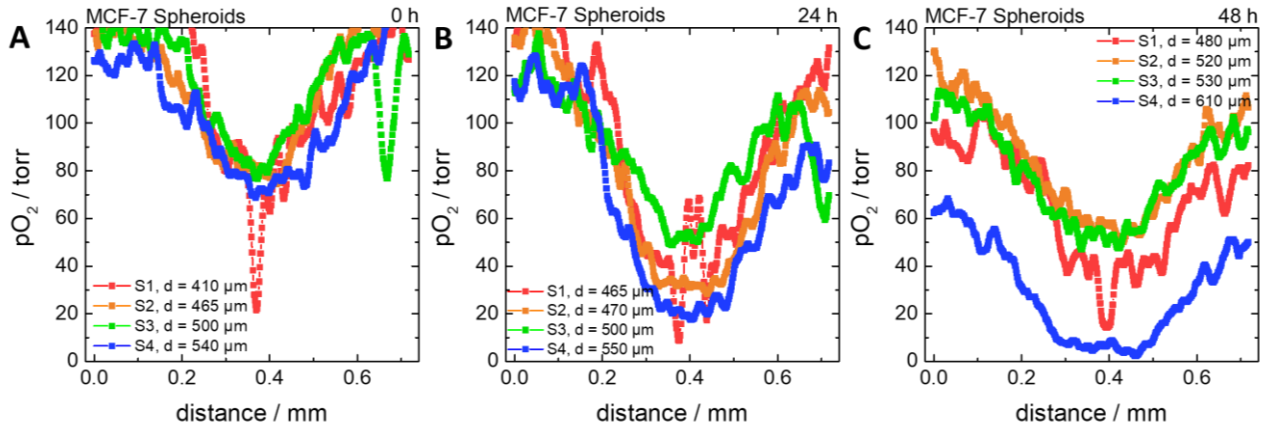


Fig. 4.8 Image-based detection of the oxygen distribution in a spatial profile beneath MCF-7 spheroids in four different diameters grown to oxygen-sensitive sensor foils (A) directly after the start of the measurement, (B) after 24 h and (C) after 48 h of recording. Images were calibrated and profile plots evaluated after data smoothing according to the Savitzky Golay method with 20 data points. Experiments were performed in a cell culture incubator at 37 °C and 0 % CO_2 using L-15 medium.

SK-MEL-28 spheroids were observed to be very soft and as a consequence, the attachment on solid surfaces was followed by a fast collapse of the spherically shaped structure resulting in disk-like morphologies. This observation could possibly explain the fast depletion of oxygen beneath SK-MEL-28 cells due to the firmly attached spheroids and thus the hindered diffusion of dissolved oxygen from the supernatant medium.

Fig. 4.9 shows profile plots of three SK-MEL-28 spheroids in different sizes.

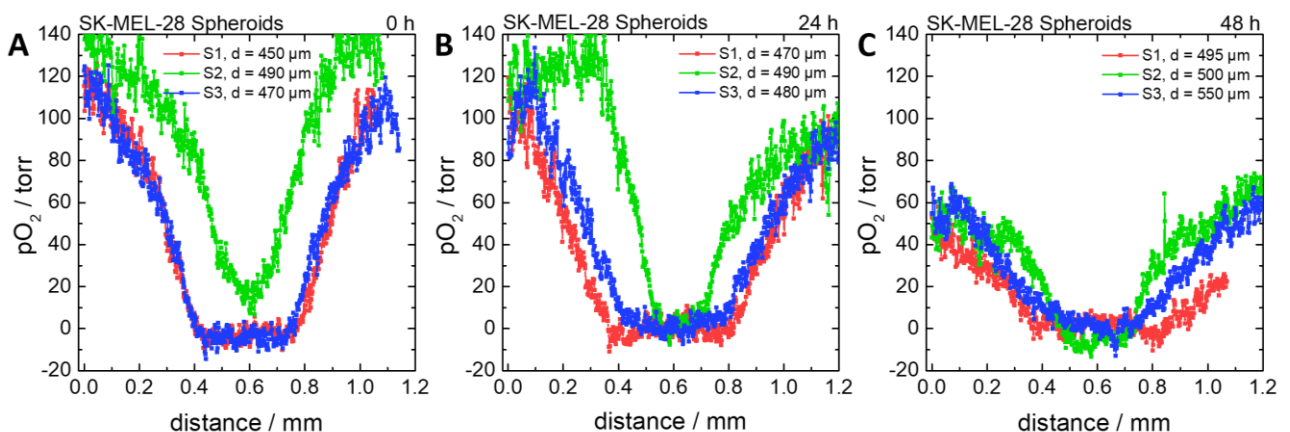


Fig. 4.9 Image-based detection of the oxygen distribution in a spatial profile beneath SK-MEL-28 spheroids with three different diameters attached to oxygen-sensitive sensor foils. (A) Directly after the measurement start, (B) after 24 h and (C) after 48 h of recording. Images were calibrated and profile plots were evaluated with data smoothing according to the Savitzky Golay method with 20 data points. Experiments were performed in a cell culture incubator at 37 °C and 0 % CO_2 using L-15 medium.

The spheroid S2, initially 490 μm in size, first revealed a V-shaped profile which broadened over time resulting in a similar pO_2 profile compared to S1 and S3 with 0 torr oxygen concentration available centrally beneath the spheroid. Oxygen concentrations increased when moving away from the core of the spheroid to pO_2 values between 50 torr and 70 torr after 48 h. S1 and S3 caused initially similar oxygen distributions with a strong decrease of pO_2 in the periphery of the spheroids from 120 torr to approximately 50 torr within 48 h. After 48 h, the oxygen respiration of the cells pertaining to spheroid S1 led to a characteristic oxygen profile which was also observed in investigations with MCF-7 spheroids: directly beneath the center of the spheroid, pO_2 values slightly increased while the oxygen concentration was around 0 torr at little distance from the center resulting in a W-shaped pO_2 profile.

For further quantification of the oxygen distribution profiles, the *area above the curve* (AAC) was calculated by determining the AUC from which the integrated area with an upper integration limit of $y = 140$ torr was subtracted and the absolute values are given in Tab. 4.2 for the two cell lines under test. Increasing AACs indicate increasing oxygen depletion beneath the spheroid. The AACs increased in all cases over the course of the measurement, indicating a nearly linear time-dependent oxygen depletion. The AACs of the four MCF-7 spheroids (S1-S4) increased on average (210 ± 48) % with respect to the integrated area at the beginning of the measurement. The AACs determined for the SK-MEL-28 spheroids S1 and S3 increased by around 31 % while S2 led to a 143-% increase of the AAC within 48 h.

Tab. 4.2 Summarized *areas above the curve* (AACs) which were calculated by subtracting the area with an integration limit of $y = 140$ torr from the AUCs of the spatial oxygen distributions. Absolute values are given and the raw data for the determination of the AACs are the oxygen profile plots of MCF-7 and SK-MEL-28 spheroids in Fig. 4.8 and Fig. 4.9.

t / h	MCF-7				SK-MEL-28		
	S1	S2	S3	S4	S1	S2	S3
	AAC / torr·mm						
0	14.1	16.3	14.9	24.5	102.1	53.4	105.4
24	35.6	43.1	37.4	52.3	117.1	70.4	106.3
48	53.2	40.2	43.9	79.4	135.9	129.5	136.4

The averaging of multiple measurements is quite challenging since the spheroids differ in size and shape and averaging process would lead to the loss of details in the *profile plot evaluation*. All in all, the experiments showed that oxygen depletion beneath 3D tissues was highly dependent on the cell type and therefore on the tissue structure which influenced the contact area to the oxygen-sensitive sensor foil and consequently had an impact on the resulting oxygen profiles.

4.2 INFLUENCE OF THE SENSOR FOIL THICKNESS

The sensor foil-based technique offers the possibility of measuring changes in oxygen levels directly beneath the cells, allowing for the detection of small changes in the respiratory activity of the cells due to the proximity to the sensor foil. The oxygen molecules are required to be in direct contact to the oxygen-sensitive dyes located in the sensor foil matrix implying that the matrix exhibits an oxygen-permeable structure. This led to the assumption that the thickness of the sensor foil correlates with the rate of the decrease of the oxygen partial pressure. Since thin sensor foils contain lower oxygen amounts in their matrix compared to thicker ones, the state of hypoxia should be reached faster with thinner sensor foils assuming constant cellular oxygen consumption. Consequently, a thicker sensor foil matrix should lead to a slower *oxygen consumption rate* even though the respiration is constant, which is due to the larger volume of dissolved oxygen beneath the cells being accessible for their respiration.

For the investigation of the influence of the sensor foil thickness, three different oxygen-sensitive sensor foils with increasing thickness were examined. The standard sensor foil with a thickness of $6\ \mu\text{m} - 8\ \mu\text{m}$ (Fig. 4.10 A) was tested in comparison to a twofold thickness sensor foil ($12\ \mu\text{m} - 16\ \mu\text{m}$, Fig. 4.10 B) and a fourfold thickness sensor foil with $24\ \mu\text{m} - 32\ \mu\text{m}$ in height (Fig. 4.10 C). The foils were kindly produced and provided by PreSens GmbH. The NRK cells were seeded to confluence onto the sensor foils and after the *standard pre-experiment protocol*, the culture medium was replaced with L-15 medium. After airtight sealing, the recording was started for 24 h. Fig. 4.10 schematically shows the tested sensor foil thicknesses with the confluent cell monolayer on top and the airtight sealing of the petri dishes.

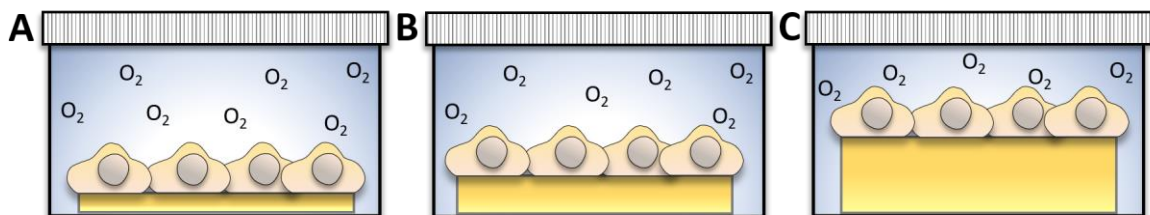


Fig. 4.10 Schematic illustration of the study of how the sensor foil thickness influences the rate of the $p\text{O}_2$ decrease when the cellular respiration of NRK cells is monitored. (A) Depiction of the standard oxygen-sensitive sensor foil $6\ \mu\text{m} - 8\ \mu\text{m}$ in height, (B) sensor foil with twofold thickness ($12\ \mu\text{m} - 16\ \mu\text{m}$) and (C) sensor foil in fourfold thickness ($24\ \mu\text{m} - 32\ \mu\text{m}$). All sensor foils have been covered with adherently growing cells.

Following the experiments, the sensor foils were calibrated according to the described protocol (chapter 3.4.4). A linear regression of the curves in the time interval from 1 h to 4 h of the measurements yielded the AOCRs. The consumption rate decreased from $(18.3 \pm 0.1)\ \text{torr}\cdot\text{h}^{-1}$ over $(16.4 \pm 0.6)\ \text{torr}\cdot\text{h}^{-1}$ to $(15.0 \pm 0.7)\ \text{torr}\cdot\text{h}^{-1}$ with increasing sensor foil thickness. The AOCR values were used to calculate the *oxygen consumption rate* for every thickness. With the standard sensor foil, consumption rates of

(28.7 ± 0.2) $\text{amol}\cdot\text{s}^{-1}$ were obtained per cell which decreased to (26 ± 1) $\text{amol}\cdot\text{s}^{-1}\cdot\text{cell}^{-1}$ by doubling the sensor foil thickness. The fourfold thickness revealed an OCR value of (24 ± 1) $\text{amol}\cdot\text{s}^{-1}\cdot\text{cell}^{-1}$. All AOCR and OCR values are summarized in Tab. 4.3.

Tab. 4.3 Summary of the *apparent oxygen consumption rates* (AOCR) obtained by linear regression and the corresponding calculated *oxygen consumption rate* (OCR) on a single cell level for the three tested sensor foil thicknesses. Mean \pm SEM, n = 3.

Sensor foil thickness	Sensor foil thickness / μm	AOCR / $\text{torr}\cdot\text{h}^{-1}$	OCR / $\text{amol}\cdot\text{s}^{-1}\cdot\text{cell}^{-1}$
1x	6 – 8	18.3 ± 0.1	28.8 ± 0.2
2x	12 – 16	16.4 ± 0.6	26 ± 1
4x	24 – 32	15.0 ± 0.7	24 ± 1

4.3 DETECTION OF HORIZONTAL OXYGEN GRADIENTS

In the previous chapter, the influence of the sensor foil thickness was investigated. Since oxygen molecules can freely enter the cell via diffusion across the cellular membrane, cells can incorporate oxygen via the apical membrane as well as via the basolateral membrane. To mimic an irreversible inhibition of the oxygen uptake from the apical membrane side, a small circularly shaped cover slip was placed on top of the cells (see Fig. 4.11). This experiment also served to mimic the situation of a spheroid being attached to the sensor foil where the oxygen supply for cells growing in deeper layers are highly restricted due to multiple cell layers on top.

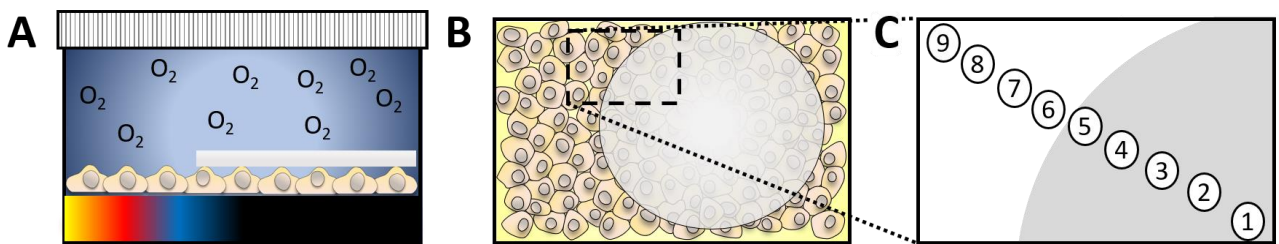


Fig. 4.11 Schematic illustration of the respiratory activity investigation carried out with NRK cells after the inhibition of oxygen diffusion from the apical (upper) side via cover slip coverage. (A) Side view of the measurement setup with cells growing on top of the sensor foil, covered with a cover slip on the right-hand side. (B) Schematic top view of the measurement setup with a cover slip covering a part of the cell monolayer. (C) Selected ROIs for the evaluation of the time-dependent, lateral pO_2 gradient.

The experimental procedure was done according to the *standard pre-experiment protocol*. After the addition of L-15 medium, the cover slip was placed on top of the cell monolayer, the petri dishes were filled air bubble-free and sealed airtight and data acquisition was performed during 24 h. The images were calibrated, and several ROIs were selected to follow the time-dependent, lateral pO_2 gradient. The ROIs were selected as illustrated in Fig. 4.11 C, from the center of the cover slip to the corner of the image, where the cells were uncovered and were provided free access to the available oxygen in the supernatant L-15 medium.

The calibrated false color images of the measurement are shown in Fig. 4.12. The four images represent oxygen concentrations directly after the start of the measurement and after 3 h, 6 h and 9 h of data acquisition. Bright, yellow-colored areas correspond to 149.3 torr oxygen partial pressure whereas dark, blue/black areas illustrate low oxygen levels of 0 torr pO_2 . After 3 h of measurement time, an oxygen gradient could be observed radiating out from the center of the cover slip (lower right-hand side) to the opposite corner of the image. 3 h later, the gradient was still present, however hardly any oxygen was left underneath the cover slip. The uncovered cells needed around 12 h to completely consume the initially available oxygen.

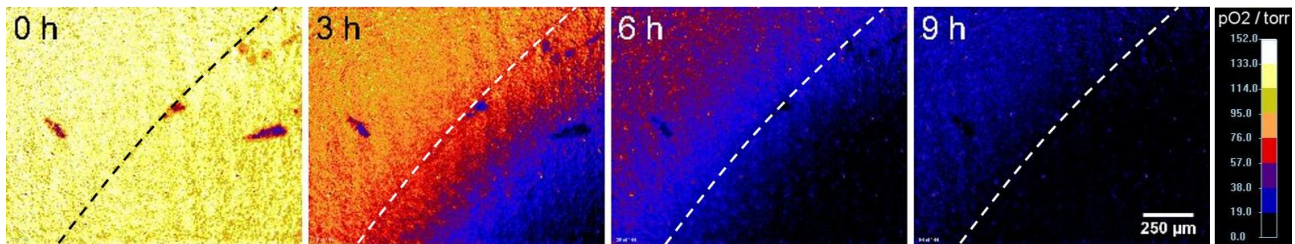


Fig. 4.12 Calibrated false color images of the investigation of the respiratory activity of NRK cells partly covered with a glass cover slip to inhibit the oxygen diffusion from the apical side. Pictures were taken directly after the measurement start and after 3 h, 6 h and 9 h of recording. The dotted line indicates the edge of the glass cover slip covering the cells in the lower right part of the images. Bright yellow represents 149.3 torr of oxygen partial pressure whereas dark blue/black represents hypoxic states. The experiments were performed in a standard cell culture incubator at 37 °C and 0 % CO₂.

In Fig. 4.13 A and B, the pO₂ values from two individual experiments are plotted against the time, each with the same nine selected regions of interest. The time courses for ROIs 1 – 4 revealed a sharp decrease of the oxygen partial pressure within the first 1 h – 2.5 h in both cases. The pO₂ values gained from ROI 5, a region where the cells are still covered by the glass cover slip, decreased constantly while the pO₂ values for ROIs 6 – 9 also decreased, but with a slower rate. The cells next to the cover slip (ROIs 6 – 9) needed around 12 h to completely consume the initially available oxygen (see Fig. 4.13 B).

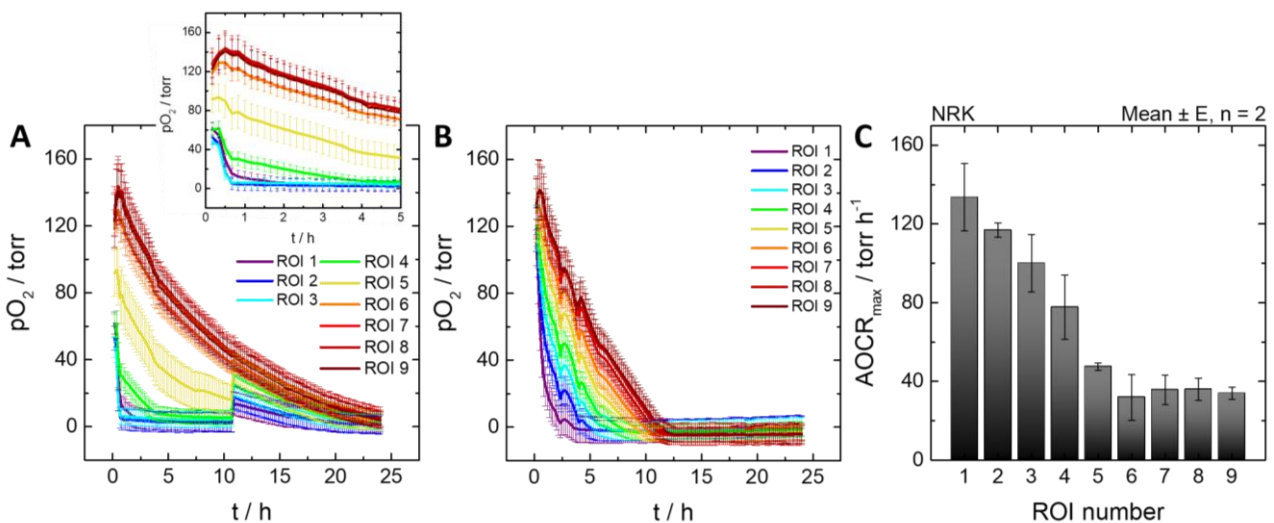


Fig. 4.13 Image-based monitoring of the partial oxygen pressure as a function of time beneath NRK cells which were partly covered by a glass cover slip. (A, B) Two individual experiments depicting pO₂ values from nine regions of interest (ROIs) as a function of time, with a zoom-in of the first 5 h of the first experiment. (C) Calculated mean *apparent oxygen consumption rates* (AOCR_{max}) for each of the nine ROIs from the two experiments: increasing ROI number meaning increasing distance from the center of the cover slip and thus free access to dissolved oxygen in the L-15 medium. E (error) depicts the spread of the two averaged data points from the two individual data sets. The experiments were performed in a standard cell culture incubator at 37 °C and 0 % CO₂.

The standard data evaluation consists of a linear regression of the time courses within the time interval of 1 h – 4 h. Since the cells beneath the cover slip consumed the dissolved oxygen rapidly, the first derivatives of the time courses were calculated and the maximal values of the first derivative within the first 1.5 h yielded the AOCR_{max} values. Fig. 4.13 C depicts the averaged AOCR values from the two measurements for the nine

ROIs. ROIs 1 – 5, representing the area of the cell monolayer which was covered by the glass cover slip, revealed decreasing *oxygen consumption rates* from (134 ± 17) torr·h⁻¹ (ROI 1) to (48 ± 2) torr·h⁻¹ (ROI 5) with increasing distance from the center of the cover slip. The regions next to the cover slip (ROI 6-9) exhibited nearly constant averaged consumption rates of (34 ± 2) torr·h⁻¹ or (54 ± 3) amol·s⁻¹·cell⁻¹ (see Tab. 4.4). Linear regression in the time interval from 1 h – 4 h for the same ROIs (6-9) yielded significantly smaller consumption rates of approximately 16 torr h⁻¹.

Tab. 4.4 summarizes all AOCRs determined via the first derivative (AOCR_{max}) as well as by linear regression of the time-resolved detected oxygen partial pressure. ROIs 6 – 9 were fitted linearly in the standard time interval from 1 h – 4 h while ROIs 1 – 5, located beneath the cover slip, were fitted linearly between 0.33 h and 0.66 h (AOCR_{linearFit}). The time intervals were chosen since the oxygen partial pressure was initially low beneath the cover slip and was therefore consumed rapidly compared to the area next to it. Next to the cover slip, the oxygen partial pressure first increased, caused by temperature effects, which was then followed by decreasing values due to the respiratory activity of the cells.

Tab. 4.4 Summarized *apparent oxygen consumption rates* (AOCRs) either determined by the first derivative (AOCR_{max}) or by linear regression between 0.33 h – 0.66 h (ROI 1-5, beneath cover slip) and 1 h – 4 h (ROI 6-9, next to cover slip) (AOCR_{linearFit}) with the corresponding calculated *oxygen consumption rates* (OCRs) (compare chapter 3.4.5). Mean ± E, n = 2 (E (error) depicts the spread of the two averaged data points from the two individual data sets).

ROI	AOCR _{max} / torr·h ⁻¹	AOCR _{linearFit} / torr·h ⁻¹	OCR _{max} / amol·s ⁻¹ ·cell ⁻¹	OCR _{linearFit} / amol·s ⁻¹ ·cell ⁻¹
1	134 ± 17	130 ± 13	209 ± 27	203 ± 20
2	117 ± 4	117 ± 4	188 ± 6	188 ± 6
3	100 ± 15	100 ± 15	157 ± 23	157 ± 23
4	78 ± 16	78 ± 16	122 ± 26	122 ± 26
5	48 ± 2	14 ± 2	74 ± 3	22 ± 4
6	32 ± 12	15 ± 2	50 ± 18	23 ± 3
7	36 ± 8	16 ± 2	56 ± 12	25 ± 3
8	36 ± 6	16 ± 2	56 ± 9	25 ± 3
9	34 ± 3	16 ± 2	53 ± 5	25 ± 3

Since the ROI evaluation determines the time-dependent oxygen partial pressure at a defined position for a temporal resolution, the false color images were also used to determine oxygen gradients via *profile plot evaluation* to yield a spatial resolution. The *profile plot evaluation* was performed using ImageJ. Due to the diagonally oriented gradient, a profile line of only one pixel in width was chosen. Since the sensor foils and the embedded luminophores are not distributed equally, some pixel errors occurred and slight fluctuations could be observed within the profile plot. To even out pixel fluctuations, the profile plots were smoothed by a sliding average of 50 points, while 1136 pixels were determined in total. Fig. 4.14 shows the averaged oxygen partial pressure profiles at different time points during the experiments. The values on the x-axis

indicate the distance from the center of the cover slip ($d = 0.0$ mm) to the uncovered area; a distance of 1.8 mm corresponds to the upper left corner of the images in Fig. 4.12 while the dashed line indicates the edge of the glass slip. Even the first image taken of the sensor foils revealed slightly smaller pO_2 levels of around 120 torr beneath the cover slip in comparison to around 140 torr next to it. After 3 h of recording, a drastic decrease of the pO_2 to 0 torr could be observed in the center of the cover slip at $d = 0.0$ mm, and the oxygen partial pressure decreased to 100 torr next to the cover. With time passing, a constant decrease of the oxygen levels next to the cover glass was detected resulting in no gradient between covered and uncovered cell areas. After 12 h of data collection, pO_2 levels were equal over the whole field of view, yielding a homogenous 0 torr oxygen partial pressure after 24 h.

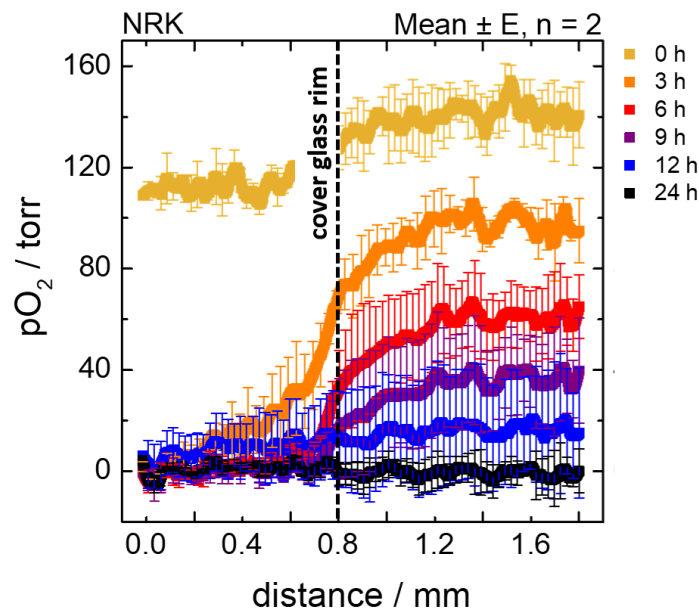


Fig. 4.14 Profile plot evaluation of the sensor foil images upon recording the respiratory activity after blocking oxygen diffusion from the apical side by a glass cover slip on top of adherent and confluent NRK cells (compare Fig. 4.12 and Fig. 4.13). Profile plots were evaluated using Image J and subsequently averaged. Distance on the x-axis describes the length of the profile and thus the way from the center of the cover slip ($d = 0$ mm) to the uncovered cells ($d = 1.8$ mm). The dashed line indicates the rim of the cover slip. E (error) depicts the spread of the two averaged data points from the two individual data sets.

The experiments showed that the blocking of the oxygen diffusion by a cover slip was highly efficient and that the cells centrally below the cover slip only needed up to 3 h to completely consume all of the oxygen which was initially available in the sensor foil matrix and the microenvironment of the cells. The profile plot evaluation confirmed that covered cells but which were located closer to the edge of the cover slip had access to more oxygen via diffusion processes across a distance of 200 μ m and that the oxygen partial pressure decreased to similar values across the entire field of view after approximately 12 h.

4.4 VISUALIZATION OF VERTICAL OXYGEN GRADIENTS ABOVE ADHERENT CELLS

The sensing of the respiratory activity of cells growing on sensor materials is strongly dependent on the available oxygen in the supernatant medium on the apical membrane side. Cells seeded on the bottom of measurement wells consume oxygen, hence an oxygen gradient will be established and intensified over time. The vertical O_2 concentration gradient (VOG) from the medium surface towards the cells growing on the bottom was measured using specific sensors: the *Multiwell Insert Optical Sensor* (MIOS) which is a triangular-shaped prism with a right angle between the triangle arms. The MIOS is serving as an optical light guide element and exhibits one plane parallel to the medium surface forming the readout plane and one plane oriented orthogonally to the well bottom and dipping into the cell culture medium (compare Fig. 4.15). The hypotenuse lateral face of the light guide element provides an inclined plane which is coated with the oxygen-sensitive sensor foil. The small triangles can be incorporated into a MIOS holder, which simultaneously serves as lid for a standard multiwell plate, positioning the MIOS elements above the cell layer in each well. Fig. 4.15 shows an image of a standard 24-well plate with the corresponding lid equipped with 24 MIOS elements.

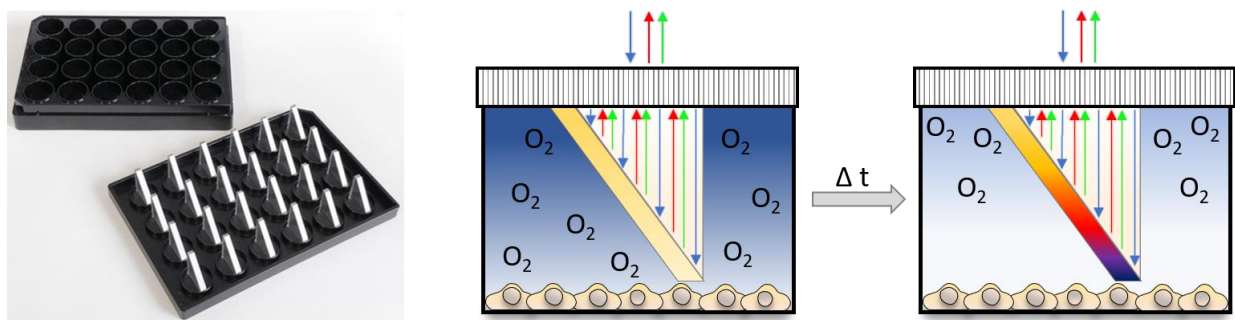


Fig. 4.15 Sensing of the vertical oxygen gradient - formed in cell culture medium above adherent NRK cells cultivated on the bottom of a 24-well plate - with the help of *Multiwell Insert Optical Sensor* (MIOS) elements. The MIOS triangles were integrated into the lid of a 24-well plate and suspended in the cell culture medium after the closing of the plate. The MIOS elements are optically transparent prism light guide elements; one leg is horizontal and facing the camera and one leg is vertically oriented and the sloped hypotenuse is coated with the oxygen-sensitive sensor foil. The MIOS sensors allow for a horizontal readout of the vertical O_2 gradient by signal projection through the light guide element.

The schematic illustrations sketch the working principle. For measurements, the VisiSens TD was focused on the horizontal leg of the MIOS sensor that is aligned parallel with the medium surface. That way, the excitation light is propagated through the light guide element to the oxygen-sensitive sensor foil and excites the luminophores. The emitted luminescence signal is projected back to the readout plane. This technique allows for a horizontal readout of the vertical oxygen gradient formed in the culture medium. The MIOS sensors were developed by Daniela Obermaier (PreSens GmbH) and kindly provided by PreSens GmbH.

In this thesis, NRK cells were seeded on the bottom of 24-well plates in two different seeding densities ($8 \cdot 10^4$ cells \cdot cm $^{-2}$, $25 \cdot 10^4$ cells \cdot cm $^{-2}$). The culture medium was exchanged 24 h after cell inoculation and

replaced by L-15 medium after 48 h. Data was then collected for 24 h in a standard cell culture incubator at 37 °C and 0 % CO₂. The recorded images were calibrated according to the protocol (see chapter 3.4.4) and *profile plot evaluation* was performed using ImageJ with profiles in the dimensions of 150 x 6 pixels.

Fig. 4.16 illustrates the 2D imaging data, false color-coded, and the corresponding profile plots at different time points of the measurements yielding the vertical oxygen gradient with low oxygen concentrations near the bottom and higher oxygen concentrations close to the top of the well.

In order to test the sensitivity of the MIOS system responding to different oxygen conditions and to quantify the diffusion rate of oxygen from the medium, two different cell densities were applied. Subconfluently seeded cells were examined in Fig. 4.16 A, whereas confluent cell monolayers were monitored in Fig. 4.16 B.

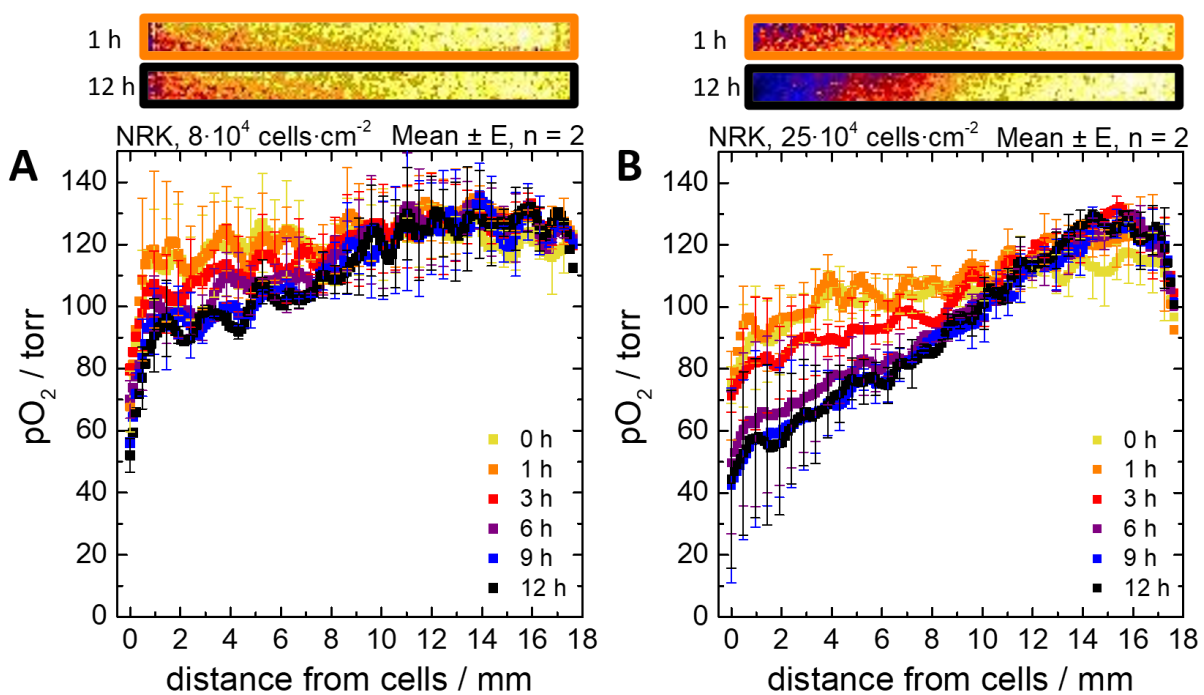


Fig. 4.16 Profile plot evaluation of vertical oxygen gradients in L-15 medium above adherent NRK cells at different time points. Recorded, false color-coded images of the horizontally projected sensor foil signal after 1 h and 12 h are shown on the top. The profile plots show the oxygen partial pressure as a function of distance from the cells. In the false color images, areas of high oxygen concentration are color coded yellow and areas of low oxygen concentrations are black. (A) Cells were seeded in a density of $8 \cdot 10^4 \text{ cells} \cdot \text{cm}^{-2}$ and (B) $25 \cdot 10^4 \text{ cells} \cdot \text{cm}^{-2}$. The depicted measurements were done twice with E (error) signifying the spread of the two averaged data points from the two individual data sets. Experiments were performed in a standard cell culture incubator at 37 °C and 0 % CO₂.

The left side of the profile plots mirrors the oxygen concentration close to the adherently growing cells and the right-hand side of the plots corresponds to areas close to the surface of the supernatant medium. The partial oxygen pressure was plotted for different time points during the measurement. In the beginning of the measurement, subconfluently seeded NRK cells revealed approximately constant oxygen partial pressure values of around 120 torr with respect to the distance from the cell layer. After 12 h of recording, a decrease of pO_2 to around 80 torr close to the cells could be observed with constantly increasing oxygen values up to

120 torr in a distance of 6 mm from the cells. Within the distance of 10 mm to 18 mm from the cells, a constant oxygen partial pressure was observed which remained the same during the entire measurement. This unchanging oxygen concentration could be due to oxygen diffusion from ambient air into the culture medium.

In contrast to the slight change in oxygen levels within the supernatant medium elicited by subconfluent cell numbers, a confluent cell layer led to a rapidly established oxygen concentration gradient in the medium. Even directly after the beginning of the recording, a difference between 80 torr directly above the cells and 110 torr in a distance of 10 mm from the cells was detected. The oxygen partial pressure in a distance between 11 mm – 18 mm from the cells was approximately constant during the whole measurement. The shorter the distance from the cells, the more the oxygen partial pressure decreased, but at all times an increasing distance from the cells was accompanied by steady and almost linearly increasing O_2 concentrations reaching a constant 110 torr in a distance of 11 mm. After 12 h, a final pO_2 value of approximately 45 torr was detected close to the cells.

The linear regression of the profile plots between 0 mm and 11 mm exhibited an oxygen decrease per millimeter distance of (2.9 ± 0.1) torr·mm⁻¹ in the beginning which increased to (5.1 ± 0.1) torr·mm⁻¹ after 12 h of measurement time at $25 \cdot 10^4$ cells cm⁻². This corresponds to a difference of $7.2 \mu\text{mol}\cdot\text{L}^{-1}$ in the oxygen concentration within 1 mm of medium fluid. The cells inoculated in a lower cell density started with a slope of (0.9 ± 0.1) torr·mm⁻¹ and ended at (3.4 ± 0.2) torr·mm⁻¹ after 12 h.

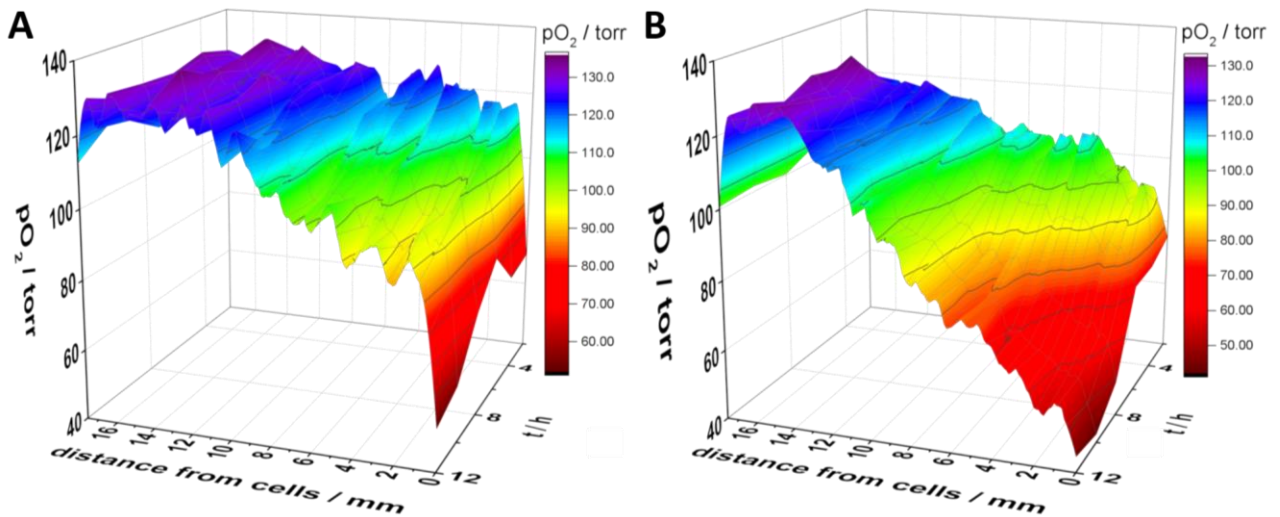


Fig. 4.17 3D surface colormap of the detection of vertical oxygen gradients in L-15 medium above adherent NRK cells on the bottom of the well. The ordinate shows the oxygen partial pressure values plotted as a function of the distance from the cells, as well as in a time-dependent way. (A) Sensing of the vertical oxygen gradient above cells seeded in lower cell density ($8 \cdot 10^4$ cells·cm⁻²) and (B) cells were inoculated to yield a confluent monolayer ($25 \cdot 10^4$ cells·cm⁻²). Depicted experiments have been performed twice at 37 °C and 0 % CO₂.

The 3D surface colormap (Fig. 4.17) demonstrates the emerging vertical oxygen gradient in the medium above adherent cells in a time- and spatially resolved way. The ordinate represents oxygen partial pressure values, plotted against the distance from the cells on the x-axis and the time on the y-axis inverted. This illustration shows the time-resolved emergence of O_2 gradients as profile plots represent only single time points. Differences in the occurring gradients due to differing cell numbers are emphasized meaning higher numbers of oxygen consumers entailed increased VOGs. Nevertheless, the oxygen concentration at the medium surface - the air-liquid interface - remained constant in both cases.

4.5 DISCUSSION

Monitoring of the cell-specific respiratory activity of cell monolayers

The non-invasive, label-free and real-time sensing of the respiratory activity of cell monolayers via the sensor foil-based technique was performed using different cell lines. The time-resolved pO_2 curves were fitted linearly in the time interval between 1 h and 4 h resulting in AOCR values. Since the individual cell types differ in size and thus the number of cells per area required to yield confluent monolayers is varying, the AOCR was converted into *oxygen consumption rates* per cell.

The two skin cancer cell lines yielded the highest and lowest consumption rates. SK-MEL-28 respired (107 ± 2) $\text{amol}\cdot\text{s}^{-1}\cdot\text{cell}^{-1}$ while SpiCa cells converted only (19 ± 2) $\text{amol}\cdot\text{s}^{-1}\cdot\text{cell}^{-1}$. The high consumption rates which were determined for SK-MEL-28, were found in literature to be even higher of around $120 \text{ pmol}\cdot\text{min}^{-1}$ as detected for a seeded cell number of 10.000 cells with the help of the Seahorse technique (see Fig. 1.6) which corresponds to $200 \text{ amol}\cdot\text{s}^{-1}\cdot\text{cell}^{-1}$ (Plitzko, B. *et al.* 2018). The *oxygen consumption rates* found for kidney and HDMEC cells ranged between $28 \text{ amol}\cdot\text{s}^{-1}\cdot\text{cell}^{-1}$ and $42 \text{ amol}\cdot\text{s}^{-1}\cdot\text{cell}^{-1}$. Guarino, R. D. *et al.* 2004 reported about OCRs of $1.25 \text{ fmol}\cdot\text{min}^{-1}\cdot\text{cell}^{-1}$ for MDCK II cells, which corresponds to $20 \text{ amol}\cdot\text{s}^{-1}\cdot\text{cell}^{-1}$ and consequently is in good accordance with the determined range from $(32.6 \pm 0.5) - (42 \pm 2) \text{ amol}\cdot\text{s}^{-1}\cdot\text{cell}^{-1}$ within this thesis. Tab. 4.5 summarizes the determined OCR values and the ones described in literature.

Tab. 4.5 Summary of *oxygen consumption rates* (OCR) for different tested cell lines in comparison to values reported in literature. OCR values were calculated from AOCR data by linear regression of the time-resolved oxygen partial pressure values (compare chapter 3.4.5).

Cell line	OCR / $\text{amol}\cdot\text{s}^{-1}\cdot\text{cell}^{-1}$	Literature OCR / $\text{amol}\cdot\text{s}^{-1}\cdot\text{cell}^{-1}$	Method
A 549	62 ± 13	33 (Gardner, P. R. <i>et al.</i> 1994)	Gilson oxygraph with Clark electrode in cell suspension
		55 (Ahmad, S. <i>et al.</i> 2001)	Clark-style polarographic O_2 electrode in cell suspension
		89 (Molter, T. W. <i>et al.</i> 2008)	Fluorescence quenching of embedded platinum phosphor in the vicinity of adherent single cells in a closed system
MDCK II	$32.6 \pm 0.5, 42 \pm 2$	20 (Guarino, R. D. <i>et al.</i> 2004)	Fluorescence detection of an embedded ruthenium-based fluorophore beneath a cell suspension in an open system
NRK	31.8 ± 0.5	20-40 (Ruggiero, C. <i>et al.</i> 2014)	Seahorse XF24 with adherent cells
SK-MEL-28	107 ± 2	200 (Plitzko, B. <i>et al.</i> 2018)	Seahorse XF24 with adherent cells

NRK cells are a typical model cell line in this thesis and were used to investigate multiple parameters and influences on the metabolic activity. Since the experiments require control conditions to be able to validate the impact of the experimental modulators, several investigations of the respiratory activity of NRK cells

under the influence of normal L-15 medium were done for reasons of comparison. Tab. 4.6 summarizes the *apparent oxygen consumption rates* of NRK cells in L-15 medium. The consumption rates ranged from $20.3 \text{ torr}\cdot\text{h}^{-1}$ to $15.1 \text{ torr}\cdot\text{h}^{-1}$. The AOCR value which was obtained from the MIOS experiments constitutes an exception as the oxygen decrease was measured in the supernatant medium instead of directly beneath the adherent cells. Changes in the $p\text{O}_2$ were determined in an ROI at the tip of the MIOS element and plotted as a function of time. Individual experiments were always performed using the same cryo batch and consecutive subcultivation events to avoid changing respiratory activity due to ageing of cells. Although OCR values from different experiments are in good accordance with each other, the aforementioned reasons could account for the slightly different consumption rates yielded by the different experiments. Nevertheless, the detection of the respiratory activity in general was very reproducible with small error margins.

Tab. 4.6 Summarized *apparent oxygen consumption rates* (AOCRs) and the corresponding *oxygen consumption rates* (OCRs) of NRK cells under L-15 medium obtained via linear regression of the time-resolved oxygen partial pressure. Consumption rates were determined according to the protocol described in chapter 3.4.5.

Experiment (chapter number)	Details	Cell line	AOCR / $\text{torr}\cdot\text{h}^{-1}$	OCR / $\text{amol}\cdot\text{s}^{-1}\cdot\text{cell}^{-1}$
Cell-specific respiration (chapter 4.1)			20.3 ± 0.3	31.8 ± 0.5
Sensor foil thickness (chapter 4.2)	Normal sensor foil thickness (1x)	NRK	18.3 ± 0.1	28.7 ± 0.2
Cover slip experiments (chapter 4.3)	ROI 9 (cells next to the cover slip)		16 ± 2	24 ± 1
MIOS experiments (chapter 4.4)	ROI at the tip of the MIOS element		6 ± 3	15 ± 7
pH studies (chapter 5.5.1)			15.1 ± 0.1	23.6 ± 0.2

Monitoring of the cell-specific respiratory activity of 3D cell tissue

The investigations of the respiratory activity of three-dimensional tissue models were done with spheroids in different sizes and from three different cell lines. The respiratory activity is highly dependent on the cell line due to their origin and function within a living organism as was observed in chapter 4.1.1 and has already been discussed. Moreover, the cell number used to create a spheroid influences the packing density and spheroid size and thus affects cellular respiration and consequently the generation of oxygen gradients and metabolic zones within spherical tissue.

The attachment of spheroids on the sensor foils led to the formation of adherent, hemispherical structures, allowing for an estimation of oxygen tensions in a cross section of the spheroid. The three examined spheroid types revealed slightly different oxygen profiles and consequently different rates of oxygen depletion within the individual zones of the tissue. The observed profiles are best described as W-, V- and U-shaped beneath SK-MEL-28, U373 and MCF-7 spheroids, respectively. MCF-7 spheroids exhibited the largest area with a significant oxygen depletion with time. These findings were in accordance with the performed ROI

evaluations showing nearly 0 torr pO_2 centrally beneath the spheroids in all cases, while the rate of the oxygen partial pressure decrease in the periphery and next to the spheroid were strongly depending on the respective tissue. MCF-7 spheroids showed a higher tendency to form cell monolayers around the spherically shaped part meaning that the cells from the outer layers adhered to the sensor foil surface around the sphere. This outgrowing monolayer could also have caused the rapid oxygen depletion next to the spheroid observed in Fig. 4.5. The cell lines chosen for spheroid generation all represent cancer tissue and nonetheless, differences could be detected. As already mentioned earlier, the respiratory activity is strongly dependent on the cell type and its origin and differences between normal and cancer tissue should be even more pronounced. Spheroids are reported to decrease cellular packing density with increasing spheroid size in order to facilitate transport of oxygen and nutrients (Murphy, K. *et al.* 2017) what could possibly cause drastically changed oxygen concentration profiles.

The comparison of spheroids from lung cells of a Chinese hamster (V-79 cells) and mouse epithelial breast cancer cells (EMT6 cells) also showed significant differences in respiratory rates. V-79 spheroids are reported to reveal a sigmoidally shaped decrease of the oxygen consumption with an increasing diameter accompanied by a decreased uptake of O_2 and glucose (Freyer, J. *et al.* 1984). Similar experiments, carried out with EMT6 spheroids in a sealed system using a Clark-type electrode setup, showed a linear dependency between the oxygen consumption and the spheroid diameter (Freyer, J. *et al.* 1985) indicating that these two cell lines also exhibit highly different oxygen gradients toward the center of the spheroid. Similar to these results, the calculated AACs, which were plotted against the diameter of the spheroids, revealed nearly linear dependencies between the oxygen depletion and the spheroid size (compare Fig. 4.18 B) in the case of the SK-MEL-28 spheroids. The correlation between the area above the oxygen concentration profile and the tissue diameter was different in the case of MCF-7 spheroids. The AAC increased faster within the first 24 h of measurement time and slightly slowed down in the following 24 h, except for the spheroid S1, for which the increase in AAC was more pronounced from 24 – 48 h. The differences in the correlation between the respiration activity and the spheroid size for the two cell lines confirmed that the respiration was strongly cell type-dependent. The time-dependent change of the AAC (see Fig. 4.18 A) exhibited a nearly linear increase in the oxygen depletion beneath the spheroids for all sizes under test. However, it is striking that the AAC for the SK-MEL-28 spheroids were drastically larger compared to the ones for the MCF-7 spheroids. The different AAC values could hint at the influence of tissue integrity or structure on the detected oxygen gradients or respiration activity. The SK-MEL-28 spheroids seemed to be very soft as the spherical structure at the beginning of the measurement rapidly changed to a disk-like shape. Thus, the oxygen concentration rapidly decreased in a larger area due to inhibited oxygen diffusion which, in turn, resulted in larger AAC values.

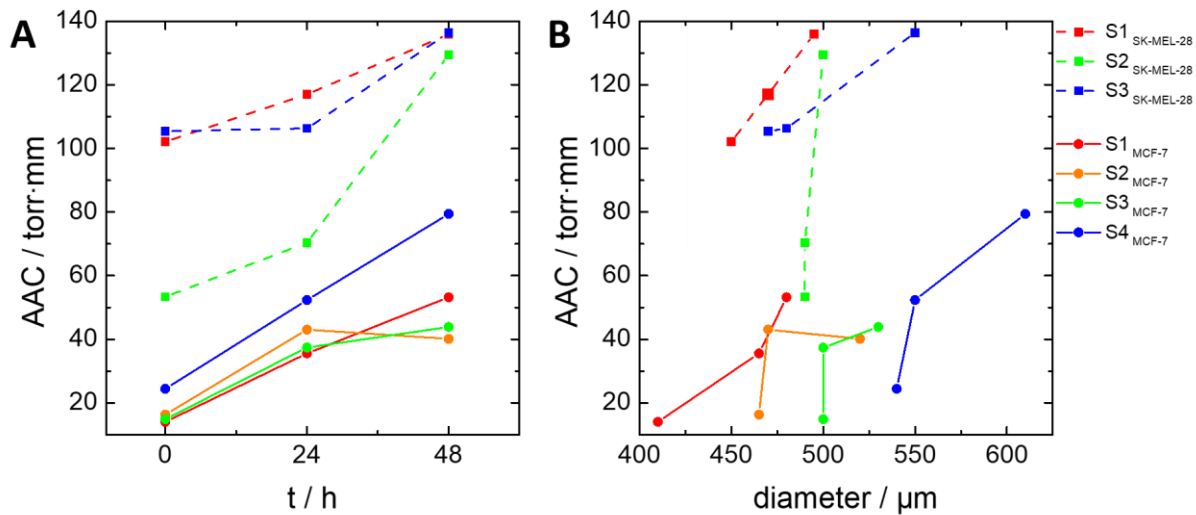


Fig. 4.18 Calculated *areas above the curves* (AAC) of the profile plot evaluation of different sized MCF-7 and SK-MEL-28 spheroids plotted as function of time (**A**) and against the respective spheroid diameter (**B**). Raw data can be seen in Fig. 4.8 and Fig. 4.9 and AACs are summarized in Tab. 4.2.

Additionally, an eightfold decrease in O_2 uptake and a twofold increase in glucose consumption with increasing diameter could be detected in EMT6 spheroids (breast cancer tissue) in contrast to lower consumption rates of both O_2 and glucose by V-79 spheroids (normal tissue) (Freyer, J. *et al.* 1984; Freyer, J. *et al.* 1985). This specific behavior allows for the discrimination between normal and cancer tissue due to significantly accelerated aerobic glycolysis. Hence, the consumption of glucose and the production of lactate is generally elevated in tumor cells and is furthermore reported to be two- to threefold higher in three-dimensional tissue compared to cell monolayers (Khaitan, D. *et al.* 2006). Hypoxia in certain tissues also induces an inhibition of the mitochondrial electron transport chain causing increased formation of reactive oxygen species (ROS). These ROS stabilize the HIF-1 α leading to an enhanced shift from OXPHOS to anaerobic glycolysis (Warburg effect) (Chandel, N. *et al.* 2000). This in turn entails decreased *oxygen consumption rates* at low amounts of accessible dissolved oxygen causing different metabolic zones within a spheroid.

The second parameter being examined in this thesis was the effect of spheroid size on emerging oxygen gradients in a cross section of the tissue. Differently sized SK-MEL-28 spheroids and the 610-nm-sized MCF-7 spheroid exhibited quite similar time-dependent changes of the oxygen profile resulting in a W-shaped oxygen concentration profile. Most notable was the observation of an increased partial oxygen pressure centrally beneath the core of the spheroid. This observation could confirm different metabolic zones. Since O_2 and nutrient availabilities decrease towards the spheroid core and are accompanied by increasing amounts of metabolic waste, this could contribute to the three areas consisting of the hypoxic/necrotic core, the middle layer of quiescent cells and the outer layer of proliferating cells (Hirschhaeuser, F. *et al.* 2010; Nath, S. *et al.* 2016). Since oxygen consumption in the central necrotic tissue is ceased, available oxygen or unconverted molecules could cause a slight increase of pO_2 . Mueller-Klieser, W. *et al.* 1986 could observe an increase in central pO_2 values (in the core of the spheroid) with increasing spheroid diameter and with

increasing glucose concentration in the supernatant medium by microelectrode detection. This correlation is in agreement with the mathematically and experimentally determined correlation of spheroid diameter and the size of necrotic areas. The necrotic core of WiDr spheroids (human colon adenocarcinoma cells) grew 70 % after a 116 % size increase of a spheroid diameter from 600 μm to 1300 μm while the thickness of the viable spheroid periphery decreased from 280 μm to 175 μm (Groebe, K. *et al.* 1991; Groebe, K. *et al.* 1996). HepG2 spheroids were reported to reveal a positive hypoxic area of 30 % after an initial cell density of $1 \cdot 10^5$ / chip which increased to 80 % following a tenfold higher initial cell density (Anada, T. *et al.* 2012). The necrotic cross section in EMT6 spheroids increased from 1 % to 38 % for diameters of 468 μm and 1347 μm (Freyer, J. *et al.* 1985). It was also reported that spheroids exhibiting hypoxia and necrosis seem to reveal a similar gene expression profile like *in vivo* grown tumors and were more resistant to anti-proliferative drugs (Däster, S. *et al.* 2017). The emergence of hypoxia and necrosis are discussed to play a key role in tumor progression, resistance to radiation and cancer treatments, metastasis and angiogenesis and is consequently an important aspect of tumor physiology and for the examination of efficient treatment strategies (Santini, M. *et al.* 1999; Tatum, J. *et al.* 2006).

The studies in this thesis investigating the respiratory activity of three-dimensional tissue models could show that this cellular phenotype is highly dependent on the cell line as well as on the architecture of the tissue meaning whether the cells form very compact and densely packed spheroids or rather soft structures. Especially in the case of the MCF-7 spheroids, the oxygen profiles seemed to be depending on the spheroid size. Furthermore, SK-MEL-28 and large MCF-7 spheroids led to the formation of W-shaped profiles probably indicating the different, biologically relevant zones within the tissue. For future investigations it would be interesting to compare spheroids offering a size difference of at least 100 μm in diameter and in a wider range in order to obtain a better correlation between the oxygen profiles and the spheroid size.

Detection of the influence of the sensor foil thickness

Changing extracellular measurement conditions like altered sensor foil thickness normally should not influence the metabolic activity of the cells and hence the *oxygen consumption rate* should stay constant. The comparison of single cell *oxygen consumption rates* could be misleading but allows for a comparison with other investigations. Changes of the sensor foil thickness led to different oxygen contents inside the sensor foil matrix being accessible for the cells. The thicker the sensor foil, the more oxygen can be stored inside the foil matrix and the longer it takes for the cells to respire the oxygen completely, reaching the hypoxic state which is detectable via luminescence signal ratios. Doubling the sensor foil thickness increased the basolateral medium volume from 1.6 – 2.1 pL to 3.2 – 4.2 pL beneath a single cell. The volume was calculated based on typical NRK cell dimensions with a radius of 9.2 μm (used to calculate the area of a single cell), an average height of the subcellular cleft of 73.3 nm (PhD Thesis Björn Reiss) and a standard sensor foil thickness

of 6 – 8 μm (both used to calculate the overall height). When aqueous media with physiological salinity is equilibrated in the incubator atmosphere, the oxygen mass concentration in the medium is $6.40 \text{ mg}\cdot\text{L}^{-1}$ which corresponds to a concentration of $199.90 \text{ }\mu\text{mol}\cdot\text{L}^{-1}$ of dissolved oxygen, and consequently $0.32 - 0.43 \text{ fmol}$ of oxygen is dissolved in the basolateral compartment (subcellular cleft plus sensor foil in which an equal amount of oxygen is dissolved with respect to the supernatant medium) beneath each cell. Taking the OCR of around $28 \text{ amol}\cdot\text{s}^{-1}\cdot\text{cell}^{-1}$ into account, an oxygen consumption time of only $11.5 \text{ s} - 15.3 \text{ s}$ can be calculated – the time needed for one cell to respire the oxygen dissolved in the basolateral compartment completely. The same calculations for the apical compartment above one cell (the single supernatant medium column) yielded a complete consumption time of 5.3 h for the dissolved oxygen in the supernatant L-15 medium. Doubling and quadrupling the sensor foil thickness led to theoretical consumption times of $23 \text{ s} - 30.6 \text{ s}$ and $46 \text{ s} - 61.2 \text{ s}$ being responsible for decreased *oxygen consumption rates* due to the longer presence of free oxygen and a possibly even higher oxygen back diffusion across the polymer which can quench luminescence and consequently lead to higher detected oxygen concentrations. Results showed 10 % decreased AOCR values between standard and twofold thickness of the sensor foils and again a 10 % decrease between twofold and fourfold thickness of the sensor foils, although respiratory activity is assumed to be constant. The calculated consumption time of around 5.3 h for the oxygen from the supernatant medium was observed to be 15 h and hence much larger. This effect could also be caused when the *oxygen consumption rates* are higher than the diffusion rates of the dissolved oxygen, which becomes the rate-determining factor. The oxygen conditions change from a normoxic state to a hypoxic state with time. Under hypoxic conditions, cells respond in three ways: (i) cells start to inhibit proliferation to keep the number of O_2 -consuming cells constant, (ii) the rate of oxidative phosphorylation is decreased with a simultaneously increased glycolysis rate and (iii) the production of angiogenic factors is accelerated (Semenza, G. *et al.* 2013). Cells are able to adapt to changing oxygen levels due to the HIF-1 transcription factor. HIF-1 stimulates glycolysis and actively represses mitochondrial respiration (Papandreou, I. *et al.* 2006). The decrease in cellular respiration accompanied by decreasing dissolved oxygen is responsible for the longer measured oxygen consumption time compared to the pre-calculated respiration time. In addition, the AOCR values have been determined in the beginning due to a linear regression between $1 \text{ h} - 4 \text{ h}$ of recording; in the chosen time interval however, normoxic oxygen levels were present, resulting in higher mitochondrial respiration.

All in all, the predicted decrease in OCR values with increasing sensor foil thickness could be confirmed by the performed experiments but it is important to keep in mind that only the oxygen accessibility beneath the cells was increased while cellular respiration was assumed to be constant.

Detection of horizontal oxygen concentration gradients with cover slips

The two measurements performed in this thesis differ due to a distinct feature. Experiment 1 (left-hand side, Fig. 4.13) shows a sharp increase in the pO_2 levels pertaining to ROIs 1 – 5 after 11 h. This increase is caused by a ruptured air bubble, which was trapped between the cell layer and the cover slip. The exact same placement of the cover slip was difficult to reproduce since the distance to the cells could not be measured or adjusted. Slightly differing distances led to varying rates of the decrease in the oxygen partial pressure. Nevertheless, the experiments demonstrated the influence of the accessible oxygen from the apical membrane side. Since the oxygen dissolved in the medium beneath the cells was respired within seconds, the cells consumed the oxygen offered from the apical membrane side until a hypoxic zone was created close to the cell monolayer due to the cover slip-blocked oxygen diffusion from the medium surface. Cells covered by the glass cover slip on average respired $(134 \pm 17) \text{ torr}\cdot\text{h}^{-1}$, which seemed to be a drastically increased consumption rate compared to $(16 \pm 2) \text{ torr}\cdot\text{h}^{-1}$ respired by uncovered cells with free access to dissolved oxygen. Similar to the already discussed influences of the sensor foil thickness, the respiratory activity was not directly influenced by the cover glass. However, the oxygen diffusion was blocked by the cover glass and consequently the access to O_2 was restricted for the cells. After the formation of hypoxic zones, the cellular metabolism adapted its energy production to the extracellular low oxygen level presumably by shifting from the mitochondrial respiration to glycolysis (Semenza, G. *et al.* 2013; Papandreou, I. *et al.* 2006) which entailed decreasing OCR values. In literature there are several reports about microfluidic devices being able to create horizontal oxygen tension gradients above a certain cell culture area within the microfluidic channels. For instance, the cell culture area was confined by PDMS-patterned microchannels on both sides. Through the microchannels, oxygen-scavenging and oxygen-producing solutions could be passed through. The oxygen scavengers in question were pyrogallol and NaOH and the oxygen-generating substances were H_2O_2 and NaOCl. Generated oxygen could freely enter the cell culture area by diffusion through the PDMS barrier and was bound in the opposing microchannel leading to a linear oxygen gradient above the cells. Chen, Y.-A. *et al.* 2011 and Chang, C.-W. *et al.* 2014 used the described microfluidic device to investigate cell viability under different oxygen tensions and reported about slightly elevated cell viability of A549 caused by hypoxic conditions ($[O_2] \leq 0,5 \%$) but drastically decreased cell viability under increasing oxygen tension up to hyperoxia conditions ($[O_2] \geq 30 \%$). In Chen's work, oxygen concentrations were determined with fluorescence imaging using an oxygen-sensitive dye and cell viability was investigated by live/dead staining. This study demonstrates the importance of being able to sense oxygen tensions and gradients above cultured cells, since the adjustment of culture conditions is highly important and should be as natural as possible to ensure optimal culture conditions for the cells as they are used as living sensors.

Apart from the two-dimensional approach, the experiments were also performed to study multicellular spheroids growing on top of the sensor foil. Multiple layers of cells reduce the diffusion of oxygen, resulting in horizontal oxygen concentration gradients with decreasing pO_2 values in direction of the spheroid's core.

Different gradient profiles are discussed to yield information about the different layers of the spheroid and indicate an occurring necrosis. A parabolic profile represents small spheroids lacking a necrotic core while a steep decrease in pO_2 levels towards the spheroids core with a central plateau seems to be characteristic for large spheroids with central necrosis (Mueller-Klieser, W. *et al.* 1984).

Sensing of vertical oxygen concentration gradients above adherent cells

The vertical oxygen concentration gradient (VOG) occurs due to the consumption of dissolved oxygen by cells adhering on the bottom of the well and the insufficiently fast oxygen diffusion along the gradient from the liquid surface to the well bottom. Furthermore, oxygen ingress from the ambient air into the medium at the liquid-air interface is also not fast enough to compensate the consumption at the bottom. The investigations detected oxygen levels close to *in vitro* living cells. It is widely assumed that cells are exposed to normoxic conditions, with the normal mass concentration of dissolved oxygen in medium being $6.4 \text{ mg}\cdot\text{L}^{-1}$ or $199.9 \text{ }\mu\text{mol}\cdot\text{L}^{-1}$. The VOG studies showed that different oxygenation levels emerged and changed in the individual liquid layers in a distance- and time-dependent manner. Pettersen, E. *et al.* 2005 reported about the investigation of the vertical and pericellular oxygen depletion above adherent human breast cancer T-47D cells by using an O_2 Clark-type microsensor held by a micromanipulator. Normally, cultured cells experiencing normoxic conditions reached low oxygen conditions or hypoxia in their local microenvironment after around 12 h of measurement time. The comparison of different cell seeding densities showed that the degree of oxygen depletion is strongly dependent on the number of oxygen consumers. The initially seeded cell densities of $8\cdot 10^4 \text{ cells}\cdot\text{cm}^{-2}$ and $25\cdot 10^4 \text{ cells}\cdot\text{cm}^{-2}$ were exposed to 80 torr and 45 torr after 12 h, respectively, corresponding to a VOG of $4.8 \text{ }\mu\text{mol}\cdot\text{L}^{-1}$ and $7.2 \text{ }\mu\text{mol}\cdot\text{L}^{-1}$ between the liquid-air interface and a position 1 mm above the adherent NKR cells. Pettersen, E. *et al.* 2005 reported about an oxygen gradient between 50 torr and 128 torr within 1.6 mm of supernatant liquid layer with an oxygen consumption of $146 \text{ fmol}\cdot\text{h}^{-1}\cdot\text{cell}^{-1}$ ($= 40.5 \text{ amol}\cdot\text{s}^{-1}\cdot\text{cell}^{-1}$). Looking at the very tip of the light guide element, *apparent oxygen consumption rates* of $(2.3 \pm 0.4) \text{ torr}\cdot\text{h}^{-1}$ or $(12 \pm 2) \text{ amol}\cdot\text{s}^{-1}\cdot\text{cell}^{-1}$ were found for $8\cdot 10^4 \text{ cells}\cdot\text{cm}^{-2}$ and $(7 \pm 4) \text{ torr}\cdot\text{h}^{-1}$ or $(11.6 \pm 7.2) \text{ amol}\cdot\text{s}^{-1}\cdot\text{cell}^{-1}$ for the experiments performed with $25\cdot 10^4 \text{ cells}\cdot\text{cm}^{-2}$. The determination of the AOCRs was done by linear regression of the oxygen partial pressure in the time interval between 2 h – 5 h and for the calculation of the OCRs, the initial cell number and growth area (1.9 cm^2) as well as the supernatant medium volume (2 mL) was taken into account. The single cell consumption rates proved to be very similar, even if proliferation should have occurred when cells had been seeded subconfluently. Proliferation or growth rates are reported to decrease with increased cell density, while cell division in confluent layers led to detachment in parts during cell division and slightly inhibited reattachment of daughter cells because of already confluent substrate surfaces (Shields, R. *et al.* 1977; Tremel, A. *et al.* 2009). Moreover, there are studies about significantly lower proliferation rates of near-confluent cells compared to

subconfluent cells, while both cells layers were exposed to hyperoxic medium conditions. It was also reported that oxidant injury increases necrosis and apoptosis in near-confluent cell layers of MCDK II cells (Jyonouchi, H. *et al.* 1997, Jamnongwong *et al.* 2010). These reasons for inhibited proliferation could cause relatively stable cell numbers in the discussed experiments and could consequently explain the similar results of comparable single cell respiratory activities and an emerging, cell number-dependent vertical oxygen gradient in the medium above adherent cells.

The influence of hypoxia on the proliferation rate is strongly dependent on the cell type, similar to dissolved oxygen being available in different amounts for individual tissue types. Naureckas, E. T. *et al.* 1995 reported higher proliferation rates of airway smooth muscle cells from hyperoxia-exposed rats, while hypoxia on the other hand induced constant proliferation rates in lung alveolar epithelial cells (Clement, A. *et al.* 1992).

The determined VOG of $7.2 \mu\text{mol}\cdot\text{L}^{-1}\cdot\text{mm}^{-1}$ can only be constant if there is an equilibrium established between the oxygen consumption by the cells and the oxygen ingress at the liquid-air interface. The Stokes-Einstein equation explains the diffusion rate of small molecules under consideration of Fick's law of diffusion in combination with the Brownian movement of colloidal particles (Edward, J. T. *et al.* 1970) and allows to determine the diffusion coefficient of oxygen in water at 37°C resulting in $D = 2.18 \cdot 10^{-9} \text{m}^2\cdot\text{s}^{-1}$. To get an estimate of the time needed for oxygen to diffuse a certain distance in water, the random walk model for three dimensions was applied ($L^2 = 6\cdot D\cdot t$, while L is the length or displacement of the diffusive molecule, D depicts the diffusion coefficient and t is the time) (Karlsson, G. E. *et al.* 2004). As the equation already demonstrates, there is no linear correlation between the molecule displacement and the corresponding time. Using the diffusion coefficient for oxygen at 37°C and a time interval of one second yields a diffusion distance of $11.4 \mu\text{m}$. Since the vertical oxygen gradient was determined per millimeter, the random walk model yielded a diffusion time of 76.5 seconds for one millimeter of liquid layer in all directions. The use of the MIOS elements allows for the determination of oxygen concentrations in a height range of up to 18 mm above adherent cells, which according to the random walk model, translates to around 413 min (6.9 h) of diffusion time for one oxygen molecule from the medium surface to the cell monolayer. However, this rough estimation of diffusion time does not take into account that the flux (the number of diffusing molecules per time interval and area) is influenced by existing concentration gradients. Thus, oxygen flux is faster for high concentration differences and slower for steady oxygen gradients as defined by Fick's law. Dissolved oxygen in water normally is in an equilibrium with the oxygen in the atmosphere according to Henry's law (Holley, E. R. *et al.* 1977). The MIOS elements were attached to the lid of the 24-well plate. The specially aligned lid is additionally equipped with small grooves, fitting the rim of each well for tight adjustment of the lid and consequently of the light guide elements. On the upside, evaporation of the medium during the measurement was prevented but, on the downside, the tight closing slightly hindered the diffusion of

ambient oxygen to the medium surface. This way, the hindered diffusion of ambient oxygen led to slightly decreased oxygen partial pressures of 130 torr – 140 torr at the medium surface. The partial pressures are equivalent to oxygen values of 18.2 – 19.6 % or 87 – 93 % air saturation instead of the ambient 21 % oxygen and 100 % air saturation. The hindered oxygen ingress as well as decreasing oxygen concentrations resulted in an overall decreased oxygen content, consequently causing smaller oxygen diffusion rates.

Oppegard, S. *et al.* 2013 described a device for the establishment of oxygen gradients in 3D constructs. The device consists of two microchannels which are covered by gas-permeable membranes and enclose an agarose construct.

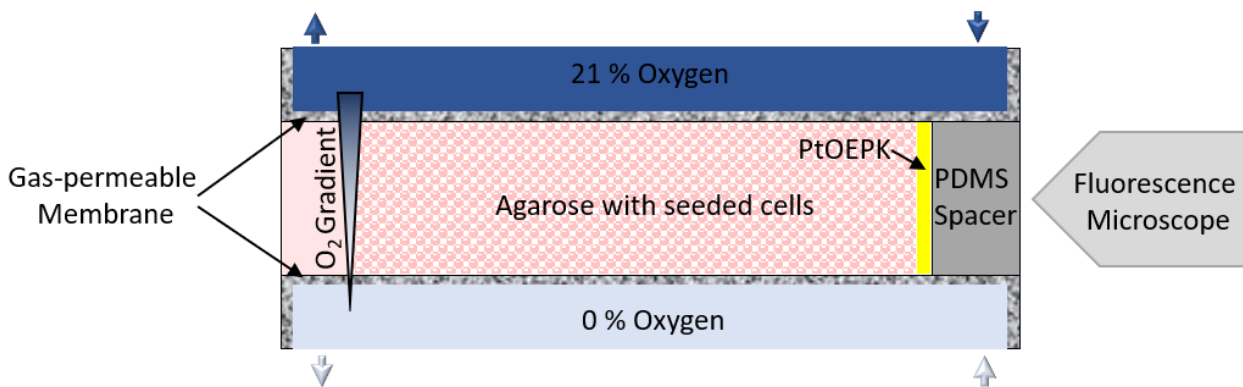


Fig. 4.19 Schematic of the device described by Oppegard, S. *et al.* 2013 for the observation of oxygen gradients in 3D constructs. The agarose layer containing seeded cells is sandwiched by two microchannels (with 21 % and 0 % oxygen) connected via gas-permeable membranes. The vertical side of the agarose is additionally equipped with a PtOEPK oxygen-sensing layer and the emitted fluorescence is detectable via a fluorescence microscope. Adapted from Oppegard, S. *et al.* 2013.

The agarose is equipped with an oxygen-sensing platinum (II) octaethylporphine ketone (PtOEPK) on its vertical side, allowing to measure oxygen gradients within the agarose. The agarose offers the possibility of seeding cells in three dimensions while the microchannels were designed for gas transport of varying oxygen concentrations. This approach could offer the possibility to detect oxygen gradients within three-dimensional tissue models while the performance of the MIOS elements in a purely aqueous environment was validated and their easy handling and high throughput is another advantage. Additionally, reproducible oxygenation during cell culture could lead to more reliable experiments since oxygen tensions directly affect energy metabolism. The advantage of the MIOS elements lies in the possibility of facile size and dimension modifications, offering the possibility of using these elements within cell culture devices of various geometries.

4.6 OUTLOOK

The sensor foil-based monitoring of the respiratory activity of mammalian cells offers the possibility of a very broad variety of assays and applications. The non-invasive and real-time detection of changes in the oxygen partial pressure yielded highly detailed results, allowing to draw conclusions about special dependencies or changes in metabolic rates. Within this thesis, the image-based system was used to discriminate between different cell types and the same cell type either grown as a monolayer or in more complex cellular structures. The variation of the sensor foil thickness, the inhibition of oxygen diffusion to the sensor foil and initial investigations with respect to emerging vertical oxygen gradients yielded information about different diffusion processes being important for a better understanding of dissolved and accessible oxygen for mammalian cells. The MIOS elements furthermore could be a useful tool to refine experimental setups and cell culture conditions could be monitored and adjusted to specific cellular needs. Different cell culture vessels exhibit slightly different geometries leading to varying oxygen ingress and therefore emerging vertical oxygen gradients can be significantly different. These variations can be easily examined and refined by the MIOS light guide elements.

Since reliable monitoring systems for the detection of three-dimensional tissue models keep getting more important in current research, further development of the system could simplify and improve the performance of experiments. The oxygen-sensitive sensor foil so far is intransparent and hence unsuited for phase-contrast microscopy. Additionally, one problem that arose during the experiments carried out with spheroids, was the time-consuming positioning of the petri dish to place the spheroids in the field of view of the camera. Clear, transparent sensor foils would facilitate the observation of the cells' vitality and degree of attachment within cellular monolayers as well as in the case of spheroids, it would make the localization a lot easier. Another adverse aspect of this techniques relies in the detection of only one specimen. A higher throughput would enable a simultaneous observation of multiple spheroids leading to statistically more reliable results. Higher throughput could possibly be achieved by moveable stages coupled to programmable stepping motors, since the high resolution should be maintained. The combination of transparent sensor foils and higher throughput would furthermore allow for the investigations of: (i) cellular adhesion, proliferation and migration, (ii) the degree of spheroid attachment and spreading and (iii) cellular vitality and morphology with a simultaneous detection of cellular respiration.

5 MONITORING OF THE pH-DEPENDENCY OF CELLULAR PHENOTYPES

This study relies on the monitoring of several cellular phenotypes under different extracellular pH values (pH_e) as the key factor. The main goal was to analyze how cells react to variations in the pH_e of their extracellular environment and how cells adapt their intracellular pH (pH_i) to changes in the extracellular pH_e . These studies were done using two different human skin cancer cell lines (SK-MEL-28 and SpiCa), a human lung cancer cell line (A549) and NRK cells served as a model for non-cancerous cells being exposed to different pH_e . The original idea was to investigate one acidic, one alkaline and one neutral pH-adjusted buffer. For control reasons, pure L-15 was tested in the first experiments. After a few examinations, it turned out that L-15, a system which is only phosphate-buffered and therefore lacks any pH-buffering capacity in the presence of CO_2 , became increasingly acidic with an increasingly large gas phase above the medium in the storage container. It was therefore decided to always adjust the control medium to a pH of 7.4. Consequently, the cellular responses to the pH_e of 6.4, 7.2, 7.4 and 7.8 were examined.

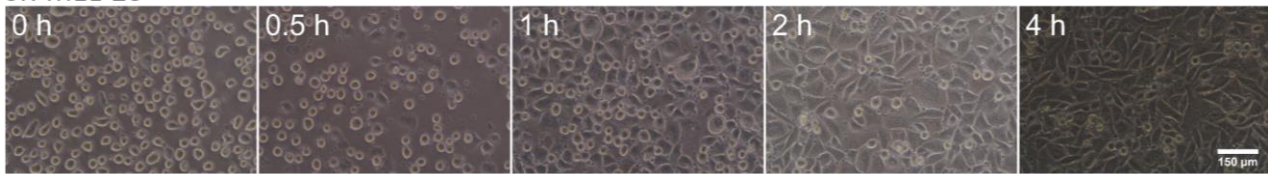
5.1 pH-DEPENDENCY OF ADHESION PROCESSES

The adhesion process was examined using the ECISTM technique. Following the enzymatic detachment from the growth surface, the cells were counted and divided into four centrifugation tubes. Each tube contained sufficient cells to yield a confluent cell monolayer after inoculation into 8W10E arrays. After the centrifugation, the cells were resuspended in L-15 medium adjusted to four different pH_e (6.4, 7.2, 7.4, 7.8) and inoculated into the wells in a real-time manner.

The previous detachment by trypsin lead to spherically shaped cell bodies which sedimented to the bottom of the respective substrate after inoculation. Beginning with cell sedimentation and the formation of cell-substrate contacts, the adhesion process with subsequent spreading and the formation of cell-cell contacts was followed, resulting in adherent and confluent monolayers. Fig. 5.1 depicts the adhesion of SK-MEL-28 and A549 cells to demonstrate the different steps of the process and to illustrate the cellular shape changes during the process via microscopic images. The phase contrast images highlight the initially round shape of the cells which disappeared due to morphological changes during the adhesion process. SK-MEL-28 cells needed around half an hour for the attachment of the first few cells. Already 1 h after cell inoculation, most of the cells had attached to the substrate surface exhibiting a cobblestone-like morphology, which later

turned into the characteristic polygonal shape of adherent cells. A549 needed around 1 – 2 h for the adhesion of the first cells and the typical cobblestone morphology can be seen after 24 h.

SK-MEL-28



A549

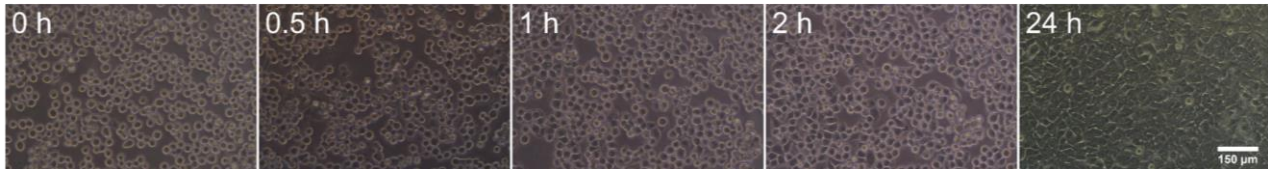


Fig. 5.1 Microscopy-based detection of the adhesion process of SK-MEL-28 and A549 cells with $10 \cdot 10^4$ cells·cm⁻² and $32 \cdot 10^4$ cells·cm⁻² followed for 4 h and 24 h, respectively. Adhesion was monitored with L-15 as supernatant at a pH_e of 7.4, a temperature of 37 °C and 0 % CO₂. The spherically shaped, detached cells start to form cell-substrate and later cell-cell contacts resulting in well-spread and adherent cell monolayers. Images were taken with the *Nikon Diaphot* microscope equipped with a Nikon digital camera using a 10x magnification. Scale bar depicts 150 µm.

The ECISTM-based observations of the adhesion were done by recording the capacitance signal at high frequencies (≥ 10 kHz) due to the direct proportionality to the degree of cell coverage (see chapter 3.3.4.1). The capacitance signals were normalized with respect to the starting capacitance value (C_0) and the individual experiments were averaged with $n = 3$ (12) meaning three individual experiments were performed in quadruplicate.

At first it was examined whether a precoating of the working electrode accelerated the adhesion process. Fig. 5.2 depicts the capacitance time courses during the adhesion of NRK cells with and without fibronectin-precoated (FN) electrodes. The neutral and alkaline extracellular pH_e did not differ much in their time-dependent capacitance signals. The first drop in capacitance occurred due to the sedimentation of the cells with subsequent adhesion and spreading. The cells exposed to an acidic environment however, revealed drastically retarded and incomplete adhesion characteristics as can be seen in the slowly decreasing capacitance, yielding normalized values of 0.57 and 0.4 for uncoated and FN-coated electrodes, respectively. In contrast to FN-coated electrodes, the uncoated substrates provoked slower adhesion processes yielding constant normalized capacitance values of 0.13 – 0.15 after 20 h of recording for a pH_e of 7.2, 7.4 and 7.8. The coated ones exhibited a sharp drop of the capacitance signal up to 4 h followed by a moderate decrease of the capacitance until 12 h when constant capacitance values of (0.14 ± 0.08) were reached for the pH_e 7.2, 7.4 and 7.8. The error bars indicate that the cell reaction following an exposition to acidic L-15 medium was most heterogeneous, while the adhesion processes under physiological or alkaline environments were highly reproducible. Nevertheless, due to the accelerated cellular adhesion on the precoated electrodes, the precoating process was performed for all following experiments.

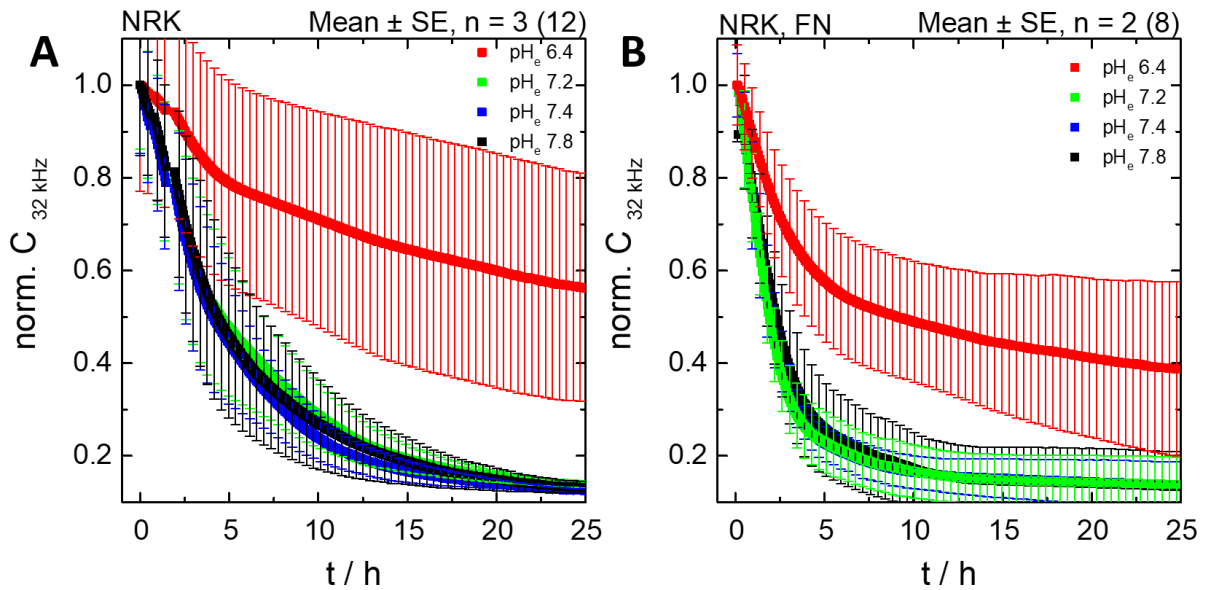


Fig. 5.2 Normalized capacitance signal of the ECIS™-based monitoring of the pH-dependent adhesion process of NRK cells on 8W10E arrays. **(A)** Adhesion process on uncoated and **(B)** on fibronectin-precoated working electrodes. Rate of the decrease of the capacitance signal, indicating the adhesion speed of the cells, is higher using precoated electrodes. Experiments were performed in at least two individual experiments in quadruplicate for each condition in a standard cell culture incubator at 37 °C and 0 % CO₂. Capacitance was normalized with respect to the value at t = 0 h. Averaged capacitance values of NRK cells at t = 0 h: pH_e 6.4: (57 ± 9) nF, pH_e 7.2: (57 ± 11) nF, pH_e 7.4: (57 ± 12) nF, pH_e 7.8: (59 ± 13) nF and NRK cells with previous FN coating: pH_e 6.4: (53 ± 2) nF, pH_e 7.2: (53 ± 2) nF, pH_e 7.4: (52 ± 2) nF, pH_e 7.8: (51 ± 3) nF.

The time courses of capacitance were used to calculate the AUC in the full time range between 0 h – 25 h and in order to determine the maximal slope (the fastest spreading rate) within the first 2 h of the experiment, the first derivative was calculated. A comparison of the data is shown in Fig. 5.3. The comparison was performed to check if the determination of the AUC or the slope of the curves contained more information about the adhesion process and to decide which protocol was suited best for following experiments.

The AUC indicates the rate of the adhesion process; low AUC values correlate with accelerated cellular adhesion. Integration of the capacitance time courses of the cells being exposed to an acidic environment resulted in AUCs of (18 ± 3) h and (13 ± 2) h without and with a previous coating step of the electrodes, respectively. A physiological and alkaline pH-adjusted medium revealed AUCs fluctuating between (7.1 ± 0.7) h at pH_e 7.4 and (7.7 ± 0.8) h at pH_e 7.2 in the case of the uncoated electrodes, while FN-coating led to faster adhesion since the AUC values were smaller and ranged between (5.5 ± 0.2) h at pH_e 7.2 and (5.8 ± 0.3) h at pH_e 7.8. These AUCs indicate a decrease of 22 % – 29 %. In contrast to the AUC values, the spreading rates rise for accelerated adhesion and spreading. The spreading rates revealed by the cells which were exposed to an acidic extracellular environment were relatively similar with (-7 ± 1) nF·h⁻¹ and (-8 ± 4) nF·h⁻¹ while physiological and alkaline buffers led to spreading rates of around -17 nF·h⁻¹ and -13 nF·h⁻¹ for FN-coated and uncoated substrates, respectively.

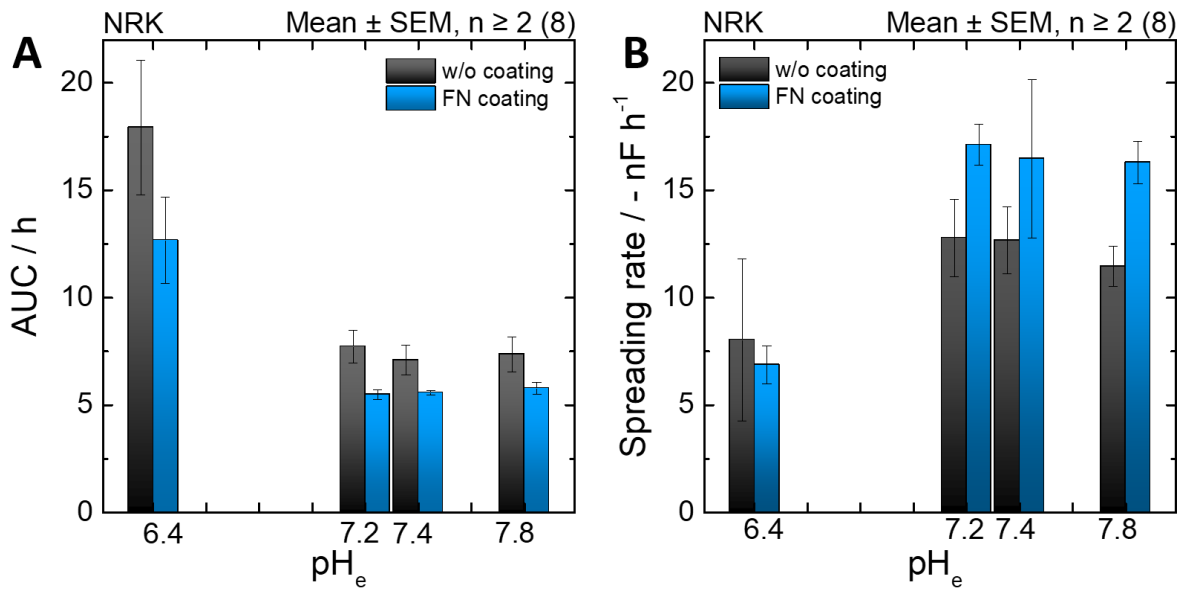


Fig. 5.3 Evaluation of the capacitance time courses (Fig. 5.2) from the examination of the adhesion processes of NRK cells in a pH-dependent manner. **(A)** Integration of the time courses in the time interval between 0 h and 25 h yielding the *area under the curve* (AUC) with an integration limit of $y = 0$ for bare and fibronectin-coated (FN) gold working electrodes of 8W10E arrays. Low AUC values correlate with fast adhesion. **(B)** Determination of the maximal spreading rate according to the maximum value of the first derivative determined within the first 2 h of the measurements. At least two independent experiments were performed. The experiments were conducted in a standard cell culture incubator at 37 °C and 0 % CO₂.

The observed trends of the pH-dependent adhesion of NRK cells were similar for both evaluation methods. Since the adhesion profiles of SK-MEL-28 and A549 cells were more complex as they revealed more than one slope, the AUC evaluation was chosen for the quantification of the pH-dependent adhesion of SK-MEL-28, SpiCa and A549 cells. Fig. 5.4 shows the pH-dependent adhesion behavior of the aforementioned cell lines, while the experimental protocol was similar to the adhesion investigations with NRK cells. Once again, 8W10E arrays were precoated with fibronectin to accelerate the adhesion process due to the recognition of the extracellular matrix molecules by the cells. The pH-adjusted L-15 media were additionally supplemented with 1 % FCS for the experiments performed with the SK-MEL-28 and the SpiCa cells as these cell types were cultured with higher FCS concentrations of 10 % and 20 %, respectively, in contrast to only 5 % FCS content in the culture medium of NRK and A549 cells (compare Tab. 3.1).

The SK-MEL-28 cell seeding process triggered an instant and drastic decrease of the capacitance, reaching a minimum after 1 h which already indicated a slight pH-dependency (see Fig. 5.4 A). The extracellular pH_e of 7.8 and 7.4 led to a drop in capacitance to around 0.6, while a pH_e of 7.2 and 6.4 revealed a less pronounced decrease to capacitance values of 0.65 and 0.69 after around 1 h. Following the initial dip, the capacitance values increased again up to 0.80 - 0.83 in normalized capacitance values with a subsequent decrease of all physiological and alkaline buffers, except for the cells being exposed to acidic L-15 medium which kept increasing. After 63 h of measurement time, the final normalized capacitance values resulted in (0.85 ± 0.03) , (0.78 ± 0.03) , (0.72 ± 0.02) and (0.68 ± 0.02) in the order of increasing extracellular pH_e.

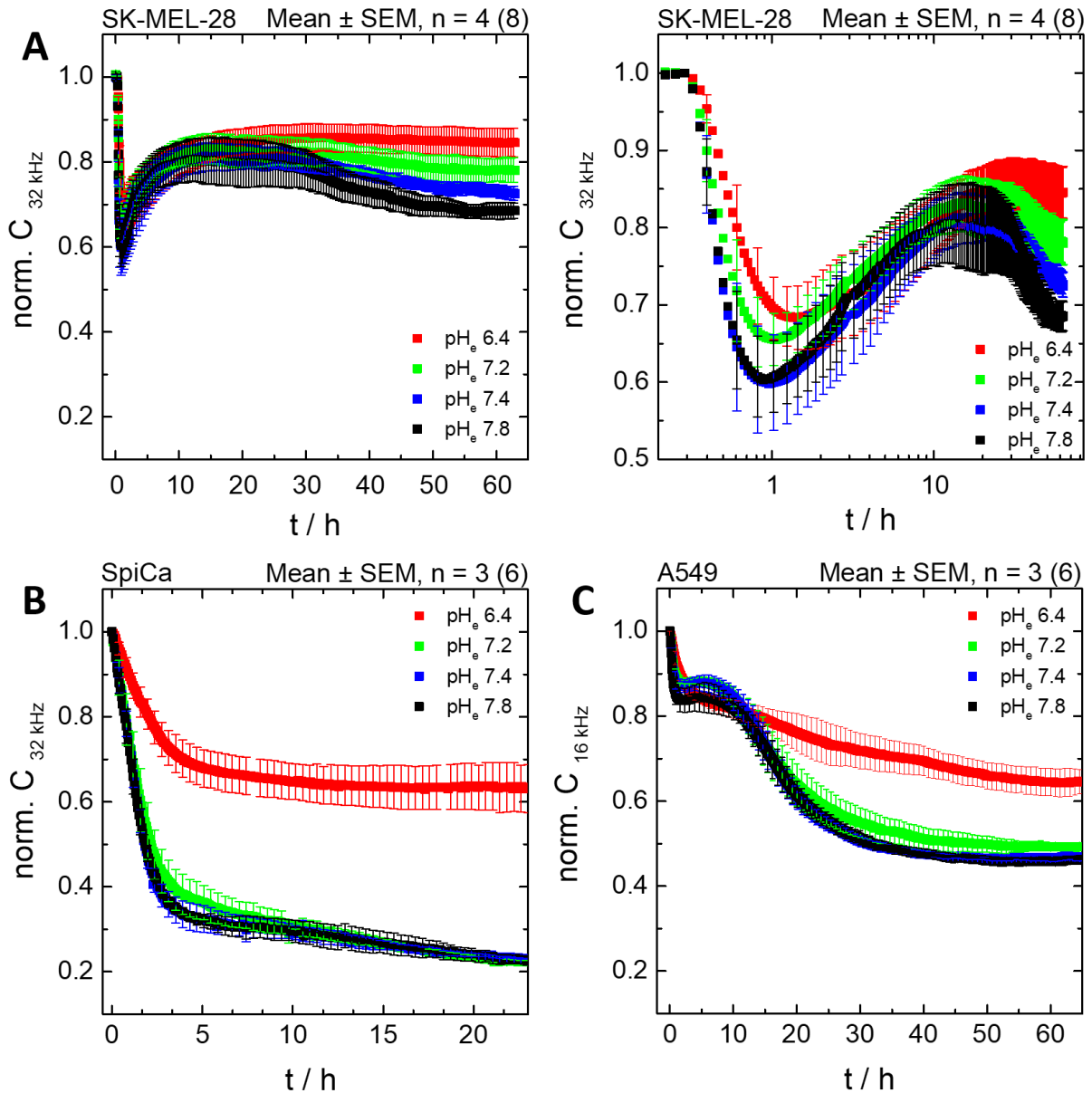


Fig. 5.4 Monitoring of the pH-dependent adhesion of three different cell lines in pH-adjusted L-15 medium on fibronectin-coated 8W10E ECIS™ arrays. **(A)** Adhesion behavior of SK-MEL-28 cells: normalized capacitance values are plotted as a function of time (left-hand side) and using a logarithmical scale of the x-axis on the right-hand side. **(B)** Monitoring of the SpiCa adhesion process under different extracellular pH_e and **(C)** pH-dependent adhesion monitoring using A549 cells. The capacitance is directly proportional to the degree of cell coverage and decreases with increasing coverage. Capacitance values were normalized with respect to the first value after the addition of L-15 medium which had previously been adjusted to four pH_e. Every cell line was examined in three individual experiments, each in duplicate. Data is shown as Mean ± SEM. Averaged initial capacitance values for SK-MEL-28 cells: pH_e 6.4: (50.9 ± 0.4) nF, pH_e 7.2: (49.1 ± 0.3) nF, pH_e 7.4: (52 ± 1) nF, pH_e 7.8: (49.6 ± 0.8) nF; SpiCa cells: pH_e 6.4: (49 ± 1) nF, pH_e 7.2: (50 ± 2) nF, pH_e 7.4: (48.1 ± 0.8) nF, pH_e 7.8: (49.0 ± 0.8) nF and A549 cells: pH_e 6.4: (35 ± 2) nF, pH_e 7.2: (28 ± 1) nF, pH_e 7.4: (26 ± 1) nF, pH_e 7.8: (25 ± 1) nF. Experiments were performed at T = 37 °C and 0 % CO₂.

In the case of SpiCa cells, the time-dependent capacitance values were quite similar to the time courses obtained for NRK cells (compare Fig. 5.2 and Fig. 5.4 B). Cell inoculation sparked a sharp decrease of the normalized capacitance within the first three hours, followed by a much slower and steadily decreasing capacitance resulting in normalized capacitance values of (0.64 ± 0.06), (0.22 ± 0.01), (0.23 ± 0.01) and (0.23 ± 0.01) in the order of increasing pH_e. Final capacitance values as well as the profile of the time courses

were identical under a pH_e of 7.2, 7.4 and 7.8 whereas cell adhesion in the acidic environment yielded a significantly less pronounced capacitance decrease.

The adhesion profile of A549 cells showed, similar to the SK-MEL-28 cells, a two-phasic decrease of the capacitance, reaching a minimum after 2 h (Fig. 5.4 C). Again, the adhesion process did not seem to be significantly different under the influence of an extracellular pH_e of 7.2, 7.4 and 7.8. Similar to the other cell lines under test, the adhesion process under acidic conditions was only partially inhibited or slowed down. The pH_e of 6.4 led to a final capacitance value of (0.64 ± 0.03) after 60 h whereas the cells adhering under more alkaline environments reached an average capacitance value of (0.47 ± 0.02) .

For further data analysis, the time courses of normalized capacitance were used to determine the *area under the curve* (AUC). Since the adhesion process for different cell types requires varying amounts of time, time intervals for the area integration were chosen accordingly. The area was integrated in a time interval between 0 h and 25 h for NRK and SpiCa cells, while the interval was expanded to an integration time of 50 h for A549 and SK-MEL-28 cells. Fig. 5.5 illustrates AUCs for the four cell lines under test as change in per cent with respect to the area of the control experiments in which cells were exposed to an extracellular pH_e of 7.4 and Tab. 5.1 summarizes the absolute calculated areas.

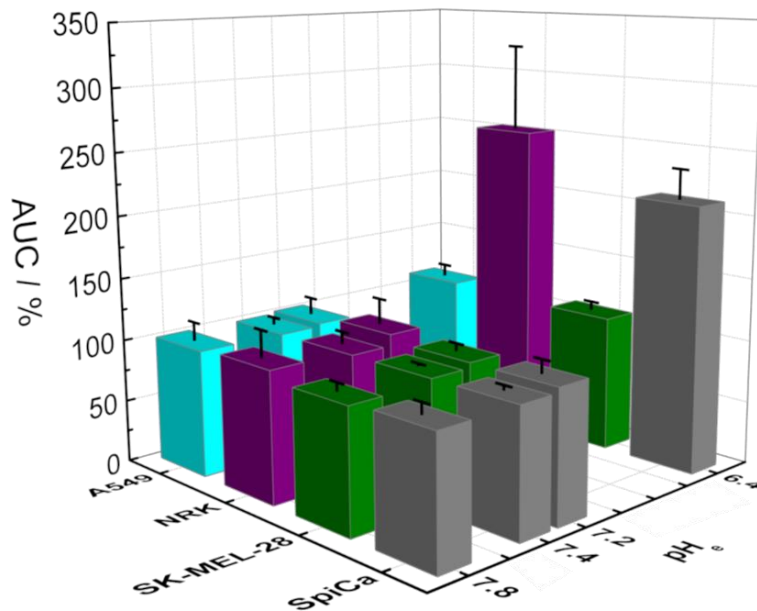


Fig. 5.5 Area under the curve (AUC) values normalized with respect to the calculated AUC of the ECISTM-based detected adhesion processes of the cells exposed to an extracellular pH_e of 7.4 (see Fig. 5.2 and Fig. 5.4). Higher bars indicate decreasing adhesion of the cells. Experiments were performed at $T = 37\text{ }^\circ\text{C}$ and $0\text{ }\%$ CO_2 .

Tab. 5.1 Summary of the calculated *area under the curve* (AUC) from the ECIS™-based detections of pH-dependent adhesion and spreading processes of four different cell lines (see Fig. 5.2, Fig. 5.4). Increasing AUCs indicate limited adhesion because increasing cell attachment is accompanied by decreasing capacitance values. Mean \pm SEM, n = 3 (6).

pH _e	A549	NRK	SK-MEL-28	SpiCa
	AUC / h			
6.4	36.5 \pm 0.8	18 \pm 3 / 13 \pm 3 (FN)	52 \pm 2	16 \pm 1
7.2	33 \pm 2	7.7 \pm 0.8 / 5.5 \pm 0.2 (FN)	50 \pm 2	8.0 \pm 0.5
7.4	33 \pm 2	7.1 \pm 0.7 / 5.6 \pm 0.1 (FN)	48 \pm 1	7.6 \pm 0.3
7.8	33 \pm 3	7.4 \pm 0.8 / 5.8 \pm 0.3 (FN)	57 \pm 2	7.6 \pm 0.4

All cell lines under test have in common that their adhesion and spreading behavior seemed neither to be disturbed, inhibited nor drastically accelerated by exposure to an extracellular pH_e of 7.2 and 7.8. AUCs were quite similar to the ones obtained for a pH_e of 7.4. An acidic environment, however, led to significantly different adhesion rates. NRK and SpiCa cells seemed to be the cell types affected the most by an acidic pH_e. AUCs increased by 154 % (132 % after FN precoating) and 111 % compared to the control experiment under the physiological pH_e of 7.4 for NRK and SpiCa cells, respectively. The increasing area resulted due to a less steep decrease in the normalized capacitance values, implying an impaired adhesion. A549 and SK-MEL-28 cells revealed only 11 % and 8 % smaller areas, respectively, in the presence of the acidic pH_e of 6.4.

5.2 PH-DEPENDENCY OF PROLIFERATION RATES

The examination of the cellular proliferation focuses on the pH-dependent rate of cell division. The cells were inoculated in subconfluent cell seeding densities into 8W10E+ arrays and 24-well plates. After the *standard pre-experiment protocol*, the cells were exposed to four different pH-adjusted L-15 solutions and the proliferation was observed by recording the capacitance and also via image-based microscopy using the 24-channel microscope zenCell owl.

The use of the zenCell owl, however, revealed one disadvantage. The software calculates the cell-covered area in the field of view, but the automatic recognition oftentimes was not precise enough, leading to incomplete cell coverage values although the cell monolayer was already confluent. The recognition accuracy was strongly cell line-dependent which is possibly due to differences in the contrast of the cell bodies. The process of subconfluent cell seeding sometimes entailed slightly inhomogeneous cell distributions resulting in areas with more and areas with fewer adherent cells. The initially inhomogeneous cell distribution in the field of view led to a varying cell coverage in the beginning of the measurements and thwarted the calculation of mean values for multiple experiments.

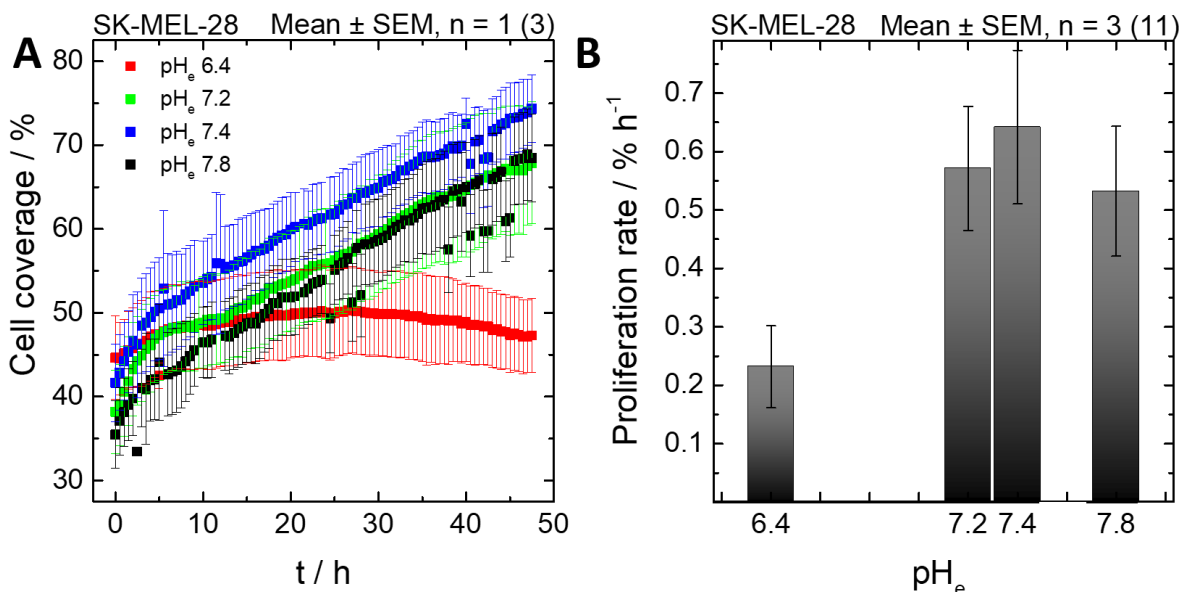


Fig. 5.6 Image-based detection of proliferation events of SK-MEL-28 cells with the 24-channel microscopic device zenCell owl. Cells were inoculated in subconfluent seeding density with $2 \cdot 10^4$ cells·cm⁻² 48 h prior to the experiment with a medium exchange 24 h after seeding. **(A)** Time-dependent degree of cell coverage in the field of view with cells being exposed to L-15 medium adjusted to four different extracellular pH_e. Exemplary data is shown for one experiment performed in triplicate for each condition. **(B)** Linear regressions of the time-resolved changes in cell coverage from three individual experiments and an elevenfold determination of each condition in total with the corresponding standard error of mean. All experiments were carried out at 37 °C and 0 % CO₂.

Fig. 5.6 depicts one experiment observing the pH-dependent proliferation of SK-MEL-28 cells during a time course of 48 h. In the measurement, initial cell coverage values between 35 % and 45 % could be seen. The cells exposed to an acidic environment were able to increase the cell coverage from around 44 % to 50 %

within 24 h, however, a subsequent decrease of the cell coverage was observed, resulting in $(47 \pm 4) \%$ after 48 h of recording. The cells in contact with higher pH_e values of 7.2, 7.4 and 7.8 were able to increase the cell coverage by 30 %, 33 % and 33 % ending up at 68 %, 75 % and 69 % cell coverage, respectively.

The time-resolved cell coverage curves were fitted linearly yielding the proliferation rate. All experimental data was evaluated this way before averaging (see Fig. 5.6 B). Steeper slopes indicate a higher proliferation rate and thus faster cell division. The proliferation rate increased with increasing pH_e from $(0.23 \pm 0.07) \% \cdot h^{-1}$ over $(0.57 \pm 0.1) \% \cdot h^{-1}$ and up to $(0.64 \pm 0.1) \% \cdot h^{-1}$ at a pH_e of 7.4. Increasing the pH_e even further to 7.8, representing alkaline extracellular conditions, led to a proliferation rate of $(0.53 \pm 0.1) \% \cdot h^{-1}$.

The image-based investigations of proliferation events were also performed using NRK, SpiCa and A549 cells. Every cell line was subjected to the four pH_e -adjusted L-15 media during proliferation in at least three independent experiments. All individually performed experiments can be seen in the supplementary information in Fig. 11.1 – Fig. 11.4. Fig. 5.7 summarizes the averaged pH-dependent proliferation rates for all of the four cell lines under test. A549 cells exhibited the most notable pH-dependency due to steadily increasing proliferation rates with increasing pH_e . Likewise, NRK and SpiCa cells showed a pH-dependent cell division but with the difference that the proliferation rates were equal for the cells being exposed to the two lowest pH_e and to the two highest pH_e in the case of NRK and SpiCa cells, respectively. As already discussed in Fig. 5.6, SK-MEL-28 cells revealed a slightly different pH-dependency. Cell division became faster with increasing pH_e up to a value of 7.4 but further increasing the pH_e led to a decreased proliferation rate. Tab. 5.2 summarizes all proliferation rates obtained from the investigations of the four cell lines and Fig. 5.7 depicts the proliferation rates with respect to the rate of the cells exposed to a pH_e of 7.4.

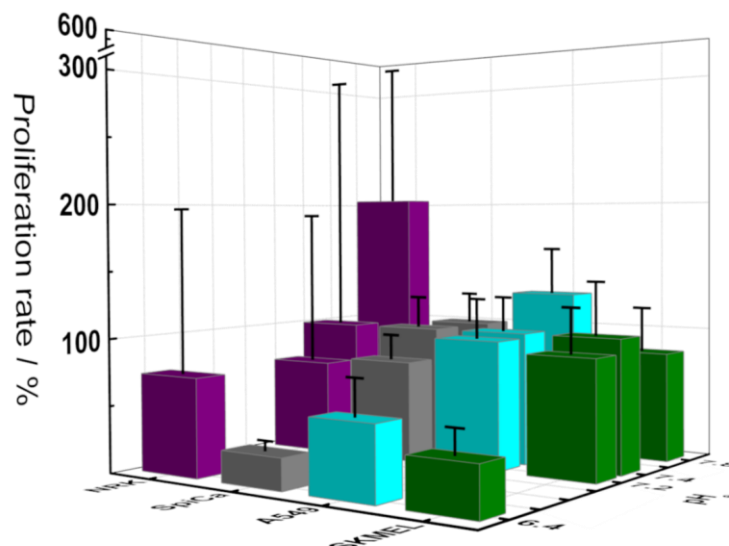


Fig. 5.7 Summary of proliferation rates normalized with respect to the results of the cells exposed to pH_e 7.4 from the image-based monitoring of the pH-dependent proliferation of four different cell lines (NRK cells – purple, SpiCa cells – grey, A549 cells – cyan and SK-MEL-28 cells – green) (compare Fig. 5.6, Fig. 11.1-11.4). Every cell line was tested in three independent experiments in triplicate for each condition. Higher bars indicate increasing proliferation and are depicted with the corresponding standard error. Experiments were performed at $T = 37 \text{ }^\circ\text{C}$ and $0 \text{ } \%$ CO_2 . Mean \pm SE, $n = 3$ (9).

Tab. 5.2 Summary of the calculated and averaged proliferation rates from the image-based investigations of pH-dependent proliferation of four different cell lines. Listed values are graphically depicted in Fig. 5.7 and Fig. 11.1-11.4. Increasing rates indicate faster proliferation. Mean \pm SE, n = 3 (9).

pH _e	NRK	SpiCa	A549	SK-MEL-28
	Proliferation rate / %·h ⁻¹ \pm SE			
6.4	0.11 \pm 0.08	0.07 \pm 0.01	0.3 \pm 0.1	0.23 \pm 0.07
7.2	0.11 \pm 0.07	0.23 \pm 0.03	0.46 \pm 0.08	0.6 \pm 0.1
7.4	0.2 \pm 0.2	0.30 \pm 0.04	0.48 \pm 0.06	0.6 \pm 0.1
7.8	0.3 \pm 0.2	0.30 \pm 0.04	0.60 \pm 0.09	0.5 \pm 0.1

The pH-dependent proliferation was additionally analyzed using the ECISTM technique as an independent experimental approach. For the ECISTM investigations, cells were also inoculated in subconfluent seeding densities onto 8W10E+ arrays. Following the *standard pre-experiment protocol*, the cells were exposed to L-15 medium adjusted to the same four pH_e values 48 h after cell seeding and the capacitance was recorded. Within this thesis, the cell proliferation of SK-MEL-28 and SpiCa cells was monitored. Proliferation of NRK and A549 cells was already monitored during the master's thesis (see chapter 5.6). Fig. 5.8 shows the recorded capacitance signal as a function of time at the most sensitive AC frequency of 32 kHz for both cell lines under the exposure to four different pH_e. Data represents the average time course of normalized capacitance for three individual experiments. Before averaging, the capacitance was normalized with respect to the first value after the start of the measurement.

The recording of the capacitance values of the SK-MEL-28 proliferation was started 48 h after cells had been seeded in a subconfluent amount. After the incubation with the different pH_e solutions at t = 0 h, the signal started to increase for the first 20 h to values of (1.12 \pm 0.04), (1.10 \pm 0.02), (1.12 \pm 0.02) and (1.08 \pm 0.02) in the order of increasing pH_e, and were followed by a decrease in normalized capacitance by 0.02, 0.07, 0.09 and 0.10 resulting in final capacitance values of (1.10 \pm 0.03), (1.03 \pm 0.02), (1.03 \pm 0.01) and (0.98 \pm 0.01). The total capacitance decrease after the initial increase implied that the cell division of SK-MEL-28 cells seemed to be at least partly dependent on the extracellular pH_e.

The SpiCa cells revealed quite similar proliferation rates under the influence of extracellular pH_e conditions of 7.2, 7.4 and 7.8. The corresponding capacitance time courses decreased in a similar way and reached a final normalized capacitance of around 0.41 after 90 h of measurement time. In contrast to these steadily decreasing capacitance signals, cells which were exposed to an acidic environment exhibited a constant increase of the capacitance and revealed final normalized capacitance values of (1.08 \pm 0.03).

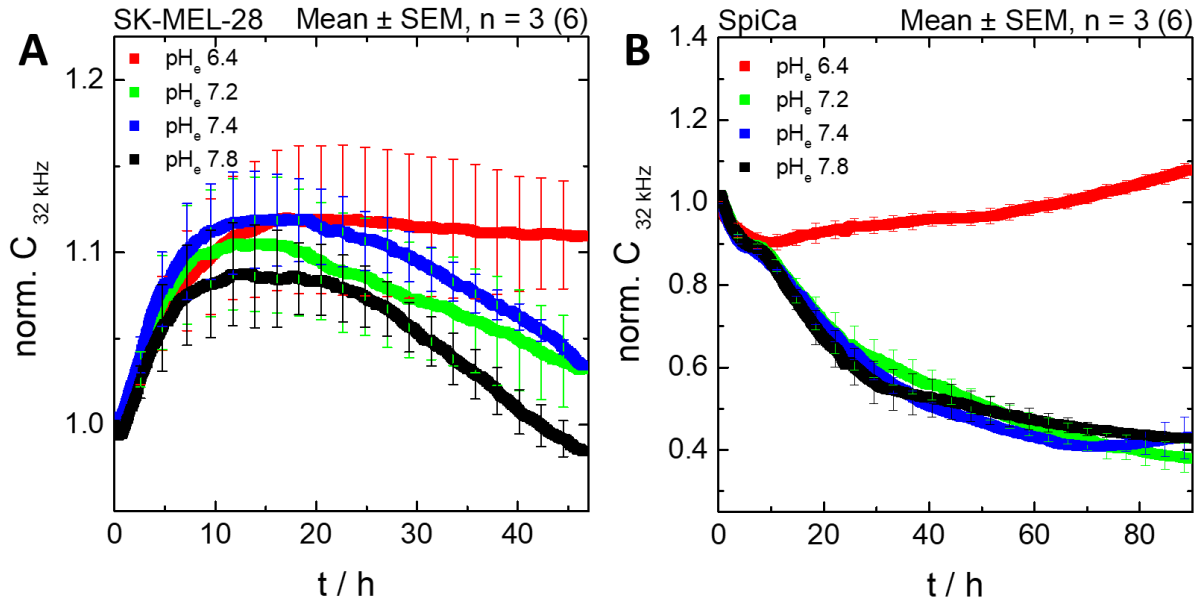


Fig. 5.8 ECIS™-based monitoring of pH-dependent proliferation for two different cell lines which were seeded in subconfluent cell densities with $2 \cdot 10^4$ cells·cm⁻² onto 8W10E+ arrays 48 h prior to the experiment. Proliferation of (A) SK-MEL-28 cells and (B) SpiCa cells exposed to L-15 medium adjusted to four different extracellular pH_e (+ 1 % FCS). Decreasing capacitance results from increasing cell coverage of the working electrodes. The averaged capacitance values were gained from three individual experiments, in which every pH_e condition was measured twice. Capacitance was normalized with respect to the first data point at t = 0 h after the pH-adjusted L-15 media were added. Averaged values are shown with the respective standard error of mean, while some error bars were omitted for clarity reasons. Capacitance was normalized to the value at t = 0 h. Averaged capacitance values before normalization at t = 0 h of SK-MEL-28 cells were: pH_e 6.4: (39.6 ± 0.8) nF, pH_e 7.2: (38 ± 2) nF, pH_e 7.4: (40 ± 2) nF, pH_e 7.8: (39 ± 1) nF; of SpiCa cells: pH_e 6.4: (41 ± 6) nF, pH_e 7.2: (42 ± 4) nF, pH_e 7.4: (44 ± 5) nF, pH_e 7.8: (40 ± 5) nF. Experiments were performed at T = 37 °C and 0 % CO₂.

The capacitance curves of every measurement were integrated to yield the AUC. Using the investigations with SK-MEL-28 cells, the AUC was determined in a time interval from 0 h to 45 h with an integration limit of 0.9 on the y-axis, while capacitance time courses revealed by SpiCa cells were integrated in an interval from 0 h to 90 h without an integration limit on the y-axis. AUCs were averaged for the same conditions and can be seen in Tab. 5.3. The smaller the area, the higher the proliferation rate due to the direct proportionality of the capacitance decrease to the degree of cell coverage on the working electrode. The calculated values already reflect a pH-dependency of the proliferation. Compared to a pH_e of 7.4, SK-MEL-28 cells showed a slightly elevated proliferation by 8 % and 19 % for pH_e values of 7.2 and 7.8, respectively. The acidic pH_e of 6.4 led to an inhibition of the proliferation events due to a 7 % increase of the calculated AUC values.

The rate of cell division of SpiCa cells seemed to be insignificantly different for pH_e values of 7.2, 7.4 and 7.8 while the acidic environment led to a, by 73 %, drastically increased area with respect to a pH_e of 7.4. The AUCs for NRK cells steadily decreased with increasing pH_e meaning an increase in the proliferation rates. A549, in contrast, exhibited quite similar AUCs of (62 ± 1) h and (59 ± 1) h for a pH_e of 6.4 and 7.8, respectively, but an increased area after exposure to a pH_e of 7.2. The increased area indicated a partly inhibited proliferation of A549 cells after exposure to an extracellular pH_e of 7.2.

Tab. 5.3 Summarized *area under the curve* (AUC) of four cell lines being exposed to different extracellular pH_e in L-15 medium while the proliferation was observed via ECIS™. Time courses of capacitance were integrated from 0 h – 45 h with an integration limit of 0.9 on the y-axis for SK-MEL-28 cells, from 0 h – 70 h for NRK* cells and from 0 h – 90 h for SpiCa and A549* cells without a y-axis integration limit. Decreasing areas indicate faster proliferation. Mean \pm SEM, n = 3 (6).

pH_e	SpiCa	SK-MEL-28	NRK*	A549*
	AUC \pm SEM / h			
6.4	88 \pm 2	9 \pm 2	69 \pm 1	62 \pm 1
7.2	52 \pm 4	8 \pm 1	51 \pm 3	71 \pm 2
7.4	50.6 \pm 0.4	8.5 \pm 0.7		
7.8	52 \pm 3	6.9 \pm 0.8	47 \pm 2	59 \pm 1

* Experiments were performed during my master's thesis at the University of Regensburg in 2016.

5.3 PH-DEPENDENCY OF WOUND HEALING BEHAVIOR

The migration of cells represents a phenotype which is highly cell-specific and dependent on extracellular conditions. To be able to investigate the cellular wound healing behavior, cells need to be grown to a confluent monolayer and a wound or cell-free area needs to be artificially created. To create such cell-free areas, different techniques were used in this thesis. On the one hand, there is the *scratch assay* in which cells are mechanically removed with the help of a pipet tip to create a linear cell-free area; on the other hand, short electrical pulses can be applied (a function integrated in the ECISTM technique), by which the cell membrane is permeabilized, resulting in cell death and hence creating a circular cell-free area in the dimensions of the working electrode.

The *scratch assay* was used in combination with the 24-channel microscopic zenCell owl device. The cells were grown to confluent monolayers and 48 h after seeding, including a medium exchange after 24 h, the cells were mechanically removed by scratching a pipet tip over the well bottom surface. After the wounding, mechanically removed as well as dead cells were washed away and the measurement was started subsequent to the addition of L-15 medium adjusted to four different pH_e . The scratch created a linear wound or cell-free area which was repopulated by the surrounding vital cells over time. Since the wounding was done manually, the wounds slightly differed in size and shape and consequently in the initial degree of cell coverage. The repopulation was then followed by an increasing degree of cell coverage in the field of view.

Fig. 5.9 displays microscopic images of the pH-dependent migration of SK-MEL-28 cells 1 h, 6 h, 12 h and 24 h after wounding. The black lines outline the borders of the initial wound size while the white lines highlight the advancing borders of the cell layer migrating into the cell-free area. The extracellular conditions of pH_e 6.4 and 7.2 led to an incomplete wound closure after 24 h, while further increased extracellular pH_e enhanced the wound closure rate of SK-MEL-28 cells. The cell-free area visibly decreased if one compares the images taken after 12 h of measurement time with the initially taken ones. At a pH_e of 6.4, only little migrational activity was observed while under the influence of a more physiological or alkaline environment after 12 h, there was only a very small cell-free area left. Images of the investigations of pH-dependent migration of A549, NRK and SpiCa cells can be seen in the supplementary part (Fig. 11.5 – Fig. 11.7). The time-resolved changes in cell coverage of the individual experiments of all cell lines are summarized in the supplementary part in Fig. 11.8 – Fig. 11.11.

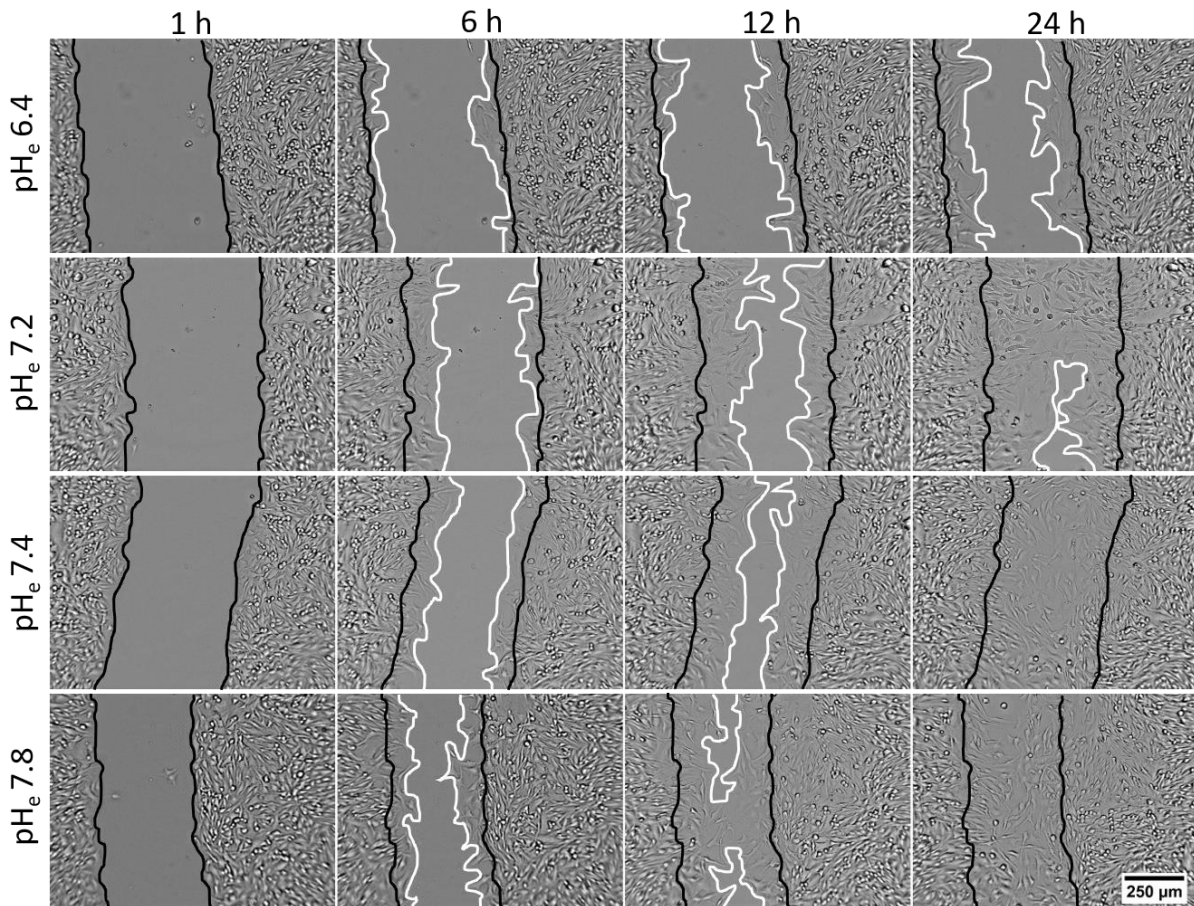


Fig. 5.9 Microscopic images with digital phase contrast of the pH-dependent migration of initially confluent SK-MEL-28 cells 1 h, 6 h, 12 h and 24 h after wounding. Migration was observed with L-15 as supernatant medium adjusted to four pH_e (6.4, 7.2, 7.4 and 7.8) at 37 °C and 0 % CO_2 . Black lines mark the borders of the original cell-free area of the wound at $t = 0$ h. White lines highlight the progressing border of the cell layer closing the cell-free area. Scale bar depicts 250 μm .

The corresponding change of the cell coverage as a function of time following the pH-dependent migration of SK-MEL-28 cells is shown in Fig. 5.10. The starting values, representing the initial wound sizes, differed between cell coverage values of $(54 \pm 3) \%$ for pH_e 7.2 and $(66 \pm 3) \%$ for pH_e 7.8. The cells exposed to an alkaline environment needed 17 h to close the created wound completely. With increasing acidity, the wound closure turned out to be increasingly incomplete resulting in $(99 \pm 1) \%$, $(90 \pm 6) \%$ and $(71 \pm 2) \%$ cell coverage under a pH_e of 7.4, 7.2 and 6.4 after 24 h. As the different starting values could be misleading, the time courses were fitted linearly from the very beginning to the point 100 % cell coverage was reached (Fig. 5.10, pH_e 7.8). The corresponding time interval was used to fit all data sets linearly even though 100 % of cell coverage was not reached in the other cases. Repopulation of the cell-free areas was determined in three independent investigations with an at least sevenfold determination in total. Results were averaged and are depicted in Fig. 5.10 B. The migration rate rose from $(1.1 \pm 0.3) \% \cdot h^{-1}$, over $(1.8 \pm 0.3) \% \cdot h^{-1}$ to $(2.2 \pm 0.2) \% \cdot h^{-1}$ in the order of increasing pH_e from 6.4 to 7.4. The most alkaline extracellular milieu caused a decrease in the migration rate to $(2.0 \pm 0.3) \% \cdot h^{-1}$. Tab. 5.4 lists all migration rates for the four cell lines (A549, SpiCa, SK-MEL-28 and NRK cells) under the four different pH_e .

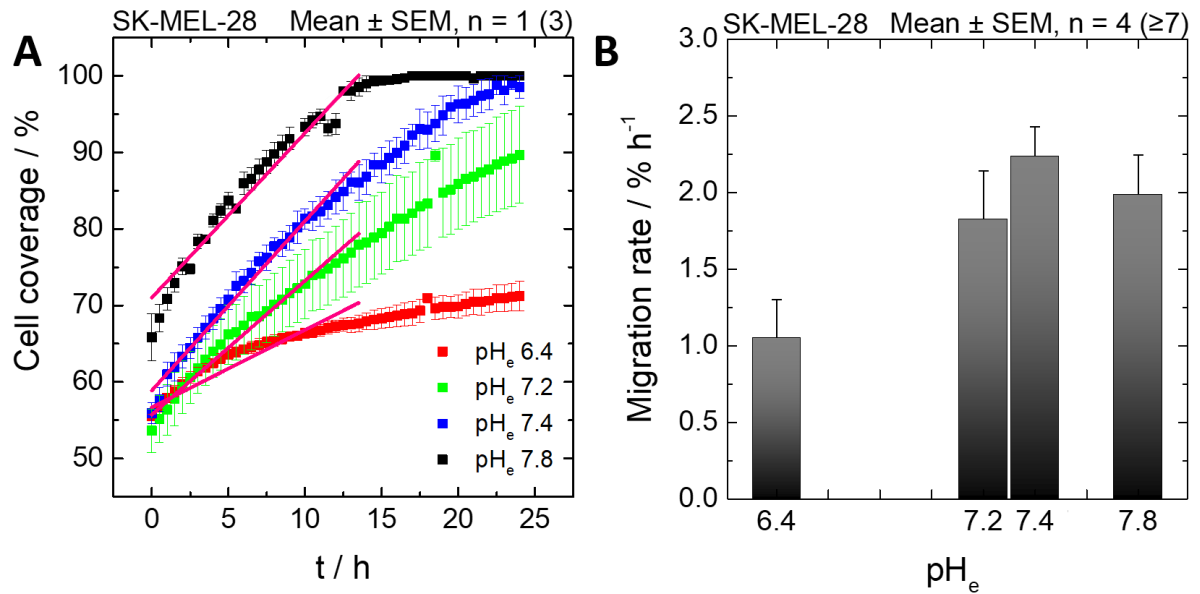


Fig. 5.10 Image-based monitoring of the migration behavior of SK-MEL-28 cells using the 24-channel microscopic device zenCell owl. (A) The degree of cell coverage in the field of view is plotted against the time following the migration of cells being exposed to L-15 adjusted to four different extracellular pH_e . One exemplary experiment in triplicate is shown with the corresponding linear regression (depicted in purple) in the time interval from $t = 0$ h until a cell coverage of 100 % was reached for one condition. Increasing cell coverage is caused by progressing wound closure. (B) Determined linear regression values (migration rates) for the time-dependent changes in cell coverage. Four individual experiments with an at least sevenfold determination of each condition in total were averaged and are depicted with the corresponding standard error of mean. All experiments were carried out in a standard cell culture incubator at 37 °C and 0 % CO_2 .

Tab. 5.4 Summary of the averaged migration rates from the microscopy-based investigation of pH-dependent migration of four different cell lines (compare Fig. 5.10, Fig. 11.5-11.11). Higher rates indicate increasing migration rates. Mean \pm SE, $n \geq 3$ (≥ 7).

pH_e	A549	SpiCa	SK-MEL-28	NRK
	Migration rate / $\% \cdot \text{h}^{-1} \pm \text{SE}$			
6.4	0.26 ± 0.06	0.19 ± 0.03	1.1 ± 0.3	0.7 ± 0.1
7.2	0.44 ± 0.07	0.55 ± 0.04	1.8 ± 0.3	1.6 ± 0.2
7.4	0.44 ± 0.06	0.62 ± 0.04	2.2 ± 0.2	1.9 ± 0.2
7.8	0.37 ± 0.07	0.62 ± 0.06	2.0 ± 0.3	2.8 ± 0.2

The most notable differences in the migration rates were observed for NRK and SK-MEL-28 cells while the strictest pH-dependency of the migration behavior was observed for NRK and SpiCa cells. The migration rate grew from $(0.7 \pm 0.1) \% \cdot \text{h}^{-1}$ to $(2.8 \pm 0.2) \% \cdot \text{h}^{-1}$ for NRK cells and from $(0.19 \pm 0.03) \% \cdot \text{h}^{-1}$ to $(0.62 \pm 0.06) \% \cdot \text{h}^{-1}$ for SpiCa cells with increasing pH_e from 6.4 to 7.8.

The wound healing behavior of A549 and SK-MEL-28 cells, in contrast, seemed to be disturbed under the influence of an acidic as well as an alkaline environment. Their migration rates increased from $(0.26 \pm 0.06) \% \cdot \text{h}^{-1}$ to $(0.44 \pm 0.06) \% \cdot \text{h}^{-1}$ and from $(1.1 \pm 0.3) \% \cdot \text{h}^{-1}$ to $(2.2 \pm 0.2) \% \cdot \text{h}^{-1}$ for a pH_e from 6.4 to 7.4 in the case of A549 and SK-MEL-28 cells, respectively. The increase was then followed by a decline to migration velocities of $(0.37 \pm 0.07) \% \cdot \text{h}^{-1}$ and $(2.0 \pm 0.3) \% \cdot \text{h}^{-1}$ for the most alkaline extracellular milieu.

Fig. 5.11 depicts the migration rates which were normalized with respect to the physiological pH_e of 7.4 and, in the case of NRK cells, led to an almost linear pH-dependency within the pH_e range.

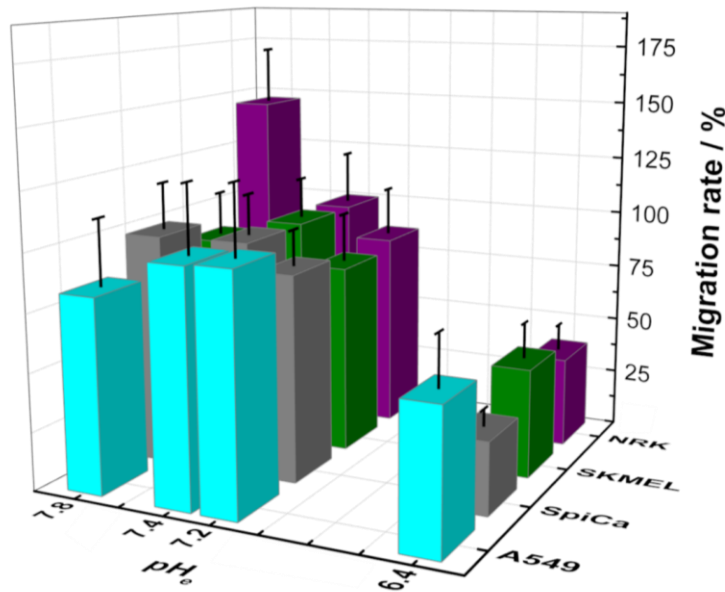


Fig. 5.11 Summarized migration rates which were normalized with respect to the results gained for the cells exposed to a physiological pH_e of 7.4 (compare Fig. 5.10, Fig. 11.5-11.11). Data was obtained from the image-based detection of the pH-dependent migration of four different cell lines exposed to four pH_e . Every cell line was tested in at least three independent experiments and a sevenfold determination of every condition in total. Higher bars indicate faster migration. Bars are depicted with the corresponding standard error. Experiments were performed at 37 °C and 0 % CO_2 with pH-adjusted L-15 medium as supernatant.

The second wounding technique relied on the application of electrical pulses resulting in cell death of the ones grown on top of the working electrodes of 8W1E ECIS™ arrays (see chapter 3.3.4.3). This technique was used to monitor the pH-dependent wound healing behavior of SK-MEL-28 and SpiCa cells. The protocol between the two cell lines differed with respect to the time point of the pulse application. SK-MEL-28 cells were wounded 7 h after the addition of L-15 medium which was previously adjusted to the respective pH_e (compare chapter 3.3.4.3), while SpiCa cells had 24 h to adapt their metabolism to the pH_e values in accordance with the protocol from the master's thesis in which NRK and A549 cells have already been tested (2016, Lisa Sauer under the supervision of Prof. Dr. Joachim Wegener, University of Regensburg).

Fig. 5.12 A compiles the time-dependent impedance magnitudes at the most sensitive frequencies of 32 kHz and 16 kHz recorded for confluent SK-MEL-28 and SpiCa cell layers under the influence of four different extracellular pH_e . Data represents the mean time course of at least three individual experiments where the impedance magnitude was normalized with respect to the last impedance value before the wounding occurred. Following the wounding, the impedance signal dropped to IZI values of the cell-free electrode followed by a recovery of the impedance magnitude after a cell line- and pH-dependent lag phase. SK-MEL-28 cells revealed slightly fluctuating impedance values prior to wounding, which in turn led to different

normalized IZI values for the cell-free conditions of (0.69 ± 0.04) , (0.59 ± 0.04) , (0.58 ± 0.05) and (0.76 ± 0.03) after the pulse application in the order of increasing pH_e . After 50 h of data recording, the acidic environment led to minimally different impedance values of (0.71 ± 0.04) while the most alkaline condition caused the highest change in normalized impedance to a final value of (1.1 ± 0.1) which is similar to the IZI value of the cell-covered electrode. Thus, at a pH_e of 7.8, a complete wound closure was observed due to cellular migration of the surrounding vital cells reclaiming the area of the wound. The cells exposed to pH_e of 7.2 and 7.4 exhibited very similar normalized impedance time courses, reaching a final normalized impedance value of around 0.84 which signifies incomplete wound closure after 50 h of measurement time.

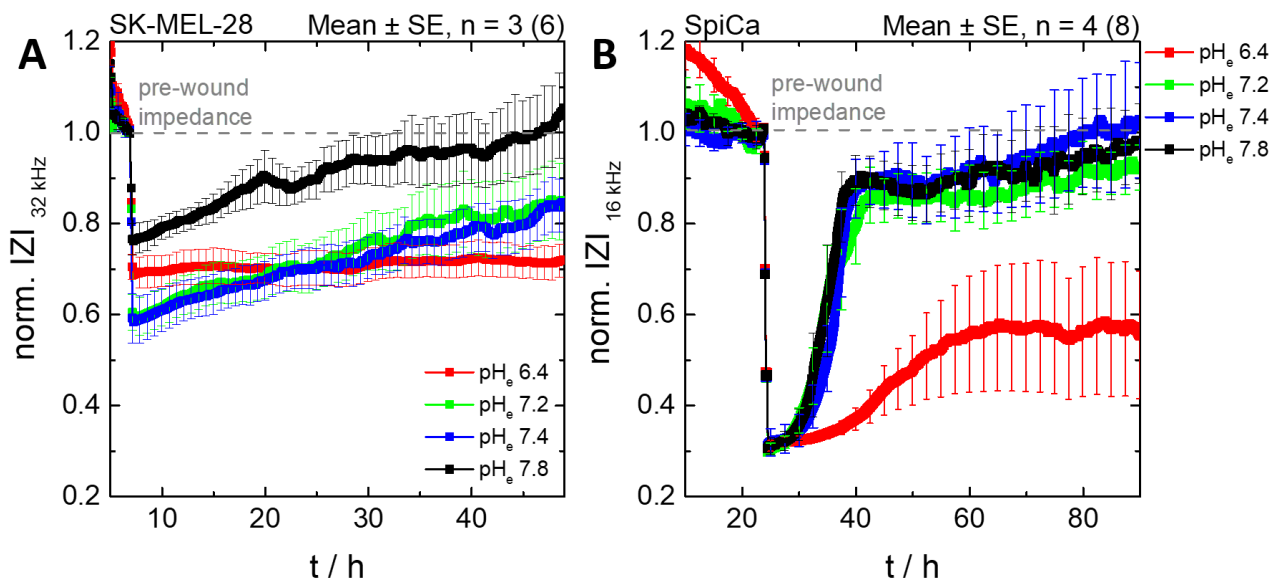


Fig. 5.12 ECIS™-based analysis of the pH-dependent migration at the most sensitive frequency of two different cell lines grown to confluence on 8W1E arrays. The sharp drop in impedance is caused by the application of an electrical wounding pulse (32 kHz, 2400 μA for 30 s) inducing irreversible membrane permeabilization resulting in cell death. The subsequent increase in impedance occurred due to the migration of still vital cells from the periphery of the electrode into the cell-free area. **(A)** Migration of SK-MEL-28 cells exposed to four different extracellular pH_e in L-15 medium (supplemented with 1 % FCS) recorded for a time period of 50 h. **(B)** Time-resolved impedance magnitude of SpiCa cells during the pH-dependent wound healing in L-15 medium (supplemented with 1 % FCS). The depicted averaged impedance values were gained from three and four independent experiments in which every pH_e condition was measured twice and data is given with the respective standard error of mean. Some error bars were omitted for clarity reasons. Impedance was normalized to the IZI value before wounding ($t_{\text{SK-MEL-28}} = 7$ h, $t_{\text{SpiCa}} = 24$ h, compare chapter 3.3.4.3). Averaged impedance values prior to the wounding were: SK-MEL-28 cells: pH 6.4: (2.3 ± 0.2) k Ω , pH 7.2: (3.1 ± 0.5) k Ω , pH 7.4: (2.8 ± 0.5) k Ω , pH 7.8: (2.4 ± 0.5) k Ω and SpiCa cells: pH 6.4: (9.0 ± 1.2) k Ω , pH 7.2: (9.4 ± 1.2) k Ω , pH 7.4: (9.2 ± 1.8) k Ω , pH 7.8: (9.3 ± 1.4) k Ω . $T = 37$ °C, 0 % CO_2 .

In contrast to the SK-MEL-28 cells, the SpiCa cells displayed a significantly faster migration behavior according to the ECIS™ technique (Fig. 5.12 B). After the application of the pulse, the impedance reproducibly dropped to normalized impedance values of 0.3 - representing impedance values of the cell-free electrodes - followed by a rapid recovery of the impedance to pre-wounding values in the case of physiological and alkaline environments. A complete wound closure was achieved 16 h after pulse application as indicated by the impedance recovery. The acidic medium however, led to a delayed and generally weaker increase of the

impedance resulting in normalized IZI values of (0.6 ± 0.1) , suggesting only partial wound closure due to inhibited migration events.

The individually recorded, time-resolved impedance curves were used to determine the AUC. The calculated AUCs constitute a way of transforming an entire time course into one single integrating parameter for an easier comparison. Fig. 5.13 shows the AUCs which were normalized with respect to the cellular response of cells being exposed to a pH_e of 7.4. In the case of the SK-MEL-28 cells, the AUC values showed a similar migration behavior at a pH_e of 7.4 and 6.4, while the migration rate was increased by around 7 % for a pH_e of 7.2 and even by 62 % for a pH_e of 7.8 with respect to the physiological pH_e .

The SpiCa cells being exposed to different extracellular pH_e displayed only minor differences of around 5 % for $\text{pH}_e \geq 7.2$ with an averaged area of around 54 h, but a significantly decreased AUC of (31 ± 10) h for the cells being exposed to a pH_e of 6.4. At this pH_e , the averaged area was 44 % smaller than the area obtained for a pH_e of 7.4. NRK and A549 cells also revealed quite similar AUCs for $\text{pH}_e \geq 7.2$ with minor fluctuations of around 5 % while an acidic environment lowered the averaged area from approximately 11 h and 78 h to (9 ± 1) h and (57 ± 3) h, respectively. Tab. 5.5 summarizes all absolute AUCs for all four cell lines from the observation of their pH-dependent migration behavior.

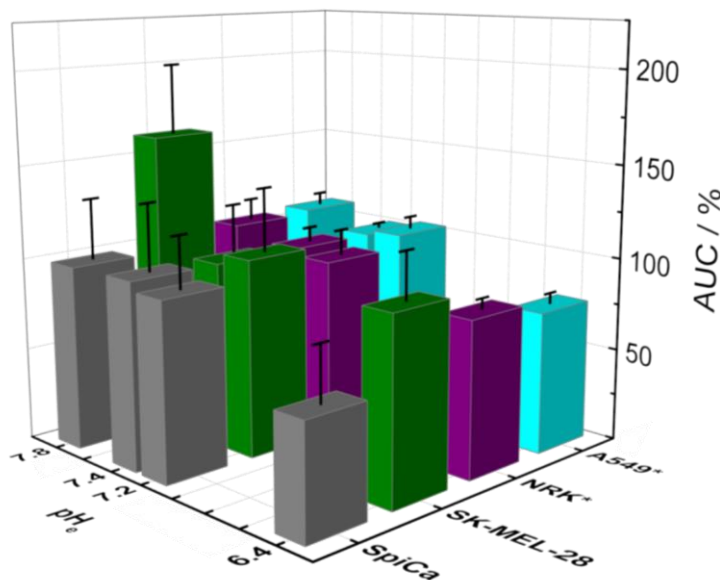


Fig. 5.13 Summarized *area under the curve* (AUC) for the ECISTM-based migration assays (compare Fig. 5.12). Data was normalized with respect to the signal of cells being exposed to a physiological pH_e of 7.4. Results for A549 and NRK cells were obtained during my master's thesis at the University of Regensburg in 2016 (*). Higher bars indicate faster migration and are depicted with the corresponding standard error of mean. Experiments were performed at 37 °C and 0 % CO_2 .

Tab. 5.5 Summarized *area under the curve* (AUC) values for the ECIS™-based monitoring of the migration of SpiCa, SK-MEL-28, NRK* and A549* cells which were exposed to L-15 medium previously adjusted to different extracellular pH_e (compare Fig. 5.12). Time courses of impedance were integrated from 7 h – 50 h with a y-axis integration limit of 0.5 for SK-MEL-28 cells and from 24 h – 90 h with no y-axis integration limit for SpiCa cells (compare chapter 3.3.4.3). A higher AUC value indicates a faster migration. Mean ± SEM, n ≥ 3 (≥ 6).

pH _e	SpiCa	SK-MEL-28	NRK*	A549*
	AUC / h			
6.4	31 ± 10	13 ± 2	9 ± 1	57 ± 3
7.2	52 ± 6	14 ± 3	10.5 ± 0.7	77 ± 9
7.4	55 ± 10	13 ± 2	10.9 ± 0.9	75 ± 2
7.8	54 ± 8	21 ± 2	11.5 ± 0.4	81 ± 3

* Experiments were performed during my master's thesis at the University of Regensburg in 2016.

5.4 PH-DEPENDENCY OF CELLULAR MICROMOTION

The cellular micromotion of confluent cell monolayers allows to draw conclusions about the viability of the cells. The *rapid time collection* (RTC) mode of the ECIS™ technique offers the possibility to quantify these cellular micromotions. Cells were grown to confluence on 8W1E arrays and after the *standard pre-experiment protocol* and a 24-h incubation with L-15 medium adjusted to four different pH_e , the cellular micromotions were monitored for 10 min with five samples per second.

The calculated variance values (see chapter 3.3.4.4) were normalized with respect to the variance displayed by cells which were exposed to a pH_e of 7.4. The variance was afterwards averaged and is depicted with the corresponding standard error in Fig. 5.14.

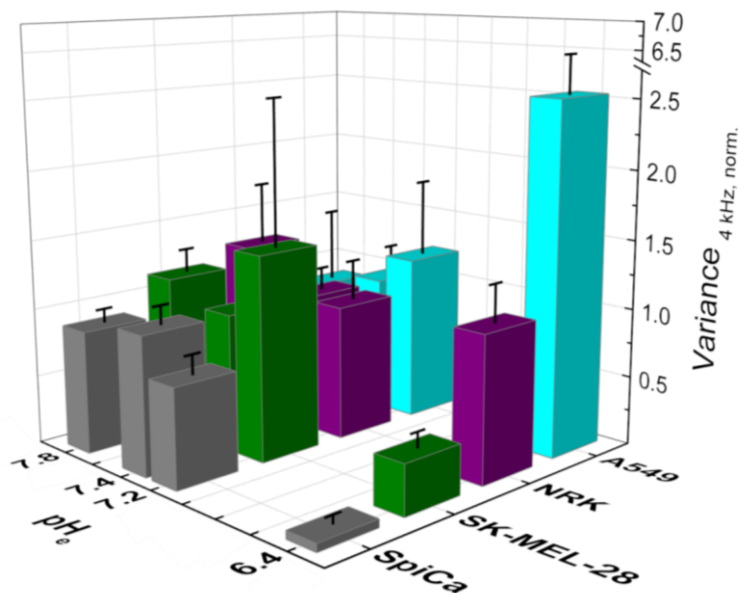


Fig. 5.14 Detection of the cellular micromotion by recording the impedance magnitude at 4 kHz in a time resolution of five samples per second. From the impedance magnitude, the variance was calculated and normalized with respect to a pH_e of 7.4. Subsequently, the data for each distinct pH_e and the respective cell line was averaged. Extracellular pH_e was adjusted in L-15 medium. Higher variance indicates increased cellular micromotion. The experiments were performed at 37 °C and 0 % CO_2 . Mean \pm SE, $n \geq 2$ (see Tab. 5.6).

The cellular micromotions of the cell lines in question - SpiCa, SK-MEL-28, NRK and A549 - were very different following the treatment with an acidic L-15 medium. Cellular micromotion was nearly completely suppressed in SpiCa cells showing (0.1 ± 0.4) normalized variance values in contrast to drastically elevated movements by A549 cells with a norm. variance value of (2.5 ± 4) . The cellular movement in the case of NRK and A549 cells seemed to be only weakly pH-dependent for the normal cells but much more pronounced for the lung cancer cells. While the NRK micromotion and hence the variance only weakly increased from 1.0 to (1.3 ± 0.5) under increasing pH_e up to 7.8, A549 showed an inverted dependency according to decreasing cellular

movements displayed in decreasing variance values from (2.5 ± 4) to (0.9 ± 0.6) under pH_e from 6.4 to 7.8. The cellular movement of SpiCa cells entailed increasing variance values from (0.1 ± 0.4) to (1 ± 0.1) under increasing pH_e from 6.4 to 7.4 followed by a slight decrease in the normalized variance to (0.9 ± 0.1) under alkaline conditions (pH_e 7.8). Cellular micromotion exhibited by SK-MEL-28 cells was slightly more active under extracellular pH_e conditions of 7.2 and 7.8 as mirrored by variance values of (1.5 ± 1) and (1.1 ± 0.2) , respectively. An acidic environment, on the contrary, decreased cellular movement to variance values of (0.4 ± 0.2) with respect to physiological conditions at a pH_e of 7.4 at (1.0 ± 0.4) . Tab. 5.6 summarizes all normalized and averaged variance values.

Tab. 5.6 Normalized variance values of the magnitude of impedance at 4 kHz which was recorded in the ECISTM-based micromotion measurement to monitor cellular movement of various cell lines under the influence of L-15 medium adjusted to four different extracellular pH_e . Cells were grown to confluence on 8W1E arrays 48 h prior to the experiments and after a 24-h incubation period with the pH-adjusted L-15 solution, micromotion was monitored at 37 °C and 0 % CO_2 .

pH_e	SpiCa Mean \pm SE, n = 2 (\geq 3)	SK-MEL-28 Mean \pm SE, n = 2 (4)	NRK Mean \pm SE, n = 5 (10)	A549 Mean \pm SE, n = 5 (\geq 9)
6.4	0.1 ± 0.4	0.4 ± 0.1	1.0 ± 0.3	2.5 ± 4
7.2	0.7 ± 0.2	1.5 ± 1	1.0 ± 0.3	1.2 ± 0.6
7.4	1.0 ± 0.1	1.0 ± 0.4	1.0 ± 0.2	1.0 ± 0.2
7.8	0.9 ± 0.1	1.1 ± 0.2	1.3 ± 0.5	0.9 ± 0.6

5.5 PH-DEPENDENCY OF THE RESPIRATORY ACTIVITY

5.5.1 EXPERIMENTS WITH 2D CELL MONOLAYERS

The pH-dependent cellular respiration was investigated using NRK, A549, SK-MEL-28 and SpiCa cells. The cells were grown to confluence on top of the oxygen-sensitive sensor foil. After the *standard pre-experiment protocol*, the cell culture medium was exchanged for L-15 medium adjusted to four different pH_e , the petri dishes were filled completely, sealed airtight and the measurement was started. Since all the previous protocols for the studies of pH-dependencies included 24 h of preincubation with the pH-adjusted solutions, the cellular respiration in this chapter was investigated with and without preincubation. Fig. 5.15 shows the averaged time-dependent changes of the oxygen partial pressure for both assays.

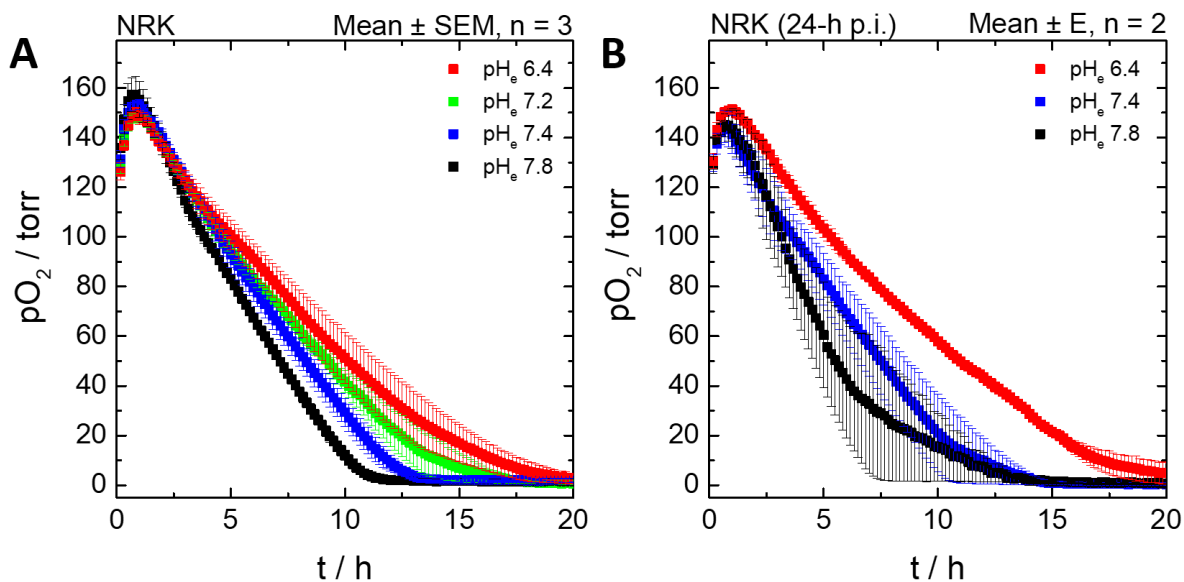


Fig. 5.15 Sensing of the pH-dependent respiration of confluent NRK cells. Changes in oxygen partial pressure are plotted as a function of time. **(A)** Start of measurement directly after the medium was exchanged against L-15 medium adjusted to four pH_e values. **(B)** 24-h preincubation (p.i.) with pH-adjusted L-15 medium before the measurement was started. Experiments were performed at $T = 37^\circ\text{C}$ and 0% CO_2 .

The oxygen partial pressure increased within the first hour to values of around 150 torr, caused by temperature effects due to the inevitable cooling of the sample during the preparation of the petri dishes. The ensuing decrease was dependent on the cellular respiration and the rate of oxygen consumption. The cells exposed to the most alkaline pH_e needed around 12 h to consume the available oxygen completely. Decreasing pH_e led to extended time periods of 13.5 h, 17 h and 21 h until 0% oxygen concentration levels were reached. A preincubation with the respective pH-adjusted L-15 medium for 24 h was almost indistinguishable from the respiration of NRK cells without preincubation. Alkaline and physiological conditions caused a complete oxygen consumption within 14.5 h and the process was completed within 20 h in the case of the cells in an acidic environment. To be able to adequately compare the time-resolved changes in pO_2 , the curves were fitted linearly in the time interval between 1 h and 4 h resulting in the *apparent*

oxygen consumption rate (AOCR). The AOCR values confirmed the increased cellular respiration from (13 ± 1) torr·h⁻¹ to (20 ± 3) torr·h⁻¹ under increasing pHe values and verified that measurements with and without a preincubation led to similar oxygen consumption rates (see Tab. 5.7).

Tab. 5.7 Summary of the *apparent oxygen consumption rates* (AOCRs) obtained from the linear regression of the pO₂ time courses (compare Fig. 5.15) as well as calculated *oxygen consumption rates* (OCRs) (compare chapter 3.4.5). NRK cells were exposed to L-15 medium which was previously adjusted to four different pHe. Mean ± SEM, n ≥ 2.

pHe	NRK		NRK (24-h preincubation)	
	AOCR / torr·h ⁻¹	OCR / amol·s ⁻¹ ·cell ⁻¹	AOCR / torr·h ⁻¹	OCR / amol·s ⁻¹ ·cell ⁻¹
6.4	13 ± 1	21 ± 2	12.8 ± 0.9	20 ± 1
7.2	14.3 ± 0.7	22 ± 1		
7.4	15 ± 1	24 ± 1	15.1 ± 0.6	24 ± 1
7.8	20 ± 3	32 ± 5	23 ± 3	35 ± 4

One aim was to compare cellular phenotypes of healthy and cancerous cell lines under the influence of different pHe values. Therefore, the pH-dependent respiratory activity of A549, SK-MEL-28 and SpiCa cells was also investigated. The confluent cell lines in general required different amounts of time to respire the available oxygen (A549 around 4.5 h, SK-MEL-28 approx. 8 h and SpiCa as long as 20 h, compare Fig. 5.16).

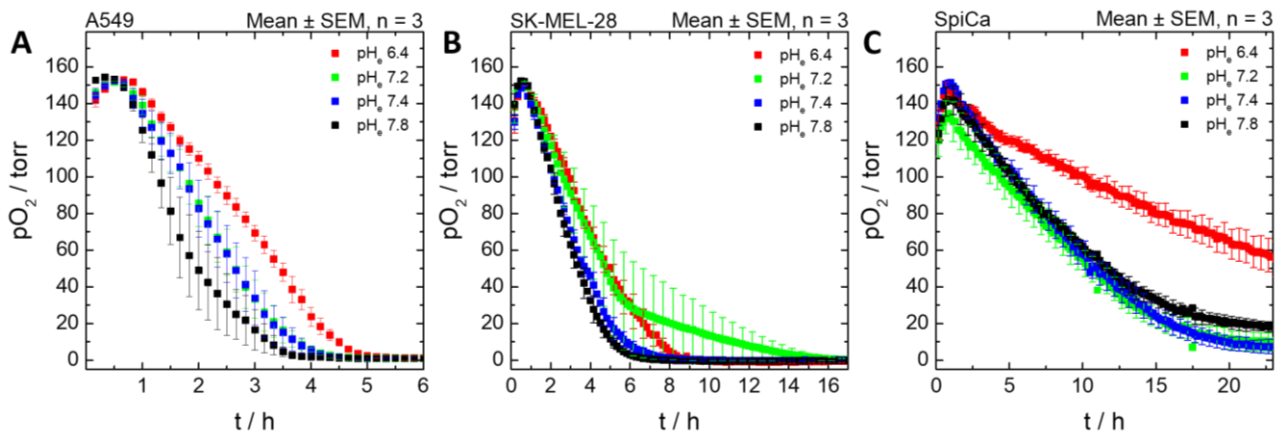


Fig. 5.16 Sensing of the pH-dependent respiration of (A) A549, (B) SK-MEL-28 and (C) SpiCa cells via the measurement of changes in the oxygen partial pressure (pO₂) which were plotted against the time. Data recording was started directly after the cell culture medium was exchanged against L-15 medium adjusted to four pHe. Every cell line was investigated in three independent experiments in a standard cell culture incubator at 37 °C and 0 % CO₂.

A549 and SpiCa cells revealed similar pH-dependent trends. Their respiratory activity generally increased with rising pHe but showed similar consumption rates under the influence of pHe of 7.2 and 7.4 of around 63 amol·s⁻¹·cell⁻¹ (A549 cells) and 19.5 amol·s⁻¹·cell⁻¹ (SpiCa cells). In contrast to A549 and SpiCa cells, SK-MEL-28 cells showed quite similar respiratory activities when exposed to pHe values of 6.4 and 7.2 with (101 ± 8) amol·s⁻¹·cell⁻¹ and (99 ± 23) amol·s⁻¹·cell⁻¹, but also showed increasing respiration under the highest pHe of (128 ± 18) amol·s⁻¹·cell⁻¹. Tab. 5.8 summarizes the corresponding AOCR and OCR values.

Tab. 5.8 Summary of the *apparent oxygen consumption rates* (AOCRs) from the linear regression of the pO_2 time courses (compare Fig. 5.16) and the corresponding *oxygen consumption rates* (OCRs) (compare chapter 3.4.5) of A549, SK-MEL-28 and SpiCa cells exposed to four different pH_e . Mean \pm SEM, $n = 3$.

pH_e	A549		SK-MEL-28		SpiCa	
	AOCR / $\text{torr}\cdot\text{h}^{-1}$	OCR / $\text{amol}\cdot\text{s}^{-1}\cdot\text{cell}^{-1}$	AOCR / $\text{torr}\cdot\text{h}^{-1}$	OCR / $\text{amol}\cdot\text{s}^{-1}\cdot\text{cell}^{-1}$	AOCR / $\text{torr}\cdot\text{h}^{-1}$	OCR / $\text{amol}\cdot\text{s}^{-1}\cdot\text{cell}^{-1}$
6.4	36 \pm 3	44 \pm 4	26 \pm 2	101 \pm 8	7 \pm 2	13 \pm 5
7.2	52 \pm 13	63 \pm 16	25 \pm 6	99 \pm 23	10 \pm 1	20 \pm 2
7.4	51 \pm 11	63 \pm 13	30 \pm 4	117 \pm 15	9.8 \pm 0.9	19 \pm 2
7.8	79 \pm 24	97 \pm 29	32 \pm 5	127 \pm 18	13 \pm 2	25 \pm 5

5.5.2 EXPERIMENTS WITH 3D TISSUE MODELS

Three-dimensional tissue models reveal a higher structural complexity than 2D monolayers and therefore show a more realistic response to stimulations, reflecting *in vivo* tissue better. Since in cultured tissues no blood vessels or capillaries are formed, nutrient and oxygen supply decreases towards the core of the spheroid. Within this study, the respiratory activity of SK-MEL-28 cells either grown as cell monolayers (see chapter 5.5.1) or as spheroids was investigated. On the one hand, the spheroid's respiration was monitored during spheroid adhesion directly after the placement on the sensor foil (see Fig. 5.17 A) and on the other hand, the spheroids were allowed to attach to the oxygen-sensitive sensor foil during 24 h in cell culture medium (see Fig. 5.17 B). After the addition of L-15 medium adjusted to four different pH_e values, the petri dishes were filled completely and sealed airtight. The corresponding sensor foil images can be seen in the first column of Fig. 5.17 A and B. The images were calibrated, translated into false color images (columns two and three) and were used to evaluate profile plots with subsequent data smoothing over 20 points according to the Savitzky Golay method. The oxygen partial pressure of the spheroids depicted in Fig. 5.17 A were measured directly after spheroid inoculation using the VisiSens TD system with excitation and emission readout from above, whereas the spheroids in Fig. 5.17 B were illuminated by LEDs from below. The differently positioned LEDs are the reason for the different aspects of the images in the first columns. The spheroids in (A) were clearly visible in contrast to the spheroids in (B) which were illuminated and recorded from below meaning only changing fluorescence signals due to differing oxygen concentrations close to the sensor foil could be observed. Directly after placing the spheroid on the sensor foil and starting the measurement in (A), small air bubbles were observed to emerge at the sensor foil surface, which disappeared with time, explaining the air bubble-free images after a previous 24-h preincubation for spheroid adhesion (Fig. 5.17 B, columns one and two). Another difference, which can be attributed to the different attachment periods for the spheroids, was observed directly after the start of the measurement since the formed oxygen concentration gradients were more pronounced after a previous 24-h attachment process in Fig. 5.17 B (second column). The darkening of the false color images from light yellow to dark blue corresponds to

decreasing oxygen partial pressure from 100 torr to 0 torr of oxygen which cannot be observed in the second column of (A). In the beginning, the spheroids in Fig. 5.17 A and B on average were $(470 \pm 25) \mu\text{m}$ and $(460 \pm 56) \mu\text{m}$ in diameter, respectively. However, the false color images after 24 h of recording suggested that the spheroids in (A) were significantly smaller than the spheroids in (B). Interestingly, the images in Fig. 5.17 A after 24 h of measurement time were quite similar compared to the images of Fig. 5.17 B directly after the start of the recording. This led to the conclusion that prolonged incubation times for cellular attachment cause a stronger connection between the spheroid and the sensor foil. A larger contact area between the spheroid and the sensor foil causes a more semi-spherical structure and therefore a more representative cross section of the spheroid's core.

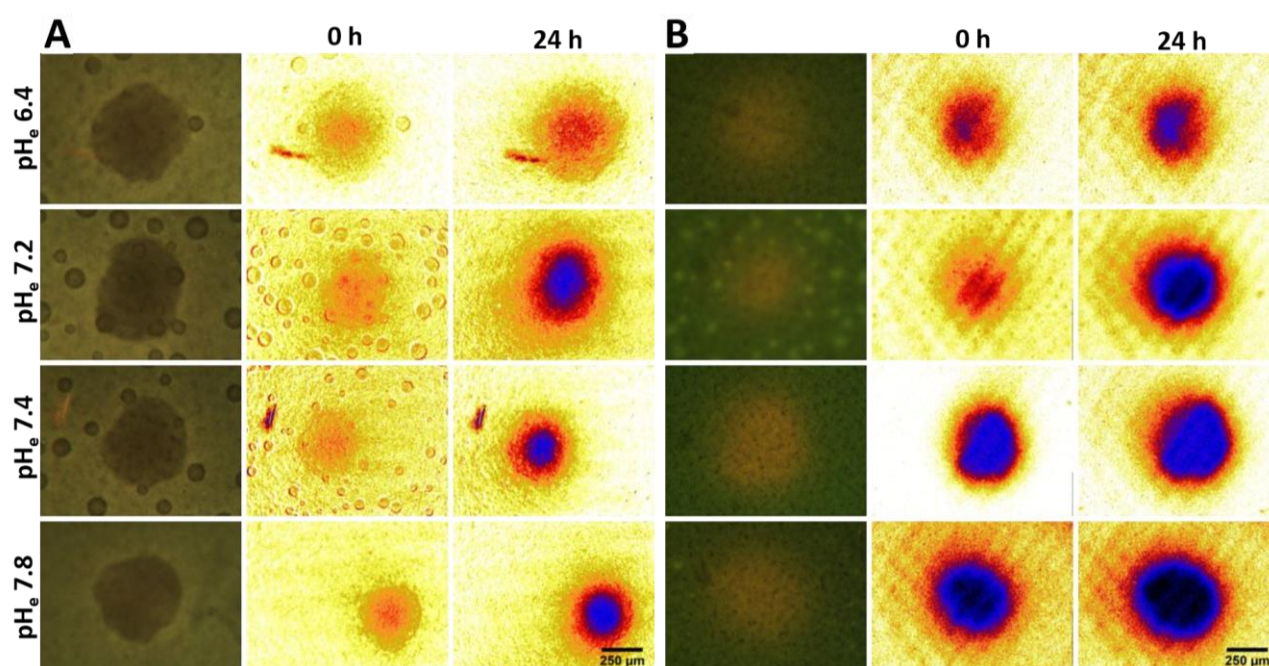


Fig. 5.17 Sensor foil-based monitoring of the pH-dependent respiratory activity of eight SK-MEL-28 spheroids exposed to four different extracellular pH_e conditions. The first columns of (A) and (B) show optical photographs of the sensor foil and in columns two and three, the corresponding calibrated false color images after 0 h and 24 h of recording time are shown. (A) SK-MEL-28 spheroids measured during the adhesion process directly after placement on the oxygen-sensitive sensor foil with illumination from above. The images of the spheroids being exposed to pH_e of 6.4 to 7.4 revealed small air bubbles emerging at the sensor foil surface, which vanished after 24 h of recording. (B) SK-MEL-28 spheroids were allowed to attach to the sensor foil surface for 24 h prior to the experiment. The sensor foil was illuminated, and the fluorescence signal detected from below the petri dish. The false color images show a color change from light yellow to dark blue representing oxygen concentrations from 100 torr in the beginning to 0 torr in the end. The experiments were performed at 37 °C and 0 % CO_2 under L-15 medium adjusted to the respective pH_e .

Another important aspect of the investigation was the pH-dependency of the respiratory activity within the different metabolic zones inside the spheroid (see Fig. 1.4). The images show that the spheroids exposed to an acidic environment respired less oxygen compared to the spheroids under more physiological or even alkaline conditions. Evidence for the slower oxygen consumption is given by the weaker color changes during the course of 24 h for the spheroids exposed to pH_e of 6.4 (Fig. 5.17, first row). The respiration of the spheroids, which were exposed to more physiological and alkaline pH-adjusted buffer solutions, seemed not

to be as strongly affected compared to the acidic environment. In all cases, the oxygen concentration decreased with time, as can be seen in the larger and simultaneously darker parts of the false color areas reflecting the spheroids.

The recorded and calibrated images were used to extract profile plots (800 x 12 pixels in size) to be able to plot emerging oxygen gradients in a cross section of the spheroids. Fig. 5.18 depicts the pO_2 profile cross sections of the SK-MEL-28 spheroids after 1 h, 6 h and 24 h of recording in a pH-dependent manner.

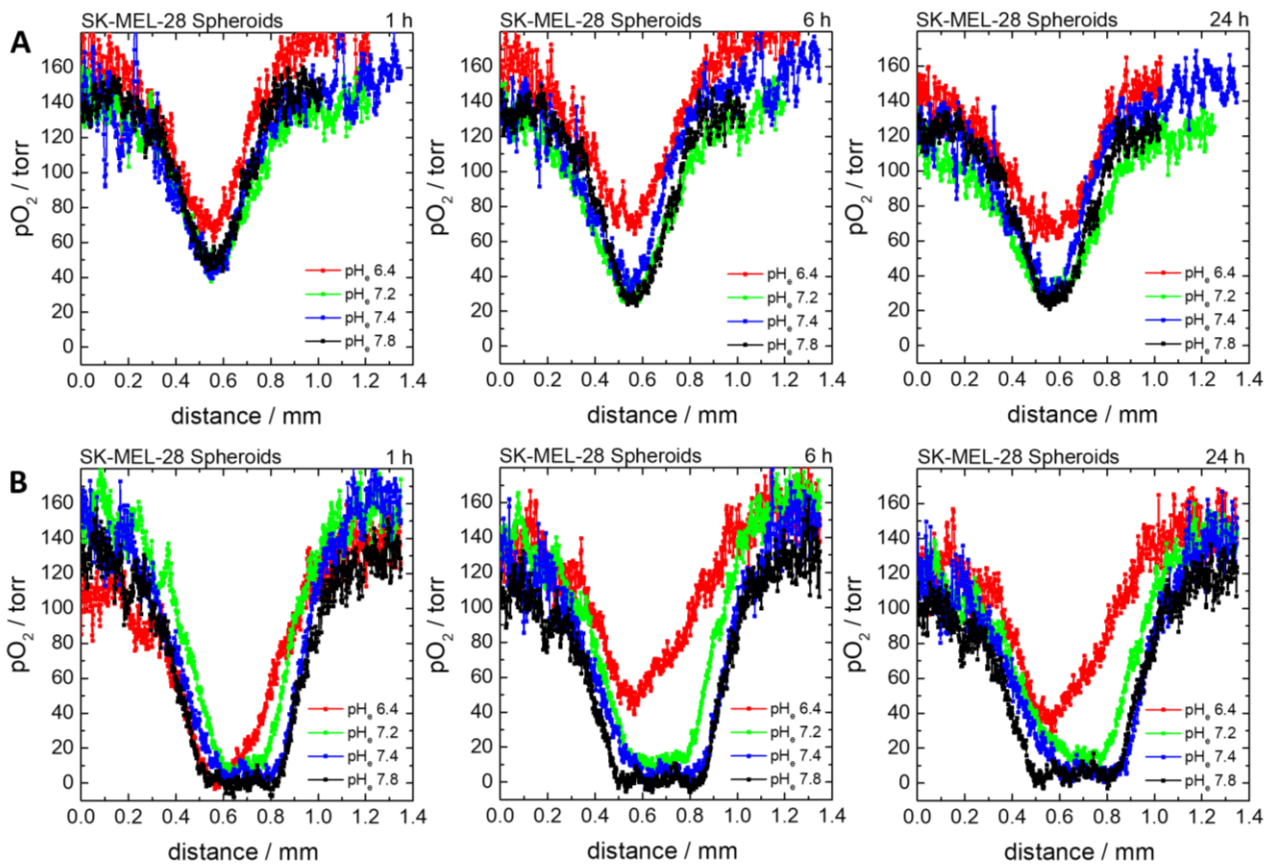


Fig. 5.18 Sensor foil-based sensing of spatial, pH-dependent oxygen profiles of eight SK-MEL-28 spheroids exposed to four different extracellular pH_e conditions. Images were calibrated and used to determine the oxygen distributions in a cross section of the spheroid via *profile plot evaluation*. (A) SK-MEL-28 spheroids investigated directly after spheroid inoculation on the oxygen-sensitive sensor foil and thus they were monitored during the adhesion process. (B) SK-MEL-28 spheroids which were allowed to attach to the sensor foil during 24 h prior to the experiment. The pO_2 was calculated from the images depicted in Fig. 5.17 and plotted against the profile length. The experiments were performed at 37 °C and 0 % CO_2 using L-15 medium adjusted to the respective pH_e .

The spheroids' respiration in Fig. 5.18 A was monitored directly after inoculation on the sensor foil whereas the spheroids in Fig. 5.18 B, similar to the images in Fig. 5.17, were allowed to attach to the sensor foil for 24 h before the start of the experiment. The major difference between (A) and (B) was the profile shape and the degree of the recorded oxygen depletion with time. The spheroids in (A) disclosed a V-shaped oxygen concentration profile. In the case of the spheroids exposed to physiological and more alkaline conditions, an oxygen concentration of around 45 torr was detected centrally beneath the spheroids which almost halved to around 25 torr after the full 24 h of measurement. In contrast to that, the spheroids treated with an acidic

medium consumed only around 5 torr of dissolved oxygen due to the decrease of 69 torr to 64 torr within 24 h.

In contrast to the V-shaped profiles, the spheroids which were allowed to attach for 24 h (Fig. 5.18 B), rather displayed U-shaped or weakly W-shaped profiles. Directly after the start of the measurement, the profiles of all four spheroids looked identical with an O_2 concentration of around 120 torr next to the spheroid and minimal pO_2 values of around 0 torr of oxygen under the spheroid's core. With time, the oxygen partial pressure next to the spheroids slowly decreased to levels of around 110 torr, while a slight recovery of the oxygen concentration centrally beneath the spheroid, in a distance of the profile of 0.65 mm, was observed from initially 0.6 torr to 7 torr after 24 h. Furthermore, a pH-dependency was observed as the spheroid exposed to a pH_e of 7.8 displayed the broadest profile with minimal oxygen values in a distance between 0.5 mm and 0.8 mm. With decreasing pH_e , the area of hypoxic conditions also got smaller, resulting in a pO_2 level of 40 torr oxygen concentration as the minimal pO_2 value shown by the spheroid which was exposed to an acidic environment at a pH_e of 6.4. For further data evaluation, the *area above the curve* (AAC) with an upper integration limit of $y = 150$ torr on the y-axis was calculated. Tab. 5.9 summarizes all AACs showing one similarity and one difference between the spheroids which were monitored during their adhesion to the sensor foil and spheroids which had already adhered to the sensor foil. The similarity was observed for the spheroids exposed to a pH_e of 7.2. In both cases, the increase in the AAC values from 1 – 24 h was highest at around 33 torr·mm and 27 torr·mm for the adhering one and the already attached spheroid, respectively. This large difference in the AAC values indicates a very active respiration of the spheroids. The main difference was observed for the spheroids exposed to an acidic environment. The spheroid still adhering to the sensor foil (see Tab. 5.9 A) seemed to actively respire the still available oxygen according to the increasing AAC while the already attached one appeared to be inhibited in its respirational activity according to the decreasing AAC.

Tab. 5.9 Calculated *area above the curve* (AAC) of the pH-dependent profile plots of the SK-MEL-28 spheroids (see Fig. 5.18). AAC values were determined with an upper integration limit of $y = 150$ torr. In (A), the AACs of the spheroids monitored during the adhesion to the sensor foil are summarized and in (B), the AACs are given for the spheroids which had attached to the sensor foil prior to the experiment.

t / h	AAC / torr·mm				
	pH_e 6.4	pH_e 7.2	pH_e 7.4	pH_e 7.8	
A	1	10.7	46.7	39.9	36.4
	6	22.6	59.6	45.9	51.4
	24	37.4	79.8	56.7	61.2
B	1	90.2	63.7	82.1	103.4
	6	47.7	74.8	98.4	114.5
	24	59.5	90.4	105.6	119.0

The results have shown that the given attachment time of the spheroid as well as spheroid shape and surface character are important parameters influencing the oxygen concentration gradient being formed beneath spheroids. In order to generate reliable and reproducible results, it is highly important to closely determine the size and shape of spheroids prior to the experiments.

5.6 ADAPTION OF THE INTRACELLULAR pH_i TO CHANGES IN THE EXTRACELLULAR pH_e

The previous chapters demonstrated the influence of altered extracellular pH_e on different cellular phenotypes. Since the extracellular and intracellular compartments are not functioning independent from each other and are connected via transmembrane channels and selective ion carriers, it was investigated how the intracellular pH_i changes according to altered extracellular conditions. Therefore, the cells were stained with the pH-sensitive dye BCECF-AM revealing a pK_a of ~ 6.98 (compare chapter 3.5). The pK_a of an acid indicates the specific pH value at which the acidic form and the corresponding base are present in equal amounts. Thus, pH values higher than the pK_a cause increasing deprotonation and pH values lower than the pK_a value lead to increasing protonation of the respective acid. After the staining and the subsequent incubation with pH-adjusted L-15 medium, the fluorescence was either detected via the CLSM or using a microplate reader (*Tecan reader*). The CLSM technique was performed with excitation at two different wavelengths ($\lambda_{\text{ex.}} = 408 \text{ nm}$ and $\lambda_{\text{ex.}} = 488 \text{ nm}$) and the emission was detected at $\lambda_{\text{em.}} = 515/30 \text{ nm}$. Fig. 5.19 shows images of NRK cells stained with BCECF-AM after having been exposed to a pH_e of 5.5 and 8.0 while the dyes were excited at wavelengths of 408 nm and 488 nm. 488 nm is the wavelength at which the corresponding emission is strongly pH-dependent, while the emission intensity after an excitation at 408 nm is used as reference signal. The emission intensities following the 408-nm excitation were identical within the error range for all cells, no matter if they were treated with acidic or alkaline media. In contrast to equal intensities of the reference emissions, the emission intensities after the 488-nm excitation increased significantly by at least 40 % with rising pH_e from 5.5 to 8, indicating equally rising intracellular pH_i . For the calculation of the pH_i from the images, a linear correlation of the calibration data was performed (see Fig. 11.12) as was described in detail in chapter 3.5.1.

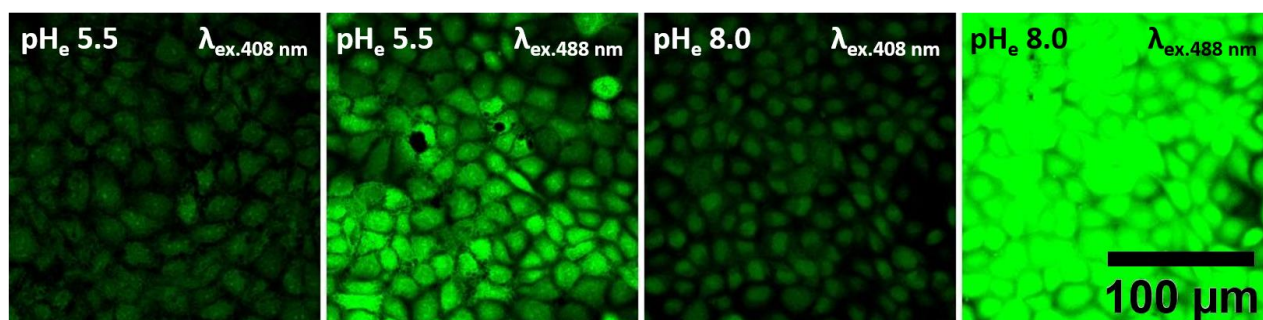


Fig. 5.19 CLSM images of NRK cells after staining with the pH-sensitive dye BCECF-AM ($10 \mu\text{M}$ in PBS^{++}). Confluent NRK cells were either exposed to L-15 medium adjusted to an acidic or an alkaline pH_e . Emission intensity after the 408-nm excitation was used as reference fluorescence intensity while the emission intensity after the 488-nm excitation was strongly pH-dependent. Calculated ratios were used to determine intracellular pH_i following a calibration using nigericin ($10 \mu\text{M}$ in pH-adjusted L-15 medium) to align the pH_i with the pH_e . Images were taken using a 60x magnification and pinhole size M.

Since the dye is highly susceptible to temperature changes and showed strong photobleaching, the intracellular pH_i values were determined using 96-well plates and the *Tecan reader* for fluorescence readout. The readout was done with a single wavelength excitation ($\lambda_{\text{ex.}} = 485 \text{ nm}$) and a dual emission detection ($\lambda_{\text{em.}} = 535 \text{ nm}$ and $\lambda_{\text{em.}} = 612 \text{ nm}$) because of more reliable results. The experiment was done with A549, NRK, SK-MEL-28 and SpiCa cells after the treatment with L-15 medium adjusted to seven pH_e . Fig. 5.20 illustrates the calculated and averaged pH_i plotted against the corresponding pH_e . The dotted line is the angle bisector and both axes are equally scaled meaning a 100 % pH_i equilibration with the extracellular pH_e for data points located on the dotted line.

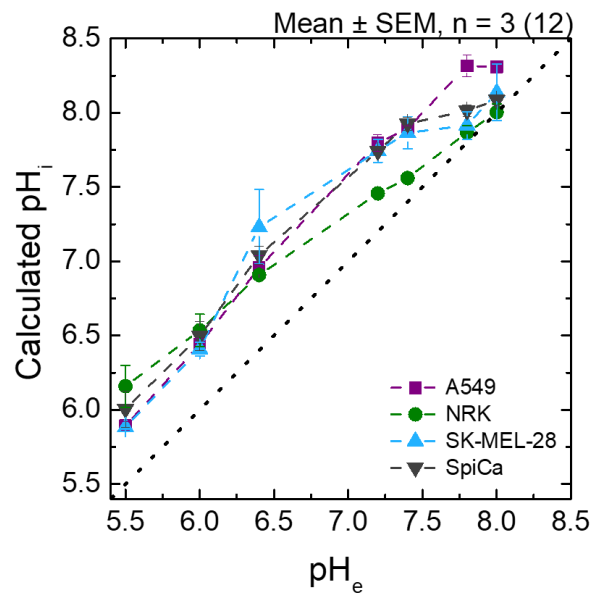


Fig. 5.20 Detection of changes in the intracellular pH_i , which were caused by the addition of L-15 medium adjusted to different extracellular pH_e , via the pH-sensitive dye BCECF-AM ($10 \mu\text{M}$ in PBS^{++}). pH_i values were determined according to the linear equation yielded by the calibration of BCECF-AM inside the cells under the presence of nigericin ($10 \mu\text{M}$ in pH-adjusted L-15 medium) (see Fig. 11.12). The experiments were performed in three independent experiments in quadruplicate on confluent cell monolayers at $T = 37 \text{ }^\circ\text{C}$, $0 \text{ } \%$ CO_2 .

The intracellular pH_i revealed by A549 cells were constantly 0.4 to 0.6 pH units higher than the experimentally set pH_e ; only the extracellular increase in pH_e from 7.8 to 8 caused no detectable change in pH_i . NRK cells, the non-cancerous cell line model, adapted their intracellular pH_i levels more and more to the given extracellular conditions with increasing pH_e . The difference in pH units between pH_e and pH_i shrank from 0.7 over 0.5 to 0.41 and further lessened from 0.26 over 0.16 to 0.07 with rising pH_e until finally a complete adaption of the pH_i to the pH_e occurred at pH 8.0 for NRK cells. The difference between pH_e and pH_i exhibited by the SK-MEL-28 cells increased from 0.33 over 0.41 to 0.8 with increasing pH_e from 5.5 to 6.4. The final increase of the pH_e from 7.2 to 8.0 eventually caused a state of equilibrium between pH_e and pH_i with decreasing differences of 0.54, 0.5, 0.11 and 0.1. SpiCa cells constantly managed to keep their intracellular pH_i around 0.5 units higher than the extracellular level, at least in a pH_e range from 5.5 to 7.4. The highest pH_e values 7.8 and 8.0 only led to slightly elevated pH_i values of (8.01 ± 0.04) and (8.09 ± 0.03) , respectively. Tab. 5.10 summarizes all pH_i values.

Tab. 5.10 Summary of the determined intracellular pH_i after changes in the extracellular pH_e . Calculation was performed with the help of a calibration curve and fluorescence signal ratios after staining of confluent cell layers with BCECF-AM (compare Fig. 5.20). Mean \pm SEM, $n = 3$ (12).

pH_e	Calculated pH_i			
	A549	NRK	SK-MEL-28	SpiCa
5.5	5.90 \pm 0.03	6.2 \pm 0.1	5.88 \pm 0.01	6.0 \pm 0.1
6.0	6.44 \pm 0.04	6.5 \pm 0.1	6.41 \pm 0.05	6.5 \pm 0.1
6.4	6.96 \pm 0.08	6.91 \pm 0.02	7.2 \pm 0.3	7.04 \pm 0.06
7.2	7.80 \pm 0.06	7.46 \pm 0.01	7.74 \pm 0.08	7.74 \pm 0.02
7.4	7.89 \pm 0.01	7.56 \pm 0.03	7.9 \pm 0.1	7.93 \pm 0.04
7.8	8.31 \pm 0.07	7.87 \pm 0.05	7.91 \pm 0.09	8.01 \pm 0.04
8.0	8.31 \pm 0.02	8.00 \pm 0.06	8.1 \pm 0.2	8.09 \pm 0.03

5.7 DISCUSSION

Comparison of pH-dependencies of different phenotypes and cell lines

The investigation of the impact of altered pH_e on different cellular phenotypes as well as the comparison between normal and tumor cells were based on the reported inverse pH gradients over the cell membranes and hence a fundamental difference in the metabolic microenvironment. Solid tumors often have to cope with insufficient vascular networks and long diffusion distances leading to a reduced oxygen transport capacity (Höckel, M. *et al.* 2001). The restricted oxygen supply and the resulting intrinsic changes of the metabolism, called Warburg effect, entail a shift of the aerobic energy metabolism to glycolysis with the subsequent anaerobic energy generation via lactic acid production (Vander Heiden, M. G. *et al.* 2009). The boosted formation of lactic acid after glycolysis leads to an extracellular acidosis of tumor cells ending in a $\text{pH}_e \geq 6$ (for squamous cell carcinomas on average between 6.15 and 7.4) while non-cancerous cells exhibit a pH_e between 7.0 and 7.4 (Vaupel, P. *et al.* 1989). The analysis of the pH-dependent cellular behavior was done using three different techniques: impedance spectroscopy using ECIS™ and two optical methods, which were the microscopic examination of proliferation and migration events as well as the sensor foil-based determination of the respiratory activity of the cells. Since the data from the individual techniques were evaluated according to different parameters - the AUC in the ECIS™ measurements, the slopes of the change in cell coverage plotted against the time in the microscopic observations via the zenCell owl and the respiration rate in the sensor foil-based experiments - the results were normalized with respect to the cell response after exposure to a pH_e of 7.4. All results are shown with the corresponding standard error taking the Gaussian error propagation into consideration. Fig. 5.21 and Tab. 5.11 summarize the studies monitoring the impact of altered extracellular pH_e on the four cell lines under test. For an assessment of the overall pH_e dependency of the individual cell lines, the results from all phenotypic assays were averaged for each pH_e , except for the results gained from the micromotion experiments because high pH-independent fluctuations were observed. The averaged values were plotted against the respective pH_e with a subsequent linear regression for the four cell lines. The linear regression showed the change in cell response or phenotypic activity as a function of one pH unit [pH^{-1}]. A549 and SK-MEL-28 cells revealed the smallest pH-dependent change of the phenotypic activity with $(0.1 \pm 0.1) \text{pH}^{-1}$ and $(0.25 \pm 0.01) \text{pH}^{-1}$, respectively. The change of phenotypic activity of NRK and SpiCa cells on average was similar at $(0.4 \pm 0.1) \text{pH}^{-1}$. Consequently, according to the lower pH-dependent changes, A549 and SK-MEL-28 cells were not as strongly affected by changing pH_e values as NRK and SpiCa cells.

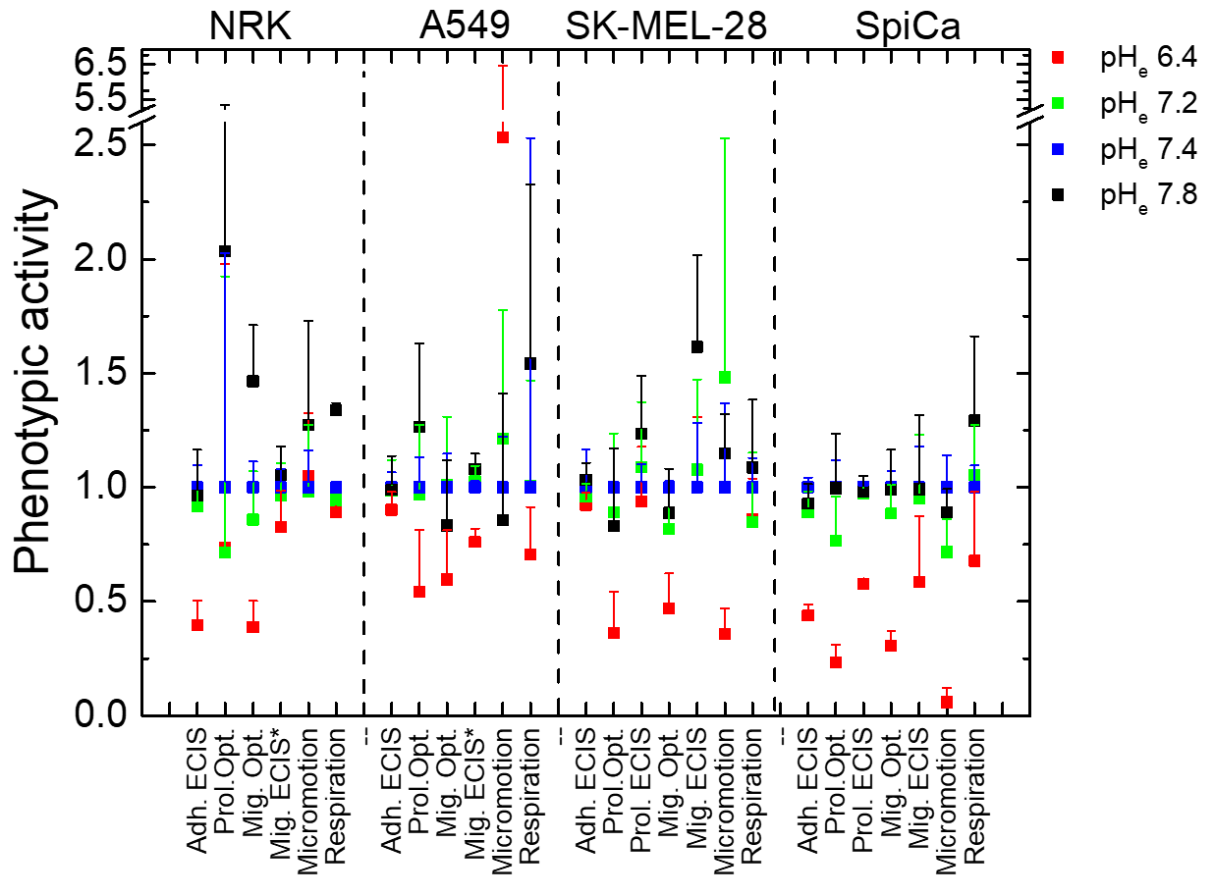


Fig. 5.21 Summarized results from the pH-dependent phenotypes of four cell lines. Investigated phenotypes included cellular adhesion followed by ECIS™ (**Adh. ECIS**), cellular proliferation monitored microscopically via the zenCell owl (**Prol. Opt.**) or impedimetrically using ECIS™ (**Prol. ECIS**), cellular migration via zenCell owl (**Mig. Opt.**) or ECIS™ (**Mig. ECIS**), cellular micromotion measurements via ECIS™ and the cellular respiration according to sensor foil-based experiments (**Respiration**). (*) signifies results gained during the master's thesis which were included for reasons of comparison. Results from the individual experiments were normalized with respect to the cell response under the physiological pH_e of 7.4. Mean values are depicted with the corresponding standard error by taking the Gaussian error propagation into account.

Tab. 5.11 Summarized results of the pH-dependent phenotypic activities of four cell lines depicted in Fig. 5.21. Results were normalized with respect to the cell response upon exposure to a pH_e of 7.4.

Cell line	Assay type	pH_e 6.4	pH_e 7.2	pH_e 7.4	pH_e 7.8
		Phenotypic activity			
NRK	Adhesion ECIS™	0.4 ± 0.1	0.9 ± 0.2	1.0 ± 0.1	0.9 ± 0.2
	Proliferation Optical	1 ± 1	1 ± 1	1 ± 1	2 ± 3
	Migration Optical	0.4 ± 0.1	0.9 ± 0.2	1.0 ± 0.1	1.5 ± 0.3
	Migration ECIS™ *	0.8 ± 0.2*	0.9 ± 0.1*	1.0 ± 0.1*	1.1 ± 0.1*
	Micromotion	1.0 ± 0.3	0.9 ± 0.3	1.0 ± 0.2	1.3 ± 0.5
	Respiration	0.89 ± 0.02	0.94 ± 0.02	1.00 ± 0.01	1.34 ± 0.03
A549	Adhesion ECIS™	0.90 ± 0.08	1.0 ± 0.1	1.00 ± 0.07	1.0 ± 0.2
	Proliferation Optical	0.5 ± 0.3	1.0 ± 0.3	1.0 ± 0.1	1.3 ± 0.4
	Migration Optical	0.6 ± 0.2	1.0 ± 0.3	1.0 ± 0.2	0.8 ± 0.3
	Migration ECIS™ *	0.76 ± 0.06*	1.03 ± 0.07*	1.0 ± 0.03*	1.08 ± 0.07*

	Micromotion	3 ± 4	1.2 ± 0.6	1.0 ± 0.2	0.9 ± 0.6
	Respiration	0.7 ± 0.2	1.0 ± 0.5	1.0 ± 0.2	1.5 ± 0.8
	Adhesion ECIS™	0.92 ± 0.06	0.96 ± 0.06	1.0 ± 0.2	1.03 ± 0.08
	Proliferation Optical	0.4 ± 0.2	0.9 ± 0.4	1.00 ± 0.02	0.8 ± 0.3
	Proliferation ECIS™	0.9 ± 0.2	1.1 ± 0.3	1.0 ± 0.1	1.2 ± 0.3
SK-MEL-28	Migration Optical	0.5 ± 0.2	0.8 ± 0.2	1.00 ± 0.03	0.9 ± 0.2
	Migration ECIS™	1.0 ± 0.3	1.1 ± 0.4	1.0 ± 0.3	1.6 ± 0.4
	Micromotion	0.4 ± 0.1	1.5 ± 1	1.0 ± 0.4	1.1 ± 0.2
	Respiration	0.9 ± 0.2	0.9 ± 0.3	1.0 ± 0.1	1.1 ± 0.3
	Adhesion ECIS™	0.44 ± 0.05	0.89 ± 0.09	1.00 ± 0.04	0.93 ± 0.09
	Proliferation Optical	0.23 ± 0.08	0.8 ± 0.2	1.0 ± 0.1	1.0 ± 0.2
	Proliferation ECIS™	0.58 ± 0.02	0.97 ± 0.08	1.00 ± 0.01	0.98 ± 0.07
SpiCa	Migration Optical	0.31 ± 0.06	0.9 ± 0.1	1.00 ± 0.07	1.0 ± 0.2
	Migration ECIS™	0.6 ± 0.3	1.0 ± 0.3	1.0 ± 0.2	1.0 ± 0.3
	Micromotion	0.05 ± 0.06	0.7 ± 0.2	1.0 ± 0.1	0.9 ± 0.1
	Respiration	0.7 ± 0.3	1.0 ± 0.2	1.0 ± 0.1	1.3 ± 0.4

* Experiments were performed during my master's thesis at the University of Regensburg in 2016.

The pH-dependent proliferation and migration was studied using an optical and an impedance-based technique in order to validate results and their reproducibility. The optical technique with the integrated automatic calculation of the degree of cell coverage exhibited the disadvantage that the correctness of cell recognition differed for the individual cell lines. On the other hand, the impedance-based investigation showed different sensitivities for the individual cell lines and particularly low sensitivity for experiments carried out with SK-MEL-28 cells. Normally, the shape of the impedance spectrum of a cell-covered electrode provides first insights into the cell-characteristic parameters R_b , C_m and α (see chapter 3.3.1) representing the resistance of the cell-cell contacts, the specific capacitance of the cell membrane and the resistance of the cell-electrode junction (Reiss, B. *et al.* 2015). However, the frequency-dependent impedance magnitude of the cell-covered electrode in the case of SK-MEL-28 cells indicated extremely low R_b and α values causing the low sensitivity. A conventional extraction of the ECIS™ parameters from the impedance spectra was not possible due to insufficient data points in the spectrum and little difference between the spectra of the cell-free and the cell-covered electrode. In literature, SK-MEL-28 cells are discussed to have few and loose cell-cell connections (Lee, J. *et al.* 2016) explaining the low R_b value, as the degradation of tight junctions facilitates the invasion properties of cancer cells to distant tissue or organs (Martin, T. A. *et al.* 2009). The resistance of cell-substrate contacts (visible in the slope of the cell-related resistive contribution in the impedance magnitude spectrum) is closely associated with the shape, size and morphology of the cells as well as with the extracellular space between basal membrane and electrode surface (Arndt, S. *et al.* 2004).

SK-MEL-28 cells display a highly irregular longitudinal morphology (see Fig. 5.22) which could be the reason for the low α values. Fig. 5.22 shows SK-MEL-28 cells in different developmental stages. Starting with an image of a single cell (A), the state of subconfluent grown SK-MEL-28 cells is shown in (B) followed by a confluent cell monolayer in (C). The photograph (C) shows the irregular morphology in contrast to NRK cells (Fig. 5.22 D) which are highly regular and exhibiting a cobblestone-like morphology.

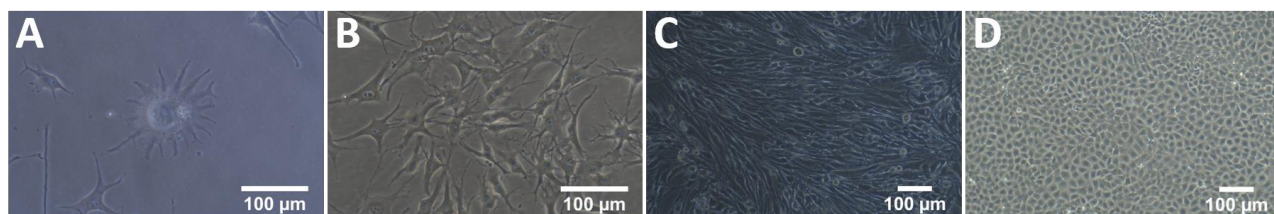


Fig. 5.22 Exemplary microscopic images of SK-MEL-28 cells. (A) at single cell level, (B) in a subconfluent cell layer and (C) as a confluent cell monolayer in comparison to (D) a confluent NRK cell monolayer. Images were taken using the *Nikon Diaphot* microscope equipped with a digital camera in a 20x (A, B) and 10x magnification (C, D). Scale bar depicts 100 μm .

The third cell-specific parameter C_m could also not be clearly determined from the raw data due to the fact that the *multiple frequency per time* (MFT) measurements were done in a frequency range between 62.5 Hz and 64 kHz. For an estimation of C_m however, higher frequencies would have been necessary as no cell-related dispersion could be observed within this frequency range and the difference between the spectrum of the cell-free and the one of the cell-covered electrode was minimal. Generally, the value of the membrane capacitance is strongly dependent on the membrane surface. Values close to $1 \mu\text{F}\cdot\text{cm}^{-2}$ signify a smooth membrane surfaces while higher values indicate invaginated or folded topologies e.g. due to microvilli on the apical membrane side (Reiss, B. *et al.* 2015). Mulhall, H. J. *et al.* 2011 reported about stronger membrane folding and thus increasing C_m values going from normal cells over dysplastic to malignant cells or with disease progression. However, due to the limited data at high frequencies, the C_m values could not be clearly determined: whether the membrane capacitance is high, which is typical for cancer cells, or low, which the missing cell dispersion in the impedance magnitude spectrum suggests, still needs to be investigated. The weak cell-cell contacts as well as equally weak cell-substrate contacts and hence a larger distance to the gold electrodes led to an unnaturally low ECISTM sensitivity for SK-MEL-28 cells. Thus, the investigations of pH-induced morphological changes were impeded, causing the minimal time-dependent signal changes during the adhesion, proliferation and migration measurements. Since proliferation and migration was complementarily monitored via a microscopic technique and SK-MEL-28 cells displayed a high contrast, the zenCell owl experiments may contain more reliable results due to well-performing automatic cell recognition and hence a reliable calculation of cell coverage values.

Within this thesis, two different skin cancer cell lines were compared with respect to their pH-dependent behavior. The metastatic potential of melanoma tumor cells, which only weakly respond to cancer therapies (Miller, A. J. *et al.* 2006), is discussed to be greater compared to non-melanoma skin cancers like squamous

cell carcinoma (e.g. SpiCa cells). Şuteu, O. *et al.* 2017 reported about net survival rates for patients suffering from cutaneous melanoma of 64 % and 75 % for male and female patients, respectively, while squamous cell carcinoma patients had a survival rate of 86 % and 100 %. The cases were diagnosed between 2006 – 2010 with a 5-year net survival rate. This statistic does not discriminate between cases with and without diagnosed tumor spreading. Kim, H.-Y. *et al.* 2017 found a by 17 % drastically decreased survival rate after tumor spreading, compared to 98 % survival without metastases. Weak cell-cell contacts favor the release of single cells into the blood stream and hence the possibility of adhering to distant tissue. This cell-characteristic behavior in combination with generally pH-independent phenotypes could lead to the aggressive formation of metastases of melanoma tumor cells like SK-MEL-28. Overall, SK-MEL-28 cells were not strongly inhibited or affected in their phenotypic behavior being exposed to differing extracellular pH_e . The most pronounced effect was detected using the ECIS™ technique, but as already mentioned, the results need to be interpreted cautiously due to the unsuitable cellular properties for the impedance-based detection on thin gold film electrodes.

Investigation of the influence of differing pH_e on adhesion processes

The adhesion characteristics of mammalian cells are highly dependent on the cell line, on cell sizes determining the speed of the sedimentation process as well as on the velocity of the formation of the extracellular matrix (ECM) which the cells can adhere to. Fibronectin (FN) was used to accelerate cellular adhesion by coating the electrode with the large protein as FN contains multiple binding sites enabling the recognition and specific binding of integrins located in the cell membrane to FN and hence to the surface (Xiao, C. *et al.* 2003). Accelerated adhesion was also observed after re-using ECIS™ arrays due to ECM residues from the cells previously having grown on top of the electrodes. As FN led to a reproducibly fast adhesion process, the FN coating was performed as a standard procedure to create constant conditions prior to each experiment.

Whenever multicellular living organisms suffer from a solid tumor, adhesion can occur when single cells leave their tumor environment, circulate the bloodstream, and reach another tissue part. This normal scenario involves several changes in pH. The leaving of the initial tumor and the subsequent adhesion at the site of normal tissue is accompanied by an increase in pH due to the acidic environment of the tumor and a more physiological pH surrounding normal tissue. Riemann, A. *et al.* 2019 reported about increased adhesion of AT1 cells (rat prostate carcinoma) when first being primed in an acidic environment and afterwards, the adhesion at a normal pH was measured impedimetrically in comparison to the adhesion behavior of non-cancerous NRK and MDCK cells. Nevertheless, this accelerated adherence was not uniform for all of the tested tumor cells. The effect of extracellular acidosis on already adherent cells led to significantly decreased adherence of tumor cells (Riemann, A. *et al.* 2019) what could also be observed within this thesis. The

adhesion protocol mimics the situation of individual cells circulating in the blood stream with the subsequent adhesion to distant tissue under a different pH_e . Acidic environments represent the adhesion to a distant tumor tissue, what was strongly inhibited in NRK and SpiCa cell experiments as represented by 153 % and 112 % higher AUC values. Apart from the observation of inhibited adhesion under acidic conditions, the effect under different extracellular pH_e was not significant for the four tested cell lines.

The recorded ECISTM-based adhesion profile after inoculation of SK-MEL-28 cells differs in comparison to the adhesion profiles of the other cell lines. The first sharp decrease in the capacitance signal was attributed to the sedimentation of the spherical SK-MEL-28 cells. Since the cell bodies are larger than in the case of the other cell types, sedimentation is a faster process. Following the sedimentation up to 1 h of recording, cells start to form integrin-mediated cell-substrate contacts due to cellular recognition of fibronectin being immobilized on the gold surface. The previously discussed presumably long distance between the basal membrane and the substrate surface in combination with the irregular shape of the cells could cause low values for α . In the time course of capacitance, a subsequent counter-intuitive re-increase in capacitance could be observed which can possibly explained by the cells minimizing the contact area to the substrate surface. This process could expand the basolateral space and consequently decrease the resistance for the electrical current to flow. In addition to the unconventional adhesion profile, the second decrease in the capacitance signal after 30 h can probably be associated with first proliferation events by the cells. In general, the total change of the capacitance during the entire time course was very small.

In contrast to the temporarily increasing capacitance signals detected for SK-MEL-28 cells, NRK, A549 and SpiCa cells showed a continuous decrease in the normalized capacitance signal, since the initial adhesion and spreading, as well as the formation of cell-substrate and cell-cell contacts increased the electrical resistance more and more until a confluent monolayer was reached.

Investigation of the influence of altering pH_e on proliferation events

Cellular alkalization is reported to induce increased cell proliferation by stimulating the synthesis of proteins, DNA and RNA resulting in very dense and disorganized cell masses with weak vascularization (Madhus, I. *et al.* 1988; Koliakos, G. *et al.* 2008). The inverse pH gradient or inside-out pH gradient of solid tumors is generated by multiple ion transporters like NHE1, V-ATPases, monocarboxylate transporters, (bi)carbonate co(transporters) and many more which are located in the cell membrane. The Na^+/H^+ exchanger NHE1 replaces extracellular Na^+ ions with intracellular H^+ ions across the membrane in order to regulate pH_i homeostasis, cell volume and cellular proliferation (Cardone, R. *et al.* 2005). Normally, NHE1 is activated when the pH_i drops below a certain threshold level but is always switched on in tumor cells leading to increased intracellular pH_i (Stock, C. *et al.* 2005) and consequently to increased cell cycle progression, to

substrate and serum-independent growth as well as to *in vivo* tumor growth (Hagag, N. *et al.* 1987; Reshkin, S. *et al.* 2000). The NHE1 exchanger therefore is only activated in normal cells when the intracellular pH_i is lowered below a certain threshold to prevent further acidosis. This additional mechanism that non-cancerous cells can rely on, could be one piece of the puzzle of explaining why NRK cells (normal cells) are not as strongly affected in their proliferation under the influence of an acidic environment as cancer cell lines (a 27-% decrease in comparison to lower rates or reduced cellular responses by 46 %, 64 % and around 77 % obtained for A549, SK-MEL-28 and SpiCa cells, respectively). Furthermore, the acidic strength should be compensated by the alkaline extracellular environment produced by the cells themselves. In the case of cancer cells, the NHE1 antiporter is constantly activated and an already acidic extracellular environment is further decreased due to the addition of an acidic culture medium. This could cause an even faster dysregulation of the inverse pH gradient and thus an acidification of the normally alkaline pH_i value which could explain the drastically decreased proliferation of A549, SK-MEL-28 and SpiCa cells. Following this train of thought, an extracellular alkalinization should be counteracted by the acidic cellular microenvironment of tumor cells. Nevertheless, the unnatural lack of H^+ ions could cause an even more pronounced alkaline intracellular pH_i in order to restore the normal, inverse pH gradient. As tumor cells are already used to alkaline pH_i , the very similar proliferation rates after exposure to pH_e of 7.2, 7.4 and 7.8 could be explained. In contrast to tumor cells, normal cells exhibit slightly acidic pH_i and an increase in the extracellular pH_e conditions of normal cells could result in an increase of the pH_i , possibly causing the 103 % accelerated proliferation in the case of NRK cells. Maintaining alkaline pH_i as it is done by tumor cells, seemed to work also for normal cells when they were forced to increase intracellular pH_i levels following extracellular pH_e changes due to the dependency of pH_i and pH_e .

Investigation of the influence of altered pH_e on migration behavior

The investigations of the pH-dependent cellular migratory activity were performed using two techniques. On the one hand, the impedance-based ECISTM technique where cells were wounded by the application of electrical pulses and on the other hand, a *scratch assay* where cells were mechanically removed and cellular migration was microscopically observed. The electrically generated wounds were circularly shaped due to the geometry of the working electrode, displaying very defined borders with a high reproducibility. The *scratch assay* led to linear but differently sized wounds revealing uneven and fringed borders. Another difference was the cell-vacant state of the wounding area because following the *scratch assay*, the wound was cell-free, whereas cell body residues in parts remained on the gold surface after the electrical wounding. A live/dead staining performed by Stolwijk, J. *et al.* 2020 illustrated the remains of dead cells after electrical wounding. One could expect that the remaining parts of the cell bodies would lead to a reduction of the migration speed as the surrounding, vital cells need to move aside the cell residues. But contrary to these

expectations, the phenotypic activity was higher in almost all cases of the ECISTM-detected migration when compared to the optical observations for the same extracellular conditions. But it is important to keep in mind that AUC and migration rates were the basis for the calculation of the phenotypic activities. For a direct comparison, a closer look at direct migration velocities would have been necessary.

As already discussed, the SK-MEL-28 melanoma cells were not the perfect cell model for the ECISTM investigation and the electrical wounding was also difficult, which is why the wounding was done already 7 h after cell inoculation. The presumably large distance between the electrode surface and the basal membrane could have prevented effective membrane permeabilization and hence cellular wounding. Moreover, the application of an electrical fence (an ECISTM feature), which should have prevented cellular adhesion on the working electrodes as well as *barrier assays* using PDMS spacers which equally should have kept the working electrode cell-free, did not function when SK-MEL-28 cells were used. Therefore, data which was collected with ECISTM will not be discussed in detail in the following.

The tumor cell lines (A549, SK-MEL-28 and SpiCa) showed a collectively increasing cellular migration with elevated pH_e up to 7.4 followed by a slight decrease in their migration rates at even higher pH_e . In contrast, the normal cells (NRK) exhibited a strong pH-dependent wound healing behavior across the full investigated pH_e range from 6.4 to 7.8 in the form of increasing migration rates and increasing phenotypic activity from (0.4 ± 0.1) (Optical) / $(0.8 \pm 0.2)^*$ (ECISTM) to (1.5 ± 0.3) (Optical) / $(1.1 \pm 0.1)^*$ (ECISTM) under decreasing extracellular proton concentration (see Tab. 5.11). As previously mentioned, the NHE1 antiporter plays a crucial role with respect to pH-dependent cellular responses. Stüwe, L. *et al.* 2007 could show that NHE1-deficient cells or wild type human melanoma cells (MV3) in which the NHE1 was blocked, were not able to respond to altered extracellular pH_e highlighting the importance of the ion exchanger and its effects on adhesion, migration and cellular morphology. The wild type human melanoma cell line MV3 was reported to show maximal migratory speed at a pH_e of 7.0 and seemed to branch out the most in a pH_e range from 6.6 to 6.8 (Stüwe, L. *et al.* 2007). Stock, C. *et al.* 2005 reported about a pH-dependent strength of the integrin-matrix interaction being the strongest between pH_e 6.6 to 6.8 which is discussed to hinder the release of focal contacts. Migration-polarized cells are moreover reported to generate differences in the proton concentrations on their membrane surface. This pH gradient across the entire cell membrane emerges due to a lower pH_e near the leading edge of the cell and a higher pH close to the rear end. Thus, the pH decreases in the direction of the movement (Stock, C. *et al.* 2007). This gradient is reported to disappear below a pH_e of 6.0 and remains intact up to alkaline pH_e of 7.3 – 7.5. It is commonly known and was also shown within this thesis, that extracellular acidification introduces intracellular acidosis. The combination of firmly attached cells with strong cell-matrix contacts, the loss of pH gradients over their cell membrane along the movement direction and rising intracellular acidosis with increasing proton concentrations could cause the inhibition of migratory events of mammalian cells. The experiments conducted within this thesis made it difficult to clearly distinguish between normal and cancer cells due to heterogenic responses of the tumor

cell lines. Nevertheless, the degree of inhibition of cell migration under exposure of an acidic environment was strongly dependent on the cell line. The most pronounced inhibitory effect of an acidic environment was observable using SpiCa cells which gave the weakest phenotypic activity of (0.31 ± 0.06) (Optical) / (0.6 ± 0.3) (ECIS™) in comparison to (0.5 ± 0.2) (Optical) / (1.0 ± 0.3) (ECIS™) and (0.6 ± 0.2) (Optical) / $(0.76 \pm 0.06)^*$ (ECIS™) revealed by SK-MEL-28 and A549 cells, respectively, (see Tab. 5.11).

An alkalinization of the extracellular environment and hence an intracellular rise in pH_i leads to an increased expression and activation of several proteins inside the cell. Alkaline pH_i values are reported to promote the activation of e.g. ADF/cofilin and gelsolin proteins, regulating the actin polymerization at the cell periphery and consequently the membrane protrusion (Maciver, S. K. *et al.* 1998; Bernstein, B. W. *et al.* 2000). The enhanced actin polymerization could be one possible explanation for the high migratory activity of NRK cells being exposed to an alkaline environment since this cell type normally exhibits a slightly acidic intracellular milieu. On the contrary, tumor cells are naturally used to a permanently activated NHE1; if their equilibrium is imbalanced due the influence of alkaline environments, NHE1 activity decreases and could slow down adhesion and migration as only a distinct equilibrium and appropriate environment allows the interactions of integrins and ECM (Stock, C. *et al.* 2006).

All in all, a direct comparison of the collected data with results discussed in literature is quite complicated due to different assay formats, substrates for cell adhesion, buffer compositions, measurement techniques as well as data acquisition and evaluation since the cellular response is very sensitive and susceptible to experimental conditions.

Investigation of the influence of altered pH_e on cellular micromotion

A directed cellular movement is a very complex process depending on a coordinated activity of the cytoskeleton, the membrane and adhesion events. Directed cellular movement can be divided into four steps: (i) forward-directed movement of the membrane (protrusion), (ii) adhesion to generate movement along the substrate, (iii) movement of nucleus and cell body (traction) and (iv) de-adhesion and tail retraction at the rear end of the moving cell (Mitchison, T. J. *et al.* 1996). In a confluent cell monolayer without cell-free areas, cells can't move laterally but they are still moving in place. In 1984, Giaever and Keese noticed fluctuations in the impedance signal which could be significantly reduced by the addition of cytochalasin B, which causes cell immobilization due to interference with the polymerization of actin filaments (Giaever, I. *et al.* 1984). They attributed these irregular fluctuations with the movement of viable cells in a confluent monolayer. As already discussed, changing extracellular pH_e can lead to altered intracellular pH_i levels influencing protein activation and expression which is also important for polymerization and depolymerization of the actin cytoskeleton. There are many more factors affecting cellular micromotions.

The detections of pH-dependent cellular micromotions were expected to confirm that cellular micromotion decreases or increases with rising or falling proton concentrations. However, the results within their error margins did not unveil clear pH-dependencies with the exception of the SpiCa cell results. Their cellular micromotion revealed reliable results even under consideration of the respective errors. The cells being exposed to a pH_e of 7.4 showed the highest phenotypic activity in the micromotion experiments of (1.0 ± 0.1) which decreased under more alkaline conditions to (0.9 ± 0.1) and under extracellular acidification to as little as (0.05 ± 0.06) (pH_e 6.4) (see Tab. 5.11). This characteristic pH-dependency was also observed in the ECIS™-based proliferation investigations and confirmed by all migration examinations with SpiCa cells.

Cellular motility speed is reported to range between $8 \mu\text{m}\cdot\text{h}^{-1}$ and $40 \mu\text{m}\cdot\text{h}^{-1}$ for single cells adherent on planar substrates, depending on cell type, substrate surface and buffer composition (Bryce, N. S. *et al.* 2005; Park, S. *et al.* 2005). Taking into account that micromotion measurements offer a time resolution of five samples per second, one cell could theoretically have moved a distance of 0.4 nm – 2 nm in between two recordings, but cellular movement within a confluent monolayer is considered to be drastically decreased as was discussed previously. The resulting fluctuations in the impedance signal of a confluent monolayer are merely caused by the cellular motion in place and can be quantified by the micromotion experiments. However, the pH environment-induced changes in cellular micromotions were not pronounced enough compared with natural fluctuations in the cell signal. More drastic changes of the cell-specific impedance signal due to irreversible cell damage under the influence of toxins yielded more reliable results.

Investigation of the influence of altering pH_e on the respiratory activity of cell monolayers and 3D tissue

Respiration is an indispensable process for aerobic organisms to produce energy to be stored in form of adenosine triphosphate (ATP). There are two basic metabolic pathways: (i) aerobic respiration via glycolysis, oxidative decarboxylation of pyruvate, the generation of reduction equivalents NADH/ H^+ in the tricarboxylic acid cycle (citric acid cycle) and eventually the reduction of O_2 in the oxidative phosphorylation (OXPHOS), altogether converting one initial sugar molecule in a series of reactions into 32 ATP molecules and (ii) anaerobic glycolysis converting glucose in the cytosol in a series of reactions to pyruvate and later to lactate to generate two ATP molecules. Normal cells revert to the anaerobic glycolysis only under hypoxic conditions, whereas cancer cells generally shift their respiration towards an increased lactate production even at normoxic oxygen levels, which is called the *Warburg effect* or aerobic glycolysis (Kim, J. *et al.* 2006; Liberti, M. V. *et al.* 2016).

The investigations of pH-dependent respiratory activities revealed quite similar results for all four tested cell lines. A generally increased respiration rate with rising pH_e values was observed. The fastest *oxygen consumption rate* was detected for NRK cells exposed to alkaline conditions provoking a 34 % enhanced

respiration compared to physiological consumption rates. A549, SK-MEL-28 and SpiCa cells also showed elevated oxygen consumption rates with phenotypic activities of (1.5 ± 0.8) , (1.1 ± 0.3) and (1.3 ± 0.4) , respectively, when compared to respiration rates at a physiological pH_e of 7.4, while in parts, corresponding errors indicate heterogeneous cell responses. An extracellular acidosis caused a slight inhibition or slowed down cellular respiration as indicated by shrinking phenotypic activities of (0.7 ± 0.1) , (0.9 ± 0.2) , (0.7 ± 0.3) and (0.89 ± 0.02) for A549, SK-MEL-28, SpiCa and NRK cells, respectively, (see Tab. 5.11).

The investigations carried out with three-dimensional tissue models yielded two important results: (i) the detection of the respiratory activity is strongly dependent on the attachment time prior to the experiment and (ii) the examined pH-dependency in general was observed to be quite similar to the one of cell monolayers with the exception of emerging oxygen gradients beneath the spheroids. Longer attachment times allow for single cells to escape the spherical cell conglomerate and adhere to the substrate surface. This phenomenon permits the *outgrowing* of cells from the outer shell to create a radially growing cell monolayer around the spheroid. Stronger adhesion and monolayer formation restrict the free diffusion of dissolved oxygen into the subcellular compartment between the sensor foil surface and the basolateral membrane, leading to a more complete oxygen depletion with time. The emerging characteristic profiles have already been discussed in chapter 4.5. Since the cellular metabolism is strongly dependent on its environment, it is not surprising that cells grown either in a monolayer or as a spherical tissue, react similar to certain extracellular stimuli, e.g. altered pH_e . In contrast to cell monolayers, an acidic pH_e caused respiratory inhibition of the cells in the outer shell of the spheroid due to the direct contact with the supernatant medium which led to even worse conditions for the cells located towards the core of the spheroid. As nutrient and oxygen supply decreases from the outer layer to the center, this vital supply is even more restricted when cells located in the periphery are affected by e.g. altered pH_e . This process was observed due to characteristic and more pronounced oxygen concentration profiles for spheroids being exposed to alkaline conditions, while spheroids under the influence of acidic environments were not able to consume the dissolved oxygen as completely as the ones in contact with physiological or alkaline pH_e levels.

There are several possible mechanisms discussed in literature that could cause the adaption of the cellular oxygen respiration to changing extracellular and hence intracellular pH_i conditions. Wan, J. *et al.* 2019 determined the maximal respiration rates, hyperpolarization of the mitochondrial membrane, increased production of reactive oxygen species and ultimately cellular apoptosis of cells exposed to certain stress conditions. Rajpurohit, R. *et al.* 2002 investigated pH-dependencies of bovine nucleus pulposus cells and found falling glycolysis rates in the presence of low oxygen and glucose concentrations and at low pH conditions. Follow-up studies revealed *oxygen consumption rates* of only 32 % at a pH_e of 6.2 compared to those at 7.4 due to a rising glycolytic rate under increasing pH (Bibby, S. R. *et al.* 2005). Nevertheless, other studies observed increasing lactate and ATP production following an extracellular acidification of SK-MEL-28 cells, indicating equally an enhanced glycolysis as well as OXPHOS. This hyperactive hybrid metabolism is

usually linked to senescent cells, however, the higher mitochondrial membrane potential normally seen in senescent cells was not observed (Noguchi, F. *et al.* 2017). The respiratory sensitivity seems to be strongly dependent on the cell line since Ippolito, J. E. *et al.* 2016 could show slightly different responses to altered pH using neuroendocrine prostate cancer cells (PNEC). The PNEC cells were observed to show increased glycolysis and lactate production with increasing pH_e while at the same time, the OCR remained approximately constant. Thus, the energy was primarily derived from OXPHOS at lower pH_e and from glycolysis with subsequent lactate production at higher pH_e values. Schwerdt, G. *et al.* 2003 reported about a substantially increased amount of lactate from 2.1 $\mu\text{mol}/\text{mg}$ protein at a pH_e of 6.6 to 29.2 $\mu\text{mol}/\text{mg}$ protein at a pH_e of 7.6. The extracellular alkalization consequently led to accelerated lactate formation as a counterbalancing mechanism in order to restore an acidic extracellular microenvironment and hence the inverse pH gradient over the cell membrane as normally revealed by cancer cells. This could be a possible explanation for the slightly enhanced respiratory activity detected for all four cell lines in this thesis. Interestingly, according to mitochondrial stainings performed by Ippolito, J. E. *et al.* 2016, mitochondria at pH 6.5 were diffusely distributed in contrast to mitochondria aggregation at pH 8.5 while the *oxygen consumption rate* was constant. In addition to pH-dependent morphological changes and unwavering OCR, extracellular acidification seemed to cause a shift of the cellular metabolism to OXPHOS while under alkaline extracellular conditions, the cells could derive their energy from OXPHOS and glycolysis alike and an enhanced mitochondrial potential was observed.

Investigation of the influence of different pH_e on the intracellular pH_i

There was one main goal to be achieved in this chapter: the detection of the intracellular pH_i after changes in the extracellular environment. The data for the detection of the intracellular pH_i in correlation to the extracellularly adjusted pH_e allows for the validation of the pH gradient over the cellular membrane, although it is important to keep in mind that the extracellularly adjusted pH_e is not necessarily equal to the pH in the microenvironment of the cells. Fig. 5.23 shows the difference between the extracellular pH_e and the detected intracellular pH_i ($\Delta pH = pH_i - pH_e$), indicating a pH-gradient between the intracellular conditions and the extracellular pH-adjusted environment. NRK cells seemed to reveal slightly more acidic intracellular pH_i values in a pH_e range between 7.2 and 7.8, compared to the three cancer cell lines. The cancerous cells appeared to adjust their intracellular conditions a little more in the alkaline direction compared to the adjusted extracellular pH_e environment. The pH gradient, meaning the difference between pH_i and pH_e , as exhibited by NRK cells, decreased from (0.70 ± 0.01) over (0.51 ± 0.01) to $(0.07 \pm 4 \cdot 10^{-4})$ with increasing pH_e from 5.5 over 6.4 to 7.8. SK-MEL-28 and SpiCa cells, in contrast, revealed increasing pH gradients from $(0.38 \pm 6 \cdot 10^{-4})$ to (0.8 ± 0.03) and from (0.5 ± 0.01) to (0.64 ± 0.01) , respectively, with rising pH_e from 5.5 to 6.4, which decreased at a pH_e of 8 to final pH differences of around 0.1 and 0.09. A549 cells exhibited an

increasing pH gradient between a pH_e of 5.5 to 7.2 from around 0.4 to 0.6 with a subsequent decrease to a pH difference of 0.3. Within this thesis, A549 cells revealed a pH_i of 7.89 ± 0.01 after incubation with L-15 medium adjusted to a pH_e of 7.4, which is in agreement with Tanaka, N. *et al.* 2019.

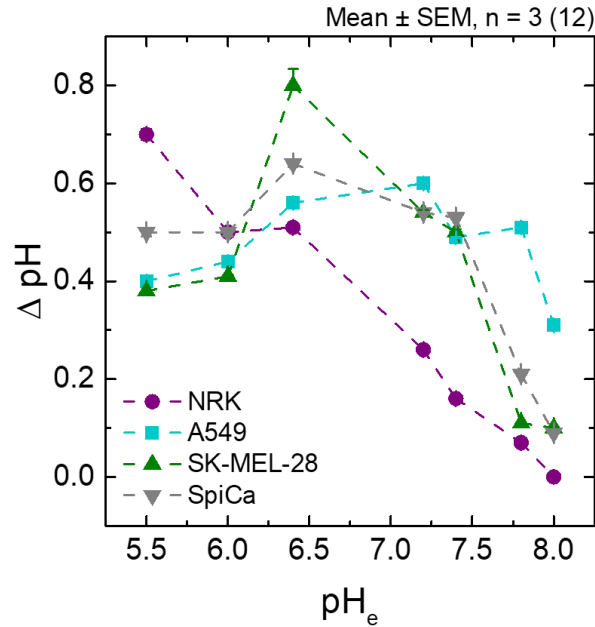


Fig. 5.23 pH gradient depicted as the pH difference between the detected intracellular pH_i and the pH-adjusted environment ($\Delta pH = pH_i - pH_e$) (compare Fig. 5.20, Tab. 5.10). The higher the pH difference, the more alkaline the pH_i was compared to the pH_e . Experiments were performed in three individual measurements, each in quadruplicate (Mean \pm SEM, $n = 3$ (12)) at 37 °C and 0 % CO_2 with L-15 adjusted to different pH_e values and the pH_i was determined using the pH-sensitive dye BCECF.

Despite these details in the pH differences, pH_i values generally increased with rising pH_e . Stüwe, L. *et al.* 2007 reported about similar observations, albeit performed with a different cell line: modified human melanoma cells MV3. In the publication, intracellular pH_i , detected via the use of BCECF, was demonstrated not to differ from the extracellular pH_e after 3 h of incubation and adaption time in an NHE1-deficient population, highlighting the crucial importance of NHE1 and the proton carrier ability. Within this thesis, the cells were incubated for 10 – 15 min with the respective pH-adjusted L-15 medium before the intracellular pH_i was measured. Longer incubation times could possibly lead to a further equilibration of the pH levels in the intra- and extracellular compartments.

5.8 OUTLOOK

The dysregulation of pH, differing between normal and cancer cells, is a well-known and quite familiar phenomenon (White, K. A. *et al.* 2017). Nevertheless, the pH-dependent behavior is not excessively discussed in literature. A more extensive characterization of the pH-dependency of cellular phenotypes could offer a more specifically targeted and sophisticated treatment of individual cancers. In combination with the knowledge of the working principles of important ion carriers and transport systems, as well as pH-sensing units within the cells causing expression of special proteins and signaling molecules, it could possibly improve the understanding of characteristic cancer behavior.

The performed assays yielded an, on average, cell line-specific pH-dependency over the variety of assays. But it is important to acknowledge that not every cell line was perfectly suited for every assay. SK-MEL-28 cells turned out to be rather unsuited for ECISTM-based investigations. Since there are studies indicating better cell adhesion to gelatin or collagen pre-coated surfaces, a surface treatment with these molecules could possibly enhance the impedimetric readout of SK-MEL-28 cells (Patel, D. *et al.* 2016; Xia, Y. *et al.* 2019). Cell-cell contacts are furthermore highly important for the building of spherical tissue models. The pH-dependent respiratory activity seemed to depend on cell packing density and tissue integrity. Supplementary investigations with respect to the strength of the cell-cell contacts to the overall structure of the spheroid could help to clarify the relation between metastatic activity (cells leaving the original tumor) and the formation of different biological zones within the spheroid.

The already discussed pH-dependent release of cytochrome c into the cytoplasm is discussed in literature to introduce apoptosis due to the activation of different caspases leading to the orchestration of biochemically induced cell death (Green, D. R. *et al.* 1998; Zou, H. *et al.* 1999). It is also reported that the initiation of apoptosis is accompanied by a more pronounced OXPHOS activity (Sergeeva, T. F. *et al.* 2017). The described protocol within this thesis for the investigation of the pH-dependent respiratory activity would be a reliable measurement setup for the examination to what extent a further increased pH_e would cause even more pronounced *oxygen consumption rates*, before a certain threshold is crossed and the alkaline pH_e causes drastically decreased OCRs due to induced apoptosis and consequently cell death.

For further and more detailed sensing of different pH gradients a closer look at the pH in the direct microenvironment of the cells is necessary. For these experiments, the planar pH-sensitive sensor foils, also produced by PreSens GmbH, could offer a great potential and a wide application range for investigations of pH changes in the microenvironment of living cells. All in all, as fundamental and essential as pH values are, in the field of pH sensing in cancerous tissues as well as pH-dependent cellular responses and metabolic reactions, many mechanisms are still unknown and need to be further investigated as reproducible pH sensing could be promising for the development of pH-targeted treatment and therapy strategies.

6 CYTOTOXICITY STUDY WITH BISPHENOL A

6.1 INFLUENCE ON THE RESPIRATORY ACTIVITY

The investigation of the cytotoxic effect of Bisphenol A (BPA) on the respiration of adherent NRK cells was performed using oxygen-sensitive sensor foils and sensor spots with the VisiSens TD and the SDR® reader, respectively. In both cases, NRK cells were grown to confluence on the respective substrate. The culture medium had been exchanged 24 h after cell seeding and after 48 h, the cells were incubated with different concentrations of BPA and the respiratory activity was observed along the BPA exposure.

6.1.1 IMAGE-BASED SENSING OF OXYGEN CONSUMPTION OF CELLS ON TOP OF THE SENSOR FOIL

The changes of the partial oxygen pressure (pO_2) were recorded for 21 h. The fluorescence intensity ratio of the oxygen-sensitive dye and the reference dye were translated into the respective partial oxygen pressure via a calibration of the sensor foil after the measurements and were plotted as a function of time. As the oxygen partial pressure exhibits a strong temperature dependence and the system inevitably cooled down during the preparation process before the measurement, the starting temperature was lower than 37 °C resulting in the first peak at 1 h in all measured time courses depicted in Fig. 6.1 A.

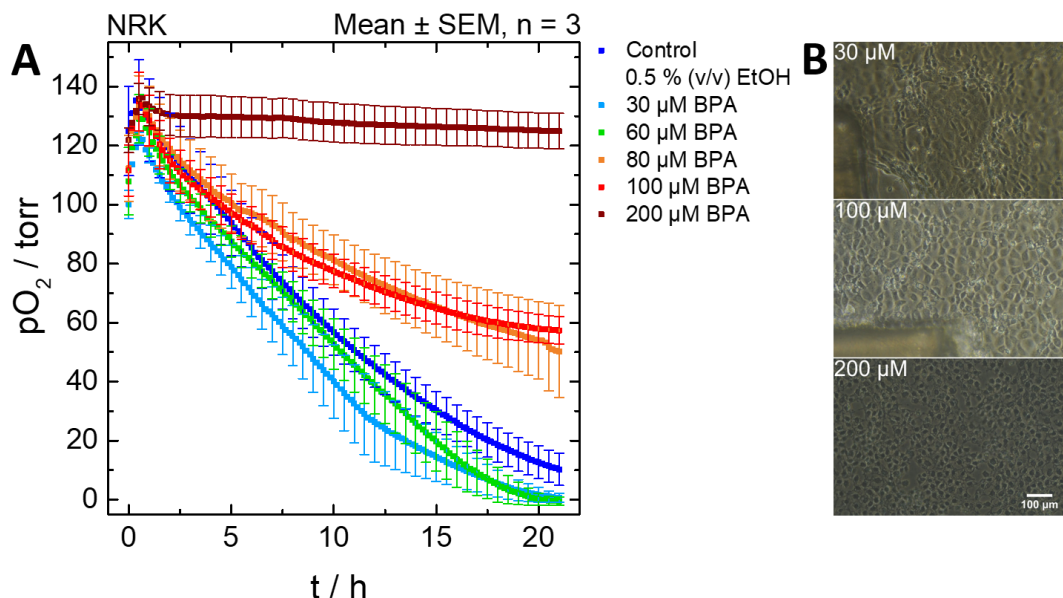


Fig. 6.1 (A) Decrease of the partial oxygen pressure underneath confluent NRK cells as a function of time under the influence of different Bisphenol A (BPA) concentrations detected with the VisiSens TD via oxygen-sensitive sensor foils. For control conditions, L-15 medium was supplemented with 0.5 % (v/v) ethanol which was equal to the solvent amount of the most concentrated BPA solution (200 μM). **(B)** Phase contrast images taken after the measurement. Scale bar depicts 100 μm. All measurements were performed in triplicate at 37 °C and 0 % CO₂.

Thereafter, a decrease in pO_2 could be observed due to the oxygen consumption of the cells. As control experiment, cells were treated with L-15 supplemented with 0.5 % (v/v) ethanol - the solvent of BPA and the concentration corresponds to the amount of solvent in the most concentrated BPA solution (200 μM) - to keep conditions constant and to be able to rule out influences of the solvent. The oxygen consumption decreased with increasing BPA concentration, except for the cells treated with the control solution resulting in (10 ± 5) torr after 21 h. The cells incubated with 30 μM and 60 μM of BPA were able to consume the available oxygen completely within 20 h, which was apparent from the drop of pO_2 to around 0 torr (see Fig. 6.1 A). Further increasing the BPA content led to correspondingly augmented partial oxygen pressures after the measurement. The treatment with 80 μM resulted in a remaining (50 ± 15) torr of the partial oxygen pressure and a pO_2 of around 57 torr and 125 torr was detected for 100 μM and 200 μM of BPA. Microscopic images of the cell monolayers after the experiment confirmed the results. The cells in contact to an extracellular BPA concentration of 30 μM and 100 μM still showed characteristic cobblestone morphology and exhibited a complete and adherent cell monolayer. Cells incubated with 200 μM BPA in contrast, displayed an altered morphology. At this concentration, the cells had the appearance of fixated and dried cell samples (Fig. 6.1 B).

A linear regression of the time courses between 1 h and 4 h yielded the *apparent oxygen consumption rate* (AOCR). The AOCR was then converted into the *oxygen consumption rate* to be able to compare results with the VisiSens TD and the SDR[®] system (compare chapter 3.4.5). The AOCR of (8.3 ± 0.1) torr·h⁻¹ yielded by the control experiments was exceeded by around 9 % and 3 % for the cells treated with 30 μM and 60 μM of BPA, respectively. As previously described, further increasing BPA concentrations led to decreasing oxygen consumption by the cells. In the presence of an extracellular concentration of 80 μM and 100 μM , the AOCR values were quite similar at (7.0 ± 0.6) torr·h⁻¹ and (7.1 ± 0.4) torr·h⁻¹, respectively. The highest concentration of BPA provoked the biggest change in the AOCR resulting in a small consumption rate of (0.6 ± 0.3) torr·h⁻¹. All calculated AOCRs and the corresponding OCRs are listed in Tab. 6.1.

Tab. 6.1 Summary of the calculated *apparent oxygen consumption rates* (AOCR) under BPA influence as well as the corresponding *oxygen consumption rates* (OCR). Values in brackets are depicted for the sake of completeness since the calculation of OCRs was difficult if oxygen depletion was not complete (see chapter 3.4.5). Experiments were performed at 37 °C and 0 % CO₂. Mean \pm SEM, n = 3, see Fig. 6.1.

c (BPA) / μM	AOCR \pm SEM / torr·h ⁻¹	OCR \pm SEM / amol·s ⁻¹ ·cell ⁻¹
Control (0.5 % (v/v) EtOH)	8.3 ± 0.1	(13.1 ± 0.2)
30	9.1 ± 0.5	14.2 ± 0.9
60	8.6 ± 0.7	14 ± 1
80	7.0 ± 0.6	(11 ± 1)
100	7.1 ± 0.9	(11 ± 2)
200	0.6 ± 0.3	(1.0 ± 0.5)

The calculated AOCR values were plotted against the respective BPA concentration, allowing to fit the data points with a 4-parameter logistic fit function. The dose-response curve revealed an EC_{50} value of $(159 \pm 235) \mu\text{M}$. The half maximal effective concentration (EC_{50}) describes the concentration of a toxin where 50 % of the maximum toxicity can be observed.

6.1.2 SENSING OF OXYGEN CONSUMPTION OF CELLS IN PROXIMITY TO THE SENSOR SPOT

The SensorDish Reader® (SDR®) was used as complementary technique for the monitoring of cytotoxic effects of BPA on adherent cells. In contrast to the measurements with the VisiSens TD, the decay time of the fluorescence lifetime of oxygen-sensitives dyes was used to examine the cellular respiratory activity in the presence of extracellular BPA. The cells were seeded to confluence in 24-well plates and grew around the sensor spot which was immobilized in the center of the wells. After the *standard pre-experiment protocol* several BPA concentrations were added, the air saturation was measured and afterwards plotted as a function of time. Fig. 6.2 shows the time courses of the air saturation.

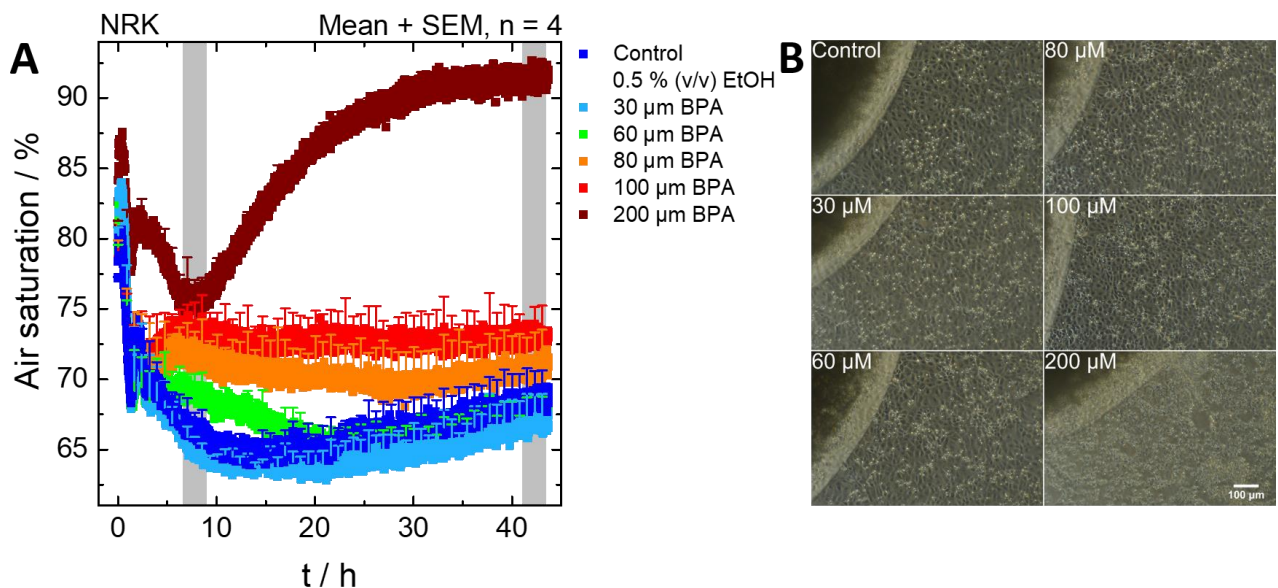


Fig. 6.2 SensorDish Reader® experiments: (A) Time-dependent changes in the air saturation being influenced by the respiratory activity of adherent NRK cells exposed to varying BPA concentrations. Measurements were performed within open systems in 24-well plates. For control conditions, L-15 medium was supplemented with 0.5 % (v/v) ethanol which was equal to the solvent amount of the most concentrated BPA solution (200 μM). Areas highlighted in grey indicate time intervals where air saturation values were averaged for further data evaluation. (B) Phase contrast images taken after the experiment. The experiments were performed at 37 °C and 0 % CO_2 .

After an initial sharp drop of the air saturation due to temperature effects, a strict concentration dependency could be observed. The initially low air saturation values occurred (i) due to the ongoing respiration of the cells which had been seeded 48 h prior to the experiment and (ii) because of the time which was needed for the preparation of the experiment during which the cells already consumed part of the available oxygen. The

control cells incubated with L-15 medium (+ 0.5 % (v/v) EtOH) and the cells under the influence of 30 μM BPA steadily respired the available oxygen until they reached a minimal air saturation of around 63 % to 65 % after 15 h. Concentrations of 60 μM , 80 μM and 100 μM led to a small initial increase in the air saturation before they reached nearly constant values of 73 % and 76 % for 80 μM and 100 μM , respectively. The cells exposed to 60 μM BPA consumed the oxygen, after a previous increase, to a minimum value of 65 % after 20 h of recording time. The most concentrated solution of 200 μM provoked a decrease in the air saturation to 66 % after 6.5 h, followed by a saturation curve increase resulting in 91.3 % air saturation after the measurement (Fig. 6.2 A). Phase contrast images taken after the experiment show the morphology of the cells after the treatment as well as the state of the cell monolayer (Fig. 6.2 B). In the upper left corner, a part of the sensor spot can be seen. The morphology of the cells treated with 200 μM BPA changed the most as the cells lost their monolayer integrity and looked similar to the one observed after the experiments with the VisiSens TD as described in chapter 6.1.1.

The main difference between the oxygen-sensitive sensor foils and sensor spots was not only the underlying measurement technique, but the sensor foils were only applied within closed systems while the sensor spots were used in open 24-well plates. Instead of calculating the slope of the time courses, averaged air saturation values were determined at two different time points. The first time interval was chosen due to the first steady-state moment under the exposition of 80 μM , 100 μM and 200 μM BPA between 6.5 h and 9 h. The highest concentration first led to a decrease of the air saturation before 6.5 h, caused by the respiration of the cells, with a subsequent and significant increase after 9 h resulting in 90 % air saturation after 45 h. Evaluating the air saturation values within this first 2.5-h interval by determining the average with a subsequent conversion into OCR values, offered the possibility of a direct comparison with the VisiSens TD experiments. The data conversion was done with the help of the Mamchaoui equation (see chapter 3.4.5). The control cells yielded an OCR of $(16.9 \pm 0.1) \text{ amol}\cdot\text{s}^{-1}\cdot\text{cell}^{-1}$ (VisiSens TD: $(13.1 \pm 0.2) \text{ amol}\cdot\text{s}^{-1}\cdot\text{cell}^{-1}$) which was used as a reference. The lowest BPA concentration of 30 μM displayed a slight increase to $(17.4 \pm 0.2) \text{ amol}\cdot\text{s}^{-1}\cdot\text{cell}^{-1}$. The *oxygen consumption rates* decreased to around $(12.5 \pm 0.1) \text{ amol}\cdot\text{s}^{-1}\cdot\text{cell}^{-1}$ for the highest concentration of 200 μM BPA. A dose-response curve of the values yielded an EC_{50} value of $(76 \pm 5) \mu\text{M}$ BPA.

Considering that the cells were growing not on top of but next to the sensor spot, which causes delayed changes of oxygen conditions due to diffusion processes, and that additional diffusion processes take place at the liquid-gas interface because of the open measurement setup, a second time interval was chosen at the end of the experiments. Prerequisites for the second interval were constant long-term signal values, indicating a state of equilibrium had been reached between 40.5 h and 43 h. The control wells as well as the two lowest BPA concentrations showed nearly similar values of 15.8, 16.6 and 16.2 $\text{amol}\cdot\text{s}^{-1}\cdot\text{cell}^{-1}$,

corresponding to a difference of only 5 %. At a concentration of 80 μM , one cell consumed (14.8 ± 0.1) amol of oxygen per second, decreasing to (13.8 ± 0.1) amol per cell and second under an extracellular concentration of 100 μM BPA. 200 μM BPA led to an *oxygen consumption rate* of only 36 % meaning (5.66 ± 0.03) $\text{amol}\cdot\text{s}^{-1}\cdot\text{cell}^{-1}$. Plotting these values as a function of concentration and fitting via a 4-parameter logistic fit function yielded an EC_{50} value of (149 ± 64) μM BPA. Tab. 6.2 lists the averaged air saturation values as well as all calculated OCRs for both time intervals.

Tab. 6.2 Summary of the averaged air saturation values obtained by the investigation of the respiratory activity of confluent NRK cells being exposed to different concentrations of BPA (see Fig. 6.2). Air saturation values were converted into the corresponding *oxygen consumption rates* (OCR) according to the Mamchaoui equation (compare chapter 3.4.5). Experiments were performed at 37 °C and 0 % CO_2 . Mean \pm SEM, n = 4.

$C_{\text{BPA}} / \mu\text{M}$	6.5 h – 9 h		40.5 h – 43 h	
	Mean Air saturation \pm SEM / %	OCR \pm SEM / $\text{amol}\cdot\text{s}^{-1}\cdot\text{cell}^{-1}$	Mean Air saturation \pm SEM / %	OCR \pm SEM / $\text{amol}\cdot\text{s}^{-1}\cdot\text{cell}^{-1}$
Control (0.5 % (v/v) EtOH)	66.2 ± 0.6	16.9 ± 0.1	68.5 ± 0.4	15.8 ± 0.1
30	64.9 ± 0.6	17.4 ± 0.2	66.8 ± 0.4	16.6 ± 0.1
60	68.8 ± 0.5	15.7 ± 0.1	67.6 ± 0.4	16.2 ± 0.1
80	71.4 ± 0.5	14.5 ± 0.1	70.8 ± 0.4	14.8 ± 0.1
100	73.2 ± 0.4	13.7 ± 0.1	72.9 ± 0.4	13.8 ± 0.1
200	75.9 ± 0.6	12.5 ± 0.1	91.3 ± 0.5	5.66 ± 0.03

6.2 DISCUSSION

At first glance, the results which were obtained with the ratiometric technique and the SDR[®] system were quite similar. The slightly lower consumption rates detected by the VisiSens TD could be due to the direct attachment of the cells on top of the sensor foil and the fact that the measurement was performed in a closed system with a limited supply of oxygen. As discussed previously, cells are able to adapt their metabolism to different levels of oxygen supply and, as in the case of the VisiSens TD measurement, no oxygen ingress from the ambient air was possible, the cells might have actively reduced their oxygen consumption. In contrast to the VisiSens TD measurement, the SDR[®] setup is an open-system approach where a constant oxygen ingress from the gas phase into the supernatant medium can occur. This in turn means that the cells at any time have access to more oxygen than the cells in the VisiSens TD setup and can therefore consume higher amounts of oxygen which would explain the higher OCR values.

Moreover, lower consumption rates of the control cells compared to 30 μ M BPA were noticeable. In the control experiment, L-15 medium was supplemented with 0.5 % (v/v) ethanol in order to keep the amount of the solvent identical to the highest BPA concentration, meaning the amount of ethanol decreased with decreasing concentrations of BPA. Consequently, L-15 medium prepared for control experiments contained 160 mM ethanol, similar to the 200 μ M BPA solution, which corresponds to an almost sevenfold higher ethanol content compared to the 30 μ M BPA solution. Ethanol is known to alter biophysical properties of biomembranes and proteins and affects many biochemical processes in living cells (Cui, S.-J. *et al.* 1997). Studies about the effect of ethanol on different cell lines (human lymphocytes, gastric mucosa cells and colon mucosa cells) showed a slightly decreased cell viability at low concentrations between 60 mM and 120 mM ethanol, which was determined via the trypan blue exclusion method (Blasiak, J. *et al.* 2000). Even a 10 – 20 % reduction of the cell number in the presence of an ethanol concentration of around 20 mM was reported in the case of PC12 cells (Pantazis, N. *et al.* 1992). A second possible explanation for higher OCR values at low BPA concentrations in comparison to the control cells could be a phenomenon called hormesis. Hormesis is an adaptive response to low concentrations of toxins leading to an enhanced metabolism. It is a modest over-compensation due to the disruption of homeostasis with a subsequent adaptive reestablishment until a state of equilibrium is reached again (Calabrese, E. J. *et al.* 2002). Either the influence of ethanol or the phenomenon of hormesis could have led to lower OCRs of the control cells and to the higher oxygen consumption under the influence of 30 μ M BPA.

Significant differences exist when the lowest and the highest concentration of BPA are compared. The 200 μ M BPA solution caused cell death in both assay types. The pO₂ levels, determined via the image-based system, revealed nearly constant signals at 125 torr. The measurements performed with the SDR[®] initially showed a strong respiratory activity, but subsequently steeply increasing oxygen levels up to 92 % air

saturation. Such high oxygen concentrations allowed to conclude that no further respiration took place due to induced cell death.

The resulting EC_{50} values of $(159 \pm 235) \mu\text{M}$ (VisiSens TD) and $(76 \pm 5) \mu\text{M}$ or $(149 \pm 64) \mu\text{M}$ (SDR[®] measurement at different time points) for BPA are listed in Fig. 6.3 B with the respective dose response curves shown in Fig. 6.3 A. The SDR[®] examinations revealed two different EC_{50} values, depending on the incubation time. Short-term investigations of up to 9 h exhibited an EC_{50} value of around 76 μM to achieve the half-maximal toxic effect while 73 μM of additional BPA content was needed to cause sufficient damage to the cells during long-term measurements of up to 43 h. Literature reports about a variety of EC_{50} values which depend on the target cell line, the incubation time as well as the detection method. EC_{50} values range from nanomolar concentrations e.g. 410 nM during the proliferation of MCF-7 cells (Stroheker, T. *et al.* 2004) to around 2.5 mM for CHO cells (Stiefel, F. *et al.* 2016). Alexander, H. C. *et al.* 1988 found EC_{50} values of $10 \text{ mg}\cdot\text{L}^{-1}$ (44 μM) and $1 \text{ mg}\cdot\text{L}^{-1}$ (4.4 μM) for *Daphnia magna* (water flea) and algae, respectively. Mørck, T. J. *et al.* 2010 reported about values between 100 μM – 125 μM after a 24-h incubation time with BPA, examined with BeWo cells (human choriocarcinoma cell line) using the alamarBlue[™] cell viability assay. The resulting EC_{50} values of $(159 \pm 235) \mu\text{M}$ and $(149 \pm 64) \mu\text{M}$ BPA from this thesis concur quite well with the ones reported in literature.

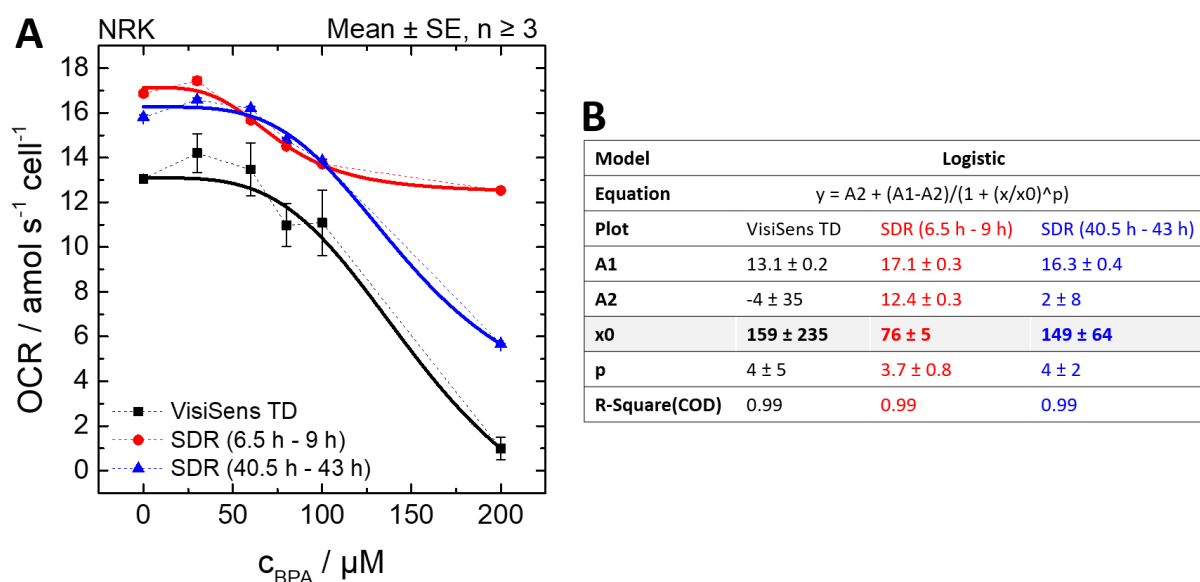


Fig. 6.3 Calculated oxygen consumption rates (OCR) plotted in the form of dose-response curves. (A) Dose-response curves for the two chosen time intervals of the SDR[®] reader and for the VisiSens TD measurement, each fitted with a 4-parameter logistic fit. (B) Summarized parameters extracted from the logistic fit and the resulting EC_{50} values ($x0$) measured with the VisiSens TD or the SDR[®] reader.

6.3 OUTLOOK

The toxic effect of BPA is still a highly discussed topic since it is still allowed to use the compound in selected products under differing statutory provisions around the world. The studies within this thesis showed a toxicity on normal rat kidney cells which is not to be neglected. However, the performed studies could be further refined with respect to the following aspects: (i) constant concentrations of ethanol in the different BPA concentrations to be able to rule out effects of changing ethanol concentrations on the cells, (ii) the application of additional concentrations between 100 μM and 200 μM BPA in order to be able to determine the EC_{50} value more precisely, (iii) performing described assays using human cell lines derived from the liver or digestive tract and (iv) replacement of PS Lab-Tek™ chambers with buffer reservoirs made of glass to avoid unspecific plastic binding of BPA in order to ensure constant BPA concentrations for the cells. Nevertheless, the performed studies in combination with ECIS™-based investigations (performed by Maria Zinkl and Saphia Azzam) allowed for an estimation of the toxicity of BPA in a very reliable manner.

7 PROFILING THE BIOLOGICAL IMPACT OF GLYPHOSATE ON ANIMAL CELLS

7.1 ACUTE TOXICITY OF GLYPHOSATE

The examination of the acute toxicity of glyphosate in the form of the pure substance and as part of a commercial formulation were performed using three different techniques. Firstly, the influence of glyphosate solutions on the cell viability was tested via PrestoBlue™ assays. These glyphosate solutions were tested either with previous adjustment to a physiological pH of 7.4 or were used as untreated solution with pH values of 2.4 and 5.8 for pure glyphosate and as ingredient in the Roundup® formulation, respectively. Secondly, the acute toxicity and the influence of the herbicide on the cellular phenotypes proliferation, migration and cellular micromotion was analyzed using ECIS™. The last technique was the monitoring of the respiratory activity of the cells under glyphosate exposure.

7.1.1 CELL VIABILITY ASSAY FOR ACUTE TOXICITY EXAMINATIONS

In the PrestoBlue™ assays, three different cell lines were grown to confluence in 96-well plates and after a 24-h incubation time with the different glyphosate/Roundup® concentrations, followed by an incubation of 1 h with the PrestoBlue™ reagent, the respective fluorescence intensities were recorded. According to the fluorescence intensities, the cytotoxicity indices (CI) were calculated (see chapter 3.7.1) and plotted against the respective concentration resulting in a dose-response curve. A 4-parameter logistic fit of the data points yielded the EC₅₀ values. Fig. 7.1 shows the CI values for the three cell lines in contact to glyphosate and Roundup® either in the form of the pH-adjusted or the untreated solution.

An abrupt increase in the toxicity can be observed for the acidic solutions in a concentration range between 1 mM and 5 mM glyphosate in comparison to the pH-adjusted solutions showing a smoother increase of the CI values. The treatment with 5 mM glyphosate (pure substance at pH 2.4 and commercial formulation at pH 5.8) led to a CI of 100 % for all three cell lines. Only the measurements performed with the MDCK II cells exhibited differences between the pure substance and the formulation in their acidic form. The pure substance showed a CI of (24 ± 3) % up to (45 ± 1) % in the sub-EC₅₀ concentration range between 0.2 mM and 2 mM while Roundup® led to a CI of only (16.2 ± 0.9) % and (24 ± 2) %, respectively. For the pH-adjusted solutions, a sigmoidally increasing CI could be observed for increasing concentrations as well as pronounced differences between the formulation and the pure substance. Thus, pH-adjusted glyphosate concentrations in the pure form below 10 mM yielded CIs between 15 % and 25 %. A high concentration of 20 mM led to CI

values of $(55 \pm 9) \%$, $(75 \pm 14) \%$ and $(40 \pm 7) \%$ for NRK, MDCK II and A549 cells, respectively, culminating in values of around 80 %, 100 % and 60 % for 40 mM of the pure glyphosate. Roundup® at a pH of 7.4 already reached 100 % toxicity at 20 mM in the case of NRK cells, and even 10 mM and 8 mM were enough to cause 100 % cytotoxicity indices for MDCK II and A549 cells, respectively.

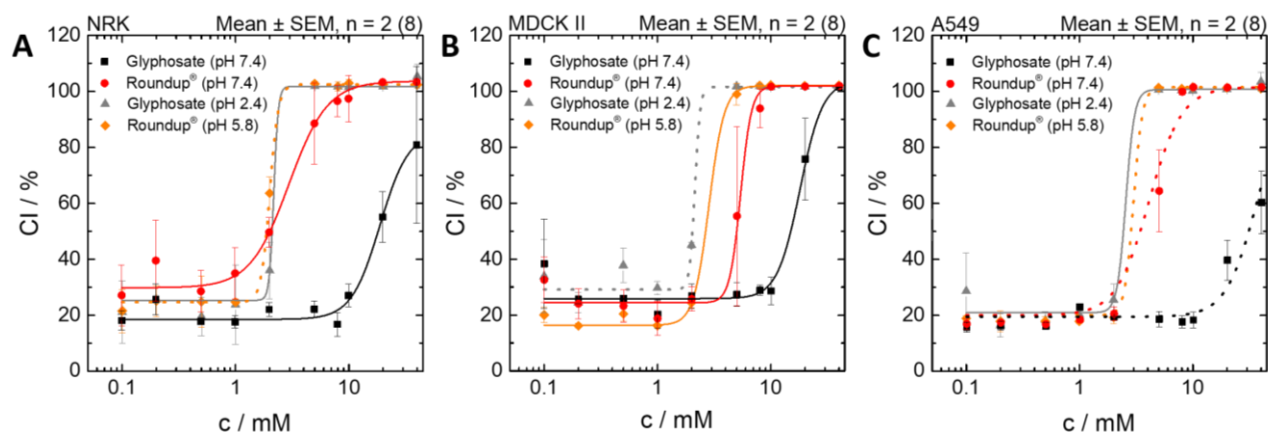


Fig. 7.1 Calculated cytotoxicity indices (CI) (obtained from the PrestoBlue™ assay) plotted against the respective herbicide concentration and fitted with the help of a logistic fit function ($y = A_1 + (A_1 - A_2) / (1 + (x/x_0)^p)$). CI was calculated on the basis of the background-corrected fluorescence of the negative control (see Chap. 3.7.1). The dose-response curves are color-coded: (black) pH-adjusted glyphosate, (red) pH-adjusted glyphosate as active ingredient in Roundup®, (grey) pure glyphosate dissolved in L-15 (pH 2.4) and (orange) commercially available Roundup® containing glyphosate, diluted with L-15 (pH 5.8) (data sets showing dotted dose-response curves had to be manually fitted as they were not ideally suited for the fit function). Experiments were conducted with NRK cells (A), MDCK II cells (B) and A549 cells (C) 48 h after cell seeding and following a 24-h herbicide exposure in two independent experiments each conducted as quadruplicate in a standard cell culture incubator ($T = 37 \text{ }^\circ\text{C}$, 0 % CO_2).

An evaluated logistic fit of the data points revealed the individual EC_{50} values. The EC_{50} value describes the amount of a toxic substance leading to the half-maximal effect and thus, cell death of 50 % of the total cell population. Tab. 7.1 summarizes the EC_{50} values for the three cell lines under the four tested conditions.

Tab. 7.1 EC_{50} values determined for glyphosate (pure substance) and Roundup® (herbicide formulation) by cell viability tests carried out with three different confluent cell lines. The values in brackets were also obtained by a logistic fit, however, the goodness of fit was imperfect and EC_{50} values were estimated with the help of the dotted fits (compare Fig. 7.1).

Cell line	Glyphosate		Roundup®	
	pH 2.4	pH 7.4	pH 5.8	pH 7.4
$\text{EC}_{50} / \text{mM}$				
NRK	1.99 ± 0.02	19 ± 8	(2.0 ± 0.5)	3.0 ± 0.2
A549	2.6 ± 0.7	(40 ± 10)	(3.0 ± 0.5)	(4 ± 1)
MDCK II	(2.2 ± 0.5)	18 ± 2	2.8 ± 0.3	5.4 ± 0.7

Since the logistic fit was not suited for all data sets (dotted dose-response curves in Fig. 7.1), some EC_{50} values are depicted with the corresponding estimated error values. These values were not calculated by the fit function, but only estimated and are given for the sake of completeness. The EC_{50} values measured after the treatment of the cells with the natural solutions (pH 2.4 and pH 5.8) vacillate between $(1.99 \pm 0.02) \text{ mM}$

(NRK, glyphosate) and (2.8 ± 0.3) mM (MDCK II, Roundup®). The pH-adjusted pure glyphosate solutions showed the highest and therefore least toxic EC_{50} value of approximately 19 mM for the three cell lines while the EC_{50} values of the pH-adjusted Roundup® solutions differed slightly between the cell lines. The half-maximal effect was achieved at (3 ± 0.2) mM Roundup® for NRK cells and (5.4 ± 0.7) mM Roundup® for MDCK II cells.

7.1.2 IMPEDANCE-BASED SENSING OF THE ACUTE TOXICITY

To be able to confirm the results of the PrestoBlue® assay, ECIS™-based acute toxicity examinations were performed. NRK cells were grown to confluence in 8W10E arrays and the impedance signal was recorded directly after the addition of the respective glyphosate solutions which were previously pH-adjusted to physiological conditions of 7.4. The applied concentrations were always calculated with respect to the concentration of the molecule glyphosate, either as pure substance or as part of the formulation in Roundup®. The addition of the different solutions led to morphological changes of the cell body due to the toxin, resulting in changing impedance values. A decreasing impedance signifies a fading membrane integrity and metabolic activity resulting in cell death. Fig. 7.2 displays the time-dependent impedance magnitude of a confluent NRK cell layer observed at an AC frequency of 16 kHz which was recorded for different concentrations of glyphosate. Data represents the mean of three individual experiments while the impedance magnitude was normalized to the first IZI value after toxin addition.

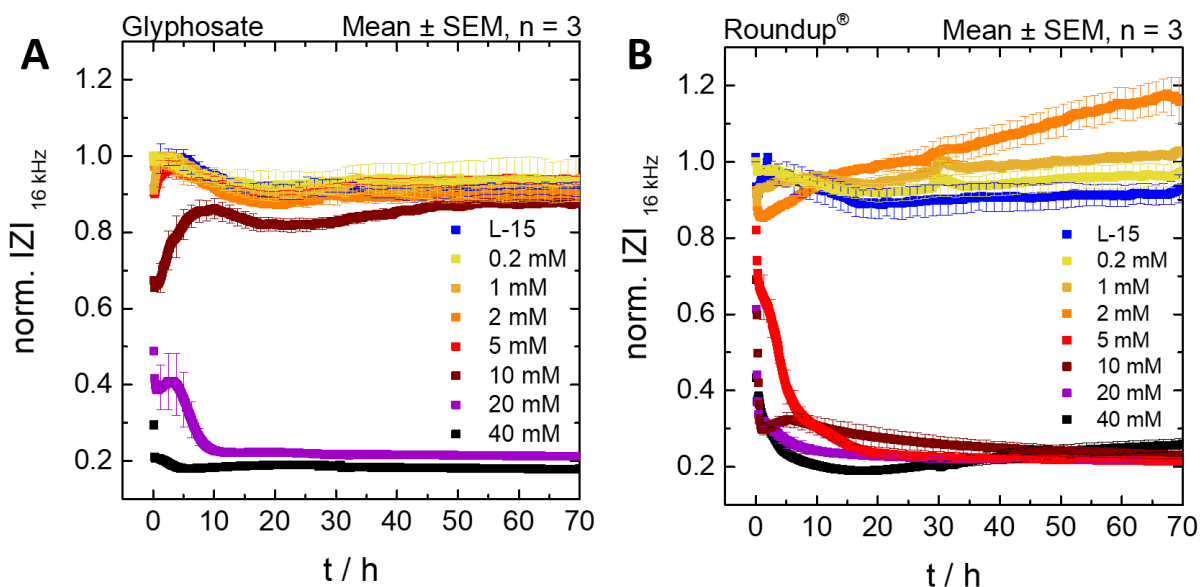


Fig. 7.2 ECIS®-based detection of the acute toxicity of glyphosate on confluent NRK cells grown on 8W10E arrays. (A) Recorded impedance magnitude as a function of time to examine the influence of pure glyphosate (pH 7.4) on the cells. (B) Time courses of impedance after the addition of glyphosate contained in Roundup® (pH 7.4). Experiments were performed in three individual experiments in a cell incubator (37 °C, 0 % CO₂). Impedance values were normalized with respect to the first value after toxin addition. The initial impedance magnitude of all wells was (1.53 ± 0.08) kΩ.

20 mM and 40 mM of pure glyphosate as well as concentrations higher than 2 mM of glyphosate in the formulation almost immediately induced cell death due to the drop of the normalized impedance to values of around 0.2. The pure glyphosate in a concentration of 10 mM led to a lower IZI value of 0.68 with a subsequent recovery of the impedance to the level of control values of around 0.9. Concentrations between 5 mM and 0.2 mM revealed time courses similar to the control experiments. Right after the start, a small increase in impedance could be observed due to turbulences in the medium following the addition, but then, constant impedance values of around 0.9 have been recorded. The addition of the three lowest concentrations of glyphosate in the herbicide Roundup® led to slightly increasing IZI values resulting in (0.98 ± 0.03) , (1.03 ± 0.04) and (1.16 ± 0.07) for 0.2 mM, 1 mM and 2 mM, respectively, while the control showed a nearly constant impedance signal of (0.94 ± 0.05) .

The time courses of impedance from Fig. 7.2 were used to calculate the AUC. For this calculation, the area under each curve of the independent experiments ($n = 3$) was determined in a time interval of 24 h with a baseline at $y = 0$ and subsequently averaged for each concentration. The AUC values were plotted as a dose-response curve and a 4-parameter logistic fit revealed the EC_{50} values for the ECIS™-based detection of the toxic effect of glyphosate on NRK cells. The pure substance caused the half-maximal effect in a concentration of (13.8 ± 0.6) mM, whereas only (4.0 ± 0.7) mM of glyphosate as part of the Roundup® formulation was needed to produce a similar effect on the cell viability. Fig. 7.3 A shows the two dose-response curves, each with the respective logistic fit, and the table in (B) summarizes the parameters of the fit functions.

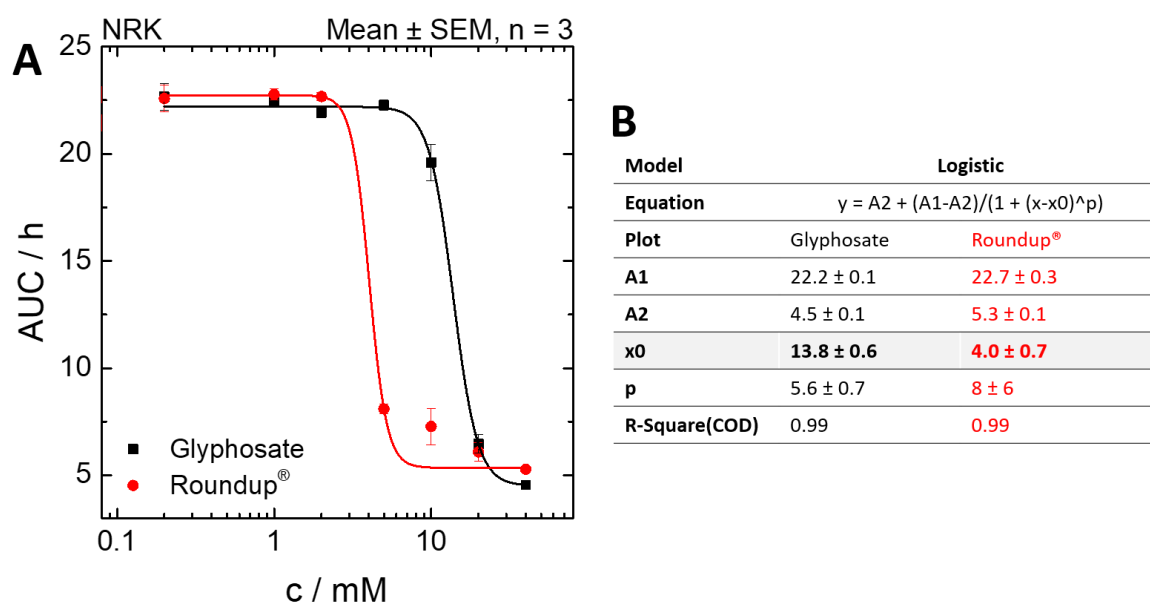


Fig. 7.3 (A) The calculated *area under the curve* (AUC) was plotted against the respective herbicide concentration and evaluated via a logistic fit function (dose-response curve). AUC values were obtained by integrating the impedance magnitudes at 16 kHz within the first 24 h of the ECIS™-based acute toxicity monitoring (compare Fig. 7.2) carried out with confluent NRK cells exposed to different concentrations of either pure glyphosate (**black**) or the glyphosate-containing formulation Roundup® (**red**). (B) Parameters of the logistic fit function, EC_{50} values are represented by the parameter x_0 .

7.2 COMPARISON OF CELLULAR PHENOTYPES UNDER THE INFLUENCE OF GLYPHOSATE

7.2.1 INFLUENCE ON PROLIFERATION RATES

The proliferation rate of cells growing on planar gold electrodes can be observed via decreasing capacitance (C) values in ECISTM measurements when the electrode was initially seeded with a well-defined but subconfluent number of cells ($2 \cdot 10^4$ cells·cm⁻²). Since the capacitance change is directly proportional to the cell coverage of the working electrode, constantly low capacitance values are due to an established confluent monolayer after the subconfluent seeding on 8W10E+ arrays (see chapter 3.3.4.2). After the *standard pre-experiment protocol* and the addition of three different concentrations of glyphosate, the capacitance was recorded. These experiments were also carried out applying glyphosate in two forms, as pure substance and as an ingredient in the herbicide formulation Roundup[®], while given concentrations were always calculated with respect to the glyphosate content.

Fig. 7.4 shows the normalized capacitance as a function of time. The capacitance was normalized with respect to the capacitance value at $t = 0$ h corresponding to the addition of the herbicides (48 h after cell seeding).

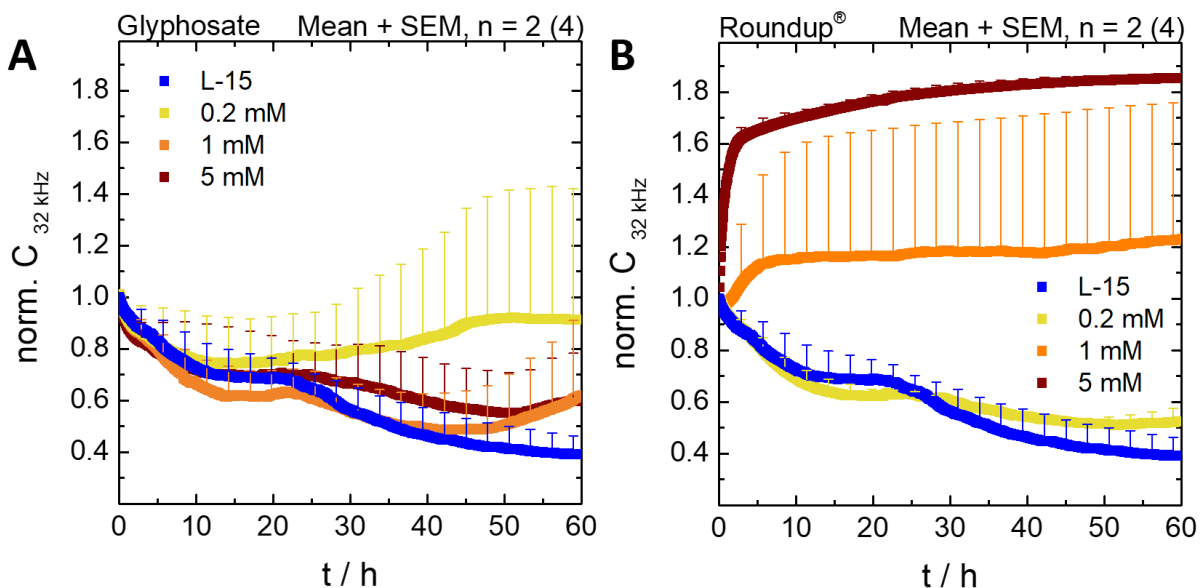


Fig. 7.4 ECISTM-based proliferation monitoring of subconfluent NRK cells ($2 \cdot 10^4$ cells·cm⁻²) grown on 8W10E+ arrays. Experiments were started 48 h after seeding and with the addition of the herbicide ($t = 0$ h) with a medium exchange 24 h prior to the addition. (A) Proliferation events under the influence of three different concentrations of glyphosate as pure substance. (B) Examination of cellular proliferation in contact to the herbicide Roundup[®] containing glyphosate as active ingredient. Capacitance values were normalized with respect to the first value after toxin addition. The initial averaged capacitance of all wells was (23 ± 6) nF. Experiments were performed in two individual experiments in which every condition was tested twice in a standard cell incubator (37°C , 0% CO_2).

After 23 h, a transient increase in the capacitance could be observed which was again followed by a decreasing capacitance due to cell division. Glyphosate in the pure form did not seem to affect proliferation much, and the magnitude of the error bars suggested that there were no significant differences. The NRK

cells incubated only with L-15 as a control, displayed normalized capacitance values of (0.39 ± 0.07) after 60 h of recording. The capacitance values under toxin influence were slightly higher at (0.9 ± 0.5) , (0.6 ± 0.3) and (0.6 ± 0.2) with increasing glyphosate concentration from 0.2 mM over 1 mM to 5 mM. In contrast to the effects of pure glyphosate, the glyphosate-containing Roundup® formulation led to significant changes in the normalized capacitance. The recorded capacitance under the influence of 0.2 mM Roundup® was quite similar to the control conditions, whereas the capacitance strongly increased for 1 mM and 5 mM of glyphosate included in the herbicide. 1 mM led to a capacitance increase to final values of (1.23 ± 0.5) after 60 h with an initial increase after 5 h. The error bars indicate a highly heterogeneous cellular response following the exposure with 1 mM Roundup®. 5 mM induced an even stronger effect on the cells, as the capacitance increased significantly directly after addition and eventually resulted in (1.85 ± 0.01) after 60 h of measurement time.

The normalized and time-resolved capacitance was used to determine the *area under the curve* (AUC). The time courses were integrated within the first 24 h and 60 h of recording without an integration limit ($y = 0$). Tab. 7.2 shows the calculated AUCs from the examination of the proliferation rates under the influence of glyphosate.

Tab. 7.2 Calculated *area under the curve* (AUC) of the proliferation experiments with subconfluent NRK cells ($2 \cdot 10^4$ cells·cm⁻²) on 8W10E+ ECIS™ arrays. AUC was integrated within the time intervals of 0 h – 24 h and 0 h – 60 h of the normalized capacitance (32 kHz) (compare Fig. 7.4). AUC values were additionally plotted against the respective herbicide concentration to obtain EC₅₀ values via a logistic fit (EC₅₀ values were manually estimated for imperfect fits). Experiments were performed at 37 °C and 0 % CO₂ in two independent experiments and in quadruplicate in total, Mean \pm SEM, n = 2 (4).

c / mM	AUC (0 h – 24 h) / h		AUC (0 h – 60 h) / h	
	Glyphosate	Roundup®	Glyphosate	Roundup®
L-15	18 \pm 3		35 \pm 7	
0.2	19 \pm 4	17 \pm 1	50 \pm 18	37 \pm 2
1	17 \pm 3	27 \pm 10	36 \pm 9	70 \pm 29
5	18 \pm 3	41 \pm 2	40 \pm 9	106 \pm 4
EC ₅₀ / mM	-	~ 1.5	~ 3.7	~ 1

The bigger the AUC, the more incomplete the proliferation, as proliferation events led to a decreasing capacitance signal and in turn to smaller AUC values. The AUCs in the 60-h time interval for different concentrations of glyphosate were relatively similar at (36 ± 2.4) h, only 0.2 mM revealed a slightly higher AUC of (50 ± 18) h. Increasing Roundup® concentrations, in contrast, entailed increasing AUC values. Pure L-15 showed an AUC of (35 ± 7) h as reference, which was increased to (37 ± 2) h, (70 ± 29) h and (106 ± 4) h under increasing concentrations of glyphosate included in Roundup®. The increasing AUC indicated decreasing proliferation activity of the NRK cells and the highest values were even correlated with immediate cell death and detachment of the cell bodies. The integration time of 24 h led to quite similar results. AUC

values were constant when determined for the cells being exposed to pure glyphosate while higher herbicide concentrations in the formulation exhibited larger AUC values. The AUCs were additionally used to determine an EC_{50} value via a logistic fit function. Since the data sets were not perfectly suited for the fitting, the dose-response curves were used to estimate EC_{50} values (compare Tab. 7.2).

7.2.2 INFLUENCE ON MIGRATION BEHAVIOR

The velocity of mammalian cell migration is a direct indicator with respect to their vitality and thus their metabolic activity. ECISTM offers the possibility to create reproducible wounds in the cell monolayer in the geometry of the working electrode by the application of electrical pulses which cause a permeabilization of the cellular membrane and consequently cell death. With time, the cell-free working electrode is repopulated by the surrounding, vital cells. This repopulation can be observed by increasing impedance values, and the time needed to again reach pre-wounding impedance values is an indicator for possible toxic effects of a substance in question (see chapter 3.3.4.3). In this experiment, NRK cells were seeded to confluence in 8W1E arrays, the culture medium was exchanged after 24 h and another 24 h later, the cells were incubated with different concentrations of glyphosate either as pure substance or as active ingredient in the herbicide formulation Roundup[®]. Following a 24-h incubation time, the cellular membranes of the cells growing directly on top of the working electrode were irreversibly permeabilized by electrical pulses.

Fig. 7.5 compiles the time-dependent impedance magnitudes at an AC frequency of 16 kHz recorded for confluent NRK cell layers which were wounded in the presence of different concentrations of glyphosate. Data represents the mean of three individual experiments while every condition was tested twice.

The magnitude of impedance was normalized with respect to the impedance value directly after the wounding process due to differing impedance values prior to the pulse application. The differing impedance magnitudes before the wounding resulted from already drastically harmed cells after exposure to 5 mM glyphosate in Roundup[®]. Immediately after wounding and membrane permeabilization at $t = 0.5$ h, the impedance dropped to values of a cell-free electrode as the cell bodies no longer restricted the current flow. The recorded impedance values under the influence of three different concentrations of pure glyphosate, dissolved in L-15 medium, did not show significant differences to the control curve within the range of the error bars. Only 5 mM glyphosate revealed slightly higher normalized impedance magnitudes of (2.9 ± 0.1) compared to (2.6 ± 0.2) shown by the control curve after 20 h of measurement time. Nevertheless, the overall migration profile and velocity as can be seen in the slope of the curves were quite similar. In contrast to the pure substance, a strong concentration dependency of the migratory behavior for the cells under the

influence of glyphosate in Roundup® was observed. The impedance values of the cells treated with 5 mM glyphosate in Roundup® were very low already before wounding and remained unchanged to yield final values of (0.97 ± 0.02) after 22 h. Decreasing the glyphosate content to 1 mM and 0.2 mM gradually increased the impedance magnitude. Nevertheless, final normalized IZI values after 22 h were (1.7 ± 0.3) and (2.4 ± 0.3) which was still significantly lower than the control. In the case of Roundup®, drastically reduced migration velocities and incomplete wound closure were observed for higher concentrations of Roundup® (see. Fig. 7.5 B).

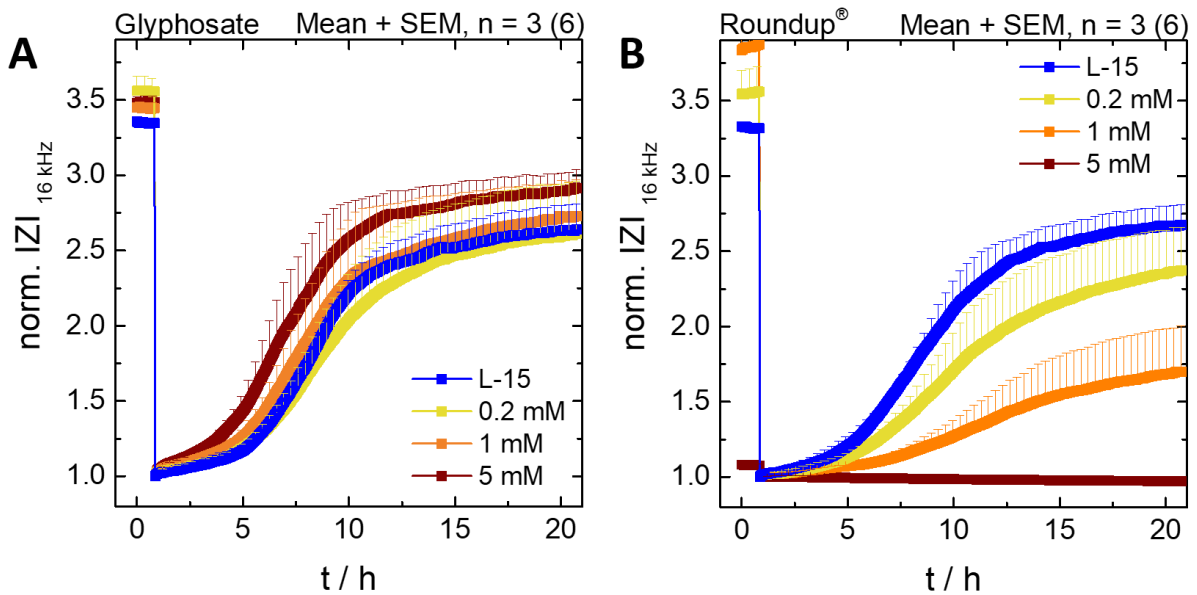


Fig. 7.5 ECIS™-based detection of the wound healing behavior of NRK cells grown to confluence on 8W1E arrays. The impedance drop was caused by the application of an electrical wounding pulse (32 kHz, 2400 μ A for 30s) inducing irreversible membrane permeabilization resulting in cell death. The subsequent increase in impedance occurred due to the migration of still vital cells from the periphery into the wound. (A) Wound healing behavior under the influence of glyphosate as pure substance. (B) Migration rate depending on glyphosate concentrations in Roundup®. Experiments were performed in three individual experiments in which each condition was tested twice. Impedance values were normalized to the first value after wounding, initial impedance magnitude values were: L-15 (2.8 ± 0.5) k Ω , Glyphosate: 0.2 mM: (2.7 ± 0.07) k Ω , 1 mM: (2.7 ± 0.1) k Ω , 5 mM: (2.6 ± 0.1) k Ω , Roundup®: 0.2 mM: (2.8 ± 0.05) k Ω , 1 mM: (2.6 ± 0.07) k Ω , 5 mM: (2.1 ± 0.08) k Ω . Experiments were performed in a standard cell culture incubator at $T = 37$ °C and 0% CO₂.

The time-dependent impedance magnitudes were used to calculate the AUC by integration from 1 h to 22 h with an integration limit of the y-axis of $y = 0.9$. The AUC values were plotted against the respective glyphosate concentration and can be seen in Fig. 7.6. The pure glyphosate in rising concentrations led to slightly increasing AUC values compared to the AUC calculated for the control conditions with (20 ± 2) h. Experiments performed with the formulation Roundup® exhibited a strong concentration dependency. Increasing concentrations of glyphosate led to decreasing AUC values. The area decreased from (15 ± 4) h over (8 ± 3) h to (1.6 ± 0.3) h for 0.2 mM, 1 mM and 5 mM glyphosate in Roundup®, respectively.

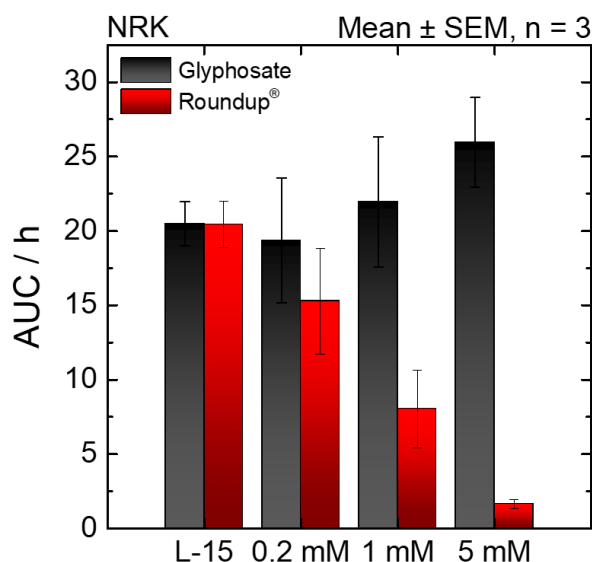


Fig. 7.6 Calculated *area under the curve* (AUC) of the migration experiments with confluent NRK cells ($25 \cdot 10^4$ cells·cm⁻²) exposed to glyphosate as pure substance or as active ingredient in the formulation Roundup® on 8W1E ECIS™ arrays. AUC values were calculated within the time interval of 1 h – 22 h from the normalized impedance (16 kHz) (compare Fig. 7.5) with a 24-h incubation time with the respective herbicide prior to wounding. Experiments were performed at 37 °C and 0 % CO₂ in three independent experiments.

7.2.3 INFLUENCE ON CELLULAR MICROMOTION

Cells and even cell monolayers are very motile systems. ECIS™ offers the possibility of measurements to quantify cellular micromotion. Thanks to the very high resolution of this measurement mode with five samples per second, it is possible to quantify the motility of the cells due to the calculation of the variance from the measured impedance magnitude at 16 kHz (see chapter 3.3.4.4).

The micromotion was examined for a confluent monolayer of NRK and MDCK II cells in 8W1E arrays. 24 h after the addition of the different glyphosate solutions, RTC data was recorded for 10 min per well. The variance values were normalized to the variance of the control wells. Higher variances can occur following extracellular changes and drastically decreased variance values indicate cell death. Fig. 7.7 depicts the variance values of NRK and MDCK II cells after 24 h of incubation with either glyphosate or the commercially available herbicide Roundup®.

At first glance, no strict concentration dependencies were observed. Glyphosate as pure substance generally increased the micromotion of both cell lines, only concentrations higher than 10 mM led to undetectable cellular movements in the case of MDCK II cells. A sharp drop in the variance values was observed for Roundup® concentrations higher than 1 mM and 5 mM for NRK and MDCK II cells, respectively. MDCK II cells treated with a concentration of 5 mM glyphosate in Roundup® revealed a variance of only (91 ± 90) % compared to the control conditions, although the errors bars indicate that the cellular response was very heterogeneous which could be due to the proximity to the EC₅₀ value which was determined in cytotoxicity

assays. Concentrations between 0.2 mM and 2 mM Roundup® on MDCK II cells led to fluctuating variance values and there was no significant trend to be observed within the margin of error.

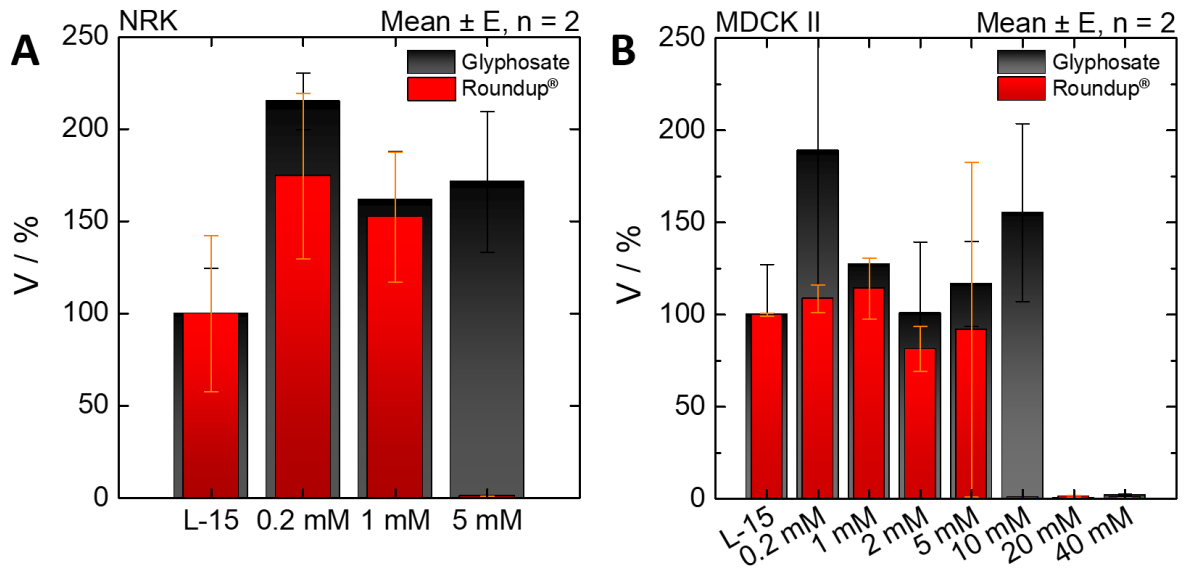


Fig. 7.7 Calculated variance values of confluent NRK and MDCK II cells after exposure to pure glyphosate and commercially available Roundup®, normalized with respect to the variance of the control experiments with L-15 as supernatant. The variance was determined via ECIS™-based micromotion measurements and further evaluation of the recorded impedance at 16 kHz. Variance values of (A) NRK cells and (B) MDCK II cells after a 24-h glyphosate and Roundup® exposure. E (error) describes the spread of the two averaged data points from the two individual data sets. Experiments were performed in a standard cell incubator at T = 37 °C and 0 % CO₂.

7.3 RESPIRATORY ACTIVITY UNDER GLYPHOSATE EXPOSURE

The monitoring of the respiratory activity of NRK cells was performed using the VisiSens TD system in combination with oxygen-sensitive sensor foils. The cells were grown on top of the sensor foil and 48 h after seeding, the cells were treated with different concentrations of glyphosate either as pure substance or as part of the herbicide Roundup®. All glyphosate-containing solutions were adjusted to a pH of 7.4 prior to cell exposure. After filling and airtight sealing of the petri dishes, the recording was started and images of the sensor foil were taken every 10 min for a time course of 24 h. The fluorescence intensities were translated into false color images directly after calibration. The evaluation of the false color images revealed the oxygen partial pressure for each picture and thus, the pO_2 could be plotted as a function of time.

Fig. 7.8 shows the decrease of the partial oxygen pressure as a function of time due to the respiratory activity of NRK cells in direct contact to glyphosate or Roundup® in the supernatant medium.

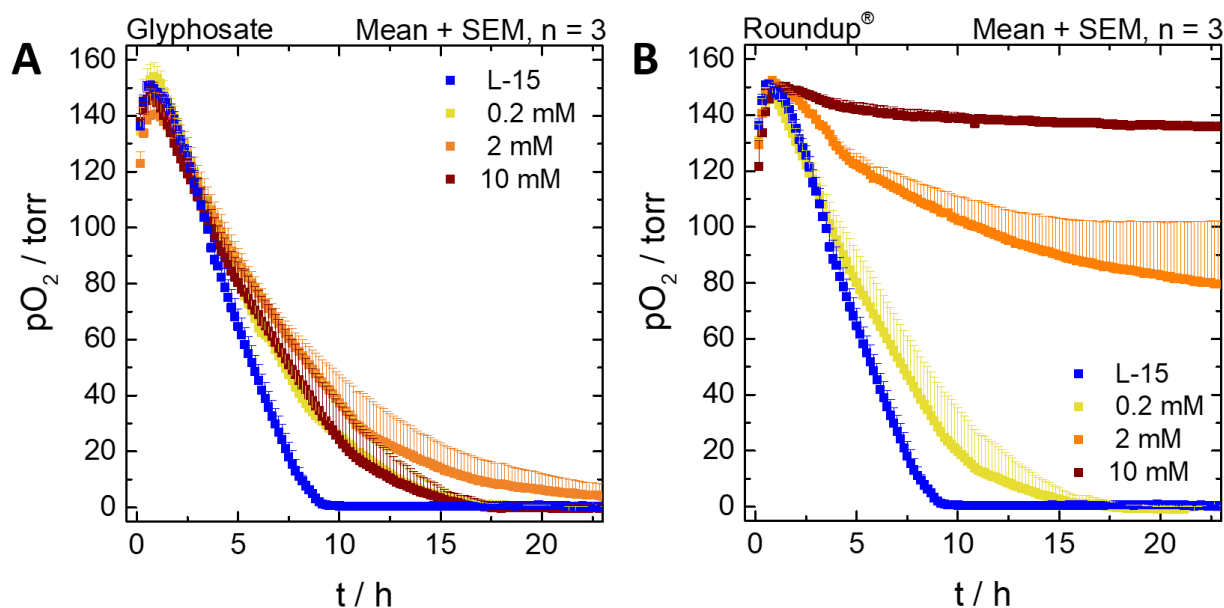


Fig. 7.8 Time-dependent sensor foil-based monitoring of the respiratory activity of confluent NRK cells being exposed to (A) glyphosate as pure substance and (B) glyphosate as part of the herbicide Roundup® in different concentrations with L-15 representing control conditions. Addition of the herbicide was done 48 h after cell seeding at $t = 0$ h. Experiments were performed in triplicate at 37 °C and 0 % CO_2 .

The cells incubated only with L-15 medium, which served as control experiment, were able to respire the available oxygen within 8.5 h, resulting in 0 torr of oxygen partial pressure. 0.2 mM and 10 mM glyphosate as pure substance led to a complete oxygen depletion in 17.6 h, whereas 2 mM glyphosate induced a slightly delayed decrease in pO_2 resulting in (5 ± 5) torr after 23 h. In contrast to the pure substance, the experiments performed with the herbicide formulation Roundup® exhibited a strong concentration-dependent decrease of the pO_2 . L-15 medium and 0.2 mM glyphosate in Roundup® led to a complete oxygen consumption within 8.5 h and 17.5 h, respectively. The decrease of the oxygen partial pressure under the influence of 2 mM and

10 mM Roundup[®], however, was drastically slowed down yielding a pO_2 of only (84 ± 40) torr and (135.7 ± 0.8) torr after 23 h, respectively.

A linear regression of the time courses between 1 h and 4 h allowed for the calculation of the AOCR. The cells incubated only with L-15 medium were able to consume (23 ± 2) torr·h⁻¹ of the available oxygen. The different concentrations of pure glyphosate only led to a fluctuation of the AOCR values between (19 ± 4) torr·h⁻¹ (0.2 mM glyphosate) and (14 ± 1) torr·h⁻¹ (2 mM glyphosate). In contrast to the pure substance, decreasing glyphosate concentrations in Roundup[®] from 10 mM over 2 mM to 0.2 mM correlate with rising AOCRs of (2.4 ± 0.9) torr·h⁻¹, over (7.4 ± 0.9) torr·h⁻¹ up to (17 ± 2) torr·h⁻¹. Tab. 7.3 summarizes the AOCRs and *oxygen consumption rates* (OCRs) for the experiments shown in Fig. 7.8.

Tab. 7.3 Summary of the calculated *apparent oxygen consumption rates* (AOCRs) from the detection of the glyphosate-dependent respiration of confluent NRK cells via an image-based detection using an oxygen-sensitive sensor foil (compare Fig. 7.8). AOCRs were used to determine *oxygen consumption rates* (OCRs). Values in brackets are depicted for the sake of completeness since the calculation of OCRs was difficult if the oxygen depletion was not complete (see chapter 3.4.5).

	AOCR ± SE / torr·h ⁻¹	OCR ± SE / amol·s ⁻¹ ·cell ⁻¹	AOCR ± SE / torr·h ⁻¹	OCR ± SE / amol·s ⁻¹ ·cell ⁻¹
	Glyphosate		Roundup [®]	
L-15	23 ± 2	35 ± 3	23 ± 2	35 ± 3
0.2 mM	19 ± 4	29 ± 6	17 ± 2	27 ± 3
2 mM	14 ± 1	22 ± 2	7.4 ± 0.9	(12 ± 2)
10 mM	17 ± 1	27 ± 2	2.4 ± 0.9	(4 ± 1)

7.4 POST-EXPOSURE CELL STAINING

In the aforementioned measurements, 24-h incubations with high concentrations of Roundup® led to a phenomenon normally observed for fixated NRK cells. Although the ECIS™ signal indicated cell death, an intact monolayer exhibiting the normal cobblestone morphology was optically observable after the measurements. In order to image the cell viability as well as to visualize the integrity of the cytoskeleton, cell stainings were performed after a previous 24-h incubation with 40 mM, 20 mM and 1 mM of glyphosate as pure substance and as active ingredient in the herbicide formulation Roundup®. For reasons of comparison and control, cells were also incubated only with L-15 medium. Cell viability was investigated by live/dead staining and the cell cytoskeleton was labeled with TRITC-phalloidin in combination with nuclei staining by DAPI (see chapter 3.2.4).

Fig. 7.9 shows the CLSM images of **(A)** NRK cells having been treated with pure glyphosate and **(B)** NRK cells after incubation with Roundup®. Following L-15 preincubation, the cells revealed the characteristic cobblestone morphology and only green fluorescence was detected after live/dead staining, indicating good cell viability. The staining of the cytoskeleton furthermore confirmed the cobblestone-like, regular and equally distributed morphology according to the emitted red fluorescence and the blue-fluorescent nuclei were quite similar in shape and size. 1 mM of glyphosate in Roundup® as well as 20 mM of the pure substance yielded results similar to the control experiments with the only difference that a few dead cells were observed after the exposure to the substances. Higher concentrations led to more drastic effects on the cell monolayer. 40 mM of the pure glyphosate irreversibly debilitated the cells ending in almost complete cellular detachment and cell death. In contrast to these observations, 40 mM as well as 20 mM of the glyphosate-containing formulation caused complete cell death as indicated by the lack of green fluorescence and the sole red fluorescence detected after live/dead staining. Nevertheless, the DAPI and phalloidin staining depicted an apparently intact cell monolayer. The cytoskeleton staining showed a strong red fluorescence which was especially concentrated in the areas of the cell-cell contacts. Regarding the patches of blue fluorescence, differences in size were observed. The highest concentration led to a significantly decreased size of the nuclei compared to the images of the DAPI staining taken after the incubation with 20 mM glyphosate in the Roundup® formulation.

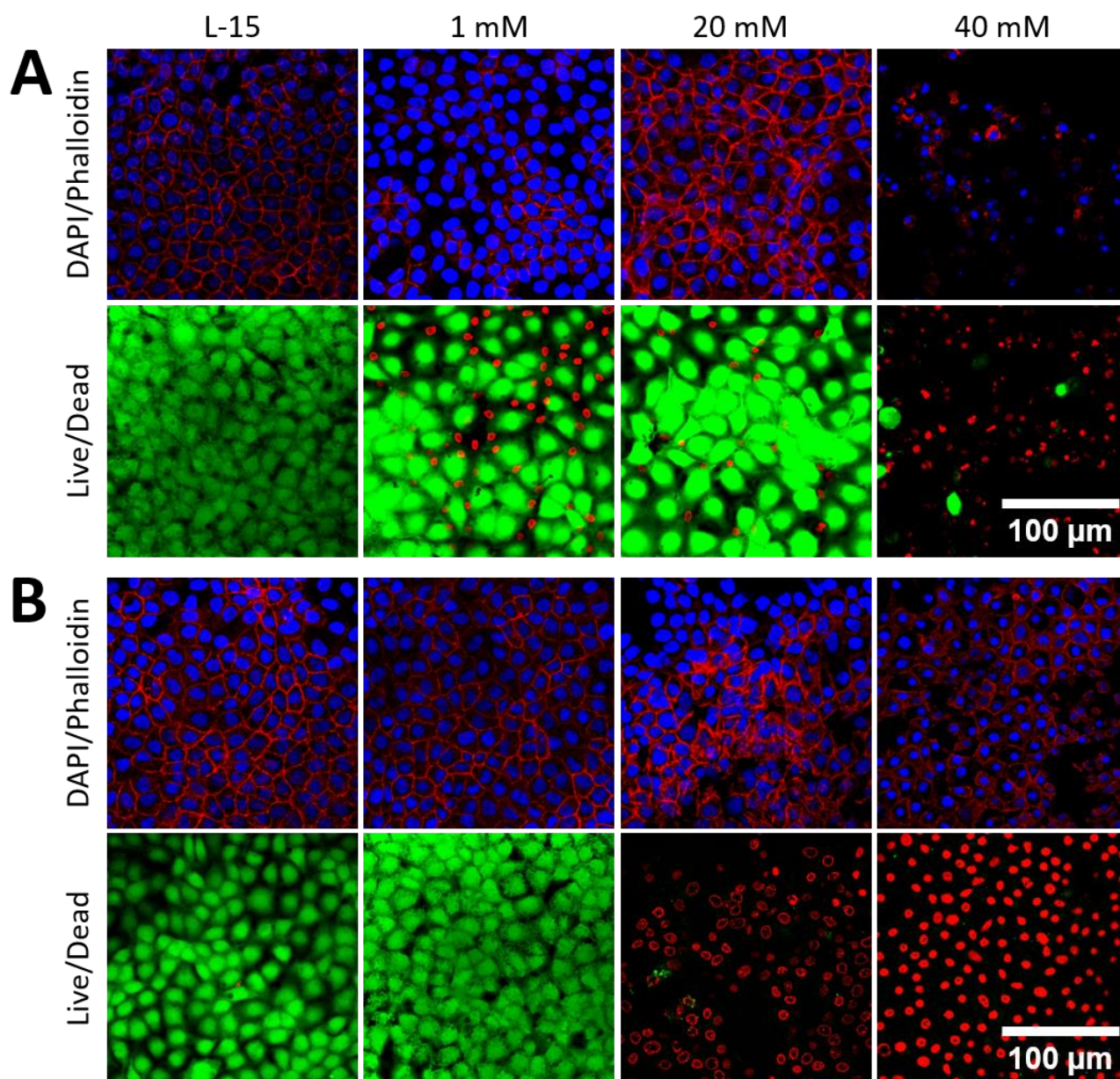


Fig. 7.9 NRK cell staining to examine the state of viability (Live/Dead), the integrity of the cytoskeleton (Phalloidin) and to locate the cell nuclei (DAPI). Living cells exhibit green fluorescence while dead cells are indicated by red emitted fluorescence due to intercalation processes of EtHD into the DNA. (A) Cell staining after the 24-h exposure to glyphosate as pure substance and (B) after the 24-h incubation with different glyphosate concentrations contained in the herbicide formulation Roundup®. CLSM images were taken with the 60x immersion objective and pinhole M.

7.5 DISCUSSION

The three different cell lines used in the study of the biological impact of glyphosate were chosen to represent human and animal cells which are both naturally exposed to the herbicide, as well as to represent the different incorporation ways of glyphosate. A549 are human lung adenocarcinoma cells and were chosen to investigate the toxicity on human cells as well as to mimic the inhalative uptake of glyphosate and its influence on lung cells. NRK and MDCK II cells are kidney cells derived from rat and dog, representing animal cells and at the same time cells which play an important role during blood filtration and the excretion of metabolic waste and toxins into the urine. There are studies reporting that the gastrointestinal tract of humans absorbs about 20 % of the glyphosate which was incorporated with the food, while 80 % are excreted in the feces. In contrast to humans, rats are suggested to excrete nearly all of the glyphosate rapidly and unchanged with the urine (McGuire, M. K. *et al.* 2016) which proves the suitability of kidney cells.

The herbicide formulation is always a mixture of an active ingredient with supplemented adjuvants, with glyphosate being the active ingredient. Although the adjuvants are said to be inert diluents, many side effects are already known. Adjuvants are often used as permeabilizing agents, stabilizers, surfactants, emulsifiers, solvents and many more. In these studies, Roundup® LB plus was used. Since the exact formulation is not officially declared, it is difficult to discuss effects and possible impacts of special adjuvants. Literature reports about a 16 % content of an unknown surfactant (Wagner, N. *et al.* 2013). Benachour, N. *et al.* 2009 and Mesnage, R. *et al.* 2013 have conducted studies on the composition of glyphosate-based herbicides and could show that the commercial formulations are significantly more toxic than the active ingredient glyphosate alone. Richard, S. *et al.* 2005 reported about a twice as much reduced cell viability after the treatment with Roundup® compared to glyphosate, with the effect being more pronounced with increasing incubation time. All in all, glyphosate is a highly controversial topic where one side is convinced that the use of glyphosate is harmless and the other side sees glyphosate responsible for the development of non-Hodgkin lymphomas and even in literature the authors sometimes do not even declare their formulation under investigation which makes it hard to compare experiments.

Detection of the acute toxicity of glyphosate

The quantification of the acute toxicity of glyphosate in the two aforementioned forms revealed clear and reproducible results. The PrestoBlue® assays performed with the pH-adjusted and the acidic glyphosate solutions showed a drastically higher toxicity for the pure glyphosate ($EC_{50} = (1.99 \pm 0.02)$ mM, NRK cells) which was dissolved in L-15 medium and revealed a pH value of around 2.4, while the pH-adjusted solutions exhibited an EC_{50} value of around 19 mM. Comparing the EC_{50} values after incubation with Roundup®,

concentrations ranged from (3.0 ± 0.2) mM (NRK cells) to (5.4 ± 0.7) mM (MDCK II cells) for the pH-adjusted solutions, while the naturally acidic solutions revealed an EC_{50} value of around 2 mM for all tested cell lines. In general, an acidic pH is reported to inhibit melanosome transport and to lead to altered microtubule and actin morphology, whereas the acidic Roundup® solution is reported to disassemble microtubule and actin filaments. Under physiological pH, the effect of Roundup® as well as the lipophilicity of pure glyphosate and thus the diffusion into the cytoplasm seems to be lower (Hedberg, D. *et al.* 2010), thereby confirming the observed decreasing toxicity of glyphosate with increasing pH. Hedberg, D. *et al.* 2010 used melanophores and fibroblasts from African clawed frog and cytoskeleton investigations were performed 24 h after incubation with glyphosate or Roundup® via immunostainings and phalloidin staining.

The EC_{50} values obtained by the PrestoBlue™ and ECIS™-based toxicity monitorings were in a similar concentration range and are in accordance with the ones found in literature. Tab. 7.4 gives an overview of selected EC_{50} values from literature which, in parts, were determined with an MTT cell viability test (similar to the PrestoBlue™ assay) and cover a broad spectrum of different cell lines. EC_{50} values determined within this work are also included for a direct comparison.

The half-maximal effects range from concentrations of 1.86 mM to 38 mM which is in good accordance with the values of 1.9 mM to 19 mM which were obtained during the studies within this work. The generally higher toxicity of glyphosate as a component of the herbicide formulation Roundup® in comparison to the pure substance is also confirmed in literature according to the corresponding EC_{50} values (Benachour, N. *et al.* 2007).

Tab. 7.4 Overview of different EC_{50} values yielded within **this thesis** in comparison to half-maximal toxic concentrations discussed in literature for pure glyphosate and the herbicide formulation (Roundup®).

Cell type	EC_{50} value	Assay type	Literature
Raji (Burkitt's Lymphoma cells, human)	5-10 mM / 0.8-1.6 mg·mL ⁻¹		Townsend, M. <i>et al.</i> 2017
DIMF (fin cell line from Oriental Weather Loach <i>Misgurnus anguillicaudatus</i>)	1.86 mM / 0.32 mg·mL ⁻¹	MTT cell viability test (24 h incubation with glyphosate or Roundup®)	Qin, Y. <i>et al.</i> 2017
HaCaT (human epithelial keratinocyte cells)	21 mM / 3.6 mg·mL ⁻¹		Elie-Caille, C. <i>et al.</i> 2010
JEG3 (human choriocarcinoma-derived placental cells)	~ 38 mM / ~ 6.4 mg·mL ⁻¹ ~ 26 mM / ~ 4.4 mg·mL ⁻¹ (Roundup®)		Benachour, N. <i>et al.</i> 2007
293 cells (human embryonic kidney cells)	~ 36 mM / ~ 6.1 mg·mL ⁻¹ ~ 18 mM / ~ 3.0 mg·mL ⁻¹ (Roundup®)		
MC3T3-E1 (osteoblastic cell line)	20.6 mM / 3.5 mg·mL ⁻¹	Adhesion inhibition	Székács, I. <i>et al.</i> 2018
NRK	13.8 ± 0.6 mM / ~ 2.4 mg·mL⁻¹ 4 ± 0.7 mM / ~ 0.7 mg·mL⁻¹ (Roundup®)	ECIS™ acute toxicity studies	

NRK	$19 \pm 8 \text{ mM} / \sim 3.2 \text{ mg}\cdot\text{mL}^{-1}$ $3.0 \pm 0.2 \text{ mM} / \sim 0.5 \text{ mg}\cdot\text{mL}^{-1}$ (Roundup®)	
A549	$\sim 20 \text{ mM} / \sim 3.4 \text{ mg}\cdot\text{mL}^{-1}$ $\sim 4.3 \text{ mM} / \sim 0.7 \text{ mg}\cdot\text{mL}^{-1}$ (Roundup®)	PrestoBlue™
MDCK II	$18 \pm 2 \text{ mM} / \sim 3.0 \text{ mg}\cdot\text{mL}^{-1}$ $5.4 \pm 0.7 \text{ mM} / \sim 0.9 \text{ mg}\cdot\text{mL}^{-1}$ (Roundup®)	

ECIS™-based monitoring of cellular phenotypes under the influence of glyphosate

After the initial attachment and spreading, living cells start to proliferate due to cell division. Cell division encompasses different developmental stages, beginning with a partial delamination followed by asymmetric morphological changes within the meta-, ana- and telophase (Wodarz, A. *et al.* 2005). Additionally, a hyperpolarization of the cell membrane can be detected during the cell division process (Kintzios, S. *et al.* 2006). The average cell division cycle is around 23 h in length as was for instance investigated for L1210 lymphoblast cells (Sandler, O. *et al.* 2015). This typical cell division cycle as well as the changes in morphology and membrane potential can lead to slightly different capacitance values occurring 23 h after the performed proliferation experiments. Thus, an ensuing slight capacitance increase can occur during cell division processes of living cells.

The incubation with 1 mM and 5 mM of glyphosate forming part of the herbicide formulation almost directly led to a strong increase in the capacitance signal with subsequently constant values. The increased capacitance indicated immediate cell death and thus the detachment of the cell bodies from the electrode surface, resulting in a drastically decreased resistance for the electrical current.

An overall comparison of all tested cellular phenotypes alleges a weakening sensitivity to glyphosate with progressing developmental stage when the subcultivation is taken as starting point. Proliferation rates as an early developmental stage were completely inhibited under concentrations of 1 mM and 5 mM glyphosate in Roundup®. Migration behavior on the other hand is a later developmental stage and is only suppressed after incubation with 5 mM of glyphosate in Roundup®, whereas decreasing concentrations correlate with faster migration behavior. The micromotion of the cells was not significantly impaired until a concentration of 5 mM glyphosate in Roundup® was added. In this case, smaller concentrations even triggered more cellular movement and no concentration-dependent behavior could be detected.

For comparison reasons, the cellular phenotypic activities were calculated and plotted against the respective herbicide concentration (see Fig. 7.10). The activities were normalized with respect to the experimental results from the cells being only exposed to L-15. Thus, the results under varying herbicide concentrations were divided by the ones from the cells under control conditions for every assay. Only proliferation experiments form an exception because the decreasing AUCs from the capacitance time courses correlate

with increasing cell proliferation in contrast to the other assays were increasing values always indicate increasing phenotypic activity. Therefore, results from the proliferation observations were calculated in a reciprocal way, so that the AUC of the cells being exposed to L-15 were divided by AUCs after herbicide exposure. Phenotypic activity values > 1 indicate increased cellular activity in comparison to the cells not being exposed to herbicides and values < 1 show an inhibited cellular activity under the respective herbicide concentration. All assays conducted in this thesis generally showed a higher toxicity for the glyphosate formulation compared to the same concentrations of the pure substance. The proliferation and respiration of NRK cells seemed to be inhibited under the influence of pure glyphosate as well as under Roundup® exposure. In contrast to these negatively influenced phenotypes, the detected cellular migration was increased with increasing glyphosate concentrations on the one hand and decreased with increasing Roundup® content on the other hand. Micromotion experiments largely revealed increased cellular activity, only 5 mM of the glyphosate formulation led to instant cell death. Tab. 7.5 summarizes all phenotypic cell responses in a concentration-dependent manner.

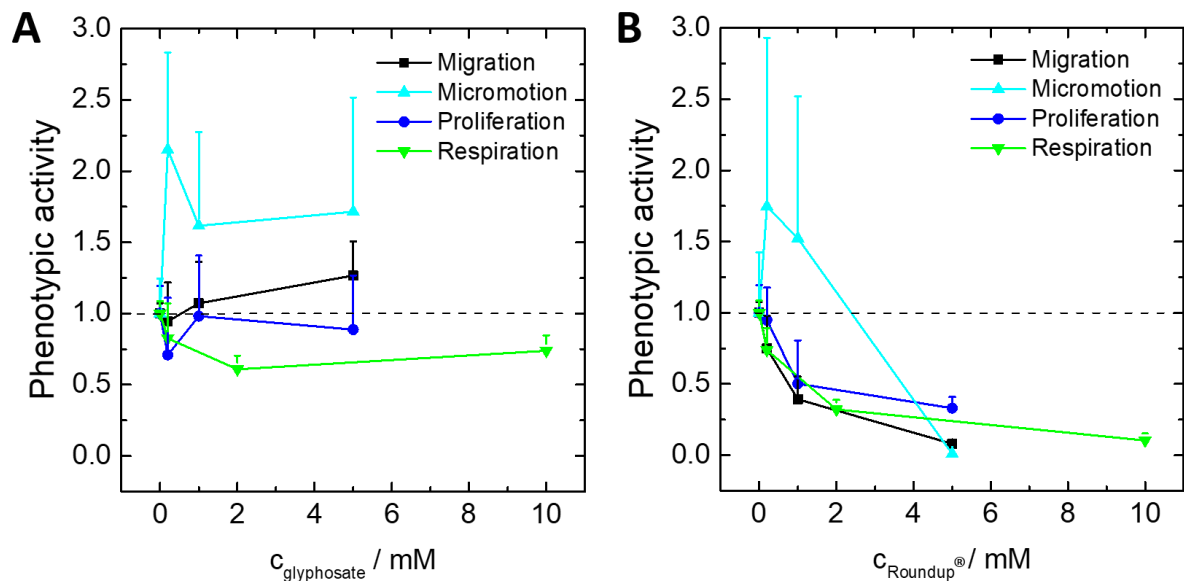


Fig. 7.10 Summarized phenotypic activity of NRK cells exposed to glyphosate either as pure substance (A) or as part of the commercial herbicide Roundup® (B). Phenotypic activity was calculated by division of the experimental result under toxin exposure by the results of the control conditions and vice versa only in the case of the proliferation assays. Mean \pm SEM, $n \geq 2$. T = 37 °C, 0 % CO₂.

Tab. 7.5 Summarized phenotypic activities of the NRK cells exposed to glyphosate either as pure substance or as part of the herbicide formulation Roundup®. Activity values were normalized with respect to the control experiments where cells were exposed only to L-15 medium and data from the proliferation assays was normalized in a reciprocal way. Mean ± SEM, n ≥ 2.

c/ mM	Proliferation		Migration		Micromotion		Respiration	
	Glyphosate	Roundup®	Glyphosate	Roundup®	Glyphosate	Roundup®	Glyphosate	Roundup®
	Phenotypic activity							
0	1.0 ± 0.2	1.0 ± 0.2	1.0 ± 0.1	1.0 ± 0.1	1.0 ± 0.2	1 ± 0.2	1.0 ± 0.1	1.0 ± 0.1
0.2	0.7 ± 0.4	0.9 ± 0.2	0.9 ± 0.3	0.7 ± 0.2	2.2 ± 0.7	1.7 ± 1.2	0.8 ± 0.2	0.7 ± 0.1
1	1.0 ± 0.4	0.5 ± 0.3	1.1 ± 0.3	0.4 ± 0.2	1.6 ± 0.7	1.5 ± 1.0		
2							0.60 ± 0.09	0.32 ± 0.07
5	0.9 ± 0.4	0.33 ± 0.07	1.3 ± 0.2	0.08 ± 0.02	1.7 ± 0.8	0.009 ± 0.005		
10							0.7 ± 0.1	0.10 ± 0.05

Pure glyphosate solutions generally led to a similar phenotypic cell response with respect to the control experiments. Solely concentrations of the pure glyphosate higher than 10 mM induced cell death according to the drastically decreased micromotion signal of MDCK II cells. The reasons for the impact of glyphosate on mammalian cells are manifold. Gene regulation, the inhibition or acceleration of protein expression as well as several effects on different cellular receptors are discussed. Gasnier, C. *et al.* 2009 discussed the disruptive effect of glyphosate on estrogen receptors and on the aromatase activity. Altered gene expressions are discussed to be related with tumor formation, tumor growth and the initiation of cellular apoptosis. Altered levels of CXCL12 (chemokine ligand 12), EGR1 (early growth response 1) and HIF-1 (hypoxia inducible factor 1) are associated with altered microvascular endothelial cell replication, cellular migration, the formation of microtubular networks and potentially showed an impact on apoptosis in MCF-7 cells (Hokanson, R. *et al.* 2007). CXCL12 is essential for the regulation of cardiac and neuronal development, stem cell motility, apoptosis and tumorigenesis (Burns, J. M. *et al.* 2006), whereas EGR1 is necessary for differentiation and mitogenesis (Gashler, A. *et al.* 1995) and HIF-1 for hypoxia sensing (Semenza, G. L. *et al.* 2001). It is even discussed that glyphosate impacts or disorders neuronal migration in the brain possibly causing autism-like neuron structures in the in-utero fetus (Beecham, J. E. *et al.* 2016). It is also discussed in literature that low cytotoxicity can induce a mobilization of the cytoskeleton as a defense mechanism towards multiple kind of stressors (Magin, T. M. *et al.* 2007) which is a possible explanation for the higher cell micromotion signals observed for low concentrations of glyphosate in the cellular motility measurements.

Sensor foil-based sensing of cellular respiration under the influence of glyphosate and post-exposure stainings

The observation of the respiratory activity of the cells revealed sensitivities similar to the migration investigations for glyphosate as part of Roundup®; however, sensitivity for the pure glyphosate solution was elevated in comparison. The three examined pure glyphosate concentrations resulted in slightly inhibited respiration rates, whereas glyphosate (Roundup®) showed significantly lower respiration rates with increasing concentration. As an alternative method, a succinate dehydrogenase activity assay can indirectly reflect the cellular respiration due to the integrity of mitochondrial dehydrogenase enzymes. Mesnage, R. *et al.* 2013 could also show higher respiration inhibition for the commercial glyphosate formulation than for the active ingredient glyphosate itself in JEG3, HEK293 and HepG2 cells.

As already mentioned, after the acute toxicity experiments it could be observed that cells treated with high concentrations of glyphosate in Roundup® seemed to display intact monolayer structures, whereas the detected impedance signal indicated cell death. Cell stainings after a 24-h herbicide incubation confirmed these observations. Cells treated with 40 mM and 20 mM of glyphosate (Roundup®) were dead according to the live/dead staining and the lack of green fluorescence, but the cytoskeleton as well as the nuclei could still clearly be detected. Most notable were the smaller sizes of the nuclei in comparison to DAPI-stained nuclei of healthy cells. Ahlbom, E. *et al.* 2001 also detected smoothly rounded nuclei in untreated cells while exposure to hydrogen peroxide, the tested toxin in the publication, led to apoptosis accompanied by shrunken and intensely fluorescent nuclei. In contrast to that, the pure glyphosate either only slightly influenced the cellular vitality by causing a few dead cells and otherwise leaving the cytoskeleton intact with normally sized nuclei or irreversibly harmed the cells leading to cell death and subsequent detachment. There are two different forms of cell death known: cell apoptosis or “programmed cell death” where the nucleus shrink and necrosis, which is characterized by cell swelling and loss of plasma membrane integrity (Rosenbaum, D. M. *et al.* 1994). Apoptosis is an ATP-consuming intrinsic suicide mechanism that is regulated by many signaling pathways whereas necrosis is a passive form of cell death initiated by toxin influence or cellular damages (Edinger, A. L. *et al.* 2004). Farkas, E. *et al.* 2018 reported about apoptotic cell death after the exposure to Roundup® and glyphosate which he evaluated using a caspase 3/7 cell viability test. Consequently, the shrinking cell nucleus as well as the remaining cell structure indicate apoptosis of the cells under the influence of glyphosate.

Even if cell-fixating properties were mostly observed after the exposure to Roundup®, pure glyphosate is discussed to reveal similar effects in literature. The observed fixated cell structures could occur due to glyphosate promoting cation-chelating efficiency what could in turn trigger effects on cell adhesion and cytoskeleton morphology as well as localization thereof (Gourlay, C. W. *et al.* 2005, Hedberg, D. *et al.* 2010). Heu, C. *et al.* 2012 investigated cell stiffness after glyphosate contact using atomic force microscopy and

measurements of the young modulus. After glyphosate treatment, there was a fourfold increase in cell stiffness of HaCaT cells to be observed and AFM examinations revealed a flattened membrane with altered distributions of native protrusions in comparison to the untreated cells, confirming the results of this work.

7.6 OUTLOOK

The performed glyphosate study allowed for an estimation of the biological impact on mammalian cells. The herbicide formulation and the active ingredient glyphosate itself in the pure form exhibited highly acidic pH values leading to an approximately 2.5-fold and tenfold increased toxic effect, respectively.

Nevertheless, glyphosate in all the different available herbicide formulations is still discussed to be cancerogenic. Based on these preliminary studies, long-term experiments would be interesting. The long-term cultivation of mammalian cells under the influence of non-cytotoxic glyphosate concentrations could reveal information about the effect on cells under the permanent influence of the herbicide. Additionally, one could perform investigations of the respective phenotypes under the influence of different pH values applied at different time points during toxin cultivation. Since a tumor invasion should cause a change in the transmembrane pH gradient, different cellular responses to extracellular pH changes should occur if normal cells turn to cancer cells. Such a study could, on the one hand, confirm cancer-inducing effects on cells and on the other hand, it could yield interesting information about changes of the cellular behavior when cells are permanently exposed to glyphosate. Possible mutations could be investigated, and it could possibly provide insights into pH-dependencies.

8 SUMMARY

This thesis was focused on monitoring two essential parameters of life in cell and tissue culture: oxygen and pH. Oxygen tension and pH are two fundamental indicators for metabolic activity and they allow discriminating between normal and cancerous tissue. The parameters were analyzed on the one hand by using analyte-sensitive, planar sensor foils detecting changes in the microenvironment of cells and on the other hand by applying different extracellular pH values to see how cells reacted in different developmental stages or phenotypes. Four different cell lines were analyzed: (i) NRK cells representing normal cells, (ii) A549 cells which are human lung cancer cells and (iii) SK-MEL-28 and SpiCa cells which are two human skin cancer subtypes.

Initial methodological investigations demonstrated the high spatial resolution of the oxygen-sensitive sensor foils. The experiments yielded highly cell line-dependent respiratory activities and *oxygen consumption rates*. Furthermore, the underlying ratiometric readout technique enabled investigations with multiple cell lines simultaneously growing on top of the same sensor foil and even the oxygen distribution beneath three-dimensional tissue models became assessable. The experiments confirmed a highly expected cell line-specific oxygen uptake and consumption reflecting that different tissue types in the body are also exposed to different oxygen tensions. Experiments carried out with pre-cultured spheroids showed differences in the emerging oxygen gradients beneath the tissue depending on: (i) previous adhesion and cultivation times, (ii) structural properties of the spheroid meaning whether it was densely packed or exhibited a softer, formable structure and (iii) the individual cell line.

Emerging gradients as well as the underlying cell-specific *oxygen consumption rates* were dependent on the sensor foil thickness. The thicker the sensor foil, the more dissolved oxygen was present within the foil and consumption rates appeared to be lower. However, one has to keep in mind that only the available oxygen within the foil was changed while the respiratory activity of the cells remained the same. Since horizontally emerging oxygen gradients beneath three-dimensional tissue models were demonstrated to show characteristic U-, W- or V-shaped profiles, the question arose if vertical oxygen gradients also exhibit characteristic profiles.

This question was addressed by using triangular glass prisms, with one leg of the prism being covered with the oxygen-sensitive sensor foil. The prisms were suspended in the supernatant medium above adherent cell monolayers. The device allowed for the mapping of vertical oxygen gradients which revealed emerging oxygen concentration gradients depending on the number of metabolically active cells on the surface, the height of the culture medium and the geometry of the respective cell culture vessel.

Besides the detection of oxygen concentrations beneath cells as an indicator of their respiration, the pH as the second key parameter was systematically varied in the supernatant medium and several cellular phenotypes were analyzed as a function of pH.

All in all, highly cell line-specific pH-dependent cell phenotypes were observed. Averaged phenotypic activities yielded increasing pH-dependencies from changes of around $(0.1 \pm 0.1) \text{ pH}^{-1}$ revealed by A549 over $(0.25 \pm 0.01) \text{ pH}^{-1}$ by SK-MEL-28 cells to around $(0.4 \pm 0.1) \text{ pH}^{-1}$ changed phenotypic activity per pH unit by NRK and SpiCa cells. Additionally, SpiCa cells were inhibited the most in their response under exposure to acidic pH conditions while NRK cells exhibited the most accelerated cell behavior under more alkaline extracellular pH values. Overall, a stronger inhibition of phenotypic behavior was observed for all the cell lines under extracellular acidification than alkaline milieus could increase the phenotypic activity. On the contrary, alkaline conditions even led to a slightly lower cellular response in the case of the cancerous cells.

To complete the picture, the intracellular pH_i was detected as a function of well-defined extracellular pH_e conditions. Intracellular pH_i , analyzed with the help of the dye BCECF, was found to be 0.1 to 0.7 pH units higher compared to the extracellularly adjusted condition for all extracellular pH_e values and every cell line. The more alkaline the extracellular environment was, the more aligned were the pH_i and the pH_e value. The studies of this thesis highlight how important a detailed cell characterization is to understand cellular responses to certain stimulations in order to be able to revert to this knowledge in the development of targeted drug design for therapeutics and diagnostics.

The last two chapters describe how the experimental techniques to monitor oxygen consumption and phenotypic behavior have been applied in toxicity studies. On the one hand, the respiratory activity was investigated under the influence of bisphenol A, a popular but toxic additive to many polymers, while on the other hand, an even wider range of cell phenotypes were analyzed following an exposition to glyphosate. The influence of BPA on the respiration activity of NRK cells yielded EC_{50} values between $(149 \pm 64) \mu\text{M}$ ($(76 \pm 5) \mu\text{M}$ for the time intervall between 6.5 – 9 h of BPA exposure) and $(159 \pm 235) \mu\text{M}$ for the sensor spot (SDR[®]) and sensor foil (VisiSens TD) based experiments, respectively.

The influence of glyphosate on the cellular respiration of NRK cells was monitored using the oxygen-sensitive sensor foil. The experiments showed a concentration-independent, slightly inhibited respiration under the exposure to pure glyphosate and a strictly concentration-dependent signal under the influence of glyphosate in the Roundup[®] formulation with a significantly slower respiration at high concentrations. Complementarily performed studies monitoring the acute toxicity on NRK cells yielded EC_{50} values between $(13.8 \pm 0.6) \text{ mM}$ (glyphosate) and $(4.0 \pm 0.7) \text{ mM}$ (Roundup[®]) detected via ECIS[™] and EC_{50} values between $(19 \pm 8) \text{ mM}$ (glyphosate) and $(3.0 \pm 0.2) \text{ mM}$ (Roundup[®]) performed via a PrestoBlue[™] cell viability assay. The obtained EC_{50} values were also confirmed by ECIS[™]-based investigations of the migration and micromotion behavior under the influence of the toxin.

9 ZUSAMMENFASSUNG

Das zentrale Thema dieser Arbeit war die Untersuchung der beiden essenziellen Metabolite Sauerstoff und pH-Wert, die sowohl über metabolische Funktionen und Aktivitäten bestimmen, als auch die Möglichkeit bieten, zwischen gesundem Gewebe und krebsartigen Zellverbänden zu unterscheiden. Die Substanzen wurden dahin gehend untersucht, dass einerseits Änderungen in der direkten Umgebung der Zellen mittels analytensensitiven and ebenflächigen Sensorfolien analysiert wurden und andererseits wurden verschiedene extrazelluläre pH Werte verwendet, um Zellreaktionen während verschiedener Entwicklungsstadien oder Phänotypen zu beobachten. Dabei wurden vier verschiedene Zelllinien untersucht: (i) NRK Zellen als Modelzelllinie für gesunde Zellen, (ii) A549 Lungenkrebszellen und (iii) SK-MEL-28 und SpiCa Zellen, welche zwei verschiedene Hautkrebszelllinien darstellen.

Anfängliche methodische Untersuchungen konnten die hohe Ortsauflösung der sauerstoffsensitiven Sensorfolie zeigen, die zur Bestimmung der Sauerstoffverbrauchsdaten eingesetzt wurden. Die Experimente ergaben zudem sehr zelllinienspezifische Atmungsaktivitäten und Veratmungsraten. Die ratiometrische Ausleseweise ermöglichte die gleichzeitige Untersuchung von mehreren Zelllinien, welche adhärent auf einer Sensorfolie wuchsen, und auch die Visualisierung von Sauerstoffgradienten unterhalb von dreidimensionalem Gewebe war möglich. Eine erwartete zellspezifische Aufnahme und Umwandlung von Sauerstoff konnte bestätigt werden, da die verschiedenen Gewebearten in lebenden Organismen ebenfalls variierenden Sauerstoffkonzentrationen ausgesetzt sind. Experimente, welche mit zuvor kultivierten Sphäroiden durchgeführt wurden, konnten Unterschiede in den unterhalb des Gewebes auftretenden Sauerstoffgradienten belegen. Diese Sauerstoffgradienten waren abhängig von (i) der vorangegangenen Adhäsions- und Kulturdauer, (ii) den strukturellen Eigenschaften der Sphäroide, also ob sie von dicht gepackter oder von eher weicher, formbarer Struktur waren und (iii) der jeweiligen Zelllinie selbst.

Die Sauerstoff-Gradienten als auch die daraus berechneten, zellspezifischen *apparenten Sauerstoffverbrauchsdaten*, zeigten eine Abhängigkeit von der Sensorfoliendicke. Je dicker die Sensorfolie gewählt wurde, umso mehr gelöster Sauerstoff befand sich in der Folie, was zu scheinbar sinkenden Verbrauchsdaten führte. Jedoch ist es wichtig zu beachten, dass lediglich die verfügbare Sauerstoffkonzentration im Folienmaterial verändert wurde, während die Atmungsaktivität der Zellen unverändert blieb. Nachdem horizontal auftretende Sauerstoffgradienten unterhalb von dreidimensionalem Gewebe charakteristische U-, W- oder V-förmige Profile aufwiesen, stellte sich die Frage, ob vertikale Sauerstoffgradienten ebenfalls charakteristische Profile aufweisen würden.

Für die Beantwortung dieser Fragestellung wurden dreieckige Glasprismen verwendet, bei denen eine Seite mit der sauerstoffsensitiven Folie versehen wurde. Diese Prismen wurden dann im überstehenden Medium

oberhalb der adhärennten Zellschicht platziert. Diese Anordnung erlaubte die Visualisierung vertikaler Sauerstoffgradienten und in der Folge die Schlussfolgerung, dass auftretende Sauerstoffkonzentrationsgradienten von der Zellanzahl auf der Wachstumsfläche, der Höhe der überstehenden Flüssigkeitssäule und der Geometrie der Zellkulturgefäße abhängig waren.

Neben der Detektion der durch Zellatmung verursachten Sauerstoffkonzentrationsänderung unterhalb der Zellen, wurde auch der zweite Parameter – der pH-Wert im Medium – systematisch variiert und verschiedene Zellverhalten als Funktion des pH-Wertes überwacht.

Insgesamt konnte eine zelltypspezifische pH-Abhängigkeit beobachtet werden. Zusammengefasste und gemittelte Zellantworten in Form der phänotypischen Aktivität ergaben steigende pH-Abhängigkeiten mit Änderungen von etwa $(0.1 \pm 0.1) \text{ pH}^{-1}$ im Falle der A549, über $(0.25 \pm 0.01) \text{ pH}^{-1}$ bei SK-MEL-28 Zellen bis hin zu (0.4 ± 0.1) veränderter phänotypischer Aktivität pro pH Einheit bei den NRK und SpiCa Zellen. Zudem war das Verhalten der SpiCa Zellen unter dem Einfluss saurer Medien überdurchschnittlich eingeschränkt, wohingegen das Verhalten der NRK Zellen am deutlichsten unter basischen extrazellulären pH Werten gesteigert wurde. Im Allgemeinen wurde bei einer extrazellulären Ansäuerung das phänotypische Verhalten stärker inhibiert, als es unter basischen extrazellulären Bedingungen erhöht wurde. Ganz im Gegenteil führten basische Bedingungen, verglichen mit einem physiologischen pH Wert, sogar zu leicht niedrigeren Zellantworten bei den Krebszellen.

Zur Vervollständigung der Studie wurde der intrazelluläre pH-Wert in Abhängigkeit von äußeren Inkubationslösungen mit systematisch variiertem pH-Wert untersucht. Der vorliegende, intrazelluläre pH-Wert wurde mittels dem Farbstoff BCECF untersucht und ergab für alle extrazellulären pH-Werte und im Falle jeder Zelllinie einen um 0.1 bis 0.7 pH Einheiten höheren pH_i -Wert im Vergleich zu dem extrazellulär eingestellten pH_e -Wert. Je alkalischer das extrazelluläre Medium war, desto mehr glichen sich pH_i - und pH_e -Werte aneinander an. Letztlich zeigen die durchgeführten Studien, wie wichtig eine detaillierte Zellcharakterisierung im Hinblick auf das Verständnis von zellulären Antworten auf bestimmte Reize ist. Dieses Wissen kann für die Entwicklung zielgerichteter Medikamente sowohl für die Therapie als auch für die Diagnose von großem Nutzen sein.

In den letzten beiden Kapiteln wurde beschrieben, wie die experimentellen Techniken zur Untersuchung des Sauerstoffverbrauches und des phänotypischen Verhaltens genutzt werden können, um umfangreiche Toxizitätsstudien durchzuführen. Zum einen wurde die Atmungsaktivität unter Einfluss des Toxins Bisphenol A untersucht und zum anderen wurden sämtliche Phänotypen nach der Behandlung mit Glyphosat beobachtet. Die Atmungsaktivitäten der NRK Zellen unter dem Einfluss von BPA ergaben EC_{50} -Werte von $(149 \pm 64) \mu\text{M}$ mit Hilfe der Technik des Sensorspots (SDR[®]) $((76 \pm 5) \mu\text{M})$ unter BPA Einfluss für das Zeitintervall von 6.5 – 9 h) und $(159 \pm 235) \mu\text{M}$ wurden mit Hilfe der Sensorfolie (VisiSens TD) bestimmt.

Der Einfluss von Glyphosat auf die zelluläre Atmung von NRK Zellen wurde mittels der sauerstoffsensitiven Sensorfolie untersucht. Die Experimente zeigten eine konzentrationsunabhängige, leicht inhibierte Atmung der Zellen unter dem Einfluss von reinem Glyphosat und in Gegenwart des Mittels Roundup® eine streng konzentrationsabhängige Atmungsaktivität der Zellen, welche bei hohen Konzentrationen stark inhibiert war. Ergänzende Studien zur Untersuchung der akuten Toxizität auf NRK Zellen ergaben EC_{50} Werte zwischen (13.8 ± 0.6) mM (Glyphosat) und (4.0 ± 0.7) mM (Roundup®) basierend auf den ECIS™ Experimenten und EC_{50} Werte zwischen (19 ± 8) mM (Glyphosat) and (3.0 ± 0.2) mM (Roundup®) anhand der PrestoBlue™ Viabilitätsassays. Diese EC_{50} -Werte konnten durch ECIS™-gestützte Messungen des Migrations- und Mikrobewegungsverhaltens unter dem Einfluss des Giftstoffes bestätigt werden.

10 REFERENCES

A

- Abe, M., D. W. Kufe (1984) Effect of sodium butyrate on human breast carcinoma (MCF-7) cellular proliferation, morphology, and CEA production. *Breast Cancer Research and Treatment*. **4**: 269–274.
- Ahlbom, E., Prins, G. S.; Ceccatelli, S. (2001) Testosterone protects cerebellar granule cells from oxidative stress-induced cell death through a receptor mediated mechanism. *Brain Research*. **892**: 255–262.
- Ahmad, S., Carl W. White; Ling-Yi Chang; Barbara K. Schneider; and Corrie B. Allen (2001) Glutamine protects mitochondrial structure and function in oxygen toxicity. *Am J Physiol Lung Cell Mol Physiol*. **280**: L779-L791.
- Ail, D., Rüfenacht, V.; Caprara, C.; Samardzija, M.; Kast, B.; Grimm, C. (2015) Increased expression of the proton-sensing G protein-coupled receptor Gpr65 during retinal degeneration. *Neuroscience*. **301**: 496–507.
- Alexander, H. C., D. C. Dill, L. W. Smith (1988) Bisphenol a: Acute aquatic toxicity. *Toxicology and Chemistry*. **7**: 19–26.
- Anada, T., Fukuda, J.; Sai, Y.; Suzuki, O. (2012) An oxygen-permeable spheroid culture system for the prevention of central hypoxia and necrosis of spheroids. *Biomaterials*. **33** (33): 8430–8441.
- Arai, T., Nishijo, T.; Matsumae, Y.; Zhou, Y.; Ino, Kosuke; Shiku, Hitoshi; Matsue, Tomokazu (2013) Noninvasive measurement of alkaline phosphatase activity in embryoid bodies and coculture spheroids with scanning electrochemical microscopy. *Analytical chemistry*. **85** (20): 9647–9654.
- Arndt, S., Seebach, J.; Psathaki, K.; Galla, H.-J.; Wegener, J. (2004) Bioelectrical impedance assay to monitor changes in cell shape during apoptosis. *Biosensors and Bioelectronics*. **19** (6): 583–594.
- Arregui, M. C., Lenardón, A.; Sanchez, D.; Maitre, M. I.; Scotta, Roberto; Enrique, Susana (2004) Monitoring glyphosate residues in transgenic glyphosate-resistant soybean. *Pest management science*. **60** (2): 163–166.

B

- Beecham, J. E., Seneff, S. (2016) Is there a link between autism and glyphosate-formulated herbicides? *J Autism*. **3** (1): 1.
- Benachour, N., Sipahutar, H.; Moslemi, S.; Gasnier, C.; Travert, C.; Séralini, G. E. (2007) Time- and dose-dependent effects of roundup on human embryonic and placental cells. *Archives of environmental contamination and toxicology*. **53** (1): 126–133.
- Benachour, N., Séralini, G.-E. (2009) Glyphosate formulations induce apoptosis and necrosis in human umbilical, embryonic, and placental cells. *Chemical research in toxicology*. **22** (1): 97–105.
- Bernstein, B. W., W.B. Painter, H. Chen, L.S. Minamide, H. Abe, J.R. Bamburg (2000) Intracellular pH modulation of ADF/cofilin proteins. *Cell Motility and the Cytoskeleton*. **47**: 319–336.
- Bibby, S. R., D. A. Jones, R. M. Ripley, J. P. G. Urban (2005) Metabolism of the Intervertebral Disc: Effects of Low Levels of Oxygen, Glucose, and pH on Rates of Energy Metabolism of Bovine Nucleus Pulposus Cells. *SPINE*. **30** (5): 587–496.
- Bigner, D. D., Bigner, S. H. (1981) Heterogeneity of Genotypic and Phenotypic Characteristics of Fifteen Permanent Cell Lines Derived from Human Gliomas. *Journal of Neuropathology & Experimental Neurology*. **40** (3): 201–229.
- Blair R. J., Meng, H.; Marchese, M. J.; Ren, S.; Schwartz, L. B.; Tonnesen, M. G.; Gruber, B. L. (1997) Human mast cells stimulate vascular tube formation. Tryptase is a novel, potent angiogenic factor. *The Journal of clinical investigation*. **99** (11): 2691–2700.
- Blasiak, J., A. Trzeciak, E. Malecka-Panas, J. Drezewoski, M. Wojewoa (2000) In vitro genotoxicity of ethanol and acetaldehyde in human lymphocytes and the gastrointestinal tract mucosa cells. *Toxicology in Vitro* (14): 287–295.
- Boedtkjer, E., Moreira, J. M. A.; Mele, M.; Vahl, P.; Wielenga, Vera T.; Christiansen, Peer M.; Jensen, Vibeke E. D.; Pedersen, Stine F.; Aalkjaer, Christian (2013) Contribution of Na⁺,HCO₃⁻-cotransport to cellular pH control in

- human breast cancer: a role for the breast cancer susceptibility locus NBCn1 (SLC4A7). *International journal of cancer*. **132** (6): 1288–1299.
- Bolger, F., McHugh, S. B.; Bennett, R.; Li, J.; Ishiwari, Keita; Francois, Jennifer; Conway, Michael W.; Gilmour, Gary; Bannerman, David M.; Fillenz, Marianne; Tricklebank, Mark; Lowry, John P. (2011) Characterisation of carbon paste electrodes for real-time amperometric monitoring of brain tissue oxygen. *Journal of neuroscience methods*. **195** (2): 135–142.
- Bookstein, C., DePaoli, A. M.; Xie, Y.; Niu, P.; Musch, M. W.; Rao, M. C.; Chang, E. B. (1994) Na⁺/H⁺ exchangers, NHE-1 and NHE-3, of rat intestine. Expression and localization. *The Journal of clinical investigation*. **93** (1): 106–113.
- Braun, J. M., Kalkbrenner, A. E.; Calafat, A. M.; Yolton, K.; Ye, Xiaoyun; Dietrich, Kim N.; Lanphear, Bruce P. (2011) Impact of early-life bisphenol A exposure on behavior and executive function in children. *Pediatrics*. **128** (5): 873–882.
- Brunelle, J., Bell, E. L.; Quesada, N. M.; Vercauteren, K.; Tiranti, V.; Zeviani, M.; Scarpulla, R. C.; Chandel, N. S. (2005) Oxygen sensing requires mitochondrial ROS but not oxidative phosphorylation. *Cell metabolism*. **1** (6): 409–414.
- Bryce, N. S., Clark, E. S.; Leysath, J. L.; Currie, J. D.; Webb, D. J.; Weaver, A. M. (2005) Cortactin promotes cell motility by enhancing lamellipodial persistence. *Current biology : CB*. **15** (14): 1276–1285.
- Buck, R., Rondinini, S.; Covington, A.; Baucke, F.; Brett, C.; Camoes, M.; Milton, M. (2002) Measurement of pH. Definition, Standards, and Procedures. *Pure Appl. Chem*. **74** (11): 2169–2200.
- Burns, J. M., Summers, B. C.; Wang, Y.; Melikian, A.; Berahovich (2006) A novel chemokine receptor for SDF-1 and I-TAC involved in cell survival, cell adhesion, and tumor development. *The Journal of experimental medicine*. **203** (9): 2201–2213.
- Busco, G., Cardone, R. A.; Greco, M. R.; Bellizzi, A.; Colella, Matilde; Antelmi, Ester; Mancini, Maria T.; Dell'Aquila, Maria E.; Casavola, Valeria; Paradiso, Angelo; Reshkin, Stephan J. (2010) NHE1 promotes invadopodial ECM proteolysis through acidification of the peri-invadopodial space. *FASEB journal : official publication of the Federation of American Societies for Experimental Biology*. **24** (10): 3903–3915.
- ## C
- Calabrese, E. J., Baldwin, L. A. (2002) Defining hormesis. *Human & experimental toxicology*. **21** (2): 91–97.
- Callis, P. R. *et al.* (2014) Binding phenomena and fluorescence quenching. I: Descriptive quantum principles of fluorescence quenching using a supermolecule approach. *Journal of Molecular Structure*. **1077**: 14–21.
- Cardone, R., Casavola, V.; Reshkin, S. J. (2005) The role of disturbed pH dynamics and the Na⁺/H⁺ exchanger in metastasis. *Nature reviews. Cancer*. **5** (10): 786–795.
- Carey, T. E., Toshitada Takahashi, L.A. Resnick, H. F. Oettgen, L. J. Old (1976) Cell surface antigens of human malignant melanoma: Mixed hemadsorption assays for humoral immunity to cultured autologous melanoma cells. *Proc. Natl. Acad. Sci. USA*. **73** (9): 3278–3282.
- Casey, J., Grinstein, S.; Orłowski, J. (2010) Sensors and regulators of intracellular pH. *Nature reviews. Molecular cell biology*. **11** (1): 50–61.
- Cereijido, M., J. Ehrenfeld, S. Fernandez-Castelo, and I. Meza (1981) Fluxes, Junctions, and Blisters in cultured Monolayers of Epithelioid Cells (MDCK). *Annals New York Academy of Sciences*. 422-441.
- Chandel, N., McClintock, D. S.; Feliciano, C. E.; Wood, T. M.; Melendez, J. A.; Rodriguez, A. M.; Schumacker, P. T. (2000) Reactive oxygen species generated at mitochondrial complex III stabilize hypoxia-inducible factor-1 α during hypoxia: a mechanism of O₂ sensing. *The Journal of Biological Chemistry*. **275** (33): 25130–25138.
- Chang, C.-W., Cheng, Y.-J.; Tu, M.; Chen, Y.-H.; Peng, Chien-Chung; Liao, Wei-Hao; Tung, Yi-Chung (2014) A polydimethylsiloxane-polycarbonate hybrid microfluidic device capable of generating perpendicular chemical and oxygen gradients for cell culture studies. *Lab on a chip*. **14** (19): 3762–3772.
- Chen, A., Dong, L.; Leffler, N. R.; Asch, A. S.; Witte, O. N.; Yang, L. V. (2011) Activation of GPR4 by acidosis increases endothelial cell adhesion through the cAMP/Epac pathway. *PLoS one*. **6** (11): e27586.

- Chen, P., Zuo, H.; Xiong, H.; Kolar, M. J.; Chu, Q.; Saghatelian, A.; Siegwart, D. J.; Wan, Y. (2017) Gpr132 sensing of lactate mediates tumor-macrophage interplay to promote breast cancer metastasis. *Proc. Natl. Acad. Sci. USA*. **114** (3): 580–585.
- Chen, S., Hong, Y.; Liu, Y.; Liu, J.; Leung, C.; Li, M.; Kwok, R. T. (2013) Full-range intracellular pH sensing by an aggregation-induced emission-active two-channel ratiometric fluorogen. *Journal of the American Chemical Society*. **135** (13): 4926–4929.
- Chen, Y.-A., King, A. D.; Shih, H.-C.; Peng, C.-C.; Wu, Chueh-Yu; Liao, Wei-Hao; Tung, Yi-Chung (2011) Generation of oxygen gradients in microfluidic devices for cell culture using spatially confined chemical reactions. *Lab on a chip*. **11** (21): 3626–3633.
- Chu, C.-S., Lin, T.-H. (2015) Ratiometric optical sensor for dual sensing of temperature and oxygen. *Sensors and Actuators B: Chemical*. **210**: 302–309.
- Clark, L., Wolf, R.; Granger, D.; Taylor, Z. (1953) Continuous Recording of Blood Oxygen Tensions by Polarography. *J Appl Physiol*. **6**: 189–193.
- Clement, A., Edeas, M.; Chadelat, K.; Brody, J. S. (1992) Inhibition of lung epithelial cell proliferation by hyperoxia. Posttranscriptional regulation of proliferation-related genes. *The Journal of clinical investigation*. **90** (5): 1812–1818.
- Cordat, E., Casey, J. R. (2009) Bicarbonate transport in cell physiology and disease. *The Biochemical journal*. **417** (2): 423–439.
- Costa, E., Moreira, A. F.; Melo-Diogo, D.; Gaspar, V. M.; Carvalho, M. P.; Correia, I. J. (2016) 3D tumor spheroids: an overview on the tools and techniques used for their analysis. *Biotechnology advances*. **34** (8): 1427–1441.
- Costa, E., Silva, D. N.; Moreira, A. F.; Correia, I. J. (2019) Optical clearing methods: An overview of the techniques used for the imaging of 3D spheroids. *Biotechnology and bioengineering*. **116** (10): 2742–2763.
- Crayton, S., Tsourkas, A. (2011) pH-titratable superparamagnetic iron oxide for improved nanoparticle accumulation in acidic tumor microenvironments. *ACS nano*. **5** (12): 9592–9601.
- Croce, M. V., A. G. Colussi, M. R. Price, A. Segal-Eiras (1999) Identification and characterization of different subpopulations in a human lung Adenocarcinoma Cell Line (A549) adenocarcinoma cell line (A549). *Pathology Oncology Research*. **5** (3): 197–204.
- Cui, S.-J., Manorama Tewari, Tim Schneider, and Raphael Rubin (1997) Ethanol Promotes Cell Death by Inhibition of the Insulin-Like Growth Factor I Receptor. *Alcoholism: Clinical and Experimental Research*. **21** (6): 1121–1127.
- D**
- Dancker, P., I. Low, W. Hasselbach, T. Wieland (1975) Interaction of Actin with Phalloidin: Polymerization and stabilization of F-actin. *Biochimica et Biophysica Acta*. **400** (2): 407–414.
- Daruich, J., Zirulnik, F.; Gimenez, M. S. (2001) Effect of the herbicide glyphosate on enzymatic activity in pregnant rats and their fetuses. *Environmental research*. **85** (3): 226–231.
- Däster, S., N. Amatruda, D. Calabrese, R. Ivanek, E. Turrini, R. A. Droeser, P. Zajac, C. Fimognari (2017) Induction of hypoxia and necrosis in multicellular tumor spheroids is associated with resistance to chemotherapy treatment. *Oncotarget*. **8** (1): 1725–1736.
- Del Guerra, A., N. Belcari, M. B. (2016) Positron Emission Tomography: Its 65 years. *Rivista del nuovo cimento*. **39** (4): 155–223.
- DeLarco, J. E., G. J. Todaro (1978) Epithelioid and fibroblastic rat kidney cell clones: Epidermal growth factor (EGF) receptors and the effect of mouse sarcoma virus transformation. *J. Cell. Physiol*. **94**: 335–342.
- Demas, J. N., B. A. DeGraff, P. B. Coleman (1999) Oxygen Sensors based on Luminescence Quenching. *Analytical Chemistry News & Features*. 793–800.

- Deng, S., McAuliffe, M. A. P.; Salaj-Kosla, U.; Wolfe, R.; Lewis, G.; Huyet, G. (2017) A pH sensing system using fluorescence-based fibre optical sensor capable of small volume sample measurement. *Proc. SPIE 10110, Photonic Instrumentation Engineering IV*. **101101C**.
- Dodds, E.C *et al.* 1936) Synthetic estrogenic agents without the phenanthrene nucleus. *Nature* (137): 996.
- Dogutan, D., Nocera, D. G. (2019) Artificial Photosynthesis at Efficiencies Greatly Exceeding That of Natural Photosynthesis. *Accounts of chemical research*. **52** (11): 3143–3148.
- Dubois, L., Lieuwes, N. G.; Janssen, M. H. M.; Peeters, W. J. M.; Windhorst, A. D.; Walsh, J. C.; Kolb, H. C. (2011) Preclinical evaluation and validation of 18FHX4, a promising hypoxia marker for PET imaging. *Proc. Natl. Acad. Sci. USA*. **108** (35): 14620–14625.
- E**
- Edinger, A. L., Thompson, C. B. (2004) Death by design: apoptosis, necrosis and autophagy. *Current opinion in cell biology*. **16** (6): 663–669.
- Edward, J. T. *et al.* (1970) Molecular volumes and the Stokes-Einstein equation. *Journal of Chemical Education*. **47** (4): 261–270.
- Ekstrand, A., C. D. James, W. K. Cavenee, B. Seliger, R. F. Pettersson, and V. P. Collins (1991) Genes for Epidermal Growth Factor Receptor, Transforming Growth Factor α , and Epidermal Growth Factor and Their Expression in Human Gliomas in Vivo. *Cancer Research*. **51**: 2164–2172.
- Elie-Caille, C., Heu, C.; Guyon, C.; Nicod, L. (2010) Morphological damages of a glyphosate-treated human keratinocyte cell line revealed by a micro- to nanoscale microscopic investigation. *Cell biology and toxicology*. **26** (4): 331–339.
- F**
- Farkas, E., Szekacs, A.; Kovacs, B.; Olah, M.; Horvath, Robert; Szekacs, Inna (2018) Label-free optical biosensor for real-time monitoring the cytotoxicity of xenobiotics: A proof of principle study on glyphosate. *Journal of hazardous materials*. **351**: 80–89.
- Fercher, A., Borisov, S. M.; Zhdanov, A. V.; Klimant, I.; Papkovsky, Dmitri B. (2011) Intracellular O₂ sensing probe based on cell-penetrating phosphorescent nanoparticles. *ACS nano*. **5** (7): 5499–5508.
- Fischer, L. (2012) New Materials for Temperature and Pressure Sensitive Fluorescent Paints. Chemistry, University of Regensburg. **Dissertation**.
- Franck, P., N. Petitpain, M. Cherlet, M. Dardennes, F. Maachi, B. Schutz, L. Poisson, P. Nabet (1996) Measurement of intracellular pH in cultured cells by flow cytometry with BCECF-AM. *Journal of Biotechnology* (46): 187–195.
- Freyer, J., Tustanoff, E.; Franko, A. J.; Sutherland, R. M. (1984) In situ oxygen consumption rates of cells in V-79 multicellular spheroids during growth. *Journal of cellular Physiology* (118): 53–61.
- Freyer, J., Sutherland, R. M. (1985) A reduction in the in situ rates of oxygen and glucose consumption of cells in EMT6/Ro spheroids during growth. *Journal of cellular Physiology*. **124**: 516–524.
- Fujie, K., K. Tsuchiya, L.-S. F. (1994) Determination of Volumetric Oxygen Transfer Coefficient by Off-Gas Analysis. *Journal of Fermentation and Bioengineering*. **77** (5): 522–527.
- Fujiwara, Y. *et al.* (2003) An oxygen sensor based on the fluorescence quenching of pyrene chemisorbed layer onto alumina plates. *Sensors and Actuators B: Chemical*. **89** (1-2): 187–191.
- G**
- Gaio, E., Scheglmann, D.; Reddi, E.; Moret, F. (2016) Uptake and photo-toxicity of Foscan[®], Foslip[®] and Fospeg[®] in multicellular tumor spheroids. *Journal of photochemistry and photobiology. B, Biology*. **161**: 244–252.
- Gardner, P. R., D. H. Nguyen, C. W. White (1994) Aconitase is a sensitive and critical target of oxygen poisoning in cultured mammalian cells and in rat lungs. *Proc. Natl. Acad. Sci. USA*. **91**: 12248–12252.

- Gashler, A., Sukhatme, V. P. (1995) Early Growth Responses Protein 1 (Egr-1): Prototype of a Zinc-finger Family of Transcription Factors. *Progress in Nucleic Acid Research and Molecular Biology*. **50**: 191–224.
- Gasnier, C. *et al.* (2009) Glyphosate-based herbicides are toxic and endocrine disruptors in human cell lines. *Toxicology*. **262**: 184–191.
- Geddes, C. D., Joseph R. Lakowicz (2002) Metal-Enhanced Fluorescence. *Journal of Fluorescence*. **12** (2): 121–129.
- Giaever, I. *et al.* (1984) Monitoring fibroblast behavior in tissue culture with an applied electric field. *Proc. Natl. Acad. Sci. USA* (81): 3761–3764.
- Giaever, I., Keese, C. R. (1991) Micromotion of mammalian cells measured electrically. *Proc. Natl. Acad. Sci. USA* (88): 7896–7900.
- Giard, D. J., S. A. Aaronson, G. J. Todaro, P. Arnstein, J. H. Kersey, H. Dosik, W. P. Parks (1973) In Vitro Cultivation of Human Tumors: Establishment of Cell Lines Derived From a Series of Solid Tumors. *Journal of the national cancer Institute*. **51** (5): 1417–1423.
- Gillies, R., Morse, D. L. (2005) In vivo magnetic resonance spectroscopy in cancer. *Annual review of biomedical engineering*. **7**: 287–326.
- Glazer, A. N., K. Peck, R. A. Mathies (1990) A stable double-stranded DNA-ethidium homodimer complex: Application to picogram fluorescence detection of DNA in agarose gels. *Proc. Natl. Acad. Sci.* **87**: 3851–3855.
- Gourlay, C. W., K. R. Ayscough (2005) The actin cytoskeleton: a key regulator of apoptosis and ageing? *Nature Review Molecular Biology*. **6**: 583–589.
- GrandView Research: <https://www.grandviewresearch.com/press-release/global-bisphenol-a-bpa-market>.
- Green, D. R., Reed, J. C. (1998) Mitochondria and apoptosis. *Science (New York, N.Y.)*. **281** (5381): 1309–1312.
- Groebe, K., W. Mueller-Klieser (1991) Distributions of oxygen, nutrient, and metabolic waste concentrations in multicellular spheroids and their dependence on spheroid parameters. *Eur Biophys J* (19): 169–181.
- Groebe, K., Mueller-Klieser, W. (1996) On the relation between size and necrosis and diameter of tumor spheroids. *Int. J. Radiation Oncology Biol. Phys.* **34** (2): 395–401.
- Guarino, R. D., Dike, L. E.; Haq, T. A.; Rowley, J. A.; Pitner, J. Bruce; Timmins, Mark R. (2004) Method for determining oxygen consumption rates of static cultures from microplate measurements of pericellular dissolved oxygen concentration. *Biotechnology and bioengineering*. **86** (7): 775–787.
- ## H
- Hagag, N., Lacal, J. C.; Graber, M.; Aaronson, S.; Viola, M. V. (1987) Microinjection of ras p21 Induces a Rapid Rise in Intracellular pH. *MOLECULAR AND CELLULAR BIOLOGY*. **7** (5): 1984–1988.
- Halestrap, A., Meredith, D. (2004) The SLC16 gene family—from monocarboxylate transporters (MCTs) to aromatic amino acid transporters and beyond. *Pflugers Archiv : European journal of physiology*. **447** (5): 619–628.
- Han, J., Burgess, K. (2010) Fluorescent indicators for intracellular pH. *Chemical reviews*. **110** (5): 2709–2728.
- He, C., Lu, K.; Lin, W. (2014) Nanoscale metal-organic frameworks for real-time intracellular pH sensing in live cells. *Journal of the American Chemical Society*. **136** (35): 12253–12256.
- Hedberg, D., Wallin, M. (2010) Effects of Roundup and glyphosate formulations on intracellular transport, microtubules and actin filaments in *Xenopus laevis* melanophores. *Toxicology in vitro : an international journal published in association with BIBRA*. **24** (3): 795–802.
- Heu, C., Berquand, A.; Elie-Caille, C.; Nicod, L. (2012) Glyphosate-induced stiffening of HaCaT keratinocytes, a Peak Force Tapping study on living cells. *Journal of structural biology*. **178** (1): 1–7.
- Hirschhaeuser, F., Menne, H.; Dittfeld, C.; West, J.; Mueller-Klieser, Wolfgang; Kunz-Schughart, Leoni A. (2010) Multicellular tumor spheroids: an underestimated tool is catching up again. *Journal of Biotechnology*. **148** (1): 3–15.

- Höckel, M., Vaupel, P. (2001) Tumor Hypoxia: Definitions and Current Clinical, Biologic, and Molecular Aspects. *Journal of the national cancer Institute*. **93** (4): 266–276.
- Hokanson, R., Fudge, R.; Chowdhary, R.; Busbee, D. (2007) Alteration of estrogen-regulated gene expression in human cells induced by the agricultural and horticultural herbicide glyphosate. *Human & experimental toxicology*. **26** (9): 747–752.
- Holley, E. R. *et al.* (1977) Oxygen Transfer at the Air-Water Interface. *Transport Processes in Lakes and Oceans*: 117–150.
- Hulth, S., R. C. Aller, P. Engström, E. Selander (2002) A pH plate fluorosensor (optode) for early diagenetic studies of marine sediments. *Limnol. Oceanogr.* **47** (1): 212–220.
- Hynes, R. O. *et al.* (1992) Integrins: Versatility, Modulation, and Signaling in Cell Adhesion. *Cell* (29): 11–25.
- I**
- Ippolito, J. E., Brandenburg, M. W.; Ge, X.; Crowley, J. R.; Kirmess, K. M.; Som, A.; D'Avignon, D. A.; Arbeit, J. M.; Achilefu, S.; Yarasheski, K. E.; Milbrandt, J. (2016) Extracellular pH Modulates Neuroendocrine Prostate Cancer Cell Metabolism and Susceptibility to the Mitochondrial Inhibitor Niclosamide. *PLoS one*. **11** (7): e0159675.
- J**
- Justus, C., Dong, L.; Yang, L. V. (2013) Acidic tumor microenvironment and pH-sensing G protein-coupled receptors. *Frontiers in physiology*. **4**: 354.
- Justus, C., Sanderlin, E. J.; Dong, L.; Sun, A.; Chi, Jen-Tsan; Lertpiriyapong, Kvin; Yang, Li V. (2017) Contextual Tumor Suppressor Function of T Cell Death-Associated Gene 8 (TDAG8) in Hematological Malignancies. *J Transl Med*. **15** (204).
- Jyonouchi, H., Sun, S.; Mizokami, M.; Ingbar, D. H. (1997) Cell density and antioxidant vitamins determine the effects of hyperoxia on proliferation and death of MDCK epithelial cells. *Nutrition and cancer*. **28** (2): 115–124.
- K**
- Kabarowski, J., Zhu, K.; Le, L. Q.; Witte, O. N.; Xu, Y. (2001) Lysophosphatidylcholine as a ligand for the immunoregulatory receptor G2A. *Science (New York, N.Y.)*. **293** (5530): 702–705.
- Kabarowski, J. *et al.* (2009) G2A and LPC: regulatory functions in immunity. *Prostaglandins & other lipid mediators*. **89** (3-4): 73–81.
- Kapuscinski, J. *et al.* (1995) DAPI: a DNA-specific fluorescent probe. *Biotechnic & histochemistry : official publication of the Biological Stain Commission*. **70** (5): 220–233.
- Karlsson, G. E., Gedde, U. W.; Hedenqvist, M. S. (2004) Molecular dynamics simulation of oxygen diffusion in dry and water-containing poly(vinyl alcohol). *Polymer*. **45** (11): 3893–3900.
- Kawai, C., Pessoto, F. S.; Rodrigues, T.; Mugnol, K. C. U.; Tórtora, V.; Castro, L. (2009) pH-sensitive binding of cytochrome c to the inner mitochondrial membrane. Implications for the participation of the protein in cell respiration and apoptosis. *Biochemistry*. **48** (35): 8335–8342.
- Kawaoka, K., Khan, A. U.; Kearns, D. R. (1967) Role of Singlet Excited States of Molecular Oxygen in the Quenching of Organic Triplet States. *The Journal of Chemical Physics*. **46** (5): 1842–1853.
- Keese, C. R., J. Wegener, S. R. Walker, and I. Giaever (2004) Electrical wound-healing assay for cells in vitro. *Proc. Natl. Acad. Sci. USA*. **101** (6): 1554–1559.
- Khaitan, D., Chandna, S.; Arya, M. B.; Dwarakanath, B. S. (2006) Differential mechanisms of radiosensitization by 2-deoxy-D-glucose in the monolayers and multicellular spheroids of a human glioma cell line. *Cancer biology & therapy*. **5** (9): 1142–1151.

- Khooa, V., David P. Dearnaley, David J. Finnigan, Anwar Padhani, Steven F. Tannerd, Martin O. Leach (1997) Magnetic resonance imaging (MRI): considerations and applications in radiotherapy treatment planning. *Radiotherapy and Oncology*. **42**: 1–15.
- Kim, H.-Y., Lee, H.; Kim, S.-H.; Jin, H.; Bae, Jeehyeon; Choi, Hyung-Kyoon (2017) Discovery of potential biomarkers in human melanoma cells with different metastatic potential by metabolic and lipidomic profiling. *Scientific reports*. **7** (1): 8864.
- Kim, J., Dang, C. V. (2006) Cancer's molecular sweet tooth and the Warburg effect. *Cancer Research*. **66** (18): 8927–8930.
- Kintzios, S., Marinopoulou, I.; Moschopoulou, G.; Mangana, O.; Nomikou, K.; Endo, K.; Papanastasiou, I.; Simonian, A. (2006) Development of a novel, multi-analyte biosensor system for assaying cell division: identification of cell proliferation/death precursor events. *Biosensors & bioelectronics*. **21** (7): 1365–1373.
- Ko, J., Park, K.; Kim, Y.-S.; Kim, M. S.; Han, J. K.; Kim, K.; Park, R.-W.; Kim, I.-S.; Song, H. K.; Lee, D. S.; Kwon, I. C. (2007) Tumoral acidic extracellular pH targeting of pH-responsive MPEG-poly(beta-amino ester) block copolymer micelles for cancer therapy. *Journal of controlled release : official journal of the Controlled Release Society*. **123** (2): 109–115.
- Koliakos, G., Paletas, K.; Kaloyianni, M. (2008) NHE-1: a molecular target for signalling and cell matrix interactions. *Connective tissue research*. **49** (3): 157–161.
- Kondrashina, A., Dmitriev, R. I.; Borisov, S. M.; Klimant, I.; O'Brien, I.; Nolan, Y. M.; Zhdanov, A. V.; Papkovsky, Dmitri B. (2012) A Phosphorescent Nanoparticle-Based Probe for Sensing and Imaging of (Intra)Cellular Oxygen in Multiple Detection Modalities. *Adv. Funct. Mater*. **22** (23): 4931–4939.
- Kurokawa, H., Ito, H.; Inoue, M.; Tabata, K.; Sato, Y.; Yamagata, K.; Kizaka-Kondoh, S. (2015) High resolution imaging of intracellular oxygen concentration by phosphorescence lifetime. *Scientific reports*. **5**: 10657.
- Kurosawa, H., Utsunomiya, H.; Shiga, N.; Takahashi, A.; Ihara, Motomasa; Ishibashi, Masumi; Nishimoto, Mitsuo; Watanabe, Zen; Abe, Hiroyuki; Kumagai, Jin; Terada, Yukihiro; Igarashi, Hideki; Takahashi, Toshifumi; Fukui, Atsushi; Saganuma, Ryota; Tachibana, Masahito; Yaegashi, Nobuo (2016) Development of a new clinically applicable device for embryo evaluation which measures embryo oxygen consumption. *Human reproduction (Oxford, England)*. **31** (10): 2321–2330.
- L**
- Lall, N., Henly-Smith, C. J.; Canha, M. N. d.; Oosthuizen, C. B.; Berrington, D. (2013) Viability Reagent, PrestoBlue, in Comparison with Other Available Reagents, Utilized in Cytotoxicity and Antimicrobial Assays. *International journal of microbiology*. **2013**: 1–5.
- Lambrechts, A., M. van Troys, C. Ampe (2004) The actin cytoskeleton in normal and pathological cell motility. *The international journal of biochemistry & cell biology*. **36** (10): 1890–1909.
- Langan, L., Dodd, N. J. F.; Owen, S. F.; Purcell, W. M.; Jackson, S. K.; Jha, A. N. (2016) Direct Measurements of Oxygen Gradients in Spheroid Culture System Using Electron Parametric Resonance Oximetry. *PLoS one*. **11** (2): e0149492.
- Larsen, M., Sergey M. Borisov, Björn Grunwald, Ingo Klimant, Ronnie N. Glud. (2011) A simple and inexpensive high resolution color ratiometric planar optode imaging approach: application to oxygen and pH sensing. *Limnol. Oceanogr*. **9**: 348–360.
- Lee, C.-M., W. Kum, C. S. Cockram, R. Teoh, J. D. Young (1989) Functional substance P receptors on a human astrocytoma cell line (U-373 MG). *Brain Research*. **488**: 328–331.
- Lee, J., K. E. Kim, S. Cheon, J. H. Song, Y. Houh, T. S. Kim, M. Gil, K. J. Lee, S. Kim, D. Kim, D. Y. Hur, Y. Yang, S. I. Bang, H. J. Park, D. Cho (2016) Interleukin-32 α induces migration of human melanoma cells through downregulation of E-cadherin. *Oncotarget*: 1-12.
- Lee, J. M., K. Park, Y. Jung, J. K. Kim, S. O. Jung, B. H. Chung (2007) Direct immobilization of protein g variants with various numbers of cysteine residues on a gold surface. *Analytical chemistry*. **79** (7): 2680–2687.

- Lee, S., Scott, A. M. (2007) Hypoxia positron emission tomography imaging with 18f-fluoromisonidazole. *Seminars in nuclear medicine*. **37** (6): 451–461.
- Lee, Z.-W., Teo, X.-Y.; Song, Z. J.; Nin, D. S.; Novera, W.; Choo, B. A.; Dymock, B. W. (2017) Intracellular Hyper-Acidification Potentiated by Hydrogen Sulfide Mediates Invasive and Therapy Resistant Cancer Cell Death. *Frontiers in pharmacology*. **8**: 763.
- Leshner-Pérez, S., Kim, G.-A.; Kuo, C.-H.; Leung, B. M.; Mong, S.; Kojima, T.; Moraes, C.; Thouless, M. D.; Luker, G. D.; Takayama, S. (2017) Dispersible oxygen microsensors map oxygen gradients in three-dimensional cell cultures. *Biomaterials science*. **5** (10): 2106–2113.
- Li, H., Wang, D.; Singh, L. S.; Berk, M.; Tan, H.; Zhao, Z.; Steinmetz, R.; Kirmani, K.; Wei, G. (2009) Abnormalities in osteoclastogenesis and decreased tumorigenesis in mice deficient for ovarian cancer G protein-coupled receptor 1. *PLoS one*. **4** (5): e5705.
- Liberti, M. V., Locasale, J. W. (2016) The Warburg Effect: How Does it Benefit Cancer Cells? *Trends in biochemical sciences*. **41** (3): 211–218.
- Liminga, G. *et al.* (1995) Cytotoxic effect of calcein acetoxymethyl ester on human tumor cell lines: drug delivery by intracellular trapping. *Anti-Cancer Drugs* (6): 578–585.
- Lin, P., Ye, R. D. (2003) The lysophospholipid receptor G2A activates a specific combination of G proteins and promotes apoptosis. *The Journal of Biological Chemistry*. **278** (16): 14379–14386.
- Liu, C., B. C. Bocchicchio, P. A. Overmyer, M. R. Neuman (1980) A Palladium--Palladium Oxide Miniature pH Electrode. *American Association for the Advancement of Science*. **207** (4427): 188–189.
- Liu, J., Huang, Y.; Kumar, A.; Tan, A.; Jin, S.; Mozhi, A.; Liang, X.-J. (2014) pH-sensitive nano-systems for drug delivery in cancer therapy. *Biotechnology advances*. **32** (4): 693–710.
- Liu, Y., Wu, M.; Zhu, L.-N.; Feng, X.-Z.; Kong, De-Ming (2015) Colorimetric and Fluorescent Bimodal Ratiometric Probes for pH Sensing of Living Cells. *Chemistry, an Asian journal*. **10** (6): 1304–1310.
- Lukic, S. and Wegener, J. *et al.* (2015) Impedimetric Monitoring of Cell-Based Assays. *John Wiley & Sons, Ltd*. Chichester, UK: 1–8.
- Lurie, D., Mäder, K. (2005) Monitoring drug delivery processes by EPR and related techniques--principles and applications. *Advanced Drug Delivery Reviews*. **57** (8): 1171–1190.
- Lynen, F., Wieland U. (1938) Über die Giftstoffe des Knollenblätterpilzes. *Annalen der Chemie*. **533**: 93–117.
- ## M
- Maciver, S. K., B. J. Pope, S. Whytock, A. G. Weeds (1998) The effect of two actin depolymerizing factors (ADF/cofilins) on actin filament turnover: pH sensitivity of F - actin binding by human ADF, but not of Acanthamoeba actophorin. *Eur. J. Biochem*. **256**: 388–397.
- Madhus, I. *et al.* (1988) Regulation of intracellular pH in eukaryotic cells. *Biochem. J*. **250**: 1–8.
- Magin, T. M., Vijayaraj, P.; Leube, R. E. (2007) Structural and regulatory functions of keratins. *EXPERIMENTAL CELL RESEARCH*. **313** (10): 2021–2032.
- Mamchaoui, K., G. Saumon (2000) A method for measuring the oxygen consumption of intact cell monolayers. *Am J Physiol Lung Cell Mol Physiol*. **278**: 858–863.
- Marathe, K., McVicar, N.; Li, A.; Bellyou, M.; Meakin, S.; Bartha, R. (2016) Topiramate induces acute intracellular acidification in glioblastoma. *Journal of neuro-oncology*. **130** (3): 465–472.
- Marc, J., Mulner-Lorillon, O.; Bellé, R. (2004) Glyphosate-based pesticides affect cell cycle regulation. *Biology of the cell*. **96** (3): 245–249.
- Martin, C. L., S.C. Reshmi, T. Ried, W. Gottberg, J.W. Wilson (2008) Chromosomal imbalances in oral squamous cell carcinoma: examination of 31 cell lines and review of the literature. *Oral oncology*. **44** (4): 369–382.

- Martin, T. A., Jiang, W. G. (2009) Loss of tight junction barrier function and its role in cancer metastasis. *Biochimica et Biophysica Acta*. **1788** (4): 872–891.
- McGuire, M. K., McGuire, M. A.; Price, W. J.; Shafii, B.; Carrothers, Janae M.; Lackey, Kimberly A.; Goldstein, Daniel A.; Jensen, Pamela K.; Vicini, John L. (2016) Glyphosate and aminomethylphosphonic acid are not detectable in human milk. *The American journal of clinical nutrition*. **103** (5): 1285–1290.
- McNamara, K. P., Nguyen, T.; Dumitrascu, G.; Ji, J.; Rosenzweig, N.; Rosenzweig, Z. (2001) Synthesis, characterization, and application of fluorescence sensing lipobeads for intracellular pH measurements. *Analytical chemistry*. **73** (14): 3240–3246.
- Meier, R. J., Schreml, S.; Wang, X.-D.; Landthaler, M.; Babilas, P.; Wolfbeis, O. S. (2011) Simultaneous photographing of oxygen and pH in vivo using sensor films. *Angewandte Chemie (International ed. in English)*. **50** (46): 10893–10896.
- Mesnager, R., Bernay, B.; Séralini, G.-E. (2013) Ethoxylated adjuvants of glyphosate-based herbicides are active principles of human cell toxicity. *Toxicology*. **313** (2-3): 122–128.
- Metzger, W., D. Sossong, A. Bächle, N. Pütz, G. Wennemuth, T. Pohlemann (2011) The liquid overlay technique is the key to formation of co-culture spheroids consisting of primary osteoblasts, fibroblasts and endothelial cells. *Cytotherapy*. **13** (8): 1000–1012.
- Miller, A. J., M. C. Mihm (2006) Melanoma. *The New England Journal of Medicine*. **355** (1).
- Min, K., Kim, J.-H.; Bae, S. M.; Shin, H.; Kim, M. S.; Park, S.; Lee, H.; Park, R.-W.; Kim, I.-S.; Kim, K.; Kwon, I. C.; Jeong, S. Y.; Lee, D. S. (2010) Tumoral acidic pH-responsive MPEG-poly(beta-amino ester) polymeric micelles for cancer targeting therapy. *Journal of controlled release : official journal of the Controlled Release Society*. **144** (2): 259–266.
- Mingels, R., Kalsi, S.; Cheong, Y.; Morgan, H. (2019) Iridium and Ruthenium oxide miniature pH sensors: Long-term performance. *Sensors and Actuators B: Chemical*. **297**: 126779.
- Missner, A., Kügler, P.; Saparov, S. M.; Sommer, K.; Mathai, J. C.; Zeidel, M. L.; Pohl, P. (2008) Carbon dioxide transport through membranes. *The Journal of Biological Chemistry*. **283** (37): 25340–25347.
- Mitchison, T. J., L. P. Cramer (1996) Actin-Based Cell Motility Review and Cell Locomotion. *Cell*. **84**: 371–379.
- Molter, T. W., McQuaide, S. C.; Holl, M. R.; Meldrum, D. R.; Dragavon, Joseph M.; Anderson, Judith B.; Young, A. Cody; Burgess, Lloyd W.; Lidstrom, Mary E. (2008) A New Approach for Measuring Single-Cell Oxygen Consumption Rates. *IEEE transactions on automation science and engineering : a publication of the IEEE Robotics and Automation Society*. **5** (1): 32–42.
- Mørck, T. J., Sorda, G.; Bechi, N.; Rasmussen, B. S.; Nielsen, J. B.; Ietta, F.; Rytting, E.; Mathiesen, L.; Paulesu, L.; Knudsen, L. E. (2010) Placental transport and in vitro effects of Bisphenol A. *Reproductive toxicology (Elmsford, N.Y.)*. **30** (1): 131–137.
- Mueller-Klieser, W. *et al.* (1984) Method for the determination of oxygen consumption rates and diffusion coefficients in multicellular spheroids. *Biophysical Journal*. **46**: 343–348.
- Mueller-Klieser, W., Freyer, J. P.; Sutherland, R. M. (1986) Influence of glucose and oxygen supply conditions on the oxygenation of multicellular spheroids. *Br. J. Cancer*. **53**: 345–353.
- Mulhall, H. J., Labeed, F. H.; Kazmi, B.; Costea, D. E.; Hughes, M. P.; Lewis, M. P. (2011) Cancer, pre-cancer and normal oral cells distinguished by dielectrophoresis. *Analytical and bioanalytical chemistry*. **401** (8): 2455–2463.
- Murphy, K., Hung, B. P.; Browne-Bourne, S.; Zhou, D.; Yeung, J.; Genetos, D. C.; Leach, J. K. (2017) Measurement of oxygen tension within mesenchymal stem cell spheroids. *Journal of the Royal Society, Interface*. **14** (127).
- N**
- Nath, S., Devi, G. R. (2016) Three-dimensional culture systems in cancer research: Focus on tumor spheroid model. *Pharmacology & therapeutics*. **163**: 94–108.

- Naureckas, E. T., M. B. Hershenson; M. K. Abe; M. D. Kelleher; C. Florio; S. I. Heisler; M. Absher; J. N. Evans; R. W. Samsel; J. Solway (1995) Bronchoalveolar lavage fluid from immature rats with hyperoxia-induced airway remodeling is mitogenic for airway smooth muscle. *Am. J. Respir. Cell Mol. Biol.* **12**: 268–274.
- Nestle, U., Weber, W.; Hentschel, M.; Grosu, A.-L. (2009) Biological imaging in radiation therapy: role of positron emission tomography. *Physics in medicine and biology.* **54** (1): R1-25.
- Prize announcement. NobelPrize.org. Nobel Prize Outreach AB 2020. Mon. 20 Jul 2020.
<<https://www.nobelprize.org/prizes/medicine/2019/prize-announcement/>>
- Noguchi, F., Inui, S.; C. Fedele, M. Shackleton, S. Itami (2017) Calcium-dependent enhancement by extracellular acidity of the cytotoxicity of mitochondrial inhibitors against melanoma. *Molecular Cancer Therapeutics.* **16** (5).
- O**
- Oppegard, S., Eddington, D. T. (2013) A microfabricated platform for establishing oxygen gradients in 3-D constructs. *Biomedical microdevices.* **15** (3): 407–414.
- Ozkan, P., Raj Mutharasan (2002) A rapid method for measuring intracellular pH using BCECF-AM. *Biochimica et Biophysica Acta* (1572): 143–148.
- P**
- Pantazis, N., D. P. Dohrman, J. Luo, C. R. Goodlett, J. R. West (1992) Alcohol Reduces the Number of Pheochromocytoma (PC12) Cells in Culture. *Alcohol.* **9**: 171–180.
- Papandreou, I., Cairns, R. A.; Fontana, L.; Lim, A. L.; Denko, N. C. (2006) HIF-1 mediates adaptation to hypoxia by actively downregulating mitochondrial oxygen consumption. *Cell metabolism.* **3** (3): 187–197.
- Park, J., J.-H. Chang; M. Choi; D.-Y. Lee; Y.K. Pak; and J.J. Pak (2007) Microfabirated Clark-type Sensor for Measuing Dissolved Oxygen. *IEEE Sensors:* 1412–1415.
- Park, S., Koch, D.; Cardenas, R.; Käs, J.; Shih, C. K. (2005) Cell motility and local viscoelasticity of fibroblasts. *Biophysical Journal.* **89** (6): 4330–4342.
- Partin, A. W., J. T. Isaacs, B. Treiger, D. S. Coffey (1988) Early Cell Motility Changes Associated with an Increase in Metastatic Ability in Rat Prostatic Cancer Cells Transfected with the v-Harvey-ras Oncogene. *Cancer Research* (48): 6050–6053.
- Patel, D., Sharma, N. (2016) Inhibitory effect of quercetin on epithelial to mesenchymal transition in SK-MEL-28 human melanoma cells defined by in vitro analysis on 3D collagen gels. *OncoTargets and therapy.* **9**: 6445–6459.
- Pedersen, P.-H., Ness, G. O.; Engebraatenr, O.; Bjerkvig, R.; Lillehaug, J. R.; Laerum, O. D. (1994) Heterogeneous response to the growth factors [EGF, PDGF (bb), TGF - α , bFGF, IL - 2] on glioma spheroid growth, migration and invasion. *Int. J. Cancer.* **56**: 255–261.
- Perez-Sala, D. *et al.* (1995) Intracellular Alkalinization Suppresses Lovastatin-induced Apoptosis in HL-60 Cells through the Inactivation of a pH-dependent Endonuclease. *The Journal of Biological Chemistry.* **270** (11): 6235–6242.
- Pettersen, E., L. H. Larsen, N. B. Ramsing and P. Ebbesen (2005) Pericellular oxygen depletion during ordinary tissue culturing, measured with oxygen microsensors. *Cell Prolif.* **38**: 257-267.
- Pierschbacher, M. D., Ruoslahti, E. (1984) Cell attachment activity of fibronectin can be duplicated by small synthetic fragments of the molecule. *Nature.* **309** (3): 30–33.
- Plitzko, B., Loesgen, S. (2018) Measurement of Oxygen Consumption Rate (OCR) and Extracellular Acidification Rate (ECAR) in Culture Cells for Assessment of the Energy Metabolism. *BIO-PROTOCOL.* **8** (10).
- Popel, A. *et al.* (1989) Theory of oxygen transport in tissue. *Biomed Eng.* **17** (3): 257–321.
- Pungor, E. *et al.* (1998) The Theory of Ion-selective Electrodes. *Analytical Sciences.* **14**: 249–256.

Q

Qin, Y., Li, X.; Xiang, Y.; Di Wu; Bai, Liwen; Li, Zhuangzhuang; Liang, Yan (2017) Toxic effects of glyphosate on diploid and triploid fin cell lines from *Misgurnus anguillicaudatus*. *Chemosphere*. **180**: 356–364.

R

Raghavan, S., Ward, M. R.; Rowley, K. R.; Wold, R. M.; Takayama, Shuichi; Buckanovich, Ronald J.; Mehta, Geeta (2015) Formation of stable small cell number three-dimensional ovarian cancer spheroids using hanging drop arrays for preclinical drug sensitivity assays. *Gynecologic oncology*. **138** (1): 181–189.

Rajpurohit, R., Risbud, M. V.; Ducheyne, P.; Vresilovic, E. J.; Shapiro, I. M. (2002) Phenotypic characteristics of the nucleus pulposus: expression of hypoxia inducing factor-1, glucose transporter-1 and MMP-2. *Cell and tissue research*. **308** (3): 401–407.

Reiß, B. (2004) Mikrogravimetrische Untersuchung des Adhäsionskontakts tierischer Zellen: Eine biophysikalische Studie. Biochemie, Westfälische Wilhelms-Universität Münster. **Dissertation**.

Reiss, B., Wegener, J. (2015) Impedance analysis of different cell monolayers grown on gold-film electrodes. *IEEE*:7079–7082.

Ren, J., Zhang, L. (2011) Effects of ovarian cancer G protein coupled receptor 1 on the proliferation, migration, and adhesion of human ovarian cancer cells. *Chin Med J*. **124** (9): 1327–1332.

Reshkin, S., Bellizzi, A.; Caldeira, S.; Albarani, V.; Malanchi, I.; Poignee, M.; Alunni-Fabbroni, M.; Casavola, V.; Tommasino, M. (2000) Na⁺/H⁺ exchanger-dependent intracellular alkalinization is an early event in malignant transformation and plays an essential role in the development of subsequent transformation-associated phenotypes. *The FASEB Journal*. **14**: 2185–2197.

Richard, S., Moslemi, S.; Sipahutar, H.; Benachour, N.; Seralini, Gilles-Eric (2005) Differential effects of glyphosate and roundup on human placental cells and aromatase. *Environmental Health Perspectives*. **113** (6): 716–720.

Richardson, J., V. Scalera, N. S. (1981) Identification of two strains of MCKK cell which resemble separate nephron tubule segments. *Biochimica et Biophysica Acta* (673): 26–36.

Richter, C. A., Birnbaum, L. S.; Farabollini, F.; Newbold, R. R.; Rubin, Beverly S.; Talsness, Chris E.; Vandenberg, John G.; Walser-Kuntz, Debby R.; Vom Saal, Frederick S. (2007) In vivo effects of bisphenol A in laboratory rodent studies. *Reproductive toxicology (Elmsford, N.Y.)*. **24** (2): 199–224.

Riemann, A., Rauschner, M.; Gießelmann, M.; Reime, S.; Haupt, V.; Thews, O. (2019) Extracellular Acidosis Modulates the Expression of Epithelial-Mesenchymal Transition (EMT) Markers and Adhesion of Epithelial and Tumor Cells. *Neoplasia (New York, N.Y.)*. **21** (5): 450–458.

Rochester, J. R. *et al.* (2013) Bisphenol A and human health: a review of the literature. *Reproductive toxicology (Elmsford, N.Y.)*. **42**: 132–155.

Roos, A., Boron, W. (1981) Intracellular pH. *Physiological Reviews*. **61** (2): 296–434.

Rosenbaum, D. M., M. Michaelson, D. K. Batter, P. Doshi, J. A. Kessler (1994) Evidence for hypoxia-induced, programmed cell death of cultured neurons. *Annals of Neurology*. **36** (6): 864–870.

Ruggiero, C., Elks, C. M.; Kruger, C.; Cleland, E.; Addison, Kaity; Noland, Robert C.; Stadler, Krisztian (2014) Albumin-bound fatty acids but not albumin itself alter redox balance in tubular epithelial cells and induce a peroxide-mediated redox-sensitive apoptosis. *Am J Physiol Renal Physiol*. **306** (8): F896–906.

S

Sandler, O., Mizrahi, S. P.; Weiss, N.; Agam, O.; Simon, Itamar; Balaban, Nathalie Q. (2015) Lineage correlations of single cell division time as a probe of cell-cycle dynamics. *Nature*. **519** (7544): 468–471.

Santini, M., Rainaldi, G. (1999) Three-Dimensional Spheroid Model in Tumor Biology. *Pathobiology*. **67**: 148–157.

- Sarkar, S., Peng, C.-C.; Kuo, C. W.; Chueh, D.-Y.; Wu, H.-M.; Liu, Y.-H.; Chen, P.; Tung, Y.-C. (2018) Study of oxygen tension variation within live tumor spheroids using microfluidic devices and multi-photon laser scanning microscopy. *RSC Adv.* **8** (53): 30320–30329.
- Savinell, R., Liu, C. C.; Kowalsky, T. E.; Puschett, J. B. (1981) Miniature Glass pH Electrode with Nonaqueous Internal Reference Solution. *Anal. Chem.* **53**: 552–554.
- Schmittlein, C. (2017) Sensors and Actuators for 2D and 3D Cell Culture Models Based on Oxygen Sensitive Culture Substrates. Chemistry, University of Regensburg. **Dissertation.**
- Schönfelder, G., Werner Wittfoht, Hartmut Hopp, Chris E. Talsness, Martin Paul, and Ibrahim Chahoud (2002) Parent bisphenol A accumulation in the human maternal-fetal-placental unit. *Environmental Health Perspectives.* **110** (11): 703–707.
- Schwartz, L., Seyfried, T.; Alfaraouk, K. O.; Da Veiga Moreira, J.; Fais, S. (2017) Out of Warburg effect: An effective cancer treatment targeting the tumor specific metabolism and dysregulated pH. *Seminars in cancer biology.* **43**: 134–138.
- Schweitzer, C., Schmidt, R. (2003) Physical mechanisms of generation and deactivation of singlet oxygen. *Chemical reviews.* **103** (5): 1685–1757.
- Schwerdt, G., Freudinger, R.; Schuster, C.; Silbernagl, S.; Gekle, M. (2003) Inhibition of mitochondria prevents cell death in kidney epithelial cells by intra- and extracellular acidification. *Kidney International.* **63**: 1725–1735.
- Semenza, G. *et al.* (2003) Targeting HIF-1 for cancer therapy. *Nature reviews. Cancer.* **3** (10): 721–732.
- Semenza, G. *et al.* (2004) Hydroxylation of HIF-1: oxygen sensing at the molecular level. *Physiology (Bethesda, Md.).* **19**: 176–182.
- Semenza, G. *et al.* (2012) Hypoxia-inducible factors in physiology and medicine. *Cell.* **148** (3): 399–408.
- Semenza, G. *et al.* (2013) HIF-1 mediates metabolic responses to intratumoral hypoxia and oncogenic mutations. *The Journal of clinical investigation.* **123** (9): 3664–3671.
- Semenza, G. L. *et al.* (2001) HIF-1 and mechanisms of hypoxia sensing. *Cell biology.* **13**: 167–171.
- Sergeeva, T. F., Shirmanova, M. V.; Zlobovskaya, O. A.; Gavrina, A. I.; Dudenkova, V. V.; Lukina, M. M.; Lukyanov, K. A.; Zagaynova, E. V. (2017) Relationship between intracellular pH, metabolic co-factors and caspase-3 activation in cancer cells during apoptosis. *Biochimica et biophysica acta. Molecular cell research.* **1864** (3): 604–611.
- Shambloott, M., Axelman, J.; Wang, S.; Bugg, E. M.; Littlefield, J. W.; Donovan, P. (1998) Derivation of pluripotent stem cells from cultured human primordial germ cells. *Proc. Natl. Acad. Sci.* **95**: 13726–13731.
- Shangguan, J., He, D.; He, X.; Wang, K.; Xu, Fengzhou; Liu, J.; Tang, J.; Yang, X.; Huang, J. (2016) Label-Free Carbon-Dots-Based Ratiometric Fluorescence pH Nanoprobes for Intracellular pH Sensing. *Analytical chemistry.* **88** (15): 7837–7843.
- Shields, R., Smith, J. A. (1977) Cells regulate their proliferation through alterations in transition probability. *J. Cell. Physiol.* **91**: 345–356.
- Shiku, H., Shiraishi, T.; Ohya, H.; Matsue, T.; Abe, H.; Hoshi, H.; Kobayashi, M. (2001) Oxygen consumption of single bovine embryos probed by scanning electrochemical microscopy. *Analytical chemistry.* **73** (15): 3751–3758.
- Singh, L., Berk, M.; Oates, R.; Zhao, Z.; Tan, Haiyan; Jiang, Ying; Zhou, Aimin; Kirmani, Kashif; Steinmetz, Rosemary; Lindner, Daniel; Xu, Yan (2007) Ovarian cancer G protein-coupled receptor 1, a new metastasis suppressor gene in prostate cancer. *Journal of the national cancer Institute.* **99** (17): 1313–1327.
- Slepkov, E. R., Rainey, J. K.; Sykes, B. D.; Fliegel, L. (2007) Structural and functional analysis of the Na⁺/H⁺ exchanger. *The Biochemical journal.* **401** (3): 623–633.
- So, P., Dong, C. (2001) Fluorescence Spectrophotometry. *Encyclopedia of Life Sciences.*
- Song, A., Stephen Parus, and Raoul Kopelman (1997) High-Performance Fiber-Optic pH Microsensors for Practical Physiological Measurements Using a Dual-Emission Sensitive Dye. *Analytical chemistry* (68): 863–867.

- Staples, C. A., Philip B. Dom, Gary M. Klecka, Sandra T. O'Block (1998) A Review of the Environmental Fate, Effects, and Exposures of Bisphenol A. *Chemosphere*. **36** (10): 2149–2173.
- Stiefel, F., Paul, A. J.; Jacopo, T.; Sgueglia, A.; Stützle, M.; Herold, E. M.; Hesse, F. (2016) The influence of bisphenol A on mammalian cell cultivation. *Applied microbiology and biotechnology*. **100** (1): 113–124.
- Stock, C., Gassner, B.; Hauck, C. R.; Arnold, H.; Mally, Sabine; Eble, Johannes A.; Dieterich, Peter; Schwab, Albrecht (2005) Migration of human melanoma cells depends on extracellular pH and Na⁺/H⁺ exchange. *The Journal of physiology*. **567.1**: 225–238.
- Stock, C., Schwab, A. (2006) Role of the Na/H exchanger NHE1 in cell migration. *Acta physiologica (Oxford, England)*. **187** (1-2): 149–157.
- Stock, C., M. Mueller, H. Kraehling, S. Mally, J. Noël, C. Eder, A. Schwab (2007) pH Nanoenvironment at the Surface of Single Melanoma Cells. *Cell Physiol Biochem* (20): 679–686.
- Stolwijk, J., Sauer, L.; Ackermann, K.; Nassios, A.; Aung, T.; Haerteis, S.; Bäumner, A.; Wegener, J.; Schreml, S. (2020) pH-sensing in skin tumors: methods to study the involvement of GPCRs, acid-sensing ion channels and transient receptor potential vanilloid channels. *Experimental dermatology*. **29** (11): 1055–1061.
- Stroheker, T., Picard, K.; Lhuguenot, J. C.; Canivenc-Lavier, M. C.; Chagnon, M. C. (2004) Steroid activities comparison of natural and food wrap compounds in human breast cancer cell lines. *Food and chemical toxicology : an international journal published for the British Industrial Biological Research Association*. **42** (6): 887–897.
- Stüwe, L., Müller, M.; Fabian, A.; Waning, J.; Mally, S.; Noël, J.; Schwab, A.; Stock, C. (2007) pH dependence of melanoma cell migration: protons extruded by NHE1 dominate protons of the bulk solution. *The Journal of physiology*. **585** (Pt 2): 351–360.
- Sun, X., Yang, L. V.; Tiegs, B. C.; Arend, L. J.; McGraw, D. W.; Penn, R. B.; Petrovic, S. (2010) Deletion of the pH sensor GPR4 decreases renal acid excretion. *Journal of the American Society of Nephrology : JASN*. **21** (10): 1745–1755.
- Șuteu, O., Blaga, M. L.; Nicula, F.; Șuteu, P.; Coza, O.; Achimaș-Cadariu, P.; Coza, D. (2017) Incidence trends and survival of skin melanoma and squamous cell carcinoma in Cluj County, Romania. *European journal of cancer prevention : the official journal of the European Cancer Prevention Organisation (ECP)*: S176-S182.
- Sutko, J. L., R. Henry (1977) Direct effects of the monovalent cation ionophores monensin and nigericin on myocardium. *The Journal of Pharmacology and Experimental Therapeutic*. **203** (3): 685–700.
- Székács, I., Farkas, E.; Gemes, B. L.; Takacs, E.; Szekacs, Andras; Horvath, Robert (2018) Integrin targeting of glyphosate and its cell adhesion modulation effects on osteoblastic MC3T3-E1 cells revealed by label-free optical biosensing. *Scientific reports*. **8** (1): 17401.
- ## T
- Tanaka, N., Yamaguchi, H.; Mano, N. (2019) Involvement of H⁺-gradient dependent transporter in PGE₂ release from A549 cells. *Prostaglandins, leukotrienes, and essential fatty acids*. **149**: 30–36.
- Tatum, J., Kelloff, G. J.; Gillies, R. J.; Arbeit, J. M.; Brown, J. M.; Chao, K. S. C.; Chapman, J. D. (2006) Hypoxia: importance in tumor biology, noninvasive measurement by imaging, and value of its measurement in the management of cancer therapy. *International journal of radiation biology*. **82** (10): 699–757.
- Thongprakaisang, S., Thiantanawat, A.; Rangkadilok, N.; Suriyo, T.; Satayavivad, Jutamaad (2013) Glyphosate induces human breast cancer cells growth via estrogen receptors. *Food and chemical toxicology : an international journal published for the British Industrial Biological Research Association*. **59**: 129–136.
- Townsend, M., Peck, C.; Meng, W.; Heaton, M.; Robison, Richard; O'Neill, Kim (2017) Evaluation of various glyphosate concentrations on DNA damage in human Raji cells and its impact on cytotoxicity. *Regulatory toxicology and pharmacology : RTP*. **85**: 79–85.
- Tremel, A., Cai, A.; Tirtaatmadja, N.; Hughes, B. D.; Stevens, G. W.; Landman, K. A.; O'Connor, A. J. (2009) Cell migration and proliferation during monolayer formation and wound healing. *Chemical Engineering Science*. **64** (2): 247–253.

V

- Valentich, J. D. *et al.* (1981) Morphological similarities between the dog kidney cell line MDCK and the mammalian cortical collecting tubule. *Annals New York Academy of Sciences* (372): 384–405.
- Vander Heiden, M. G., Cantley, L. C.; Thompson, C. B. (2009) Understanding the Warburg effect: the metabolic requirements of cell proliferation. *Science (New York, N.Y.)*. **324** (5930): 1029–1033.
- Vaupel, P., Kallinowski, F.; Okunieff, P. (1989) Blood Flow, Oxygen and Nutrient Supply, and Metabolic Microenvironment of Human Tumors: A Review. *Cancer Research*. **49**: 6449–6465.
- Vāvere, A., Biddlecombe, G. B.; Spees, W. M.; Garbow, J. R.; Wijesinghe, D.; Andreev, O. A.; Engelman, D. M.; Reshetnyak, Y. K.; Lewis, J. S. (2009) A novel technology for the imaging of acidic prostate tumors by positron emission tomography. *Cancer Research*. **69** (10): 4510–4516.
- Viñas, R., Jeng, Y.-J.; Watson, C. S. (2012) Non-genomic effects of xenoestrogen mixtures. *International journal of environmental research and public health*. **9** (8): 2694–2714.

W

- Wagner, N., Lötters, S. (2013) Effects of water contamination on site selection by amphibians: experiences from an arena approach with European frogs and newts. *Archives of environmental contamination and toxicology*. **65** (1): 98–104.
- Walsh, L. P. *et al.* (2000) Roundup Inhibits Steroidogenesis by Disrupting Steroidogenic Acute Regulatory (StAR) Protein Expression. *Environmental Health Perspectives*. **108** (8): 769–776.
- Wan, J., Kalpage, H. A.; Vaishnav, A.; Liu, J.; Lee, I.; Mahapatra, G. (2019) Regulation of Respiration and Apoptosis by Cytochrome c Threonine 58 Phosphorylation. *Scientific reports*. **9** (1): 15815.
- Wang, H.-X., Chen, Y.-H.; Zhou, J.-X.; Hu, X.-Y.; Tan, C.; Yan, Y.; Huang, Q.-L.; Shen, J.-Y. (2018) Overexpression of G-protein-coupled receptors 65 in glioblastoma predicts poor patient prognosis. *Clinical neurology and neurosurgery*. **164**: 132–137.
- Wang, X.-D., Chen, X.; Xie, Z.-x.; Wang, X.-r. (2008) Reversible optical sensor strip for oxygen. *Angewandte Chemie (International ed. in English)*. **47** (39): 7450–7453.
- Wang, X.-H., Peng, H.-S.; Chang, Z.; Hou, L.-L.; You, Fang-Tian (2012) Synthesis of ratiometric fluorescent nanoparticles for sensing oxygen. *Microchim Acta*. **178** (1-2): 147–152.
- Warburg, O., Posener, K.; Negelein, E. (1924) Über den Stoffwechsel der Carcinomzelle. *Biochem Z*. **152**: 309–344.
- Warburg, O., Wind, F.; Negelein, E. (1927) The Metabolism of Tumors in the Body. *The Journal of General Physiology*. **8**: 519–530.
- Warsinke, A., A. Benkert, F. W. Scheller (2000) Electrochemical immunoassays. *Fresenius J Anal Chem* (366): 622–634.
- Weaver, J., Burks, S. R.; Liu, K. J.; Kao, J. P. Y.; Rosen, G. M. (2016) In vivo EPR oximetry using an isotopically-substituted nitroxide: Potential for quantitative measurement of tissue oxygen. *Journal of magnetic resonance*. **271**: 68–74.
- Webb, B., Chimenti, M.; Jacobson, M. P.; Barber, D. L. (2011) Dysregulated pH: a perfect storm for cancer progression. *Nature reviews. Cancer*. **11** (9): 671–677.
- Wegener, J., C. R. Keese, I. Giaever (2000) Electric cell-substrate impedance sensing (ECIS) as a noninvasive means to monitor the kinetics of cell spreading to artificial surfaces. *EXPERIMENTAL CELL RESEARCH*. **259** (1): 158–166.
- Welsh, S., Powis, G. (2003) Hypoxia Inducible Factor as a Cancer Drug Target. *Current Cancer Drug Targets* (3): 391–405.
- Weltin, A., Hammer, S.; Noor, F.; Kaminski, Y.; Kieninger, J.; Urban, G. A. (2017) Accessing 3D microtissue metabolism: Lactate and oxygen monitoring in hepatocyte spheroids. *Biosensors & bioelectronics*. **87**: 941–948.

- Wetherill, Y. B., Akingbemi, B. T.; Kanno, J.; McLachlan, J. A.; Nadal, Angel; Sonnenschein, Carlos; Watson, Cheryl S.; Zoeller, R. Thomas; Belcher, Scott M. (2007) In vitro molecular mechanisms of bisphenol A action. *Reproductive toxicology (Elmsford, N.Y.)*. **24** (2): 178–198.
- White, J. S., J. L. Weissfeld, C.C.R. Ragin, K. M. Rossie, C. L. Martin, M. Shuster (2007) The influence of clinical and demographic risk factors on the establishment of head and neck squamous cell carcinoma cell lines. *Oral oncology*. **43** (7): 701–712.
- White, K. A., Grillo-Hill, B. K.; Barber, D. L. (2017) Cancer cell behaviors mediated by dysregulated pH dynamics at a glance. *Journal of cell science*. **130** (4): 663–669.
- Whitten, S., Bertrand García-Moreno E., Vincent J. Hilser (2005) Local conformational fluctuations can modulate the coupling between proton binding and global structural transitions in proteins. *PNAS*. **102** (12): 4282–4287.
- Wiley, S., Sriram, K.; Salmerón, C.; Insel, P. A. (2019) GPR68: An Emerging Drug Target in Cancer. *International journal of molecular sciences*. **20** (3).
- Wirasinha, R., Vijayan, D.; Smith, N. J.; Parnell, G. P.; Swarbrick, A.; Brink, R.; King, C.; Stewart, G.; Booth, D. R.; Batten, M. (2018) GPR65 inhibits experimental autoimmune encephalomyelitis through CD4+ T cell independent mechanisms that include effects on iNKT cells. *Immunology and cell biology*. **96** (2): 128–136.
- Wodarz, A. *et al.* (2005) Molecular control of cell polarity and asymmetric cell division in Drosophila neuroblasts. *Current opinion in cell biology*. **17** (5): 475–481.
- www.agilent.com/en/product/cell-analysis/real-time-cell-metabolic-analysis/xf-analyzers/cell-analysis-measuring-cell-metabolism-transient-micro-chamber
- www.biophysics.com/cultureware.php
- www.zencellowl.com
- Wyder, L., Suply, T.; Ricoux, B.; Billy, E.; Schnell, C.; Baumgarten, B. U.; Maira, S. M. (2011) Reduced pathological angiogenesis and tumor growth in mice lacking GPR4, a proton sensing receptor. *Angiogenesis*. **14** (4): 533–544.
- X**
- Xia, Y., Zhou, Y.; Han, H.; Li, P.; Wei, Wei; Lin, Nengxing (2019) lncRNA NEAT1 facilitates melanoma cell proliferation, migration, and invasion via regulating miR-495-3p and E2F3. *Journal of cellular Physiology*. **234** (11): 19592–19601.
- Xiao, C., Luong, J. H. T. (2003) On-line monitoring of cell growth and cytotoxicity using electric cell-substrate impedance sensing (ECIS). *Biotechnology progress*. **19** (3): 1000–1005.
- Xiong, X., Xiao, D.; Choi, M. M.F. (2006) Dissolved oxygen sensor based on fluorescence quenching of oxygen-sensitive ruthenium complex immobilized on silica–Ni–P composite coating. *Sensors and Actuators B: Chemical*. **117** (1): 172–176.
- Y**
- Yang, Q., Wang, H.; Lan, X.; Cheng, B.; Chen, S.; Shi, H.; Xiao, H.; Ma, Y. (2015) Reflection-mode micro-spherical fiber-optic probes for in vitro real-time and single-cell level pH sensing. *Sensors and actuators. B, Chemical*. **207** (Pt A): 571–580.
- Yeo, E.-J., Y.-S. Chun, Y.-S. Cho, J. Kim, J.-C. Lee, M.-S. Kim, J.-W. Park (2003) YC-1: A Potential Anticancer Drug Targeting Hypoxia-Inducible Factor 1. *Journal of the national cancer Institute*. **95** (7): 516–525.
- Z**
- Zabalza, A., Orcaray, L.; Fernández-Escalada, M.; Zulet-González, A.; Royuela, Mercedes (2017) The pattern of shikimate pathway and phenylpropanoids after inhibition by glyphosate or quinate feeding in pea roots. *Pesticide biochemistry and physiology*. **141**: 96–102.

- Zernike, F. *et al.* (1942) Phase contrast, a new method for the microscopic observation of transparent objects part. *Physica IX* (10): 974-986.
- Zhang, X., He, C.; Liu, X.; Chen, Y.; Zhao, P.; Chen, C.; Yan, R.; Li, M.; Fan, T.; Altine, B.; Yang, T.; Lu, Y.; Lee, R. J.; Gai, Y.; Xiang, G. (2020) One-pot synthesis of a microporous organosilica-coated cisplatin nanoplatfom for HIF-1-targeted combination cancer therapy. *Theranostics*. **10** (7): 2918–2929.
- Zhou, B., Bian, C.; Tong, J.; Xia, S. (2017) Fabrication of a Miniature Multi-Parameter Sensor Chip for Water Quality Assessment. *Sensors (Basel, Switzerland)*. **17** (1).
- Zhou, Y., Arai, T.; Horiguchi, Y.; Ino, K.; Matsue, Tomokazu; Shiku, Hitoshi (2013) Multiparameter analyses of three-dimensionally cultured tumor spheroids based on respiratory activity and comprehensive gene expression profiles. *Analytical biochemistry*. **439** (2): 187–193.
- Zimmer, G., F. Lottspeich, A. Maisner, H.-D. Klenk, G. Herrler (1997) Molecular characterization of gp40, a mucin-type glycoprotein from the apical plasma membrane of Madin–Darby canine kidney cells (type I). *Biochem. J.* **326**: 99–108.
- Zou, H., Li, Y.; Liu, X.; Wang, X. (1999) An APAF-1.cytochrome c multimeric complex is a functional apoptosome that activates procaspase-9. *The Journal of Biological Chemistry*. **274** (17): 11549–11556.

11 APPENDIX

11.1 SUPPLEMENTARY INFORMATION

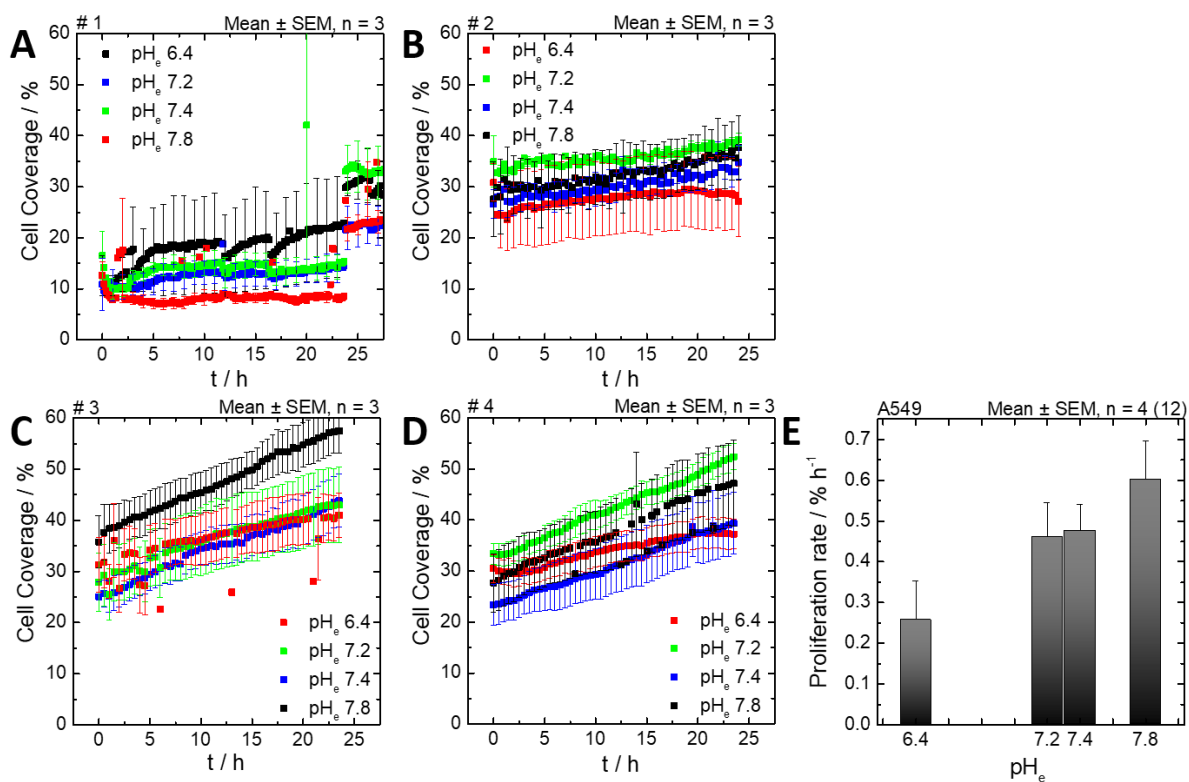


Fig. 11.1 Image-based detection of pH-dependent proliferation of A549 cells performed with the 24-channel microscopic device zenCell owl. (A-D) Time-dependent change of cell coverage from individual experiments of pH-dependent proliferation. Proliferation was observed under the influence of L-15 medium adjusted to four different pH values. (E) Calculated change of cell coverage per hour of the four individual experiments, yielded by a linear regression of the time-resolved cell coverage. Each condition of the four individual experiments was performed in triplicate (n = 4 (12)). T = 37 °C and 0 % CO₂.

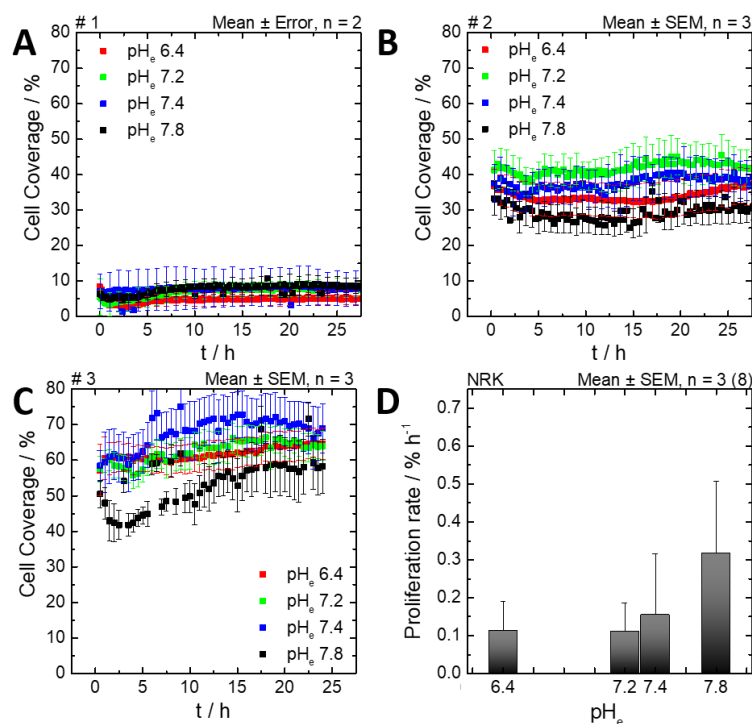


Fig. 11.2 Image-based detection of pH-dependent proliferation of NRK cells performed with the 24-channel microscopic device zenCell owl. (A-C) Time-dependent change of cell coverage from individual experiments of pH-dependent proliferation. Proliferation was observed under the influence of L-15 medium adjusted to four different pH values. (D) Calculated change of cell coverage per hour of the three individual experiments, yielded by linear regression of the time-resolved cell coverage. Each condition in the three individual experiments was performed at least twice ($n = 3$ (8)). $T = 37\text{ }^{\circ}\text{C}$ and $0\text{ }\% \text{CO}_2$.

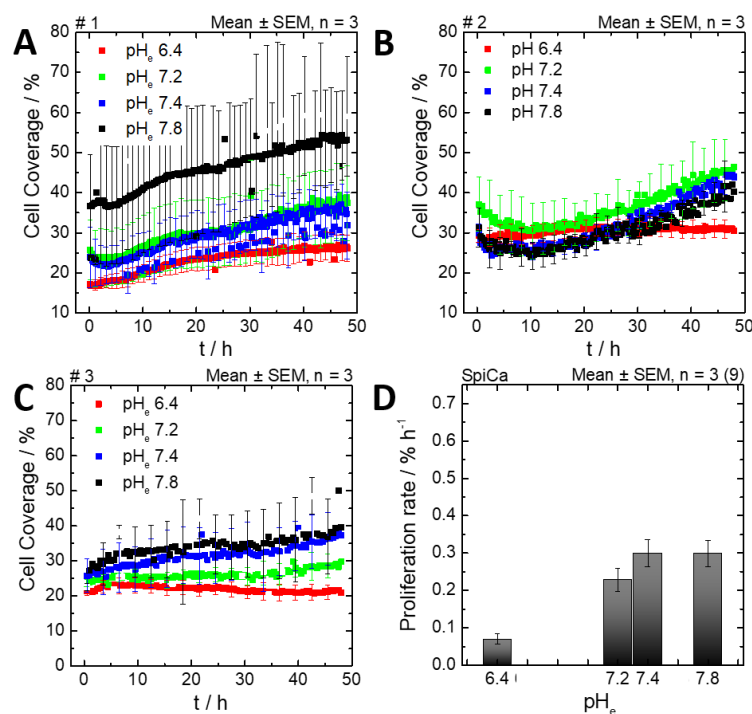


Fig. 11.3 Image-based detection of pH-dependent proliferation of SpiCa cells performed with the 24-channel microscopic device zenCell owl. (A-C) Time-dependent change of cell coverage from individual experiments of pH-dependent proliferation. Proliferation was observed under the influence of L-15 medium adjusted to four different pH values. (D) Calculated change of cell coverage per hour of the three individual experiments, yielded by linear regression of the time-resolved cell coverage. Each condition in the three individual experiments was performed in triplicate ($n = 3$ (9)). $T = 37\text{ }^{\circ}\text{C}$ and $0\text{ }\% \text{CO}_2$.

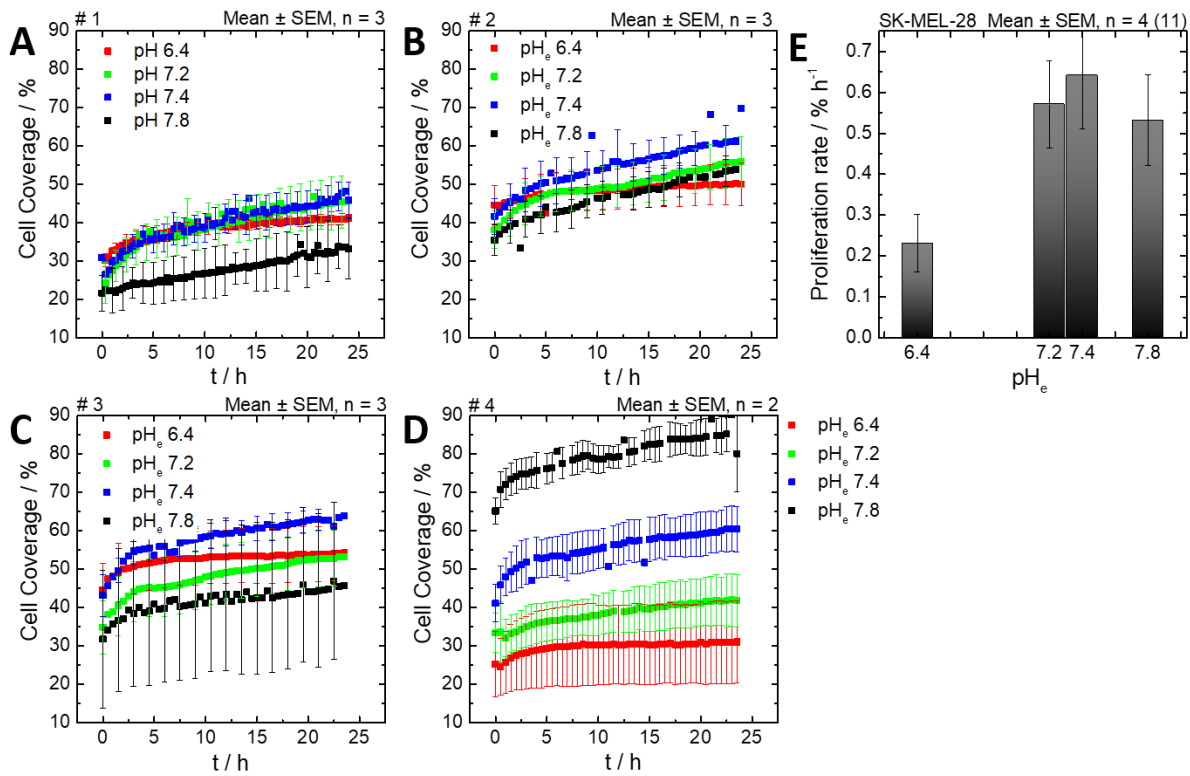


Fig. 11.4 Image-based investigation of pH-dependent proliferation of SK-MEL-28 cells performed with the 24-channel microscopic device zenCell owl. (A-D) Time-dependent change of cell coverage from individual experiments of pH-dependent proliferation. Proliferation was observed under the influence of L-15 medium adjusted to four different pH values. (E) Calculated change of cell coverage per hour of the four individual experiments, yielded by linear regression of the time-resolved cell coverage. Each condition in the four individual experiments was performed at least twice ($n = 4$ (11)). $T = 37$ °C and 0 % CO_2 .

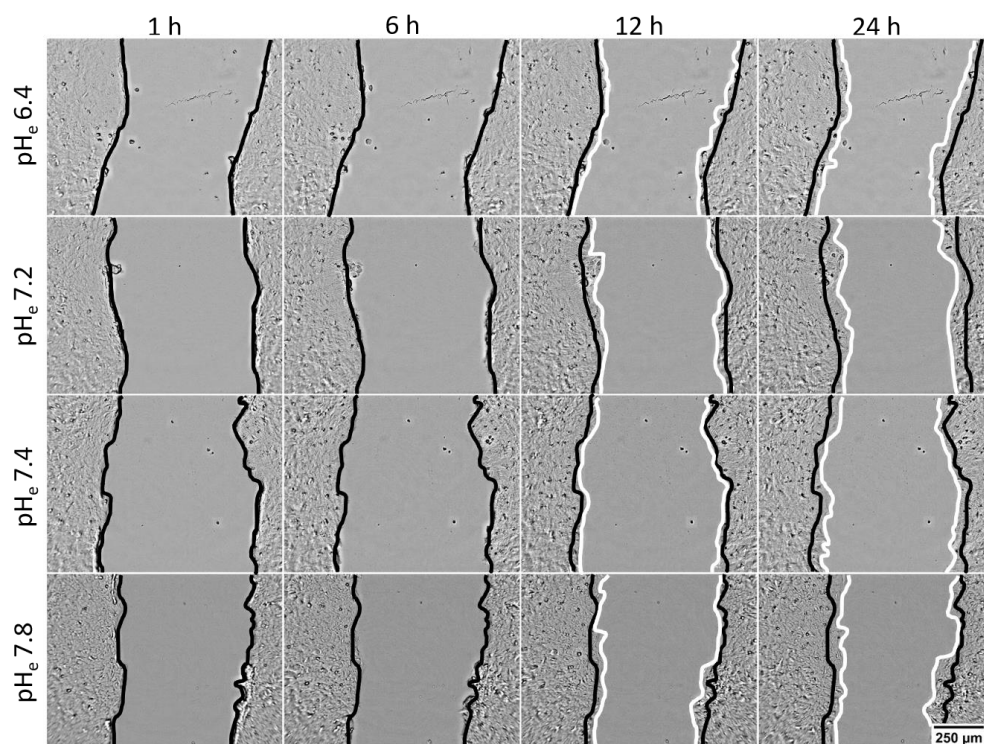


Fig. 11.5 Microscopic images with digital phase contrast of the investigation of pH-dependent migration of A549 cells 1 h, 6 h, 12 h and 24 h after wounding. Black lines outline the borders of the cell-free area of the initial wound. White lines sketch the migrating cell borders into the cell-free area. Scale bar depicts 250 μm .

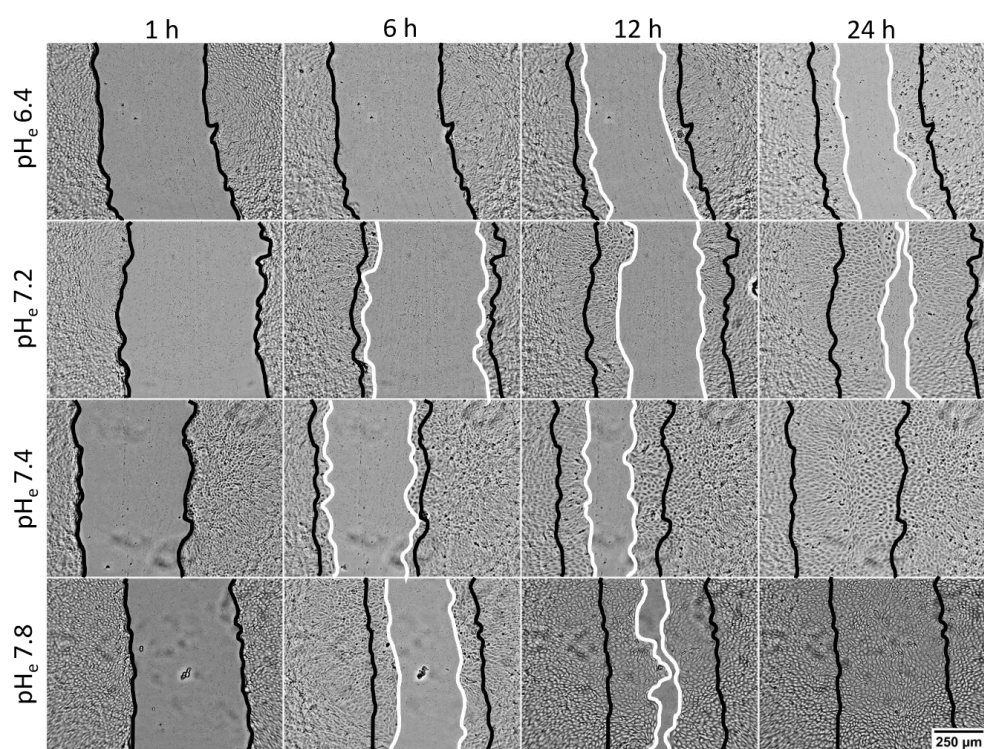


Fig. 11.6 Microscopic images with digital phase contrast of the investigation of pH-dependent migration of NRK cells 1 h, 6 h, 12 h and 24 h after wounding. Black lines outline the borders of the cell-free area of the initial wound. White lines sketch the migrating cell borders into the cell-free area. Scale bar depicts 250 μm .

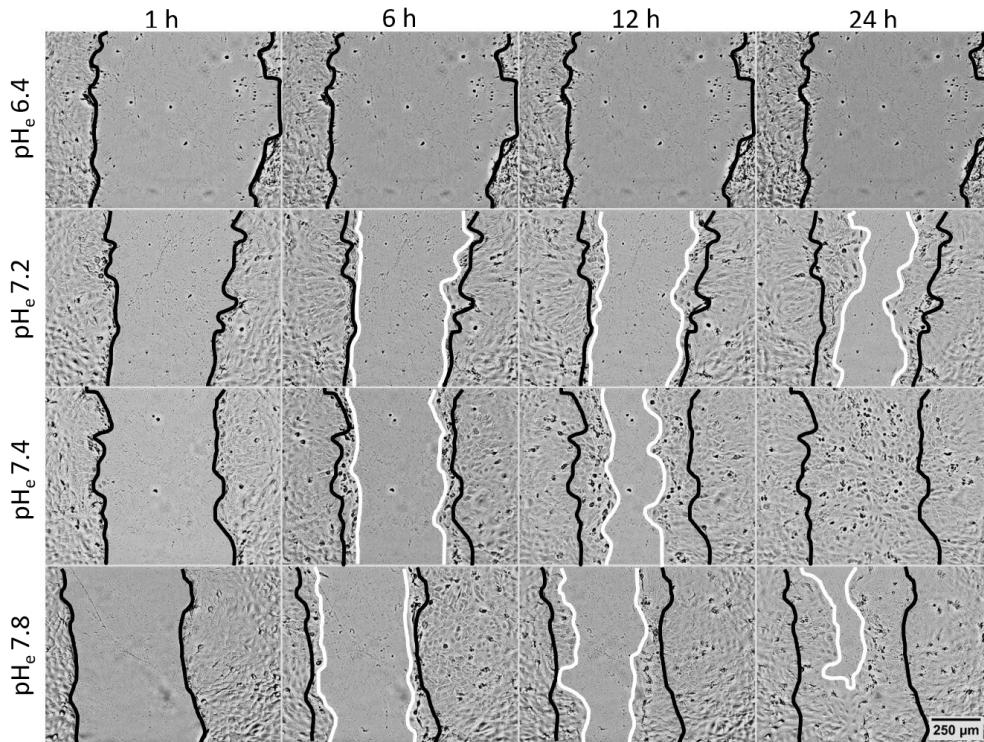


Fig. 11.7 Microscopic images with digital phase contrast of the investigation of pH-dependent migration of SpiCa cells 1 h, 6 h, 12 h and 24 h after wounding. Black lines outline the borders of the cell-free area of the initial wound. White lines sketch the migrating cell borders into the cell-free area. Scale bar depicts 250 μm .

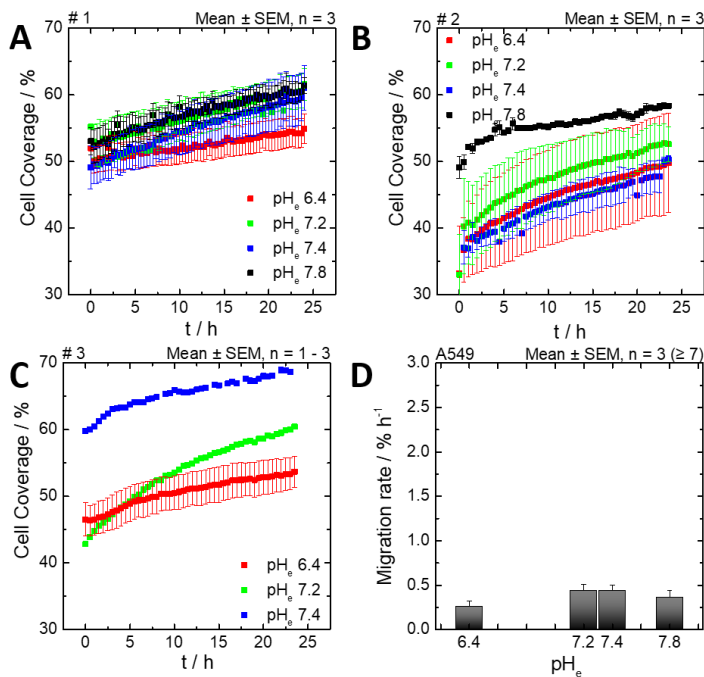


Fig. 11.8 Image-based investigation of pH-dependent migration of A549 cells performed with the 24-channel microscopic device zenCell owl. (A-C) Time-dependent cell coverage from individual experiments of pH-dependent migration after *scratch assay* wounding. Migration was observed under the influence of L-15 adjusted to four different pH values. (D) Calculated migration rate (cell coverage per hour) of the three individual experiments, according to a linear regression of the time-resolved cell coverage until reaching 100% cell coverage. T = 37 °C and 0% CO₂.

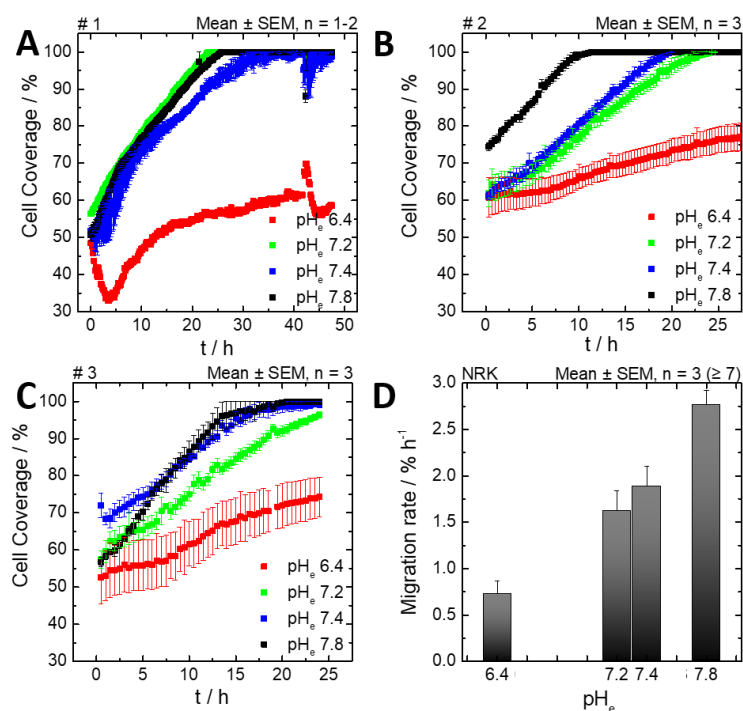


Fig. 11.9 Image-based investigation of pH-dependent migration of NRK cells performed with the 24-channel microscopic device zenCell owl. (A-C) Time-dependent cell coverage from individual experiments of pH-dependent migration after *scratch assay* wounding. Migration was observed under the influence of L-15 adjusted to four different pH values. (D) Calculated migration rate (cell coverage per hour) of the three individual experiments, according to a linear regression of the time-resolved cell coverage until reaching 100 % cell coverage. T = 37 °C and 0 % CO₂.

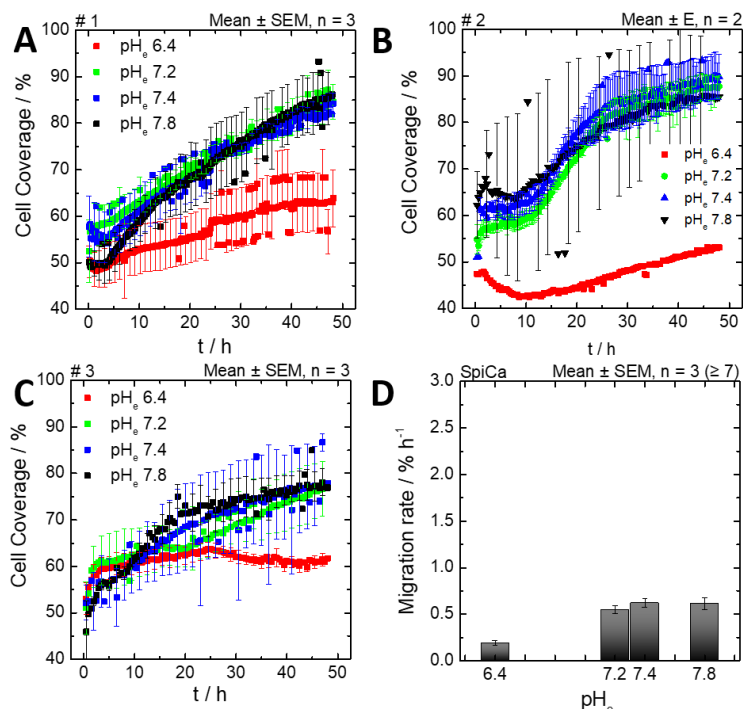


Fig. 11.10 Image-based investigation of pH-dependent migration of SpiCa cells performed with the 24-channel microscopic device zenCell owl. (A-C) Time-dependent cell coverage from individual experiments of pH-dependent migration after *scratch assay* wounding. Migration was observed under the influence of L-15 adjusted to four different pH values. (D) Calculated migration rate (cell coverage per hour) of the three individual experiments, according to a linear regression of the time-resolved cell coverage until reaching 100 % cell coverage. T = 37 °C and 0 % CO₂.

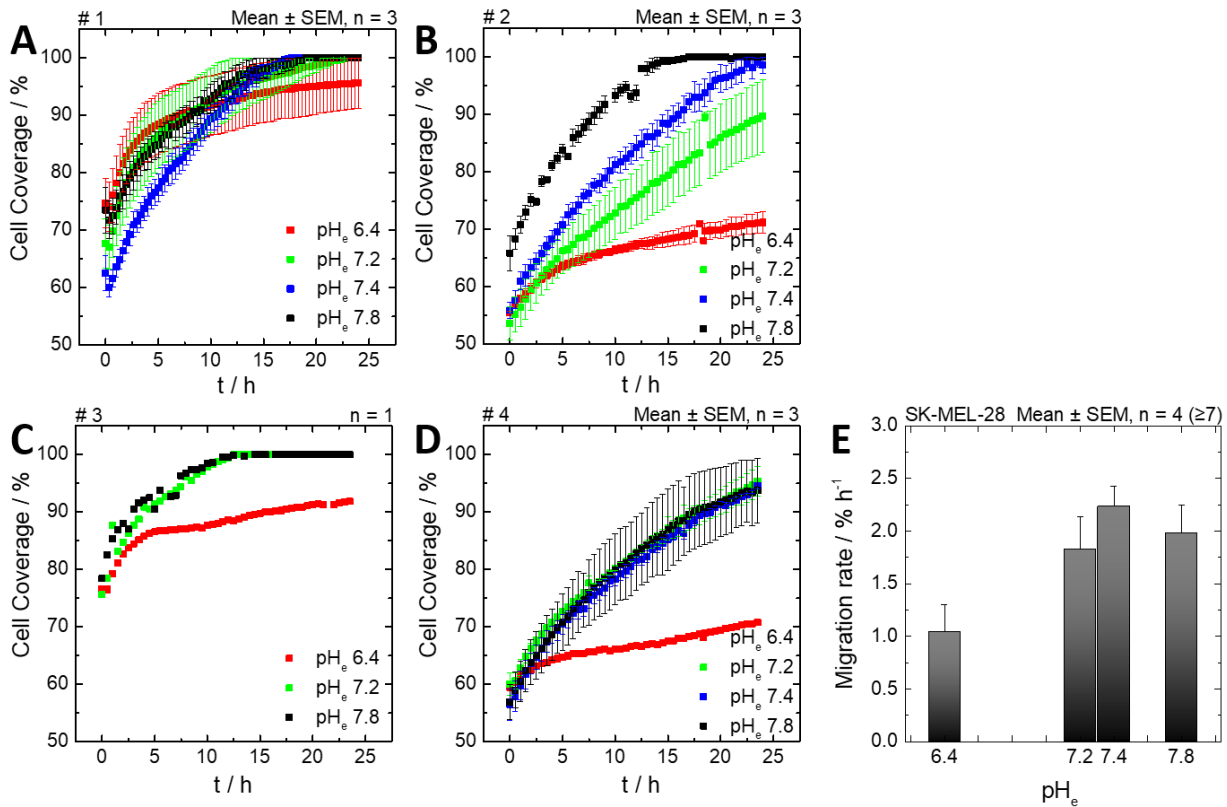


Fig. 11.11 Image-based detection of pH-dependent migration of SK-MEL-28 cells performed with the 24-channel microscopic device zenCell owl. (A-C) Time-dependent cell coverage from individual experiments of pH-dependent migration after *scratch assay* wounding. Migration was observed under the influence of L-15 adjusted to four different pH values. (D) Calculated migration rate (cell coverage per hour) of the four individual experiments, according to a linear regression of the time-resolved cell coverage until reaching 100 % cell coverage. T = 37 °C and 0 % CO₂.

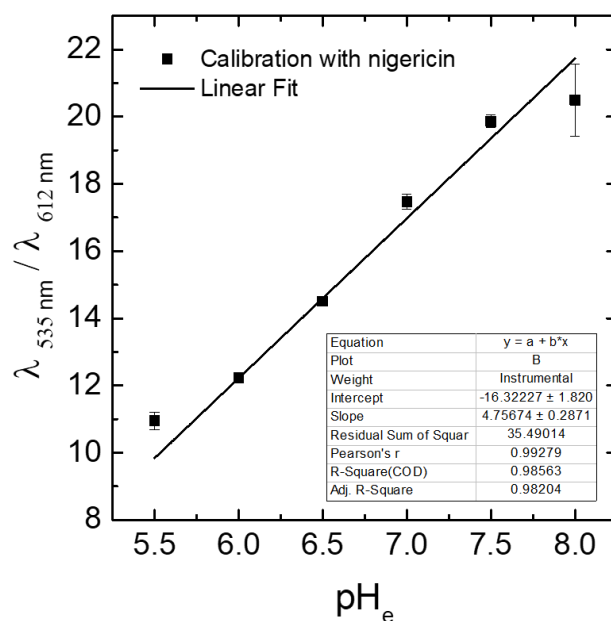


Fig. 11.12 Fluorescence signal calibration of the pH-sensitive dye BCECF for intracellular measurements. NRK cells were exposed to L-15 medium adjusted to increasing pH_e and supplemented with nigericin to ensure an equilibrium of the pH conditions between extracellular and intracellular compartments. Detected fluorescence signals were plotted against the respective pH_e value and fitted linearly. The linear fitting equation was subsequently used to determine the pH_i values.

11.2 LIST OF ABBREVIATIONS

A	
A	Area
AAC	Area above the curve
AC	Alternating current
amol	Atto (10^{-18}) mol (amount of substance)
AOCR	Apparent oxygen consumption rate
Ar	Argon
ATP	Adenosine triphosphate
AUC	Area under the curve
B	
β	Mass concentration
BCECF-AM	2',7'-bis(2-carboxylethyl)-5(6)'-carboxylfluorescein acetoxymethylester
BPA	Bisphenol A
C	
C	Capacitance
c	Concentration
$^{\circ}\text{C}$	Degree Celsius
CaAM	Calcein acetoxymethylester
CE	Counter electrode
CERM	Chip sensing embryo respiration monitoring
CCD	Charge-coupled device
CLSM	Confocal laser scanning microscope
CO_2	Carbon dioxide
D	
d	Diameter
DAPI	4',6-Diamidino-2-phenylindole
DC	Direct current
ddH ₂ O	Double-distilled water
DMEM	Dulbecco's modified eagle medium
DMSO	Dimethyl sulfoxide
DSMZ	<i>Deutsche Sammlung von Mikroorganismen und Zellkulturen</i>
E	
ECIS TM	Electric cell-substrate impedance sensing
ECM	Extracellular matrix
EDTA	Ethylenediaminetetraacetic acid
EPR	Electron paramagnetic resonance
EPSPS	5-enolpyruvoyl-shikimate-3-phosphate synthase
ESR	Electron spin resonance
EtHD	Ethidium homodimer
F	
f	Frequency
FCS	Fetal calf serum
Fig.	Figure
G	
g	Gram
Glc	D-Glucose

H	
h	Height
HEPES	4-(2-hydroxyethyl)-1-piperazineethane-sulfonic acid
Hz	Hertz
L	
L	Liter
L-15	Leibovitz medium
LED	Light emitting diode
M	
Mal	Malonoben
MDCK I & II	Madin-Darby canine kidney strain I & II
MFT	Multi-frequency/time
min	Minute
MIOS	Multiwell insert optical sensor
MW	Molecular weight
MRI / MRS	Magnetic resonance imaging / Magnetic resonance spectroscopy
N	
NADH/H ⁺	Nicotinamide adenine dinucleotide
Na ₂ SO ₃	Sodium sulfite
nF	Nano (10 ⁻⁹) farad
norm.	Normalized
NRK	Normal rat kidney
O	
O ₂	Oxygen
OC	Oxygen concentration
OCR	Oxygen consumption rate
P	
PBS ⁻	Phosphate-buffered saline (without Ca ²⁺ and Mg ²⁺)
PBS ⁺	Phosphate-buffered saline (with Ca ²⁺ and Mg ²⁺)
PDMS	Polydimethylsiloxane
PFA	Paraformaldehyde
pH _e	Extracellular pH value
pH _i	Intracellular pH value
pH _{me}	pH microenvironment
PLL	Poly-L-Lysine
pO ₂	Oxygen partial pressure
PS	Polystyrene
R	
R	Resistance
ROI	Region of interest
rpm	Revolutions per minute
RT	Room temperature
RTC	Rapid time collection measurement
S	
s	Second
SDR [®]	SensorDish Reader [®]
SECM	Scanning electrochemical microscopy
SEM	Standard error of mean
SK-MEL-28	Human skin melanoma cell line
SpiCa	Human squamous cell carcinoma

T	
t	Time
Tab.	Table
TRITC	Tetramethylrhodamine isothiocyanate
V	
V	Variance
VOG	Vertical oxygen gradient
W	
WE	Working electrode
Z	
Z	Impedance
Prefix Abbreviations	
k-, c-, m-, μ -, n-, p-, f-, a-	Kilo- (10^3), centi- (10^{-2}), milli- (10^{-3}), micro- (10^{-6}), nano- (10^{-9}), pico- (10^{-12}), femto- (10^{-15}), atto- (10^{-18})
Other Abbreviations	
8W1E	ECIS TM array with 8 wells, each with a single circular working electrode
8W10E	ECIS TM array with 8 wells and 10 circular working electrodes per well
8W10E+	ECIS TM array with 8 wells each with interdigitated electrodes

11.3 MATERIALS AND INSTRUMENTATIONS

A	
Agarose	Sigma-Aldrich, St. Louis, USA
Alexa Fluor 488 phalloidin	Invitrogen, Darmstadt, Germany
Argon Plasma Cleaner PDC 32G-2	Harrick Plasma, Ithaca, USA
Autoclave DX-45	Systec, Wettenberg, Germany
B	
BCECF-AM	Sigma-Aldrich, St. Louis, USA
Blu-Tack®	Bostik Ltd., Stafford, UK
BPA	Sigma-Aldrich, St. Louis, USA
Bunsen Burner for Cell Culture	IBS Tecnomara GmbH, Fernwald, Germany
Bürker Hemocytometer	Paul Marienfeld GmbH & Co. KG, Lauda-Königshofen, Germany
C	
Calcein AM	Invitrogen, Darmstadt, Germany
Carbolfuchsin	Sigma-Aldrich, St. Louis, USA
Cell Culture Flasks (25 cm ² , 75 cm ²)	Sarstedt, Nümbrecht, Germany
Cell Culture Incubator	Thermo Fisher Scientific Inc., München, Germany
Cell Culture Medium (DMEM)	Sigma-Aldrich, St. Louis, USA
Cell Culture Petridishes (r = 4.5 cm)	Sarstedt, Nümbrecht, Germany
Cell Culture Plate 24, 96 Well	Sarstedt, Nümbrecht, Germany
Centrifuge Heraeus Multifuge 1 S-R for Cell	Thermo Fisher Scientific Inc., München, Germany
Centrifuge Tubes (15 ml, 50 ml)	Greiner Bio-One, Kremsmünster, Austria
Cryovial TPP®	Sigma-Aldrich, St. Louis, USA
D	
DMSO	Carl Roth GmbH, Karlsruhe, Germany
DAPI	Sigma-Aldrich, St. Louis, USA
E	
ECIS™ Impedance Analyzer	Applied BioPhysics Inc., Troy, USA
EDTA	Sigma-Aldrich, St. Louis, USA
ECIS™ Arrays	Applied BioPhysics Inc., Troy, USA
EtHD-1	Biotrend Chemikalien GmbH, Köln, Germany
Ethanol	Merck, Darmstadt, Germany
F	
FCS	Sigma-Aldrich, St. Louis, USA
Fibronectin from human plasma	Sigma-Aldrich, St. Louis, USA
G	
D-Glucose	Merck, Darmstadt, Germany
L-Glutamine	Biochrom KG, Berlin, Germany
Glyphosate	Sigma-Aldrich, St. Louis, USA
H	
HEPES	Carl Roth GmbH, Karlsruhe, Germany
I	
Impedance Analyzer SI 1260	Solartron, Farnborough, UK

L	
Laminar Air Flow Work Bench HERAsafe® Latex Gloves Leibovitz Medium Liquid Nitrogen Tank GC-BR2150 M	Thermo Fisher Scientific Inc., München, Germany VWR, Pennsylvania, USA Sigma-Aldrich, St. Louis, USA Germany-Cryo GmbH, Jüchen, Germany
M	
Microplate Reader "TECAN GENios" Microscope Lens EC Epiplan-Neofluar 5x Microscope Nikon Diaphot & Nikon Eclipse 90i Microscope Nikon SMZ 1500 C-DSD230 CMO	Tecan Group, Männedorf, Swiss Zeiss, Jena, Germany Nikon Instruments Europe, Amstelveen, Netherlands Nikon Instruments Europe, Amstelveen, Netherlands
N	
Nalgene® CryoBox™ Nigericin	Sigma-Aldrich, St. Louis, USA Sigma-Aldrich, St. Louis, USA
O	
Orbital Shaker KM-2 AKKU Oxygen Sensor Foil SF-RPSu4	Edmund Bühler GmbH, Hechingen, Germany PreSens GmbH, Regensburg, Germany
P	
Parafilm® Paraformaldehyde PBS ⁻ /PBS ⁺⁺ Penicillin/Streptomycin Petri dishes pH Meter pH Sensor Foil HP5R Pipettes (10 µl, 200 µl, 100 µl) Pipette Tips (10 µl, 200 µl, 1000 µl) Polyglutamic acid sodium salt Poly-L-lysine solution PrestoBlue™	Pechiney Plastic Packaging, Chicago, USA Sigma-Aldrich, St. Louis, USA Sigma-Aldrich, St. Louis, USA Sigma-Aldrich, St. Louis, USA Sarstedt, Nümbrecht, Germany Hanna Instruments, Rhode Island, USA PreSens GmbH, Regensburg, Germany Brand GmbH, Wertheim, Germany Sarstedt, Nümbrecht, Germany Sigma-Aldrich, St. Louis, USA Sigma-Aldrich, St. Louis, USA Life technologie, USA
R	
Roundup®	Monsanto Agrar GmbH, Germany
S	
Sensor Dish Reader® Silicon Glue Aquadicht PROBAU Silicone Glue Type SG-1 Sodium dihydrogen phosphate Sodium sulfite Sterile filter (pore diameter 0.2 µm) Syringe (disposable) (5 mL, 10 mL, 20 mL) Syringe canula	PreSens GmbH, Regensburg, Germany Bauhaus, Regensburg, Germany PreSens GmbH, Regensburg, Germany Sigma-Aldrich, St. Louis, USA Merck, Darmstadt, Germany TPP (Techno Plastic Products AG), Trasadingen, Swiss Becton Dickinson, Franklin Lakes, USA Becton Dickinson, Franklin Lakes, USA
T	
Triton-X-100 TRITC-phalloidin Trypsin 0.05 % (w/v), 0.25 % (w/v)	Sigma-Aldrich, St. Louis, USA Sigma-Aldrich, St. Louis, USA Sigma-Aldrich, St. Louis, USA
V	
VisiSens TD	PreSens GmbH, Regensburg, Germany

W

Waterbath TW12
Weighting Instrument

Julabo GmbH, Seelbach, Germany
Mettler-Toledo, Columbus, USA

Z

zenCell Owl

innoME GmbH, Espelkamp, Germany

11.4 CURRICULUM VITAE

Personal Information:

Name	Lisa Pütz (formerly Sauer)
Date of birth	August 22, 1990
Place of birth	Dachau, Germany
Nationality	German

School Education and University Studies:

04/2017 – 12/2020	<p>Doctoral student (PhD) in science (Dr. rer. nat.) at the University of Regensburg, Germany</p> <p>Under the supervision of Prof. Dr. Joachim Wegener</p> <p>Institute of Analytical Chemistry, Chemo- and Biosensors</p>
10/2014 – 09/2016	<p>Master's degree in chemistry at the University of Regensburg, Germany</p> <p><u>Master's thesis:</u></p> <p><i>Nanopartikel-basierte Untersuchung der pH-Abhängigkeit der Migration von Tumorzellen</i></p> <p>Under the supervision of Prof. Dr. Joachim Wegener</p> <p>Institute of Analytical Chemistry, Chemo- and Biosensors</p>
09/2011 – 10/2014	<p>Bachelor's degree in chemistry at the University of Regensburg, Germany</p> <p><u>Bachelor's thesis:</u></p> <p><i>Entwicklung eines SPR-basierten Permeabilitätsassays</i></p> <p>Under the supervision of Prof. Dr. Joachim Wegener</p> <p>Institute of Analytical Chemistry, Chemo- and Biosensors</p>
09/2006 – 06/2010	<p>Asam Gymnasium Munich, Germany</p> <p>Qualification: Abitur</p>
09/2002 – 07/2006	<p>Secondary high school Pfaffenhofen, Germany</p> <p>Qualification: Mittlere Reife</p>
09/1999 – 07/2002	<p>Elementary & junior high school IImmunster</p>
09/1996 – 07/1999	<p>Montessori school Pfaffenhofen</p>

List of Publications

J. Stolwijk, L. Sauer, K. Ackermann, A. Nassios, T. Aung, S. Haerteis, A. Bäumner, J. Wegener, S. Schreml (2020) pH-sensing in skin tumors: methods to study the involvement of GPCRs, acid-sensing ion channels and transient receptor potential vanilloid channels, *Experimental dermatology*. **29** (11): 1055–1061.

C. Schmittlein, L. Sauer, R. J. Meier, G. Liebsch, J. Wegener (2019) Image-Based Monitoring of Oxygenation in Microfluidic Cell Culture, *Genetic engineering & biotechnology news: GEN Magazine*, **39** (1).

C. Schmittlein, R. J. Meier, L. Sauer, G. Liebsch, J. Wegener (2019) Image-Based Monitoring of Oxygenation in Microfluidic Cell Culture: PreSens Precision Sensing describes how sensor foils can serve as growth substrates and deliver 2D readouts, *Genetic engineering & biotechnology news: GEN Magazine*, **39** (1): 87-89.

Poster Presentations

R. J. Meier, C. Schmittlein, L. Sauer, J. Wegener (2019) 2D Measurements of Oxygen in Microfluidics with VisiSens.

R. J. Meier, C. Schmittlein, L. Sauer, Joachim Wegener (2018) Imaging of oxygen gradients in cell aggregates, *Conference: 3D Cell Culture – Freiburg*.

L. Sauer, R. J. Meier, J. Wegener (2018) Impedance-based Characterization of pH-dependent Cell Behavior, *Conference: IBCA Impedance Based Cellular Assays – Edinburgh*.

Application notes

L. Sauer, D. Obermeier, D. Obermeier, G. Liebsch, R. J. Meier, J. Wegener (2020) How Much O₂ Do Cells Really Face? Continuous assessment of vertical O₂ gradients in static adherent cell culture with the VisiSens™ MIOS system, *Technical Report*.

C. Schmittlein, R. J. Meier, L. Sauer, G. Liebsch, J. Wegener (2019) Monitoring Oxygenation in Microfluidic Cell Culture Using 2D Sensor Foils as Growth Substrate Oxygen Imaging with VisiSens™, *Technical Report*.

11.5 DANKSAGUNG

Als erstes möchte ich mich herzlich bei Joe für die Möglichkeit bedanken, diese Arbeit unter seiner Anleitung gemacht haben zu dürfen. Du hattest stets ein offenes Ohr für allerlei Fragen und Anliegen, bei kleineren Sackgassen sind Dir nie die Ideen ausgegangen, auch wenn sie noch so experimentell und kreativ waren. Ich habe Deine Ratschläge immer sehr geschätzt und werde auch weiterhin versuchen, sie zu beherzigen und „mein Licht nicht unter den Scheffel zu stellen“. Vielen Dank Joe für die großartige und unvergessliche Zeit.

An dieser Stelle möchte ich mich ganz herzlich bei Prof. Dr. med. Stephan Schreml und Prof. Dr. Hans-Heiner Gorris für die Übernahme des Zweitgutachtens sowie den Posten des Drittprüfers bedanken.

Ein großes Dankeschön geht auch an Dr. Robert Meier und Dr. Daniela Obermaier von PreSens GmbH für eine großartige Kooperation und die Hilfe bei allen Fragen und Problemen.

Zudem möchte ich mich bei Anne-Kathrin Mildner und Hannah Osterholz bedanken, die im Rahmen ihrer Forschungspraktika die Charakterisierung der SpiCa Zellen und die Glyphosatstudie mit bearbeitet haben und eine große Hilfe waren.

Ich bin dem ganzen Team des AGW sehr dankbar, die die letzten Jahre zu etwas ganz Besonderem gemacht haben, sei es durch aufmunternde Worte beim nachmittäglichen Kaffee, bei einem gemeinsamen Frühstück oder Grillabenden. Unvergessen bleibt natürlich auch die traditionelle Paddeltour jedes Jahr. Auch die gemeinsame Reise durch Schottland wird in Erinnerung bleiben. Besonderer Dank gilt auch Barbara, Nadja und Nicole, die stets eine helfende Hand oder die passende Antwort auf jede Frage hatten.

Jede Arbeit braucht fleißiger Leser und kritische Fragen, bis sie letztlich fertig ist. Daher ein riesiges Dankeschön an Susi, die jeden schiefen Satz gefunden und unklare Stellen kritisch hinterfragt hat. Überdies hattest Du auch stets ein offenes Ohr und bist zu einer guten Freundin geworden. Bei jeglichen EDV-Fragen und auch sonstigen Anliegen war Michi immer für mich da und hatte auch immer eine Lösung für meine Probleme, vielen Dank. Ich werde das gemeinsame Eis-Essen sehr vermissen. Letztlich würde ich mich gerne noch bei Maria, meiner Laborkollegin und Freundin bedanken: Fürs Besprechen wichtiger Dinge, fürs Zuhören und Aufmuntern, gemeinsames Lachen und Weinen, Strategiebesprechen von Experimenten und einfach für eine unvergessliche Zeit.

Ein dickes Danke geht auch an meinen Herzensmenschen Carina, danke dass Du immer da bist und in jeder Lage einfach die richtigen Worte hast!

Ich möchte mich auch ganz herzlich bei meinen Schwiegereltern Bernd und Gabi bedanken. Ihr habt immer an uns geglaubt und uns unterstützt. Vielen Dank Bernd, dass Du Dich durch die Erstfassung meiner Arbeit gearbeitet hast.

Ich bin stolzes Mitglied einer einfach großartigen Familie. Ihr habt mich immer aufgebaut, wenn ich nicht mehr konnte, habt mir immer den Rücken freigehalten. Ihr habt mir das Studium ermöglicht, ohne je Bedingungen zu stellen. Ich weiß das alles sehr zu schätzen und bin Euch unendlich dankbar. Danke Mama, Joachim, Olli und meine kleine Lucci.

Zuletzt möchte ich mich bei Pierre, meinem Mann, bedanken. Hierfür reichen ein paar Worte kaum aus. Du bist die letzten 8 Jahre mit mir durch dick und dünn gegangen, hast nie aufgehört an mich zu glauben und hast mich immer ermuntert, weiter zu machen. Du warst mir eine unendlich große Stütze während der aufregenden Zeit an der Uni Regensburg. Ohne Dich wäre diese Arbeit nicht zustande gekommen und ich freue mich auf die nächsten 100 Jahre <3.

11.6 EIDESSTATTLICHE ERKLÄRUNG

Ich erkläre hiermit an Eides statt, dass ich die vorliegende Arbeit ohne unzulässige Hilfe Dritter und ohne Benutzung anderer als der angegebenen Hilfsmittel angefertigt habe; die aus anderen Quellen direkt oder indirekt übernommenen Daten und Konzepte sind unter Angabe des Literaturzitats gekennzeichnet.

Weitere Personen waren an der inhaltlich-materiellen Herstellung der vorliegenden Arbeit nicht beteiligt. Insbesondere habe ich hierfür nicht die entgeltliche Hilfe eines Promotionsberaters oder anderer Personen in Anspruch genommen. Niemand hat von mir weder unmittelbar noch mittelbar geldwerte Leistungen für Arbeiten erhalten, die im Zusammenhang mit dem Inhalt der vorgelegten Dissertation stehen.

Die Arbeit wurde bisher weder im In- noch im Ausland in gleicher oder ähnlicher Form einer anderen Prüfungsbehörde vorgelegt.

Ort, Datum

Unterschrift